# A FLAT MODEL APPROACH TO ZIEGLER-NATTA OLEFIN POLYMERIZATION CATALYSTS

PROEFSCHRIFT

ter verkrijging van de graad van doctor aan de
Technische Universiteit Eindhoven, op gezag van de
Rector Magnificus, prof.dr.ir. C.J. van Duijn, voor een
commissie aangewezen door het College voor
Promoties in het openbaar te verdedigen
op woensdag 28 januari 2009 om 16.00 uur

door

Adelaida Andoni

geboren te Fier, Albanië

Dit proefschrift is goedgekeurd door de promotor:

prof.dr. J.W. Niemantsverdriet

Copromotoren:
dr. P.C. Thüne
en
dr. J.C. Chadwick

Adelaida Andoni

Për prindërit e mi, motrën time dhe miket e mia më të mira.

# Table of contents

# Chapter 1

## Introduction and scope

## 1.1 Catalysis

Catalysis has been, is and will continue to be indispensable for mankind. Given the fact that most products of the chemical industry are produced catalytically, catalysis can be regarded as the driving force of society. A catalyst basically boosts a chemical reaction, in other words it increases the reaction rate without being consumed itself. The word 'catalysis' originates from the Greek and means 'down' and 'loosen' [1]. Catalysis as the tool of performing reactions has been applied for thousands of years in processes such as fermentation. At the end of the eighteenth and the beginning of the nineteenth century, the influence of metals and oxides on the decomposition of several substances was investigated by many scientists. For example, it was observed that decomposition of alcohol in the presence of copper or iron produced carbon and a flammable gas [1]. Nowadays a very well-known example of catalysis is the way in which the three-way catalyst leads to a proficient decrease in pollution from car engines.

To better understand how catalysis works, a simplified schematic representation of a catalytic reaction has been depicted in Figure 1.1[*]. Let us consider a certain reaction, say $A_2+B_2 \rightarrow 2AB$. Catalysis occurs on the surface of the catalyst, therefore the so-called catalytic cycle will begin with the adsorption of the molecules onto the surface. Upon adsorption the internal bonds of the molecule will be weakened or broken. As adsorption is always exothermic, the potential energy will decrease. In the next step, the molecule undergoes one or more reactions. This leads to the formation of the desired product, which is still bound to the catalyst. Finally, desorption of the product will occur, enabling the adsorption of new reagents on the catalyst. This step is enormously important, because without it there is no catalytic cycle and therefore no catalysis. A catalyst does not change the thermodynamics of a reaction, meaning that the equilibrium remains unchanged. The rate of the reaction is enhanced as a new and a more favorable reaction pathway is established. In other words the activation energy is now lower

---

[*] The scheme in Figure 1.1 holds only for heterogeneous catalysis.

(Figure 1.1.) and as a result milder reaction conditions can be applied (lower temperatures and pressures).
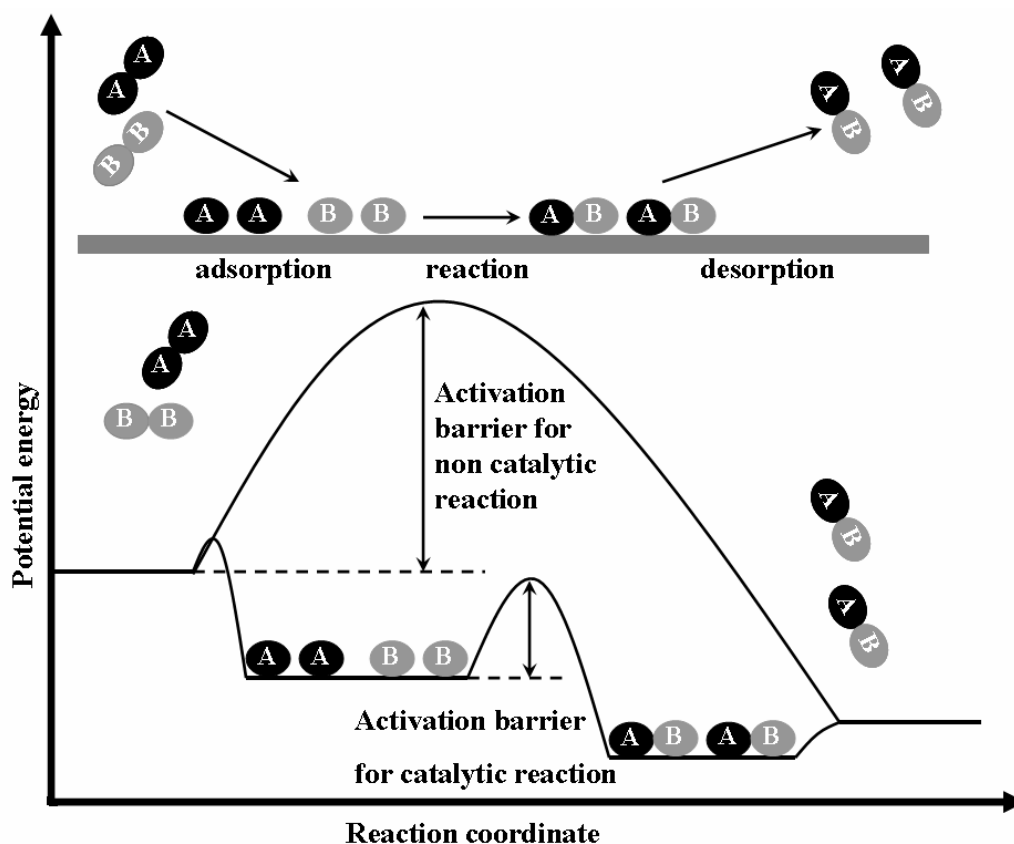


**Figure 1.1:** *Schematic representation of a catalytic reaction ($A_2+B_2 \rightarrow 2AB$) showing the potential energy diagram and displaying gas phase and catalytic reaction pathways.*

Generally speaking, catalysts are divided in two major groups: homogeneous and heterogeneous catalysts. In homogeneous catalysis all the reactants and the catalyst are in the same phase, which is commonly the liquid phase. The catalyst is usually a metal complex which dissolves in a solvent along with all the reactants. Homogeneous catalysts are frequently applied in batch processes, owing to the fact that volumes are small and the added value is high, e.g. in pharmaceuticals. Lastly, biocatalysis is an area of homogeneous catalysis where natural products (enzymes) are used in chemical reactions.

In heterogeneous catalysis the catalyst is in a different phase than the reactants. The catalyst is in the solid phase, which can be a metal or a metal oxide, whereas the reactants are in the

liquid or gas phase. Application of different types of reactions carried out in batch and continuous processes makes heterogeneous catalysis advantageous over homogeneous catalysis. Furthermore, the fairly easy separation of the catalyst from the reaction mixture offers the possibility of recycling the catalyst, lowering its costs. It is essential that the catalyst should consist of small particles with a high fraction of surface atoms (catalysis proceeds on the surface). Therefore, catalysts are usually supported i.e., dispersed on porous carriers with high surface area, such as silica, alumina, titania or carbon. However, unsupported catalysts are also in use (iron catalyst for ammonia synthesis) [2].

## 1.2    Polyethylene and polypropylene

Among the many different types of polymers, polyolefins such polyethylene (PE) and polypropylene (PP) have established a prominent position, attributable to their cost and performance balance, and their economical and environmentally friendly production. Polymers are large molecules which are made up of simple repeating units. Polyethylene is the most intensively used polymer worldwide [3]. The production of all synthetic polymers amounts to 220 Million tons per annum. Around 60 Million tons per annum are polyethylenes [3]. A polyethylene chain is a long chain of carbon atoms, with 2 hydrogen atoms attached to each carbon atom. The structure of polyethylene is depicted in Figure 1.2.
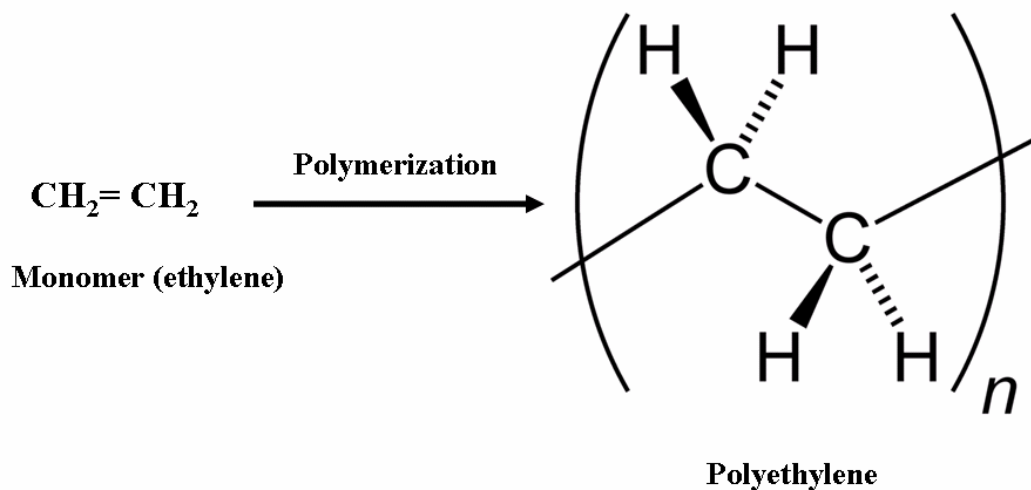


**Figure 1.2**: *The repeating of polyethylene. A single polyethylene chain can include thousands of its repeated units -CH$_2$-.*

One also can describe polymers as linear, branched and network. The degree of branching has an enormous impact on the properties of a polymer [4]. The most important types are illustrated in Figure 1.3. High density polyethylene (HDPE) has little or no branching. HDPE has a high tensile strength and high density ($\geq$ 0.94 g/cm$^3$). HDPE is resistant to many solvents and has a wide variety of applications such as plastic bags, fuel tanks and water pipes. Low density polyethylene (LDPE) consists of chains with long and short branches. The density of LDPE ranges from 0.91 to 0.94 g/cm$^3$. LDPE is broadly used for manufacturing various containers, plastic bags and computer components. Lastly, linear low density polyethylene (LLDPE) is essentially a linear polymer with significant short-chain branches (two to six atom carbons), resulting in a density in the range 0.915-0.925 g/cm$^3$.

HDPE

LDPE

LLDPE
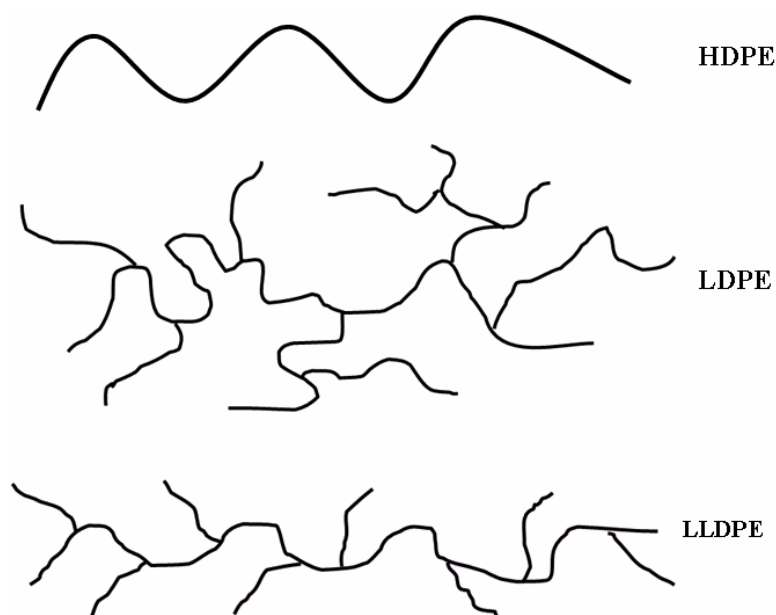
**Figure 1.3:** *Representation of the most common types of polyethylene.*

After ethylene, propylene is the simplest $\alpha$-olefin, giving a polymer with methyl side-groups along the chain (Figure 1.4). The stereochemical configuration of the methyl groups determines the tacticity of polypropylene, which can be isotactic, syndiotactic or atactic, as shown in Figure 1.5. The term tacticity stems from the Greek "taktikos", meaning relating to arrangement or order.
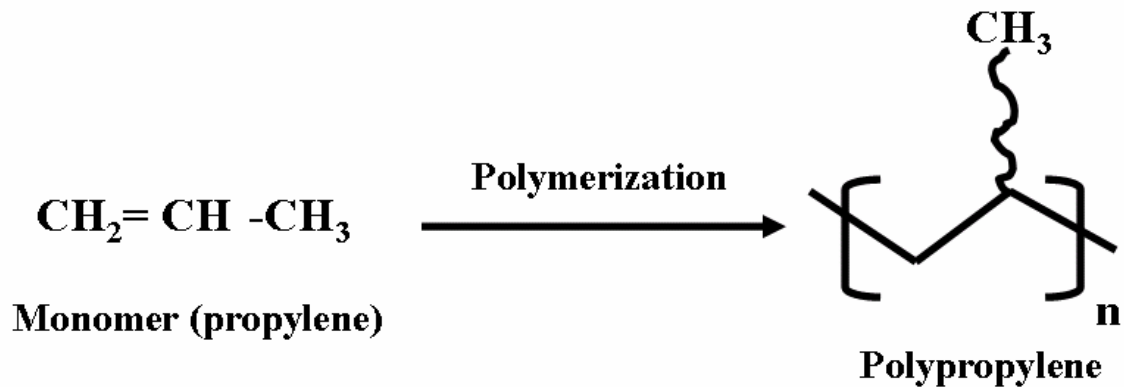
**Figure 1.4:** *Overall reaction of propylene upon polymerization.*

Isotactic polypropylene is a stereoregular polymer with all the methyl groups pointing in the same direction when the backbone is stretched. In the syndiotactic polymer, the methyl groups alternate along the chain, while a random configuration of the methyl groups leads to atactic polypropylene. Tacticity is an important concept in understanding the link between polypropylene structure and properties. The stereoregularity of the polymer structure influences crystallinity, melting temperature, solubility and mechanical properties. Because of its ordered structure, isotactic PP has a high tensile strength and a melting point of 162 °C. In contrast, atactic PP is an amorphous polymer. Polypropylene is considered to be the most versatile polymeric material, with a wide range of applications and a global production estimated to be 30 million tons in 2005 [5] and now exceeding 40 million tons.
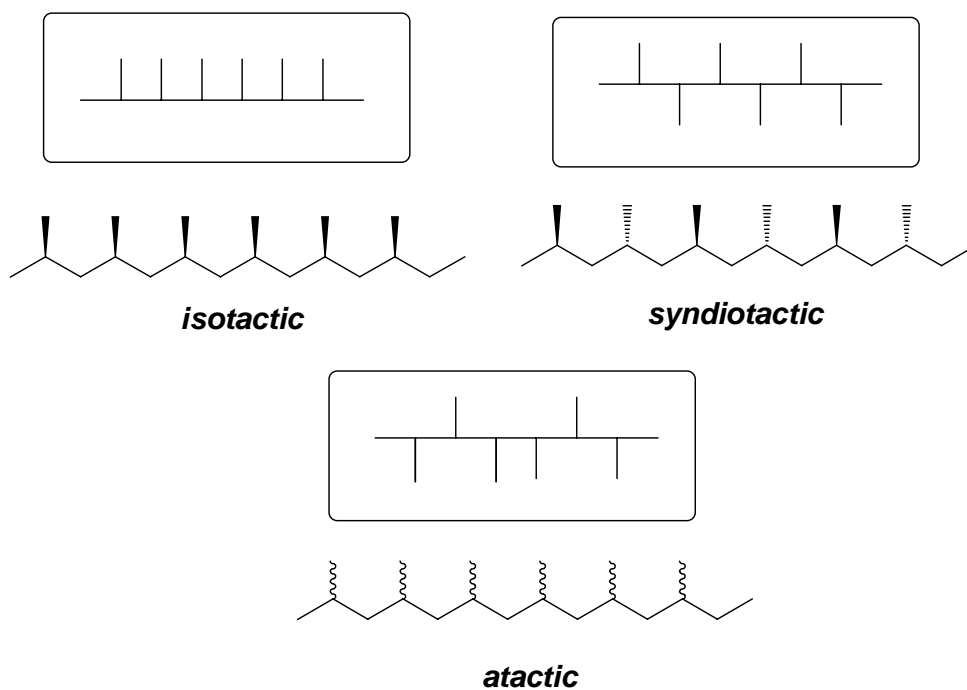
**Figure 1.5:** *Polypropylene stereoisomers; isotactic, syndiotactic, atactic.*

A very important variable which relates directly to the polymer's physical properties is the molecular weight [4]. A polymer usually does not consist of molecules with identical chain length. Distributions of chains with different molecular weight are present and the best way of representing the size of the chains is the molecular weight distribution. In general, the higher the molecular weight the tougher the polymer. However, a very high molecular weight can cause difficulties during the processing of the polymers. The molecular weight distribution is usually plotted on a logarithmic scale. Figure 1.6 presents an example of a molecular weight distribution plot of a polyethylene sample.
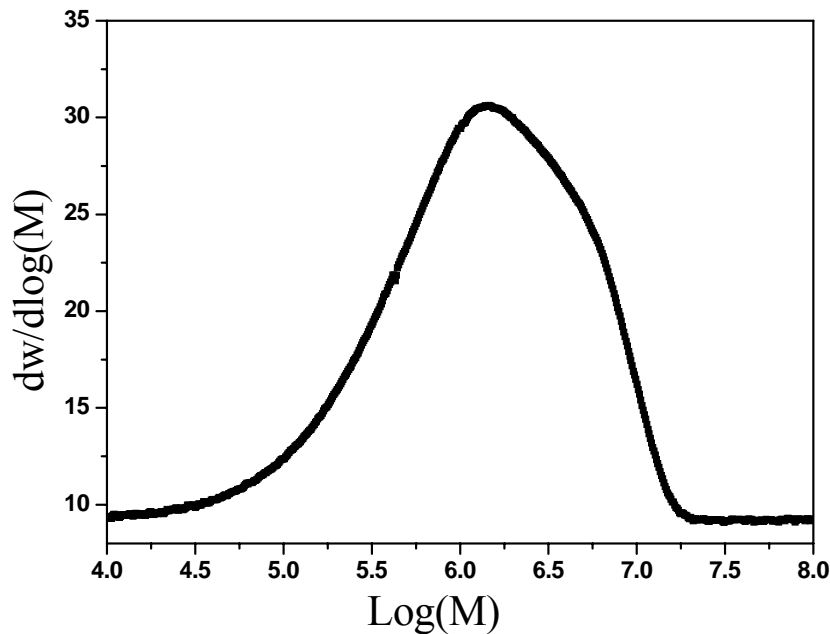
**Figure 1.6:** *A molecular weight distribution (MWD) plot of a polyethylene sample. The calculated average molecular weight values in this sample are: $M_n= 54 \times 10^4$ g/mol and $M_w= 260 \times 10^4$ g/mol.*

Molecular weight values obtained depend on the method of measurement [4]. Methods that depend on colligative properties such as freezing-point depression, boiling-point elevation and osmotic pressure give rise to the *number-average molecular weight, $M_n$*, because the number of molecules of each weight in the sample are counted. This is defined as:

$$M_n = \sum N_i M_i / \sum N_i$$

where $N_i$ is the number of molecules, or the number of moles of those molecules having molecular weight $M_i$. Thus, number-average molecular weight ($M_n$) is simply the total mass of all chains divided by the amount of chains present.

Light scattering and ultracentrifugation are the methods which determine molecular weight based on mass or polarizability of the sample [4]. The greater the mass, the greater is the contribution to the measurement. In contrast to number-average molecular weight (which is the summation of the mole fraction of each species times molecular weight), the

abovementioned methods sum the weight fraction of each species times its molecular weight. The value obtained is called the weight-average molecular weight ($M_w$) and is expressed mathematically as:

$$M_w = \sum W_i M_i / \sum W_i = \sum N_i M_i^2 / \sum N_i M_i$$

The weight-average molecular weights are always greater than number-average molecular weight, except when all molecules have the same length, in which case $M_w = M_n$. The narrower the molecular weight range, the closer are the values of $M_w$ and $M_n$. The ratio $M_w/M_n$ may therefore be used as an indication of the width of the molecular weight range in a polymer sample. This ratio is called the *polydispersity index* (PDI). Systems that have a range of molecular weights are said to be *polydisperse*. Size Exclusion Chromatography (SEC) is by far the most widely used method for the determination of molecular weight distribution (both $M_w$ and $M_n$). This method will be elaborated in more detail in **chapter two**.

## 1.3 Ethylene and propylene polymerization catalysis

The synthesis of polyethylene dates back to 1898 when the German von Pechmann accidentally heated diazomethane and polymerized it [6]. However, this route was not industrially feasible. In 1933, Fawcett and Gibson at ICI applied extremely high pressure to a mixture of ethylene and benzaldehyde and a white, waxy material was obtained [6]. This free radical polymerization led to the first industrial production of LDPE production in 1939, developed by another ICI chemist Michael Perrin [7]. After that, several researchers sought to find catalysts for ethylene polymerization. In the 1930s Marvel and Friedrich discovered that ButylLi could polymerize ethylene to produce linear polyethylene [8]. Max Fischer at BASF AG obtained a high molecular weight liquid and solid by-products with a mixture of $TiCl_4$ and Al powder [9], but it was not until the early 1950s that major breakthroughs took place. In 1951 the Americans Hogan and Banks, both working at Phillips Petroleum, discovered an ethylene polymerization catalyst comprising chromium oxide dispersed on a porous carrier material such as silica or alumina [10]. The biggest breakthrough came in 1953, when Karl Ziegler at the Max Planck Institute of Coal Research in Mülheim discovered combinations of transition metal salts and aluminum alkyls which were able to polymerize ethylene at low

temperature and pressures, giving HDPE [11]. Soon after the discovery of the Ziegler catalyst, metallocene complexes were discovered. These were able to catalyze ethylene polymerization when activated by aluminium alkyls [12, 13], but limited activity and stability of these catalysts made them unattractive from the industrial point of view. It was not until around 20 years later, in 1976, that the Germans Kaminsky and Sinn discovered a very highly active catalytic system comprising a zirconocene and methylaluminoxane [14, 15]. The methylaluminoxane (MAO) resulted from the partial hydrolysis of trimethylaluminium, which itself is an ineffective cocatalyst for metallocenes.

Polypropylene was first introduced in 1951 when the team of Phillips Petroleum Company was working on a mixture of chromium- and nickel oxide on a silica-aluminum oxide carrier [16]. This catalyst gave a semi-solid polypropylene with a molecular weight of approximately 5000-20.000. The only definite disclosure made by Phillips was that a solid, in any case partially crystalline, material had been produced [16]. In 1954, Stamatoff and Baxter conducted a series of experiments at DuPont using different catalysts for propylene [16], but a great number of experiments produced either no polymer at all or oils. The big breakthrough occurred in 1954 when Giulio Natta and his coworkers at Milan Polytechnic used the Ziegler catalyst to polymerize propylene, obtaining a tacky solid. Extraction with boiling solvents led to the isolation of amorphous and crystalline fractions which were further characterized by means of X-ray diffraction, revealing the isotactic stereoregularity of the crystalline fraction. The terms isotactic, syndiotactic and atactic to denote the different stereoisomers of polypropylene were soon established.

## 1.4   Ziegler-Natta catalysts

**The classical catalyst**: The Ziegler-Natta catalyst is unique and unchallenged in terms of versatility. The discovery in the laboratories of Karl Ziegler in the autumn of 1953 revealed that high density polyethylene could easily be made at low pressures with binary mixtures of metal alkyls and transition metal salts, such as $AlEt_3 + TiCl_4$. Then, in the spring of 1954, the Giulio Natta school demonstrated the ability of the same catalysts to polymerize propylene, subsequently developing improved, lower-valent $TiCl_3$ catalysts for the preparation of isotactic polymers from α-olefins. A Ziegler-Natta catalyst may be defined as a combination

of (1) a transition metal compound of an element from groups IV to VIII, and (2) an organic compound of a metal from groups I to III of the periodic table. The transition metal compound is referred to as the catalyst and the organometallic compound as the cocatalyst or activator. There are a great many patents concerning combinations of metal alkyls and transition metals, a few of which are used in practice. Aluminium alkyls such as $AlEt_3$, Al-*i*-$Bu_3$ and $AlEt_2Cl$ are preferred as cocatalysts, whilst transition metal compounds containing Ti, V and Cr are largely used.

Over the years, many mechanisms have been proposed for olefin polymerization with Ziegler-Natta catalysts. The most broadly accepted is the so-called monometallic mechanism proposed by Cossee and Arlman in the mid-1960s [17] for crystalline $TiCl_3$. The essential feature of this mechanism is that the surface titanium atoms, in order to ensure the electroneutrality of the system, should possess a coordination vacancy. In other words, the isospecific active site is an octahedrally coordinated titanium ion having a vacant position. The role of the cocatalyst is to form a Ti-C bond which is needed for the monomer insertion. Therefore the active center is a titanium atom having a vacant coordination site and a Ti-C bond (Figure 1.7). Polymerization occurs via two steps. First, coordination of the monomer to the active center occurs, followed by migratory insertion of the coordinated monomer into the metal-carbon bond. In this mechanism a vacant coordination site is regenerated, which enables further chain propagation. The polymer chain may or may not revert (back-skip) to the original position, depending on the ligand structure of Ti center catalyst and the presence of steric hindrance on the surface of a heterogeneous Ziegler-Natta catalyst.
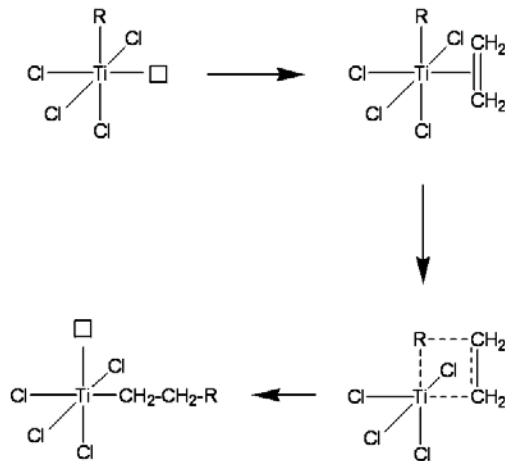
**Figure 1.7:** *Cossee-Arlman mechanism for Ziegler-Natta for olefin polymerization.*

In addition to the monomer coordination, insertion and chain propagation steps, Ziegler-Natta polymerization is characterized by a number of reactions that lead to chain termination. Polymer chain termination/transfer can occur through the steps displayed in Figure 1.8. In general, under normal polymerization conditions, chain transfer with hydrogen is the most effective process [18, 19]. For this reason molecular hydrogen is usually used to control molecular weight. Chain transfer with hydrogen leads to chain termination via formation of saturated end groups. Chain transfer can also occur via β-hydrogen transfer from the growing chain to the transition metal or to monomer, and to a lesser extent via alkyl exchange with the cocatalyst [19].

**Ti-CH₂-CH₂-Polymer**     **+**     **H₂**     →     **Ti-H**     **+**     **CH₃-CH₂-Polymer**

**Ti-CH₂-CH₂-Polymer**     **+**     **CH₂=CH₂**     →     **Ti-CH₂-CH₃**     **+**     **CH₂=CH-Polymer**

**Ti-CH₂-CH₂-Polymer**     **+**     **AlR₃**     →     **Ti-R**     **+**     **AlR₂-CH₂-CH₂-Polymer**
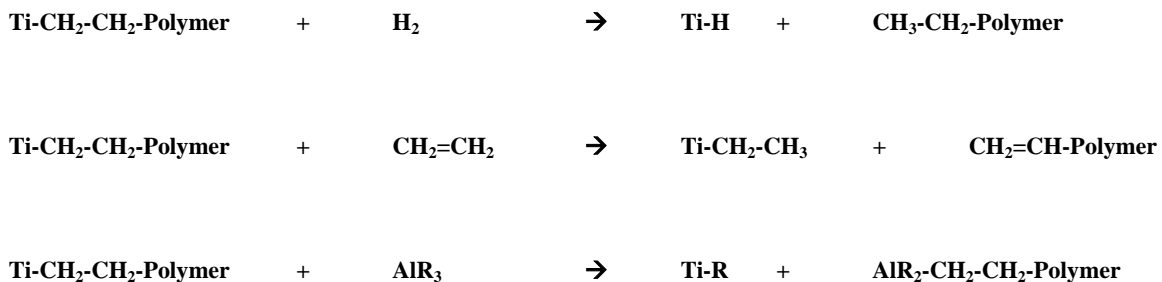
**Figure 1.8:** *Chain transfer in ethylene polymerization.*

Additionally, in propylene polymerization using titanium chloride catalysts, chain propagation occurs via primary (1,2-) insertion of the monomer. For isospecific propagation, there must be only one coordination vacancy and the active site must be chiral [19]. Corradini and coworkers have shown that the asymmetric environment of the active site compels the growing chain to adopt a particular orientation and reduce steric interactions with (chlorine) ligands present on the catalyst surface [20]. This leads to one particular prochiral face of the inserting monomer being preferred, as illustrated in Figure 1.9a, leading to isotactic polymer. However, it is essential to mention that (as will be shown later) occasionally (2,1-) insertion takes place as well in propylene polymerization (Figure 1.9b).
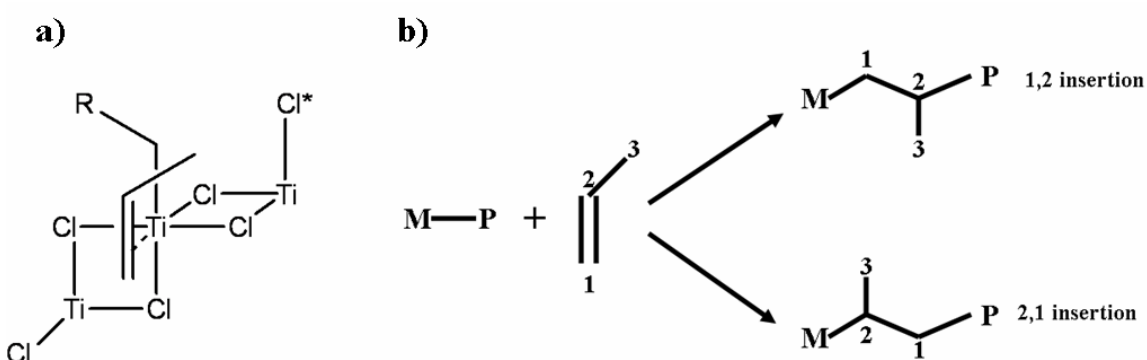


**Figure 1.9:** *a) Model for stereospecific polymerization of propylene. The orientation of the growing chain is influenced by the chlorine atom marked with an asterisk [19]. b) Scheme showing 1,2 and 2,1 insertions. M-P = metal-polymer chain.*

**Magnesium chloride support**: The production of highly active catalysts was made possible by binding $TiCl_4$ to the surface of anhydrous $MgCl_2$. The industrial process of stereospecific polymerization of propylene is carried out with Ziegler-Natta catalysts, in which the active sites are located on the edge faces of $MgCl_2$ crystallites. Actually, the foundation for the development of the high-activity supported catalysts lay in the discovery, in the late 1960s, of "activated" $MgCl_2$ able to support $TiCl_4$ and give high catalyst activity, and the subsequent discovery, in the mid-1970s, of electron donors (Lewis bases) capable of increasing the stereospecificity of the catalyst so that (highly) isotactic polypropylene could be obtained.

The finding that $MgCl_2$, mechanically or chemically activated, performs as an ideal support for the fixation of the titanium chlorides opened a new epoch in the field of the Ziegler-Natta

catalyst. This is both from an industrial and a scientific point of view. Very active catalysts may be prepared through prolonged milling of crystalline anhydrous $MgCl_2$ (usually in the $\alpha$ modification) with a Lewis base (LB), usually referred to as an 'internal donor', before contact with $TiCl_4$. Such catalysts are used in combination with an aluminum alkyl compound as cocatalyst and a second Lewis base, generally called an 'external donor' [19, 21]. Nowadays, however, the activated support is prepared by chemical means, from magnesium chloride/alcohol complexes or by reaction of magnesium alkyls or alkoxides with other halogenated compounds [19, 21]. Controlled morphology supports are prepared by rapid cooling of emulsions of molten $MgCl_2 \cdot n$EtOH adducts (n $\cong$ 2–3) in mineral oil. This process gives rise to spherical particles with a narrow size distribution.

The explanation for the success of $MgCl_2$ as a support is the crystal structure, which is very similar to that of $TiCl_3$ with respect to the interatomic distances and crystal forms. A structural layer of anhydrous $MgCl_2$ is depicted in Figure 1.10 [21]. The atoms are organized in two-dimensional hexagonal arrays, with repetition periods $a = b = 3.64$ Å, $\gamma = 120^0$ for $MgCl_2$, which constitute 'structural' triple layers. In these structural layers, the magnesium atoms are sandwiched between two layers of chlorine atoms, to which the magnesium atoms are octahedrally coordinated and strongly bonded. The stacking of structural layers along the direction normal to the layers, at a distance of 5.90 Å, in accordance with a regular hexagonal structure of packing of the bulkier halogen atoms, gives rise to the $\alpha$ (c = 17.7 Å) and $\beta$ (c = 5.90 Å) modifications, correspondingly.

In the $\delta$ modifications of $MgCl_2$, the crystal dimensions become smaller and structurally disordered, related to the way the Cl–Mg–Cl sandwich layers are piled up along the c axis. In these disordered active forms of $MgCl_2$, successive Cl–Mg–Cl sandwich layers are stacked along the $c$-axis according to a hexagonal sequence, or rotated by $\pm 60^0$ with regard to each other. In addition, the catalytic activity becomes higher [21].

The reaction of a magnesium chloride support with $TiCl_4$ leads to adsorption of the latter on lateral cleavage surfaces of $MgCl_2$, such as the (110) and (100) cuts shown in Figure 1.10. As indicated by Giannini [22], the magnesium atoms on these lateral cleavage surfaces are coordinated with 4 or 5 chlorine atoms, as opposed to 6 chlorine atoms in the bulk of the

crystal. On reaction with the cocatalyst (AlR₃), $Ti^{4+}$ is reduced to $Ti^{3+}$, and a Ti–C bond is introduced that is indispensable for the insertion of the monomer.
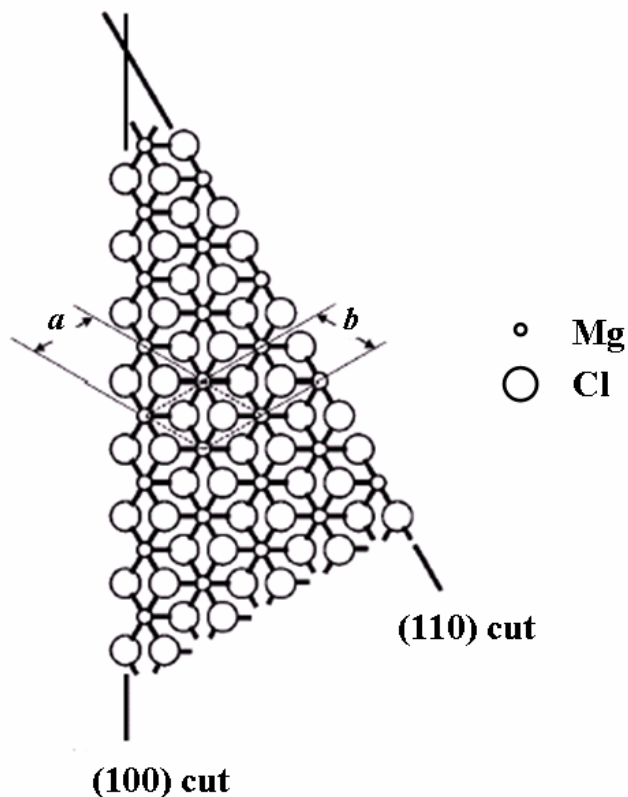


**Figure 1.10:** *Model of the Cl–Mg–Cl structural layer in MgCl₂ layer compounds showing the (100) and (110) cuts. The hexagonal unit-cell parameters a = b = 3.64 Å are also indicated [21].*

However, very recently, the crystal structure of $MgCl_2$ supports has been re-evaluated by Busico et al. who concluded that the surface with five-coordinate Mg cations should be indexed as (104) rather than (100) [23]. Periodic DFT calculations indicated that the (104) surface has relatively low energy and is the dominant lateral surface in well-formed large crystals, as well as in activated supports prepared by ball milling [23]. In this thesis (following **chapters**) we will adopt the indices (110) and (104), as advised by Busico and coworkers, for the four- and five-coordinate surfaces, respectively.

**The role of the donor**: A conventional catalyst preparation involves reaction of the $MgCl_2 \cdot n$EtOH support with excess $TiCl_4$ in the presence of an "internal" electron donor. Temperatures of at any rate 80 ºC and at least two $TiCl_4$ treatment steps are in general used, with the intention of obtaining high-performance catalysts in which the titanium is largely present as $TiCl_4$ rather than the $TiCl_3OEt$ generated in the early reaction with the support.

High-activity Ziegler-Natta catalysts including $MgCl_2$, $TiCl_4$ and an internal donor are typically used in combination with an aluminum alkyl cocatalyst such as $AlEt_3$ and an "external" electron donor which is added in polymerization step. The first catalyst systems containing ethyl benzoate as internal donor were utilized in combination with a second aromatic ester such as methyl p-toluate as external donor [24]. Subsequently, catalysts containing a diester (e.g. diisobutyl phthalate) as internal donor were developed, used in combination with an alkoxysilane external donor of type $RR´Si(OMe)_2$ or $RSi(OMe)_3$. The combination $MgCl_2/TiCl_4/$phthalate ester – $AlR_3$ – alkoxysilane is presently the most extensively used catalyst system in PP manufacture. Figure 1.11 represents chemical structures of the aforementioned donors.
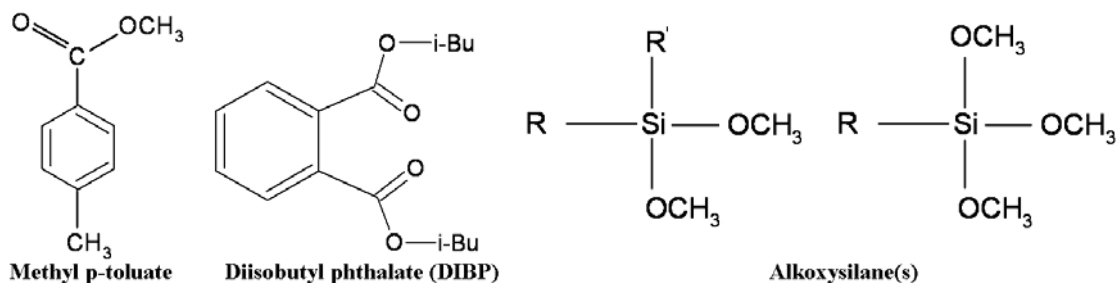


**Figure 1.11:** *Chemical structures of methyl p-toluate, diisobutyl phthalate and alkoxysilane(s).*

The function of the internal donor in $MgCl_2$-supported catalysts is dual [19]. One function is to stabilize small primary crystallites of magnesium chloride; the other is to control the amount and distribution of $TiCl_4$ in the final catalyst. Activated magnesium chloride has a disordered structure comprising very small lamellae. Bearing in mind Figure 1.10, it has been suggested that bridged, dinuclear $Ti_2Cl_8$ species can coordinate to the (100) face of $MgCl_2$ and lead though to the formation of chiral, isospecific active species. It is pointed out that

$Ti_2Cl_6$ species formed by reduction upon contact with $AlEt_3$ would be similar to analogous species in $TiCl_3$ catalysts [25, 26]. Consequently, it has been proposed [27] that a probable characteristic of the internal donor is favored coordination on the more acidic (110) face of $MgCl_2$, such that this face is prevailingly occupied by donor and the (100) face is prevailingly occupied by $Ti_2Cl_8$ dimers. It is definitely so that the role of the donor is to control the amount and distribution of $TiCl_4$ on the support surface, in addition to stabilizing small crystallites of $MgCl_2$. Nonetheless recent mechanistic and modeling studies have provided strong evidence for the formation of the active species on the (110) cut of $MgCl_2$. This will be further elaborated in the following section.

It has been shown that a monoester internal donor such as ethyl benzoate is coordinated to $MgCl_2$ and not to $TiCl_4$ in Ziegler-Natta catalysts [28]. In the search for donors giving catalysts with improved performance, it was thought [29] that bidentate donors should be able to form strong chelating complexes with tetracoordinate Mg atoms on the (110) face of $MgCl_2$, or binuclear complexes with two pentacoordinate Mg atoms on the (100) face. This initiated the development of the $MgCl_2/TiCl_4$/phthalate ester catalysts, used as mentioned above in combination with an alkoxysilane as external donor. The necessity for an external donor when using catalysts containing a benzoate or phthalate ester is because when the catalyst comes into contact with the cocatalyst, a large quantity of the internal donor is lost due to alkylation and/or complexation reactions. When the external donor is absent, poor stereospecificity is obtained due the loss of steric bulk in the vicinity of the active species on the catalyst surface. When the external donor is present, contact of the catalyst components leads to substitution of the internal donor by the external donor, as has been indicated [30, 31] with $MgCl_2/TiCl_4$/ethyl benzoate – $AlEt_3$ – methyl p-toluate and with $MgCl_2/TiCl_4$/dibutyl phthalate – $AlEt_3$ – $PhSi(OEt)_3$. The most active and stereospecific systems are those which permit the highest coordination of external donor. The effectiveness of a catalyst system depends more on the combination/choice of donors rather than on the individual internal or external donor [32].

The search for $MgCl_2$-supported catalysts which do not require the utilization of an external donor led to the identification of bidentate internal donors which not only had the right oxygen-oxygen distance for effective coordination with $MgCl_2$ but which, in contrast to phthalate esters, were not removed from the support upon contact with $AlEt_3$ and which were

not reactive with $TiCl_4$ throughout catalyst preparation. It was found [29, 33-35] that certain 2,2-disubstituted-1,3-dimethoxypropanes satisfied all these requirements. The best performance in terms of productivity and isotacticity was obtained when bulky substituents in the 2-position resulted in the diether having a most probable conformation [36] with an oxygen-oxygen distance in the range 2.8 - 3.2 Å. The successive "generations" of high-activity $MgCl_2$-supported catalyst systems for polypropylene are summarized below:

$MgCl_2/TiCl_4$/ethyl benzoate - $AlR_3$ - aromatic ester

$MgCl_2/TiCl_4$/phthalate ester - $AlR_3$ - alkoxysilane

$MgCl_2/TiCl_4$/diether - $AlR_3$

Catalyst performance has improved significantly with each generation. Table 1.1 lists the chronological development of $MgCl_2$-supported Ziegler-Natta catalysts for polypropylene with respect to the internal and external donors used.

| Internal Donor | Year of Discovery | External Donor | Productivity | Amorphous fraction | MWD |
|---|---|---|---|---|---|
| | | | kg PP/g cat. | wt-% | $M_w/M_n$ |
| Benzoate | 1971 | Benzoate | 15 – 30 | 4 – 7 | 8 – 10 |
| Phthalate | 1980 | Alkoxysilane | 40 – 70 | 1 – 5 | 6 – 8 |
| Diether | 1988 | - | 100 – 130 | 2 – 5 | 4 – 5 |
| " | " | Alkoxysilane | 70 – 100 | 1 – 2 | 4 – 5 |
| Succinate | 1999 | Alkoxysilane | 40 – 70 | 1 – 5 | 10 – 15 |

**Table 1.1:** *$MgCl_2$-based Ziegler-Natta catalysts for polypropylene. Catalyst performance for different internal and external donors [37].*

**Mechanistic aspects**:  It is well well-known that effective external donors not only enhance the isotactic index of the polymer (the amount of polymer insoluble in boiling heptane or in xylene at 25 ºC), but can also increase in absolute terms the amount of isotactic polymer formed. Major advances have been made in understanding the essential factors influencing the performance of state-of-the-art $MgCl_2$-supported catalysts. Investigations by Busico et al.

[38] have indicated that the chain irregularities in isotactic polypropylene prepared using heterogeneous catalysts are not arbitrarily distributed along the chain but are crowded together. The chain can as a result include, in addition to highly isotactic blocks, sequences which can be credited to weakly isotactic (isotactoid) and to syndiotactic blocks. This suggests that the active site can isomerise very quickly (during the growth time of a single polymer chain i.e., in less than a second) between three different propagating species. The same sequences are present, but in very different amounts due to the different active species present, in both the soluble and the insoluble fractions.

A mechanistic model has been created in which the relative contributions of these sequences can be associated to site transformations involving the presence or absence of steric hindrance in the vicinity of the active species [38]. $^{13}$C NMR studies have indicated [39] the presence of $C_1$-symmetric active species in $MgCl_2$-supported catalysts, with a mechanism of isotactic propagation which is similar to that for certain $C_1$-symmetric metallocenes, meaning that propylene insertion at a highly enantioselective site has the tendency to be followed by chain "back-skip" rather than a less regio- and stereoselective insertion when the chain is in the coordination position beforehand occupied by the monomer [38]. The possibility of chain "back-skip" occurring will increase with decreasing monomer concentration, and it has indeed been corroborated that increased polymer isotacticity is achieved at low monomer concentration. It is suggested [38] that a provisional loss of steric hindrance from one side of an active species with local $C_2$-symmetry, giving a $C_1$-symmetric species, may result in a transition from highly isospecific to fairly isospecific propagation. Loss of steric hindrance on both sides can lead to syndiospecific propagation in which chain-end control becomes effective. The model is exemplified in Figure 1.12, in which L1 and L2 represent ligands giving the necessary steric hindrance.
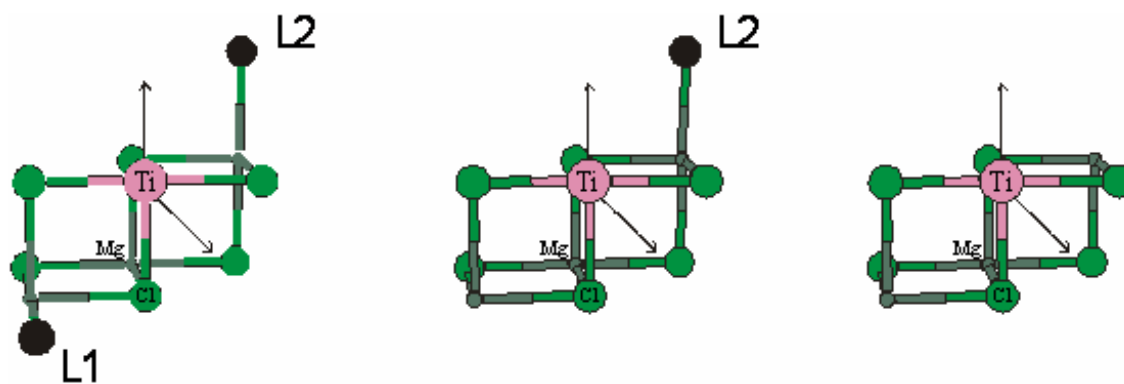
**Figure 1.12:** *Model of possible active species for highly isotactic, isotactoid and syndiotactic propagation [38].*

Assuming that the steric hindrance in the neighborhood of the active species can originate from the presence of a donor molecule, and that the coordination of such a donor is reversible, the above model offers us a clarification for the fact that strongly-coordinating, stereorigid donors usually give stereoregular polymers in which the highly isotactic sequences prevail. A number of types of active species, where the presence of a donor in the vicinity of the active Ti atom is required for high isospecificity, have been proposed [40], though the precise structure of the active species is still not resolved.

In PP production, hydrogen is used as chain transfer agent for polymer molecular weight control as mentioned. The effect of hydrogen (concentration) on polymer molecular weight is dependent on the catalyst system. A special feature of catalysts containing a diether donor, besides the very high activity, is high sensitivity to hydrogen, so that relatively little hydrogen is required for molecular weight control.

This effect can be attributed to chain transfer after the occasional secondary (2,1-) insertion rather than the common primary (1,2-) insertion. A (2,1-) insertion delays the following monomer insertion and consequently enhances the probability of chain transfer [41]. Reactivation of "dormant" (2,1-inserted) species via chain transfer with hydrogen also explains the commonly observed activating effect of hydrogen in propylene polymerization, producing yields which may be around three times those acquired in the absolute absence of hydrogen. These conclusions have been derived based on $^{13}$C NMR determination of the

relative proportions of *i*Bu- and *n*Bu-terminated chains, ensuing from chain transfer with hydrogen after primary and secondary insertion, respectively [19].

**Polymer particle growth**: Gas- or slurry-phase processes have been used for Ziegler-Natta and Phillips catalysts in polyolefin production for more than 50 years. These technologies are very efficient and well-understood. A very important feature of a heterogeneous catalyst used in gas- or slurry-phase processes for polyolefin production is its particle morphology. Heterogeneous Ziegler-Natta catalysts are microporous solids containing particle sizes typically in the range 10-100 μm [19]. Each particle consists of millions of primary crystallites with sizes of up to 15 nm. Upon contacting the solid catalyst with the cocatalyst and the monomer, diffusion through the catalyst particle will occur and polymerization will take place on the surface of each primary crystallite within the particle. As polymer is formed, the primary crystallites are pushed apart and the polymer particle grows. The particle shape is preserved and this phenomenon is referred to as replication. A simplified scheme/picture is shown in Figure 1.13. Ideally, the morphology of the particle should be spherical and the porosity should be controllable. It is essential that the mechanical strength of the catalyst is high enough to avoid disintegration but low enough to allow progressive expansion as polymerization proceeds [19].



Catalyst

Polymer growing

Final polymer particle
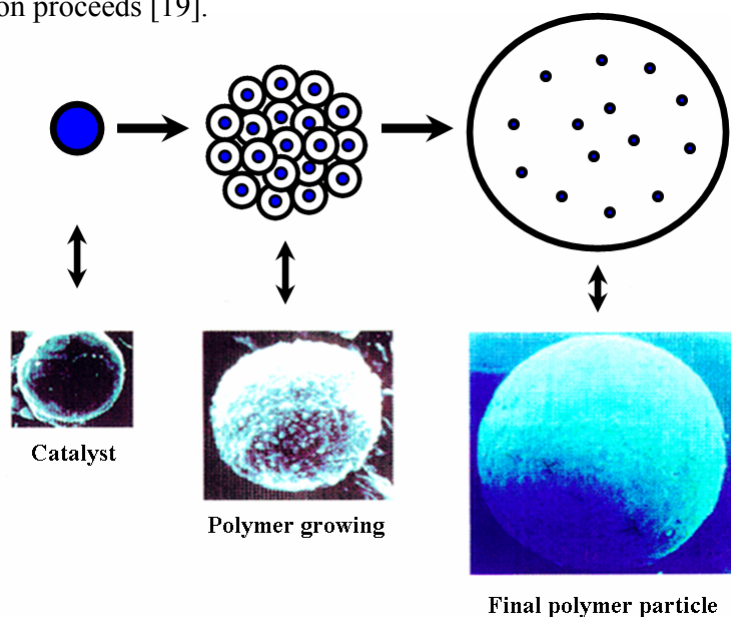
**Figure 1.13:** *"Replication" phenomenon during polymerization [7, 19].*

## 1.5    The flat model approach

An enormous amount of research is conducted all over the world with respect to the design of new catalytic systems and improvement of the existing ones. In comparison to academia, industrial research is mostly focused on developing and exploiting catalytic systems, rather than on fundamental understanding. In most cases, catalysts are very complex mixtures with a broad diversity of compounds and, despite continuous research, our knowledge of the active site and/or reaction mechanism remains unclear. Therefore, better fundamental understanding is demanded, which requires the application of spectroscopic and microscopic techniques to characterize the active catalyst, in combination with catalyst testing. This is made difficult by the fact that the active species are hidden in the pore structure of the support, limiting the exposed surface area for characterization. Furthermore, the number of active species may represent only a small proportion of the total transition metal present in the system.

A partial solution to this dilemma can be the development of model catalysts. A model catalyst is the simplified version of the existing catalyst system, prepared to obtain information on several characteristics of the catalyst which can not be obtained from the conventional catalytic system. A model is much simpler that the industrial catalyst, as the industrial support is removed or altered and promoting agents are missing. Overall, the design of a model catalyst is nothing else but a compromise between accomplishing a simple, well-defined and controllable catalyst, while at the same retaining sufficient characteristics of the industrial counterpart to make the results obtained relevant for the industrial catalyst.

A very well-known class of model catalyst is single crystals, which possess a known geometry of surface atoms, dependent on the direction of the cleavage and the crystal structure (hexagonal Rh(111) or square Rh(100)). In the past decades a large number of spectroscopic and microscopic analytical techniques have been applied which require ultra high vacuum (UHV) environment. A few of them are also applicable at higher pressures and in some cases under reaction conditions in what is called in situ spectroscopy. Single crystals have been used to unravel intrinsic kinetics of catalytic reactions by studying adsorption, desorption, and surface coverage and lateral interaction of co-adsorbates [42, 43].

In the case of Ziegler-Natta catalysts for olefin polymerization, a possible alternative in designing a model catalyst is the utilization of a flat silicon disc covered with a thin film of $SiO_2$. On top of this flat film, the support ($MgCl_2$) can easily be deposited with a technique called spin coating from an alcohol solution, creating a film of $MgCl_2$ on top of the silica. Adducts of $MgCl_2$ and ethanol are widely used in the production of industrial Ziegler-Natta catalysts. Figure 1.14 gives schematic drawings of an industrial catalyst on a support, a model catalyst on a flat support and an unsupported single crystal model catalyst.



**Industrial catalyst on porous support**

**Model catalyst on flat support**

**Unsupported single crystal model catalyst**
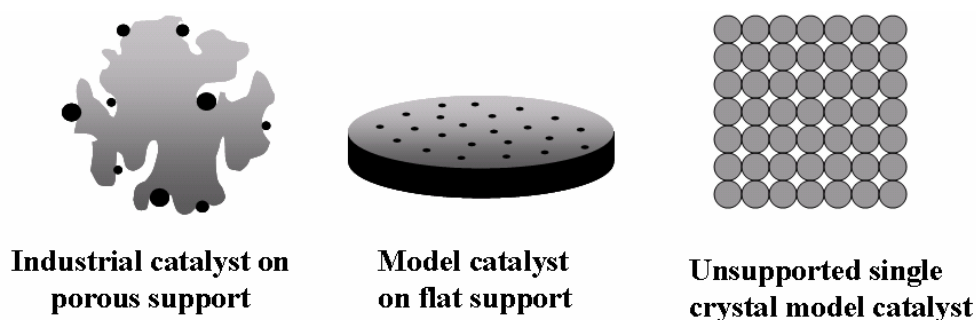
**Figure 1.14:** *Schematic drawings of (left) conventional porous catalyst; (middle) a model supported catalyst with catalytically active phase on a thin layer of flat support material; (right) a well-defined single crystal model catalyst.*

Chromium- and iron-based model catalysts have been successfully synthesized using flat silicon discs with thin silica layers [7, 44-46]. The advantages of the flat model catalyst approach are as follows:

- All catalytically active material is exposed and not hidden in pores. This makes it easier to achieve a correlation between catalyst activity and surface characterization: the surface that is probed by spectroscopy techniques is identical to the active surface.
- The silica layer is sufficiently thin to conduct and minimize the effects of charging on applying techniques like XPS, SIMS and SEM.
- The extremely flat surface facilitates the application of scanning probe techniques such as AFM, which makes it possible to visualize the catalytic surface at a nanometer resolution.

- When used to model and test polymerization catalysts, a flat active surface results in polymer growth in a direction normal to the catalyst plane to form a film. The well-defined polymer growth can be used as a tool to obtain information of the active catalyst on a micron scale.

Disadvantages intrinsic to the use of flat model catalysts are:

- Since the active phase is distributed on a very small area (dimensions in orders of centimeters), the amount of active material is extremely small. As a result the catalyst is very sensitive to impurities and extreme care should be taken in interpreting activity data. Reproducible activities similar to the conventional systems are indispensable in proving similarity with industrial catalysts.
- The small amount of active material results in small yields in absolute terms. This can trouble catalytic testing and the analysis of reaction products.

## 1.6    The flat Ziegler-Natta model catalyst

During the past decade, our group has been developing flat models for the Phillips catalyst [45-55] and iron-based model catalysts [56-58]. The Phillips catalyst has been extensively studied, whereas the investigation of iron-based model catalysts and Ziegler-Natta catalysts is more recent and rather novel.

Surface science models of olefin polymerization have mainly focused on Ziegler-Natta catalysts, aiming at an atomic description of the active ($TiCl_x$/$MgCl_2$) surface, pioneered by the Somorjai-group in the 1990s. Somorjai's group reported Ziegler-Natta model catalysts under UHV conditions [59-64]. Ultra-thin films of $MgCl_2$ were prepared via sublimation onto a gold foil, followed by gas-phase deposition of $TiCl_4$, whereas $TiCl_4$/$TiCl_2$ films were obtained by $TiCl_4$ and Mg co-deposition on $MgCl_2$ and Au. X-ray photoelectron spectroscopy (XPS) was employed to analyze the active species on the catalyst surface after exposure to the cocatalyst, $AlEt_3$. These systems were active for ethylene and propylene polymerizations.

Application of a truly and more realistic flat model, involving a flat silicon disc covered with a thin film of $SiO_2$, similar to the approach in this work, has been disclosed by Siokou and Ntais [65, 66]. These authors introduced a surface science model of Ti-based Ziegler-Natta catalysts supported on $SiO_2/Si(100)$ and prepared by spin coating THF solutions of $TiCl_4·(THF)_2$ and $MgCl_2/TiCl_4·(THF)_2$. The surface composition was characterized by X-ray photoelectron spectroscopy (XPS). However, these authors did not report any activity data for either ethylene or propylene polymerization. Additionally, Risse et al. [67] and Freund et al. [68] introduced a model system of a Pd(111) substrate covered by a $MgCl_2$ film onto which $TiCl_4$ was anchored and applied electron spin resonance to study intermediately formed radicals in the Ziegler–Natta polymerization of ethylene.

In our flat model approach, discussed in this thesis, we demonstrate the construction of a realistic flat model of a Ziegler–Natta catalyst active for ethylene and propylene polymerization. The flat Ziegler-Natta model involves the spin coating of $MgCl_2$ from ethanol solution and attempts to mimic an industrial catalyst preparation in which supports are formed by cooling emulsions of molten $MgCl_2·n$EtOH adducts in paraffin oil [69]. The flat model system has been investigated using surface science and microscopy techniques such as X-ray photoelectron spectroscopy (XPS), atomic force microscopy (AFM) and scanning electron microscopy (SEM) as well as Attenuated Total Reflectance Infrared Spectroscopy (ATR-IR).

## 1.7   Scope of this thesis

To improve the understanding of state-of-the-art $MgCl_2$-supported catalysts, relating to polymerization behavior and the effect of catalyst type on polymer composition and properties, detailed insight into the nature of the active species is required. The scope of this project is twofold:

- To develop a realistic and active model for a Ziegler-Natta system that allows a detailed study of surface chemistry and morphology, employing surface science techniques (XPS), microscopy (AFM, SEM) and Attenuated Total Reflectance Infrared Spectroscopy (ATR-IR).

- To use the model catalyst to gain fundamental understanding, in particular with regard to the role of the donor molecules that are used to control the stereoselectivity of the catalyst in propylene polymerization.

**Chapter two** explains in detail the preparation of the model catalyst, together with an introduction on the spin coating technique. Subsequently, the most important spectroscopy and microscopy techniques applied in this thesis are introduced and elaborated.

**Chapter three** demonstrates an approach to build the flat model system using deposition of $MgCl_2$ from ethanol solution by means of the spin coating technique. The next steps follow the treatment with the $TiCl_4$ and reaction with the cocatalyst solution in the presence of ethylene monomer to produce polymer films. The flat model for ethylene polymerization is systematically characterized by means of XPS, AFM and SEM.

**Chapter four** introduces a step-by-step preparation of the flat model, but now for propylene polymerization. The effect of an internal electron donor such as a diether, incorporated in the $MgCl_2$/ethanol solution will be investigated with respect to the morphology of the $MgCl_2$/ethanol films and the morphology of the polypropylene films obtained. XPS, AFM and SEM are employed yet again for characterization.

**Chapter five** describes a method for the preparation of well-defined crystallites of $MgCl_2$-supported Ziegler-Natta catalysts on $SiO_2$/Si(100) wafer with the aim to study the structure of $MgCl_2$ with respect to the formation of a particular face or faces. This has been achieved by firstly spin coating from a $MgCl_2$ solution and then applying a process called Ostwald ripening. This process will be explained in detail. The growth of the big crystallites on the flat silica/silicon facilitates their characterization using AFM and SEM-EDX (Scanning electron microscopy-Energy dispersive X-ray).

**Chapter six** deals with the effect that the type of the internal donor has on the formation of different crystallite faces of magnesium chloride. In this chapter, the different effects obtained with 9,9–bis(methoxymethyl)fluorene, diisobutyl phthalate and ethyl benzoate are described, along with the implications of these results with respect to the location and nature

of the active species present in Ziegler-Natta catalysts for polypropylene. AFM and SEM-EDX are the most exploitable techniques to characterize the structure of the support and polymer obtained.

In **chapter seven** we introduce a new technique (for Ziegler-Natta catalysts) Attenuated Total Reflectance Infrared Spectroscopy (ATR-IR) for the investigation of Ziegler-Natta catalytic systems including in situ ethylene polymerization and in situ/ex situ incorporation of the internal donors into the $MgCl_2$/ethanol films. Treatments of the $MgCl_2$/donor/ethanol with $TiCl_4$ and interactions $TiCl_4$/donors are also analyzed by IR and summarized in this chapter. Additionally the isotacticity of polypropylene films with and without donor (diether donor) has been estimated.

**Chapter eight** comprises an overview/evaluation of the most important results of the thesis along with perspectives for future research. The thesis will end with a summary of the most important results and conclusions.

## References

1. R.A. van Santen, P.W.N.M. van Leeuwen, J.A. Moulijn, B.A. Averill, Catalysis: An Integrated Approach, Elsevier, Amsterdam, 1999.
2. J.W. Niemantsverdriet, Spectroscopy in Catalysis, An Introduction, WILEY-VCH, Weinheim, 2007.
3. L.L. Böhm, Angew. Chem. Int. Ed. 42 (2003) 5010.
4. M.P. Stevens, Polymer Chemistry, An Introduction, Oxford University Press, New York, 1999.
5. S. Mukhopadhyay, S.A. Kulkarni, S. Bhaduri, J. Organomet. Chem. 690 (2005) 1356.
6. E.W. Fawcett, R.O. Gibson, M.W. Perrin, J.G. Patton, E.G. Williams, Imperial Chemical Industries Ltd. GB 471590 1937.
7. W. Han, Supported homogenous catalysts on flat model surfaces for ethylene polymerization, Ph.D. thesis, Eindhoven University of Technology 2007.
8. M.E.P. Friedrich, C.S. Marvel, J. Am. Chem. Soc. 52 (1930) 376.
9. M. Fischer, DBP874215,18,12, 1943.
10. J.P. Hogan, R.J. Banks, United States Patent US2,825,721, 1958.

11. K. Ziegler, E. Holzkamp, H. Martin, H. Breil, Angew. Chem. Int. Ed. 67 (1955) 541.

12. G. Natta, P. Pino, P. Corradini, F. Danusso, E. Mantica, G. Mazzanti, G. Moragloi, J. Am. Chem. Soc. 77 (1955) 1708.

13. D.S. Breslow, N.R. Newburg, J. Am. Chem. Soc. 79 (1957) 5072.

14. A. Andresen, H.G. Cordes, J. Herwig, W. Kaminsky, A. Merck, R. Mottweiler, J. Pein, H. Sinn, H.J. Vollmer, Angew. Chem. Int. Ed. 88 (1976) 688.

15. H. Sinn, W. Kaminsky, H.J. Vollmer, R. Woldt, Angew. Chem. Int. Ed. 92 (1980) 396.

16. H. Martin, Polymers, Patents, Profits, A Classic Case Study for Patent Infighting, WILEY-VCH, Weinheim, 2007.

17. E.I. Arlman, P. Cossee, J. Catal. 3 (1964) 99.

18. G. Cecchin, G. Morini, F. Piemontesi, Kirk-Othmer Encyclopedia of Chemical Technology, vol. 26, 2001, p. 502.

19. J.C. Chadwick, Ziegler–Natta Catalysts, Encyclopedia of Polymer Science and Technology, vol. 6, 2003, p. 517.

20. P. Corradini, V. Busico, G. Guerra, Comprehesive Polymer Science, Vol. 4, Pergamon Press, 1988, p. 29.

21. F. Auriemma, C. De Rosa, J. Appl. Cryst. 41 (2008) 68.

22. U. Giannini, Makromol. Chem. Suppl. 5 (1981) 216.

23. V. Busico, M. Causà, R. Cipullo, R. Credendino, F. Cutillo, N. Friederichs, R. Lamanna, A. Segre, V. Van Axel Castelli, J. Phys. Chem. C 112 (2008) 1081.

24. P.C. Barbè, G. Cecchin, L. Noristi, Adv. Polym. Sci. 81 (1987) 1.

25. P. Corradini, V. Busico, G. Guerra, in W. Kaminsky and H. Sinn, eds., Transition Metals and Organometallics as Catalysts for Olefin Polymerization, Springer-Verlag, Berlin, 1988, p. 337.

26. V. Busico, P. Corradini, L. De Martino, A. Proto, V. Savino, E. Albizzati, Makromol. Chem. 186 (1985) 1279.

27. E.P. Moore, Polypropylene Handbook. Polymerization, Characterization, Properties, Processing, Applications, Hanser Publishers, Munich, 1996.

28. M. Terano, T. Kataoka, T. Keii, Makromol. Chem. 188 (1987) 1477.

29. E. Albizzati, U. Giannini, G. Morini, C.A. Smith, R.C. Zeigler, in G. Fink, R. Mülhaupt, H.H. Brintzinger, eds., Ziegler Catalysts. Recent Scientific Innovations and Technological Improvements, Springer-Verlag, Berlin, 1995, p. 413.

30. V. Busico, P. Corradini, L. De Martino, A. Proto, E. Albizzati, Makromol. Chem. 187 (1986) 1115.

31. L. Noristi, P.C. Barbè, G. Baruzzi, Makromol. Chem. 192 (1991) 1115.

32. M.C. Sacchi, I. Tritto, C. Shan, R. Mendichi, G. Zannoni, L. Noristi, Macromolecules, 24 (1991) 6823.

33. E. Albizzati, P.C. Barbè, L. Noristi, R. Scordamaglia, L. Barino, U. Giannini, G. Morini (to Himont), Eur. Pat. 361494 Filed 29 Sept. 1989.

34. G. Morini, A. Cristofori (to Montell) Eur. Pat. 728724 Filed 21 Feb. 1996.

35. E. Albizzati, U. Giannini, G. Morini, M. Galimberti, L. Barino, R. Scordamaglia, Macromol. Symp. 89 (1995) 73.

36. L. Barino, R. Scordamaglia, Macromol. Symp. 89 (1995) 101.

37. J.C. Chadwick, T. Garoff, J.R. Severn, Tailor-Made Polymers via Immobilization of Alpha-Olefin Polymerization Catalysts, Eds. J.R. Severn, J.C. Chadwick, WILEY-VCH, Weinheim, 2008, Ch. 2.

38. V. Busico, R. Cipullo, G. Monaco, G. Talarico, M. Vacatello, J.C. Chadwick, A.L. Segre, O. Sudmeijer, Macromolecules, 32 (1999) 4173.

39. V. Busico, R. Cipullo, G. Talarico, A.L. Segre, J.C. Chadwick, Macromolecules, 30 (1997) 4786.

40. L. Barino, R. Scordamaglia, Makromol. Theory Simul. 7 (1998) 407.

41. J.C. Chadwick, G. Morini, E. Albizzati, G. Balbontin, I. Mingozzi, A. Cristofori, O. Sudmeijer, G.M.M. van Kessel, Macromol. Chem. Phys. 197 (1996) 2501.

42. D.L.S. Nieskens, A.P. van Bavel, J.W. Niemantsverdriet, Surf. Sci. 564 (2003) 159.

43. A.P. van Bavel, M.J.P. Hopstaken, D. Currulla, J.W. Niemantsverdriet, J.J. Lukkien, P.A.J. Hilbers, J. Chem. Phys. 119 (2003) 524.

44. P.L.J. Gunter, J.W. Niemantsverdriet, F.H. Ribeiro, G.A. Somorjai, Catal. Rev. 39 (1997) 77.

45. P.C. Thüne, A surface Science Model for the Phillips Ethylene Polymerization catalyst, Ph.D. thesis, Eindhoven University of Technology 2000.

46. E.M.E. van Kimmenade, Ethylene polymerization over flat Phillips model catalysts, Ph.D. thesis, Eindhoven University of Technology 2006.

47. P.C. Thüne, J. Loos, D. Wouters, P.J. Lemstra, J.W. Niemantsverdriet, Macromol. Symp. 173 (2001) 37.

48. P.C. Thüne, J. Loos, U. Weingarten, F. Müller, W. Kretschmer, W. Kaminsky, P.J. Lemstra, J.W. Niemantsverdriet, Macromolecules 36 (2003) 1440.

49. P.C. Thüne, C.P.J. Verhagen, M.J.G. van den Boer, J.W. Niemantsverdriet, J. Phys. Chem. B 101 (1997) 8559.

50. P.C. Thüne, J. Loos, P.J. Lemstra, J. W. Niemantsverdriet, J. Catal. 183 (1999) 1.

51. P.C. Thüne, J. Loos, A.M. De Jong, P.J. Lemstra, J.W. Niemantsverdriet, Top. Catal. 13 (2000) 67.

52. P.C. Thüne, R. Linke, W.J.H. van Gennip, A.M. De Jong, J.W. Niemantsverdriet, J. Phys. Chem. B 105 (2001) 3073.

53. E.M.E. van Kimmenade, A.E.T. Kuiper, Y. Tamminga, P.C. Thüne, J.W. Niemantsverdriet, J. Catal. 223(1) (2004) 134.

54. E.M.E. van Kimmenade, J. Loos, J.W. Niemantsverdriet, P.C. Thüne, J. Catal. 240(1) (2006) 39.

55. P.C. Thüne, J. Loos, Y. Cheng, E.M.E. van Kimmenade, B.L. Kong, J.W. Niemantsverdriet, Top. Catal. 46(1-2) (2007) 239.

56. W. Han, C. Müller, D. Vogt, J.W. Niemantsverdriet, P.C. Thüne, Macromol. Rapid Commun. 27 (2006) 279.

57. W. Han, D. Wu, W. Ming, J.W. Niemantsverdriet, P.C. Thüne, Langmuir 22(19) (2006) 7956.

58. W. Han, J.W. Niemantsverdriet, P.C. Thüne, Macromol. Symp. 260 (2007) 147.

59. E. Magni, G.A. Somorjai, J. Phys. Chem. B 102 (1998) 8788.

60. E. Magni, G.A. Somorjai, Surf. Sci. 345 (1996) 1.

61. E. Magni, G.A. Somorjai, Surf. Sci. 377–379 (1997) 824.

62. E. Magni, G.A. Somorjai, Surf. Sci. 341 (1995) L1078.

63. T.I. Koranyi, E. Magni, G.A. Somorjai, Top. Catal. 7 (1999) 179.

64. S.H. Kim, G.A. Somorjai, J. Phys. Chem. B 104 (2000) 5519.

65. A. Siokou, S. Ntais, Surf. Sci. 540 (2003) 379.

66. A. Siokou, S. Ntais, Surf. Sci. 600 (2006) 4216.

67. T. Risse, J. Schmidt, H. Hamann, H-J. Freund, Angew. Chem. Int. Ed. 41 (2002) 1518.

68. H.-J. Freund, M. Bäumer, J. Libuda, T. Risse, G. Rupprechter, S. Shaikhutdinov, J. Catal. 216 (2003) 223.

69. E. Albizzati, G. Cecchin, J.C. Chadwick, G. Collina, U. Giannini, G. Morini, L. Noristi, in: N. Pasquini (Ed.), Polypropylene Handbook, Hanser, Munich, 2005, Ch. 2.

# Chapter 2

## Experimental details

*The objective of the present chapter is to explain the experimental work carried out in this thesis. It gives an outline of the principles and the instrumental techniques applied throughout this work. The first part treats the flat model preparation and the exploitation of the spin coating technique for the catalyst preparation. A very brief description is also given regarding the operating conditions for the Ziegler-Natta catalyst. The second part deals with the techniques employed which are divided in spectroscopy, microscopy and polymer characterization.*

*Chapter 2*

## 2.1 Preparation of SiO$_2$/Si(100) planar surface for the Ziegler-Natta catalyst

The carrier for the flat model Ziegler-Natta catalyst system is a silicon disc or wafer about 120 mm in diameter. The typical size of the wafer used in this work is 3x3 cm$^2$. The preparation of the SiO$_2$/Si(100) surface has been formerly investigated and explained in the research conducted in our group [1-3]. The preparation of the flat model in this work is similar to this.

The silicon disc is initially calcined in air at 750 $^0$C for 24 hours to produce a thin layer of amorphous SiO$_2$ film which is around 20 nm thick on top of the silicon wafer. The amorphous surface consists of siloxane groups (Si-O-Si). To facilitate the spin coating of MgCl$_2$ from ethanol solution it is advisable to have a hydrophilic surface cleaned from carbon-containing impurities. This with the purpose of forming smooth, homogeneous films on the SiO$_2$/Si(100) surface upon deposition of the MgCl$_2$. An etching procedure with a mixture of concentrated ammonia and hydrogen peroxide suffices to this end.

The etching solution is a 1/1 volume mixture of 25 % NH$_4$OH (p.a. Merck) and 35 % H$_2$O$_2$ (p.a. Merck). The peroxide decomposes and oxidizes in an exothermic reaction the carbon impurities, while the strongly basic solution will dissolve slowly a few nanometers of the silica layer and the surface will be fully hydroxylated. The etching procedure is carried out at 60 $^0$C for 10 min. The etching is stopped by transferring the wafer into boiling water for the removal of NH$_4$OH and H$_2$O$_2$. This treatment is carried out for 30 min. The wafer is then dried in hot air to remove the physically adsorbed water and at more elevated temperatures to reduce the hydroxyl groups. In this work the wafers were dried at 500 $^0$C overnight (for 16 hours) and transferred at 200 $^0$C into a glove box where they were preserved before use. All the SiO$_2$/Si(100) wafers/samples used throughout the work of this thesis were prepared via this preparation method unless stated otherwise.

The wafers are then mounted on the chuck of a spin coat device. In a dry nitrogen atmosphere (under glove box conditions) the wafer is spun at 2800 r.p.m. (rotations per minute) with a solution of MgCl$_2$ in ethanol or MgCl$_2$/electron donor in ethanol for either ethylene or propylene polymerization, respectively. The solution is ejected from the wafer, leaving

behind a thin film of MgCl$_2$·$n$EtOH or MgCl$_2$(donor)·$n$EtOH. Such a wafer is ready to be treated for the next step i.e., treatment with TiCl$_4$, followed by ethylene or propylene polymerization after addition of a cocatalyst solution. The preparation procedure is depicted and summarized in Figure 2.1. During the spin coating some of the material also deposits on the back of the wafer, which may therefore also show some catalytic activity.
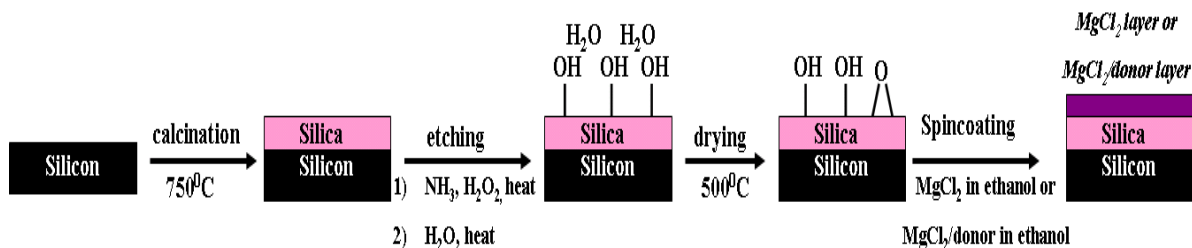


**Figure 2.1:** *Preparation of the MgCl$_2$/SiO$_2$/Si(100) model flat surface.*

## 2.2    Spin coating technique

Every preparation of a Ziegler-Natta catalyst on the flat model surface starts from the deposition of MgCl$_2$ (with or without donor incorporated) in ethanol solution onto a SiO$_2$/Si(100) surface by means of the spin coating technique. To elaborate what spin coating is, one can merely refer to the name which in essence is very informative i.e., spin to coat. Spin coating is frankly a technique which is used to coat or create films with organic, inorganic or polymeric materials from solutions by evaporating the solvent with high speed spinning. In other words it is a technique for the deposition of soluble material on planar supports by wet "impregnation", which is analogous to that of industrial impregnation procedures [4-10].

Generally a spin coat device can be schematically depicted as indicated in Figure 2.2a [2, 4]. A substrate, for example a silica/silicon wafer, is attached to a chuck, usually by means of vacuum. The wafer is covered with solution and spun at a desired speed. Spinning velocity, acceleration and spinning time are changeable parameters directly linked to the equipment. Figure 2.2b shows how the film is formed upon spinning. As the solution is ejected from the substrate by radial flow, a uniform film of, for example, MgCl$_2$ in ethanol is formed due to centrifugal forces. Upon spinning, the deposited layer becomes thinner and the shear

33

viscosity forces slow down the outer movement of the liquid. At a definite moment ejection and evaporation of liquid contribute equally in the layer thinning process [1, 2].
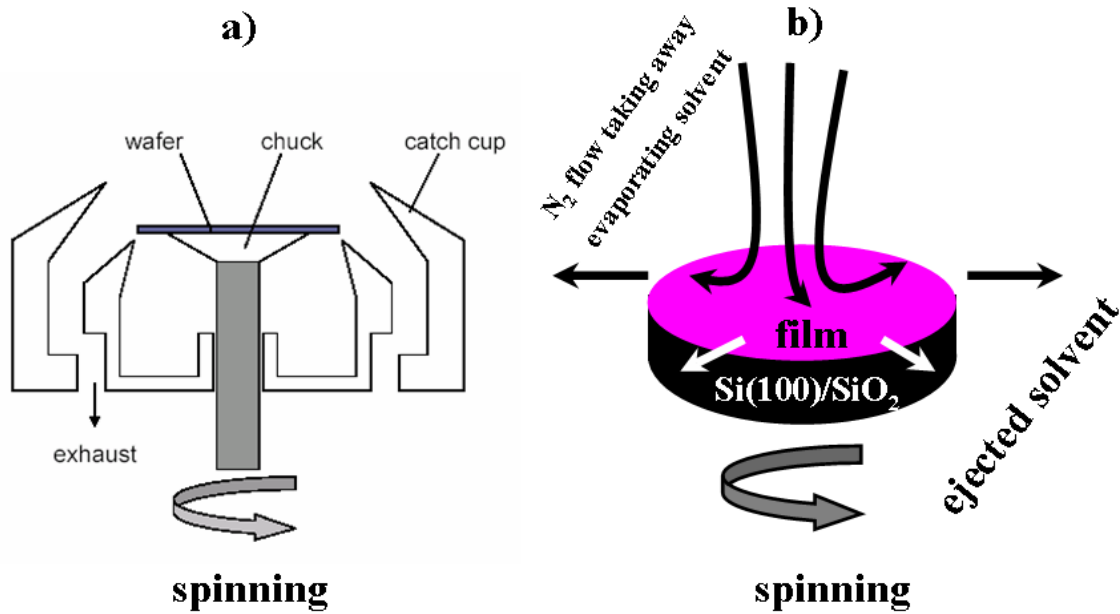


**Figure 2.2:** *a) Schematic representation of a spin coat device. The sample is mounted on a chuck by means of vacuum and spun at a desired spinning speed between 1000 and 6000 r.p.m. [2]. The excess solvent is collected on the side (exhaust). b) Evaporation of the solvent and radial liquid flow due to the centrifugal forces of the solvent determine the amount of the solute which precipitates on the wafer [1].*

From that moment the evaporation time becomes the prevailing parameter until, after a certain time $t_e$, the solvent is entirely evaporated. The evaporation time $t_e$, the spinning speed $\omega$ and the concentration of the precursor in the impregnating solution ($C_0$) determine the amount of deposited material $M$ [11-13]. The evaporation time can be determined by monitoring the disappearance of interference patterns (Newton's rings), which become noticeable when the solution layer is satisfactorily thin. The loading of the solute can be controlled by varying the concentration in the impregnating solution and is determined using the following equation [11-13]:

$$M = 1.35 C_0 \sqrt{\frac{\eta}{\rho \omega^2 t_e}} \tag{2.1}$$

where $\eta$ and $\rho$ are the viscosity and density of the impregnating solution, respectively. This equation has been verified formerly for the flat $Co/Pt/SiO_2/Si(100)$ bimetallic model catalysts prepared from $Co(NO_3)_2 \cdot 6H_2O$ and $Pt(NH_3)_4(NO_3)_2$ precursors [14] and a flat $Cr/SiO_2/Si(100)$ model catalyst prepared from $CrO_3$ [1, 2]. In general, this equation holds as long as there is no strong chemical interaction between the solute and substrate [15].

## 2.3  Working operations and reactor set up

Briefly, Ziegler-Natta catalysts are air sensitive systems. Anhydrous $MgCl_2$ can very easily adsorb water due to its hygroscopic properties. $TiCl_4$ and cocatalyst ($AlEt_3$) react rapidly and violently with water. Therefore, the delicacy of this catalytic system demands working operations to be carried out under anhydrous and anaerobic conditions in a glove box ($O_2 < 1$ ppm and $H_2O < 0.2$ ppm).

Each preparation step, starting from spin coating and ending with polymerization, is carried out in a dedicated glove box. Figure 2.3a is a picture of a spin coater device placed inside a glove box and Figure 2.3b shows a picture of a Schlenk reactor also located in the glove box and used for polymerization under continuous stirring. The wafer, prepared as explained in section 2.1, can be placed on the chuck/holder which in this case is attached to the device by a bolt. Next, deposition of $MgCl_2$ (with or without donor) from ethanol solution is done via spin coating. After treatment with $TiCl_4$ and drying under $N_2$, the wafer is placed into a solution of cocatalyst inside a Schlenk reactor which is then pressurized to run the polymerization reaction.
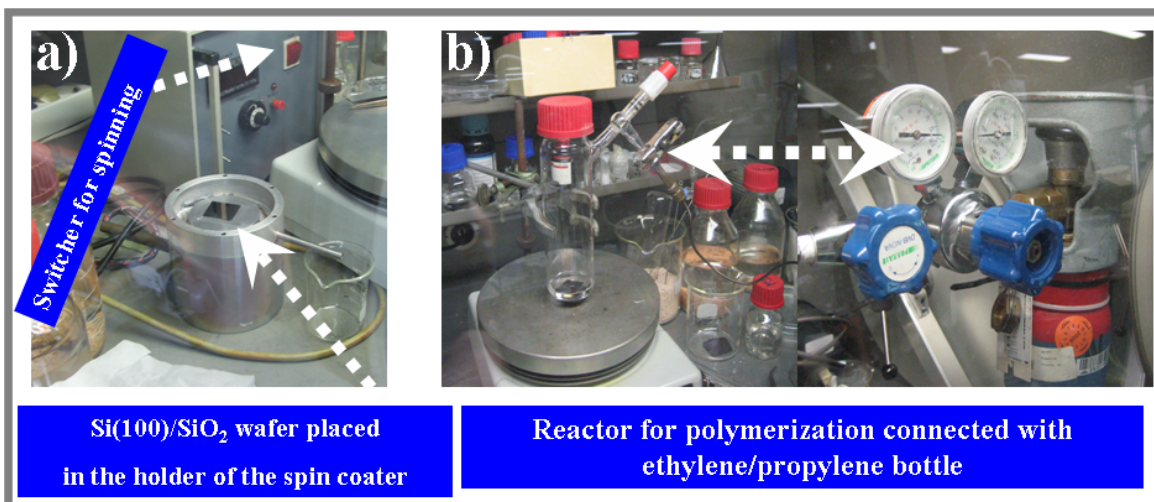
**Figure 2.3:** *a) A spin coat device located inside a glove box. b) A Schlenk reactor containing a wafer (after deposition of MgCl₂ with or without donor and treatment with TiCl₄) in a solution of cocatalyst and pressurized at a desired ethylene or propylene pressure.*

## 2.4    X-ray photoelectron spectroscopy (XPS)

XPS is amongst the most frequently applied techniques in catalysis. It is quick and easy to operate and delivers information on the elemental composition and oxidation state of all elements present. It provides qualitative and semi-quantitative information. The first commercial instruments were established in the early 1970s. XPS is based on the photoelectric effect, which was discovered by Thomson [16] and later on explained by Einstein [17]. When a material is irradiated with UV-light or X-rays, electrons are emitted. The kinetic energy of the emitted electrons depends on the wavelength of the radiation in accordance with the following equation [18]:

$$E_k = h\nu - E_b - \varphi \qquad\qquad (2.2)$$

where
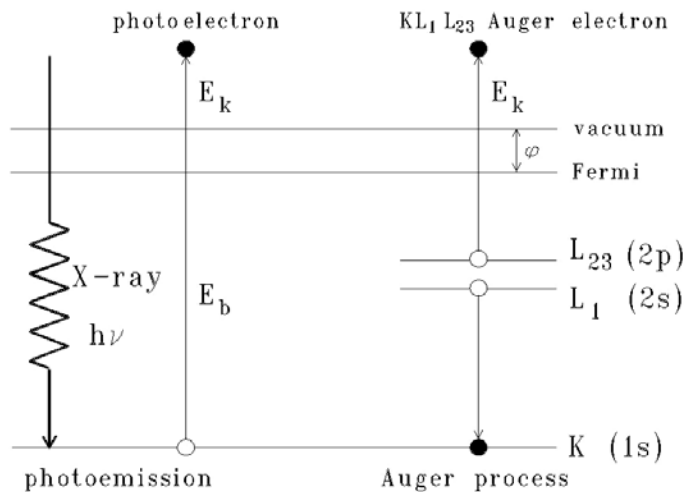
$E_k$        is the kinetic energy of the electron

$h$        is Planck's constant

$\nu$      is the frequency of the exciting radiation (speed/wavelength)

$E_b$      is the binding energy of the photoelectron with respect to the Fermi level of the sample

$\varphi$      is the work function of the spectrometer

The essential variable in equation (2.2) is the binding energy of the electron ($E_b$) which is characteristic for the atom the electron comes from. Therefore, the binding energy is element-specific. X-ray sources for XPS are often Mg Kα (1253.6 eV) and Al Kα (1486.3 eV). The intensity, *N(E)* of electrons is measured as function of their kinetic energy, usually the XPS spectrum is plotted on a binding energy scale to accentuate the reasoning.

The principle is schematized in Figure 2.4. As the sample is irradiated, an atom absorbs a photon of energy ($h\nu$) and an electron, a photoelectron to be specific, is emitted. At around the same time, but at a slower rate, an additional phenomenon occurs. The core hole created by the electron is filled with an electron from a higher shell whereas the atom relaxes from the excited state. The energy released from this step is taken up by another electron, the Auger electron, which is emitted, again with an element-specific kinetic energy. Auger electrons have fixed kinetic energies [18-20].



**Figure 2.4:** *The photoelectric effect forms the principle behind XPS. Atoms are excited with X-rays (hυ), a photoelectron is emitted with the kinetic energy ($E_k$) equal to hυ minus the binding energy ($E_b$) and the work function (φ). The empty core created by the photoelectron*

*is filled by an electron from a higher energy level ($L_1 \rightarrow K$), and the relaxation energy emits an Auger electron ($L_{23} \rightarrow Auger$) [18].*

The photoelectrons travel a very limited distance in the substance, which makes XPS very surface sensitive. The inelastic mean free path of the photoelectrons in solids is less than 1-2 nm for kinetic energies within 15-1000 eV [20], and generally the information depth of the XPS is limited to approximately three times the inelastic mean free path [18]. Hence, XPS evidently entails ultra-high vacuum (UHV) operating conditions with a pressure if possible less than $10^{-9}$ mbar.

Figure 2.5a displays a widescan spectrum of bare $SiO_2/Si(100)$ flat model carrier. The X-ray source used is Al-K$\alpha$ (1486.3 eV). The spectrum is composed of photoelectron bands which are separated into core bands and valence bands. Other peaks comprise the Auger bands, from the previously explicated Auger emission, and satellite bands. Core bands and Auger bands are the most noticeable features which make up the spectrum's element specific characteristics (Figure 2.5a). The valence bands come from the photoelectrons ejected from the valence levels, therefore they are of low binding energies. They are usually not so useful in the interpretation of the XPS spectrum. Satellite peaks originate from the X-ray source. They give rise to minor peaks with lower binding energies. Peaks for silicon, oxygen and carbon are evidently noticeable. The carbon peak is always present, irrespective of whether or not material is deposited on the wafer, due to surface hydrocarbon impurities. Figure 2.5b shows an overview XPS spectrum of $MgCl_2$ deposited from ethanol solution on a wafer via spin coating. Upon deposition of $MgCl_2$ on the planar support new peaks become visible. Besides silicon, oxygen and carbon peaks, magnesium and chlorine appear as additional peaks on the surface of the flat support.
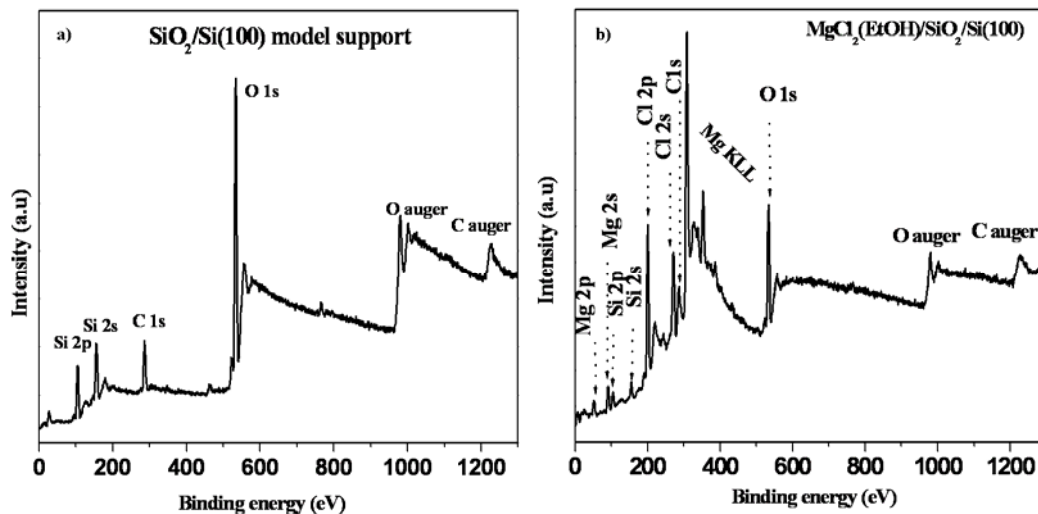
**Figure 2.5:** a) *Wide scan of the XPS spectrum of the flat SiO$_2$/Si(100) flat model support. Silicon, carbon and oxygen give distinct photoelectron peaks below binding energy of 600 eV. The less noticeable Auger peaks of carbon and oxygen appear in the higher binding energies. The valence peaks appear at binding energies lower than 15 eV. b) Wide scan of the XPS spectrum of the flat SiO$_2$/Si(100) model support after deposition of MgCl$_2$ from ethanol solution.*

During the emission of photoelectrons, the sample charges if the material is non-conductive, since it cannot compensate for the lost electrons. Due to the positive charge, introduced by the lost electrons in the sample, the peaks in the XPS spectrum all shift equally to higher energies. This problem can be effortlessly resolved by correcting the peaks using a binding energy of a known compound, such as Si 2p (103.4 eV) in supported model surfaces, or C 1s (284.6 eV) which is present in practically any surface, attributable to surface hydrocarbon impurities as noted.

Besides the ability to recognize elements, the binding energy in the XPS spectrum provides information as well on the chemical state of the element. Binding energies of metals are affected by their oxidation states. Usually, the higher the oxidation state, the higher the binding energy [18].

The quantitative information for XPS, however, has to be treated cautiously. The relative intensities of the core bands with correction factors are frequently referred to as "atomic ratios". The basic parameter which preside the relative intensities of core-level peaks ($I$) is the atomic photo-emission cross-section $\sigma(E_k)$ [18]:

$$I = F_X S(E_k)\sigma(E_k)\int_0^\infty n(z)e^{-z/\lambda(E_{k,z})\cos\theta}dz \qquad (2.3)$$

where

$I$  is the intensity of the XPS peak (area)

$F_X$  is the X-ray flux of the sample

$S(E_k)$  is the spectrometer efficiency for detecting the electron at kinetic energy $E_k$ (also called transmission function)

$\sigma(E_k)$  is the cross-section of the photoemission

$n(z)$  is the concentration, in number of atoms per unit volume

$z$  is the depth below the surface

$\lambda(E_{k,z})$  is the mean free path of the photoelectron at kinetic energy $E_k$ through the material present at depth $z$

$\theta$  is the take-off angle i.e., angle between the direction in which the photoelectron is emitted and the surface normal

Extraction of quantitative information from peak intensities should be done carefully because the area of a peak does not depend only on the amount of material present on the sample. Equation (2.3) entails that, besides the cross-section, the intensity of the XPS peak depends on the spectrometer, the concentration and distribution of the element in the surface area. The cross-sections for the elements have been calculated and tabulated. The exponential term in equation (2.3) indicates that the escape probability of the photoelectron decreases with the depth relative to the surface where the emission took place.

The mean free path of a photoelectron is not only element specific but also material specific. Quantification of the XPS spectrum is based on intensity ratios of the relevant peaks ($I_A/I_B$), but applying the intensity ratios directly necessitates the assumption of a homogeneous distribution of the elements or materials within the sample. The oversimplification may entail, for instance, that material A is homogeneously distributed on substrate B or that there are

islands of A of a certain size on substrate B, then quantitative information can be obtained on the relative concentrations of the elements by taking the ratio of the signal intensities in the same spectrum. Because of this simplification, XPS can at best be qualified as "semi-quantitative".

Overall, the important consequence of the small inelastic mean free path is that the XPS intensity for atoms located at the surface is significantly higher than for atoms underneath the surface. Atoms which are located more than a few nanometers below the surface barely contribute to the XPS signal. That is why XPS is referred as a surface sensitive technique. The information obtained regards not the bulk of the material analyzed but the surface composition.

Another important feature in XPS is that by changing the take-off angle, an easy procedure in the XPS set up, the surface sensitivity changes: the greater the take-off angle of photoelectrons between its direction and the surface normal of the sample, the greater the surface sensitivity [18]. Angle-dependency of the XPS can be used to make a coarse assessment of the vertical distribution of materials in the sample, as we have done in **chapters three** and **four** for the distribution of Ti into the $MgCl_2$ film.

To conclude XPS offers;

- quantitative information on the elements on the surface
- quantitative information on the chemical states of those elements
- quantitative information about the relative amounts of the elements

XPS is used to characterize samples of $MgCl_2$ (with or without donor), $MgCl_2/TiCl_4$ (with or without donor) in **chapters three** and **four**. Additionally, Figure 2.6 displays a picture of XPS set up where all the wafers prepared/treated with Ziegler-Natta catalyst were measured and analyzed.
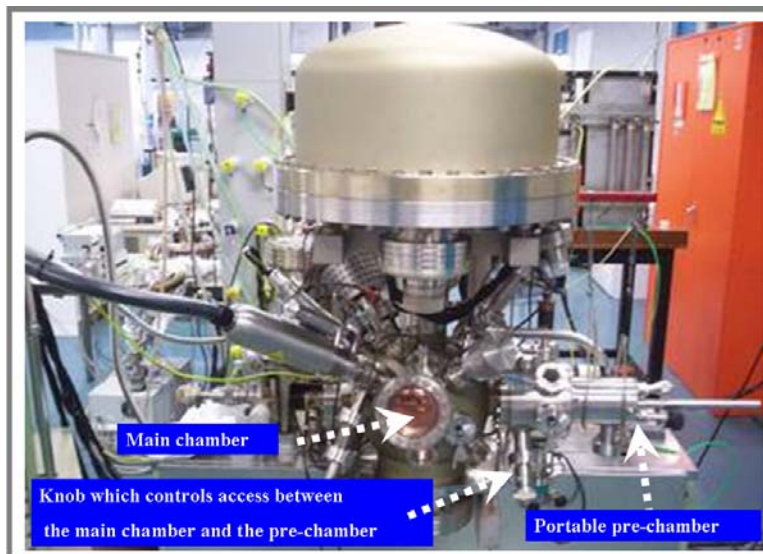
**Figure 2.6:** *XPS set up equipped with portable pre-chamber as indicated in the picture. All the wafers prepared in the glove box were transferred under $N_2$ in the pre-chamber to the XPS set up. After evacuation to about $10^{-6}$ mbar samples are introduced into the main chamber where measurements are subsequently carried out.*

## 2.5 Atomic force microscopy (AFM)

Atomic Force Microscopy (AFM) was developed in 1986 and is a member of moderately new scanning probe techniques [18, 21-23]. In contrast to conventional microscopy, the scanning probe techniques are not based on lenses and electromagnetic waves, but consist of a sharp probe i.e., a tip that scans in the proximity of the surface and the interactions between the surface and the probe are recorded. To be precise, the tip is appended on the free end of a cantilever. The deflections in the cantilever owing to the surface forces between the tip and samples are then recorded. The apex radius of an up-to-date tip is in the range of 5-10 nm.

To better understand the imaging technique of AFM, it is essential to comprehend the components of the net force between the tip and the sample. The net force is stronger than the intermolecular forces since it comprises the force between a flat surface and a spherical tip which decays at a much lower gradient ($F\sim D^{-2}$) than the force between two atoms ($F\sim r^{-7}$) (as indicated in Figure 2.7a and 2.7b) [24, 25]. This causes limitations for the resolution. Another restriction for the AFM resolution is the size of the tip. It is viable to detect very small

domains on a flat substrate with precise height (up to less than 1 Å) by AFM, if the sample deformation is not taken into account. However, the dimensions of the tip confines limits for the lateral resolution: a small feature, in the tip sized regime, is likely to show up in the AFM image wider than in fact it is, for example, a sphere is illustrated as a flat lump (Figure 2.7c) [22].

The total force is separated into three groups; I) attractive surface forces, II) forces due to sample deformation, and III) the deflection of the cantilever. The attractive surface forces are basically electrostatic in nature, significant already in the regime of 10-100 nm. The repulsive forces are short range forces and related to the sample deformation [24]. Attractive forces are described by the van der Waals potential, reliant on the polarizability and dipole moments between the molecules.
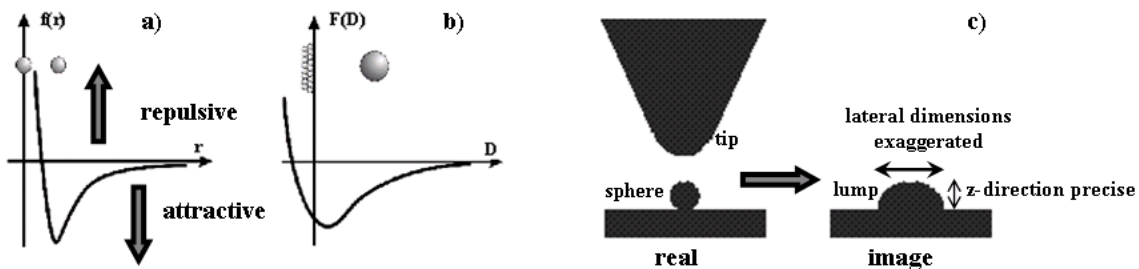


**Figure 2.7:** *a) Interaction forces between two atoms ($F \sim r^{-7}$) and b) two macroscopic particles (sphere-surface) ($F \sim D^{-2}$). D = 0 is the tip-sample contact, and D < 0 is the regime of sample deformation. [25, 26]. c) The effect of the fixed tip size to the AFM image: height is usually consistent with a precision of at least 1 Å, but the lateral dimension and the geometry of the sample are distorted.*

Another important issue is that in physical contact, the attractive surface interaction corresponds to the adhesion force ($F_{adh}$) [24-26]. AFM is generally carried out in ambient conditions (however not in this work), which influences the adhesion force in several manners, particularly as water condenses around the contact site and gives rise to capillary forces [25, 27]. Therefore, the adhesion force as a matter of fact has a capillary contribution. The deflection of the cantilever ($F_c$) is solely of mechanical nature. It depends on the cantilever material and geometry (Young's modulus, momentum of inertia). Briefly, the attractive surface force ($F_s$ which is either $F_a$ or $F_{adh}$, depending on the distance) is balanced

by the deformation ($F_d$) and the deflection of the cantilever ($F_c$) [25, 28]. In fact, these forces are enormously complicated. We limit ourselves to a simplified representation.

AFM can be operated in two modes: contact and dynamic. The dynamic mode is additionally divided into intermittent contact (tapping) and non-contact modes. In contact AFM, the static cantilever is deflected by the sample contact. To monitor a signal, the deformation forces must exceed the total surface forces i.e., $F_c = F_d - F_s > 0$ [24]. Dynamic AFM is based on vibrating the cantilever at or near its resonance frequency and measuring the changes in amplitude or frequency near the sample surface [24]. The utilization of dynamic AFM is mandatory for soft materials like polymers, which would be rigorously deformed by the tip in contact mode. In the case of $MgCl_2$ films (deposited on a wafer), which are very soft substances, only the dynamic mode is used in this thesis. When the frequency of the oscillation is maintained constant and the changes in amplitude are monitored, the operation is called intermittent contact or tapping mode [29, 30]. In non-contact mode, the oscillation amplitude is fixed and the frequency is used as a feedback parameter to measure the topology [31, 32].

In the case of the contact mode the tip is within a few angstroms of the surface and the interactions are determined by interactions between individual atoms from the tip and the surface. Contact mode is preferred in the case of atomic resolution, for example in the case of surface morphology. In the case of the dynamic mode, both sub-modes, upon scanning over the surface at a distance between 2 and 30 nm, variations in the amplitude, frequency and phase can be measured. During non contact mode operation the frequency is measured and used as a feedback signal to obtain information on the topology. In tapping mode the amplitude signal is used to measure the surface topology. This is elaborated in more detail in the following paragraphs.

Figure 2.8 illustrates the experimental set up of tapping mode AFM. The cantilever is excited at or near its resonance frequency and the sample surface is imaged whilst the feedback electronics regulate the tip-surface separation at a fixed value. The alteration in z-direction and the scanning in lateral direction are carried out with piezo crystals. The amplitude changes are recorded by focusing a laser beam at the end of the cantilever which reflects the beam onto a photo detector, usually consisting of four segments [21, 23].
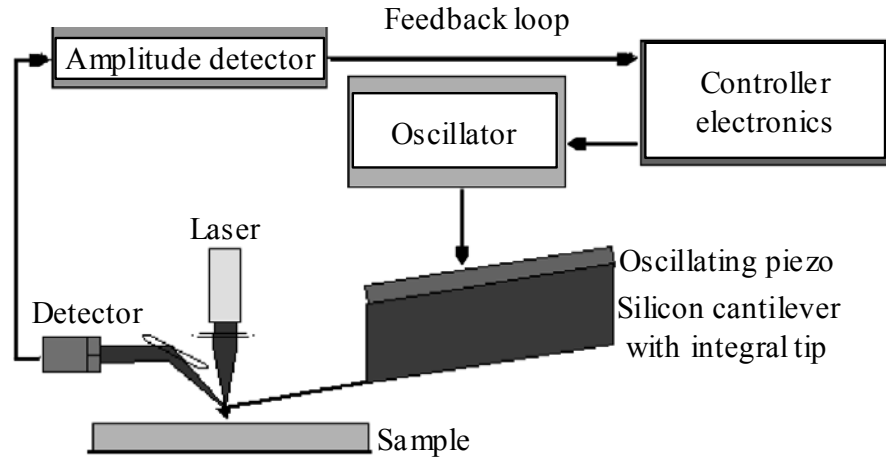
**Figure 2.8:** *Schematic overview of an AFM set up (in the tapping mode). An oscillatory piezo-crystal excites the cantilever at its resonance frequency. As the tip attached to the cantilever scans over the surface, the reduction in amplitude due to surface interactions is recorded with reflecting a laser via the cantilever on a photodetector. The distance between the sample and the tip is maintained constant by a feedback loop originating from the amplitude detector.*

In tapping mode AFM, the oscillation amplitude, phase shift, and the cantilever deflection may be recorded during the same scan. Furthermore, the tip motion is sensitive to both forces and force gradients. The principles of tapping mode - height, amplitude and phase imaging - are depicted in Figure 2.9a and 2.9b. Figure 2.9a indicates the tip excited to its resonance frequency, yet unperturbed by the surface forces of the sample.

As the tip comes closer to the sample, surface forces begin to interact with the tip in Figure 2.9b. The topography is mapped by scanning the sample on a piezo crystal under the tip and by monitoring the reduced amplitude (amplitude image), the corrected height from the feedback loop (height image), or the phase lag of the oscillation (phase image). The phase lag or phase shift is reflected by the changing angle $\phi$ in the argument of harmonic motion of the form $x = A\ cos(\omega T + \phi)$. At resonance, the phase lag is usually set to $90^0$ (Figure 2.9a).
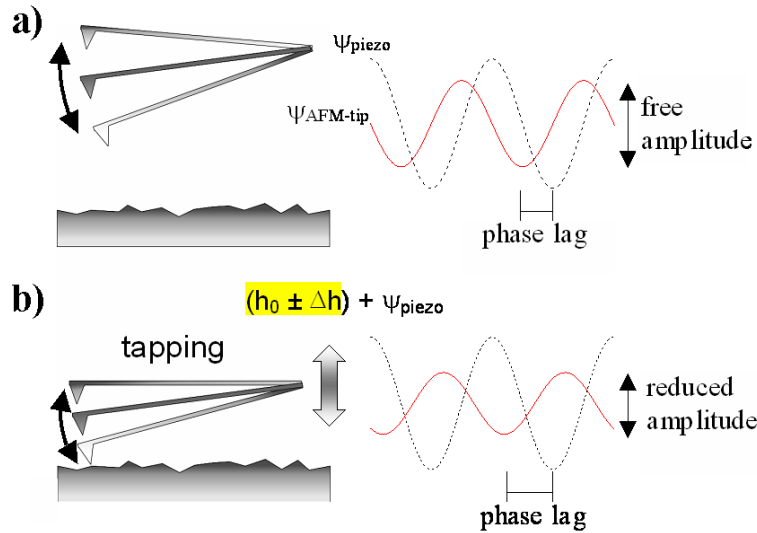
**Figure 2.9:** *a) Free oscillation in tapping mode AFM without the tip-sample interaction. Phase lag between the driving force (piezo) and the free oscillation is usually altered to $90^0$. b) Tapping mode AFM near the sample: the tip-sample interaction diminishes the amplitude (amplitude image) and gives rise to a phase lag in the oscillation (phase image). The height is altered by means of the feedback loop from amplitude detection (height image).*

The application of AFM to $MgCl_2$ films/crystals on a flat model support will be extensively discussed in **chapters three**, **four**, **five** and **six**. Additionally, Figure 2.10a shows a picture of AFM apparatus operating inside a glove box, whereas Figure 2.10b displays an AFM image of a $MgCl_2$ film deposited from ethanol solution onto a flat $Si(100)/SiO_2$ surface.
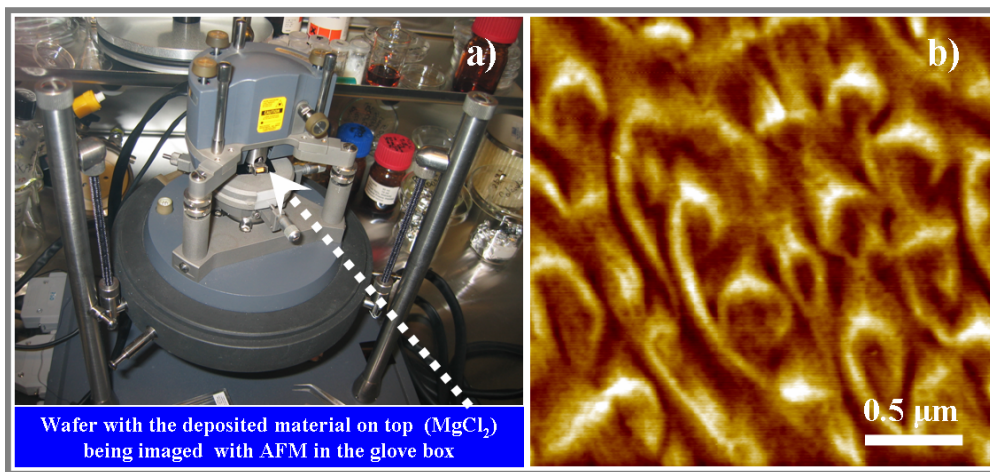


**Figure 2.10:** *a) AFM apparatus located in the glove box. b) AFM image after a wafer has been spin coated with a solution of a known concentration of $MgCl_2$ in ethanol.*

## 2.6 Scanning electron microscopy (SEM) and Energy dispersive X-ray (SEM-EDX)

The principle of scanning electron microscopy (SEM) is based on the bombarding of the sample with electrons. Electrons with energy between a few hundred eV and 50 keV leave an electron gun pass through a series of electronic magnetic lenses and then form a narrow electron beam with a very fine local spot of 1 to 5 nm size. Figure 2.11 shows interactions of a primary electron beam with a sample.

A part of the electrons will pass through the sample depending on the sample thickness. These electrons can be separated in transmitted electrons, diffracted electrons and loss electrons. Some electrons are scattered back because of elastic collisions with sample atoms, forming the backscattered electrons. Secondary electrons are formed when the primary electrons transfer energy to the sample due to inelastic scattering. Additionally, the interaction of an electron beam with a sample induces Auger electrons and X-rays and other photons from UV to infrared.

The SEM image (scanning electron micrograph) is constructed by detecting either backscattered or secondary electrons. Contrast originated from the orientation: points in the surface facing the detector appear brighter than the ones pointing away from the detector [33, 34]. Additionally, heavy atoms will appear brighter than light atoms since heavy atoms scatter electrons more efficiently.
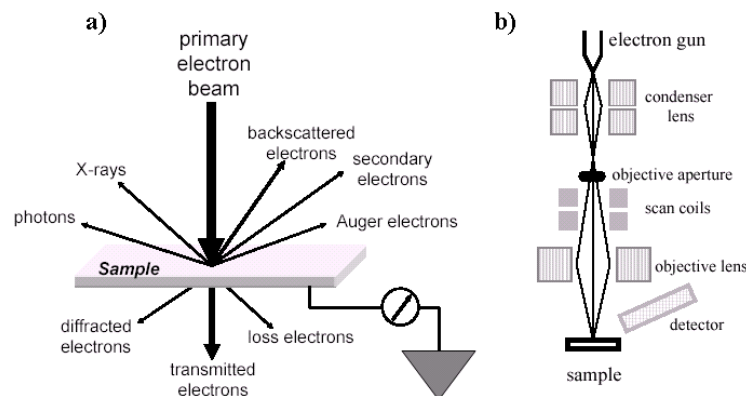


**Figure 2.11:** *a) Detectable signals upon interaction of a primary electron beam with a sample [18]. b) Schematic set up of SEM [18].*

Traditionally, SEM has to be carried out in ultra-high vacuum, although current developments have led to the invention of environmental SEM (ESEM) which permits atmospheric sampling. SEM demands almost no sample preparation with conductive samples. If the samples are non-conductive, they can be enclosed with a trim metal layer (sputtering) or low voltage can be applied to the primary electron gun [33, 34]. SEM affords a quick-and-easy visual link, paired to spectroscopic methods. The high-resolution machines deliver ~5 nm resolution but typically, like in this thesis (**chapters three**, **four**, **five** and **six**) SEM is used in the micrometer regime. Additionally, Figure 2.12 displays a picture of a typical SEM set up and a SEM image of a polyethylene sample produced with a planar model Ziegler-Natta catalyst.
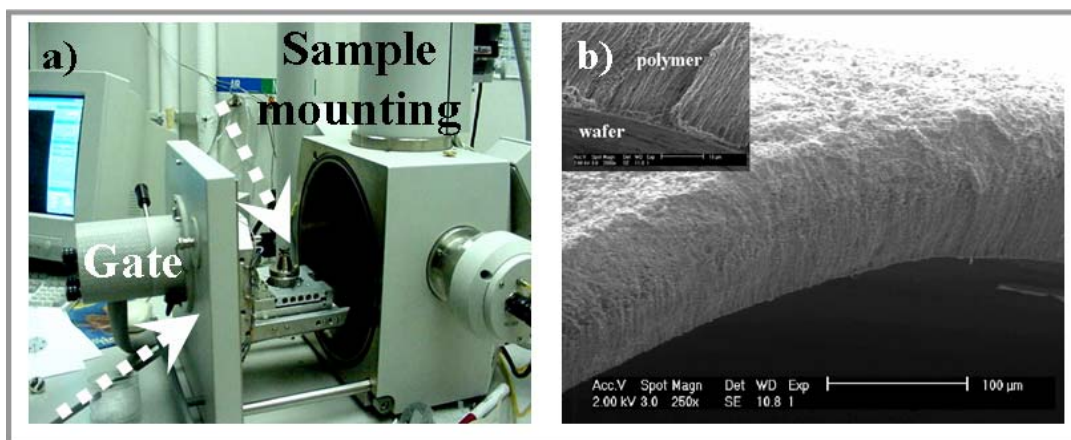


**Figure 2.12:** *a) Typical SEM set up (SEM opened sample chamber). b) SEM image of polyethylene grown on wafer after 16 hours ethylene polymerization. The inserted image displays the boundary between the wafer and the polymer grown on it.*

As indicated in Figure 2.11 X-rays are among the byproducts of electron microscopy. Energy Dispersive X-ray microanalysis or EDX is an electron beam induced X-ray spectrochemical technique which offers the possibility to determine the local chemical composition of a solid sample by means of non-destructive analysis on a microscopic scale. It is a great microanalytical tool companionable with scanning and transmission electron microscopes (SEM and TEM).

When the electron comes close to an atom core, the positive core will attract the electron, and make it change direction. The electron will accelerate when coming closer to the core, and

decelerate when moving away from the core. During the acceleration and deceleration the electron loses some energy, which is emitted as Bremsstrahlung (literal translation 'breaking radiation') [18]. The radiation in the EDX spectrum is seen as the continuum background. This continuum radiation is also known as 'white radiation'.

X-ray signals are typically generated, as noted, when a primary beam electron causes the ejection of an inner shell electron from the sample. An outer shell electron takes its place but gives away an X-ray photon. The $K_\alpha$ line arises because a primary electron creates a hole in the K shell which is filled by an electron from the L shell under emission of an X-ray quantum. $K_\beta$ radiation is emitted when the K hole is filled from the M shell, and so on [18].

The accumulated counts from a sample produce an EDX spectrum. A typical X-ray spectrum includes major spectral peaks overlaid on a broad background. As each element gives rise to characteristic spectral peaks, a qualitative composition can be extracted. Extracting quantitative information is also possible but more complicated. From the interpretation of the X-ray signal, we obtain qualitative and quantitative information about the chemical composition of the sample at the microscopic scale.

The discrete and specific energy necessary to excite any X-ray line is called the absorption edge energy, or critical excitation energy, or ionisation energy. It is always somewhat greater in energy than the corresponding X-ray emission line [18]. This means that one must choose an acceleration voltage exceeding the absorption edge energy of the line used for analysis. It must exceed, at least, the minimum energy by a suitable margin, if possible by a factor of 2 to 3 (also called the overvoltage) to efficiently excite the X-ray line with an electron beam. In other words, when measuring with SEM-EDX the incoming electron must be higher in energy than the critical excitation energy of the element, for example, for exciting the Fe $K_\alpha$ = 6.398 keV edge, a beam voltage of 20 - 25 keV is needed.

Interaction of the electron beam with a sample causes electron scattering and gives rise in an interaction volume. As illustrated in Figure 2.13 the volume that is activated by the electron beam has the shape of a pear with typical dimensions of a few micrometers.  As a consequence, X-rays formed in the interior may be absorbed on their way out and stimulate

the emission of photoelectrons [18]. It should be noted that the depth penetration is not a linear relation to the beam energy. The total depth of the electron penetration is a function of the elemental make up of the material and the accelerating voltage [18].
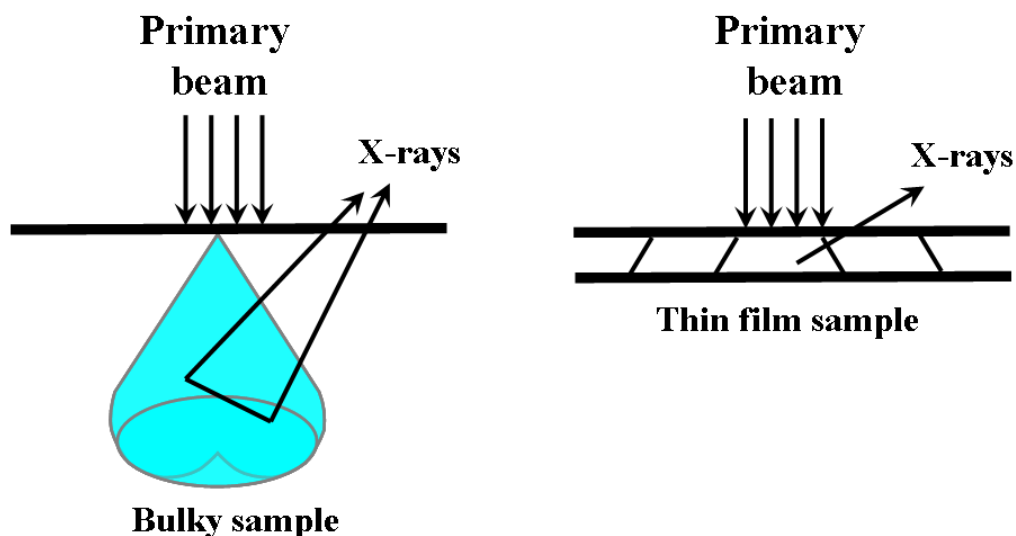
**Figure 2.13:** *Schematic representations of the interaction of a primary beam of electron with a sample which results in an interaction volume. Irradiation of a bulk sample activates a pear-shaped volume from which the X-rays are emitted. The chance of secondary processes is considerable. Secondary effects are much less important if the sample is a thin film [18].*

The spatial resolution is more or less equal to the maximum diameter of the interaction volume, therefore the spatial resolution will always be larger than usual. The interaction volume decreases with increasing atomic number. In samples with elements of high atomic number, the importance of elastic scattering causes the electrons to deviate from their initial path, and to limit the penetration depth. In samples of low atomic number, elastic scattering is less important, allowing for deeper penetration into the sample. The shape of the interaction volume therefore considerably changes with atomic number. Pear shaped interaction volumes are typical for low atomic number materials, whereas spherical interaction volumes are typical for high atomic number materials [18].

Additionally, Figure 2.14 represents carbon ($C_{K\alpha}$ line) mapping originating from polypropylene grown on the edges of $MgCl_2$ crystallites after 16 hours propylene polymerization.
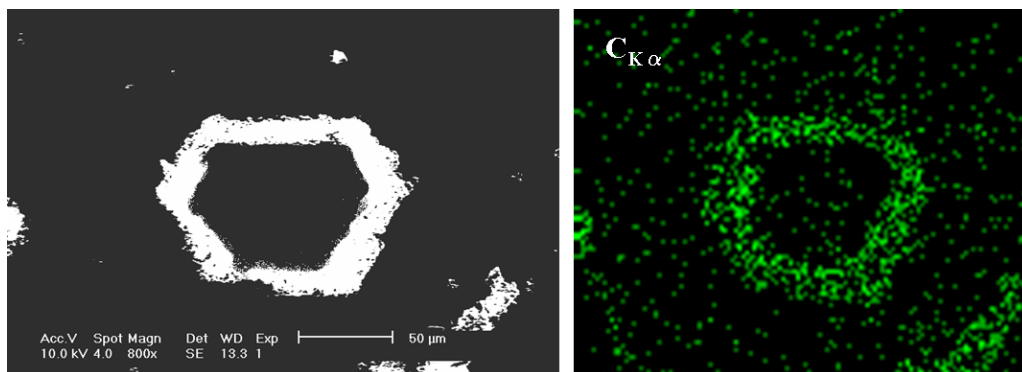
**Figure 2.14:** *Carbon mapping for the corresponding image. The applied accelerating voltage was 10 kV. The spin coated layer of MgCl$_2$/electron donor (from ethanol) has been subjected to a process called Ostwald ripening (this process will be explained in detail in **chapter five**), treated with TiCl$_4$ and polymerized for 16 hours under propylene pressure.*

## 2.7 Size exclusion chromatography (SEC)

Size exclusion chromatography is a technique which acquires the molecular weight distribution of a polymer sample by the separation of the molecules based on their size. The technique is as well established as gel permeation chromatography (GPC), a name which dates back to the time of glass columns with gels. The latter were used to perform the analysis for the determination of molecular weight distribution. Currently high pressure liquid columns are utilized and SEC is the accurate term.

In SEC a column is filled with different beads of a porous material (silica or cross-linked polystyrene) with a definite pore size. A solvent (e.g. 1,2,4-trichlorobenzene or tetrahydrofuran) goes through the column at around 1 mL/min and pressures of 50 to 200 bars. The polymer sample is dissolved in the same solvent and is infused in the solvent stream that runs through the column. In solution each polymer chain encloses a definite volume (the hydrodynamic volume) which depends on the chain size. In the column the chains are separated, based on a different ability to disseminate into the porous material. Larger molecules have a large hydrodynamic volume and will as a result have more difficulty to enter into the pores. Thus these longer chains will stay longer in the mobile solvent phase and will pass through the column quicker. Smaller molecules prefer to stay in the stationary

phase because they fit basically in all the pores and so more time is required for them to pass through the column. Eventually, a detector measures the sample concentration in the solvent flow. In this manner a plot is created of detector response versus retention time. Together with calibration data this plot is converted to a plot displaying the quantity of material as a function of molecular weight. Since SEC measures the hydrodynamic volume instead of chain size, calibration of the equipment is essential in obtaining meaningful data. Calibration is done by injecting samples of accurately known molecular weights. The combination of SEC with viscometry, applied to the liquid stream exiting the column, has also been developed and is a potent instrument in determining the degree of branching in a polymer sample.

## 2.8 Differential scanning calorimetry (DSC)

Differential scanning calorimetry (DSC) is a thermo-analytical technique in which the quantity of heat is measured that is necessary to heat a sample at a definite rate. The technique can be applied to examine phase transitions, such as fusion, crystallization, and glass transitions which are all associated by the exchange of heat. This makes DSC a popular technique in polymer research. Measuring a sample with DSC engages the preparation of two pans. One encloses the sample of known weight, the other one is empty and is used as a reference. The pans are made of a heat conducting material which is aluminum in the majority of cases. By precisely weighing the empty pans their exact heat capacity is known. Both pans are mounted in the DSC apparatus and both heated and/or cooled at the same rate in accordance with a preset temperature program. Meanwhile the difference in heat that is transferred to or from the two pans is recorded.

When no phase change is taking place during heating, the DSC plot displays a flat base line which has a positive value in line with the heat capacity of the sample. When the sample experiences a phase change such as melting, the extra energy that is needed corresponding to the empty pan is shown as a peak in the DSC plot. From the area of these peaks enthalpies can be calculated which can disclose information on morphology and purity of a sample. An example is the heat of melting for partially crystalline polyethylene, from which the degree of crystallization can be determined.

## 2.9 Attenuated total reflection – Fourier transform infrared (ATR-FTIR) spectroscopy

The principle of the ATR-IR, also known as Internal Reflection Spectroscopy, is depicted in Figure 2.15. It is based on the existence of an evanescent wave in the medium of low index of refraction when the infrared (IR) radiation propagates in a denser medium in a total internal reflection mode [35, 36]. The infrared radiation passes through an Internal Reflection Element (IRE), which is an infrared transparent crystal of high refractive index. In total reflection, when light is reflected at the interface between two media of different refractive indexes (crystal and sample), the evanescent wave expands beyond the reflecting interface in the less dense medium. The evanescent wave decays exponentially in accordance with equation 2.4 [36], which permit this technique to probe only the first micrometers in the rarer medium:

$$E = E_0 \exp[-\frac{2\pi}{\lambda_1}(\sin^2\theta - n_{21}^2)^{1/2} Z] = E_0 \exp(-\gamma Z) \qquad (2.4)$$

where

$n_{21} = n_2 / n_1$     and $n_1$ is the refractive index of the less dense medium (sample in ATR-IR), $n_2$ is the refractive index of the denser medium (internal reflection element in ATR-IR)

$\lambda_1$ is $\lambda/n_1$,     i.e., the wavelength in the denser medium

$\theta$     is the angle if incidence with respect to the normal

$Z$     is the distance from the surface as indicated in Figure 2.15

To obtain total reflection, the angle of incident radiation must exceed the critical angle ($\theta \geq \theta_C$):

$$\theta_C = \sin^{-1}\frac{n_2}{n_1} \qquad (2.5)$$

Even though the total reflection takes place at the interface when $\theta \geq \theta_C$, the electromagnetic field penetrates only a fraction of the wavelength beyond the reflecting surface into the less dense medium. The depth of penetration is expressed as follows [36]:

$$d_p = \frac{\lambda_1}{2\pi}(\sin^2\theta - n_{21}^2)^{-1/2} \qquad\qquad (2.6)$$
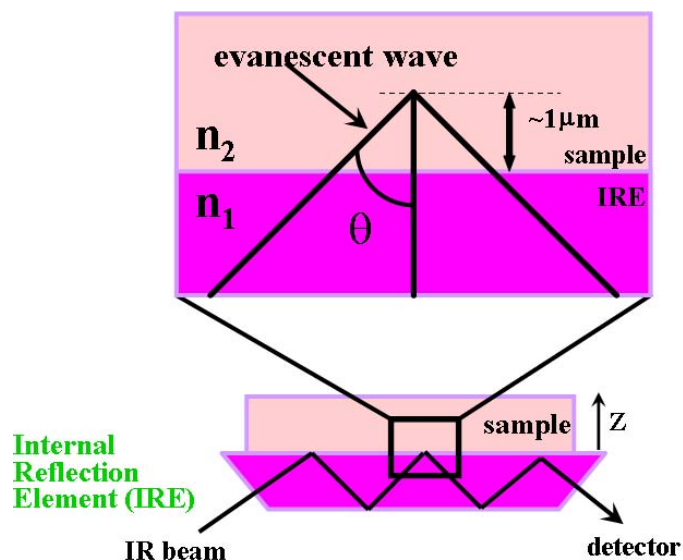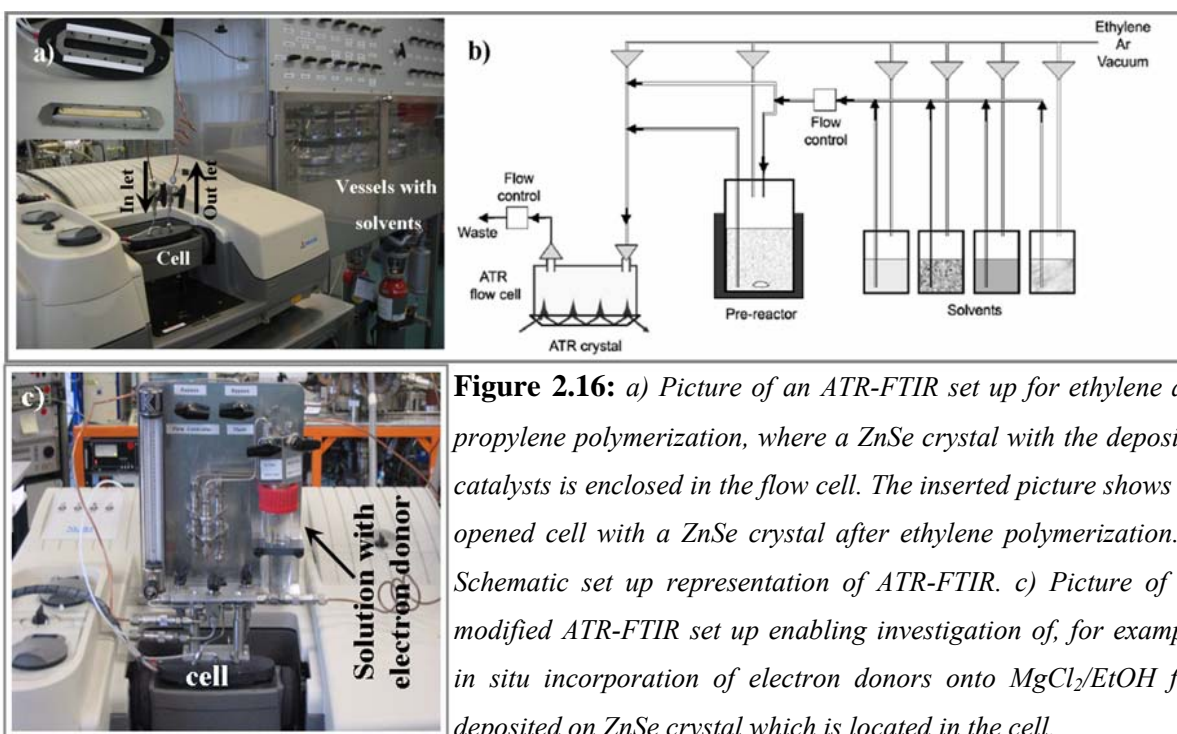


**Figure 2.15:** *The principle of ATR-IR. An IR-beam is directed on the internal reflection element (refractive index $n_1$) above the critical angle ($\theta$) to obtain total reflection and the evanescent wave penetrates in the rarer medium (refractive index $n_2$). The absorption in the rarer medium (sample) is detected after the beam departs the internal reflection element.*

An ATR-IR set up comprises an internal reflection element to which the incident IR-beam is directed in the critical or higher angle (Figure 2.15). The sample is pressed onto the internal reflection element and the evanescent wave comes into the sample, providing information from the length of the penetration depth ($d_p$), stated in equation (2.6). The internal reflection element is a manufactured material of a high refractive index, such as zinc selenide, silicon, germanium, or diamond [36]. The depth decreases as a function of decreasing wavelength (equation (2.6)), and hence it is normal to correct the ATR-IR spectra if they are compared with normal IR-spectra. Evidently, this is not necessary when the ATR-IR spectra are compared with each other [36]. The penetration depth is typically about 1 µm [24].

In the case of polyethylene film grown on ZnSe crystal the calculated depth of penetration is 2 $\mu$m [3]. Hence, in PE films thicker than about 2 $\mu$m only the first 2 $\mu$m contribute to the ATR signal. For the study of the flat model for ethylene polymerization catalyst, an ATR-IR

flow cell set up has been constructed. This set up includes solution containers, a pre-reactor and an ATR flow cell, all of which can be connected to gas supplies with a pressure up to 10 bars and a vacuum system (Figure 2.16). A solution (e.g. $Al(C_2H_5)_3$ in anhydrous toluene) can be introduced to the pre-reactor, where the solution will be saturated with ethylene at a desired pressure. The ethylene-saturated solution is introduced into the ATR cell under the ethylene pressure in a flow mode with the speed controlled by a flow meter. Both the pre-reactor and the ATR cell can be set to a desired temperature up to 150 $^0$C. In the meantime as polymer grows on the ZnSe crystal, infrared spectra are recorded to monitor the polymerization.



**Figure 2.16:** *a) Picture of an ATR-FTIR set up for ethylene and propylene polymerization, where a ZnSe crystal with the deposited catalysts is enclosed in the flow cell. The inserted picture shows the opened cell with a ZnSe crystal after ethylene polymerization. b) Schematic set up representation of ATR-FTIR. c) Picture of the modified ATR-FTIR set up enabling investigation of, for example, in situ incorporation of electron donors onto $MgCl_2$/EtOH film deposited on ZnSe crystal which is located in the cell.*

In summary, the ATR-IR provides quantitative information with some reservations. It is a practical and rapid tool for characterizing functional groups in organic material whenever applicable. We have used ATR-IR to follow in situ ethylene polymerization and analyze the incorporation of the electron donors into solution of $MgCl_2$ in ethanol in **chapter seven**. Figure 2.17 shows an ATR-IR spectrum of polyethylene grown on ZnSe crystal.
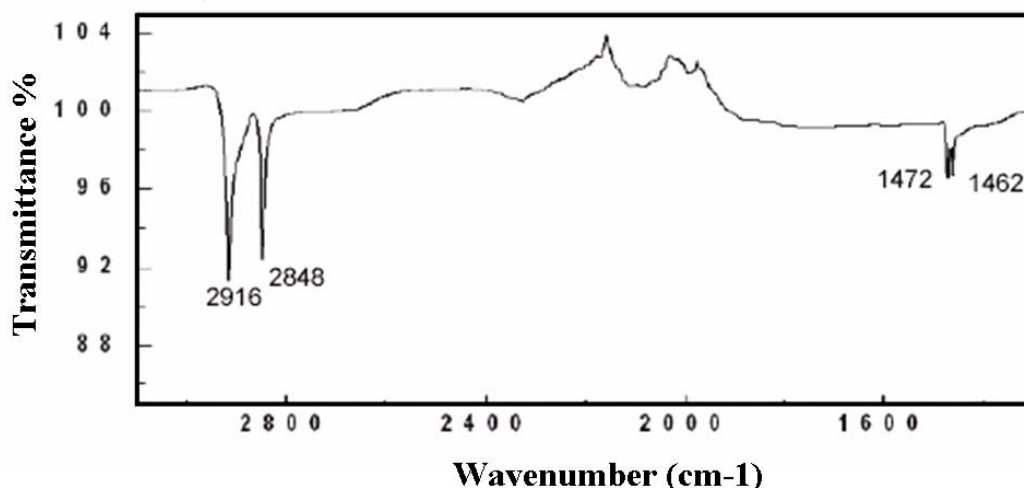
**Figure 2.17:** *ATR-IR spectrum of polyethylene on the surface of the deposited Ziegler-Natta catalyst.*

## References

1. P.C. Thüne, A surface Science Model for the Phillips Ethylene Polymerization catalyst, Ph.D. thesis, Eindhoven University of Technology 2000.

2. E.M.E. van Kimmenade, Ethylene polymerization over flat Phillips model catalysts, Ph.D. thesis, Eindhoven University of Technology 2006.

3. W. Han, Supported homogenous catalysts on flat model surfaces for ethylene polymerization, Ph.D. thesis, Eindhoven University of Technology 2007.

4. P.L.J. Gunter, J.W. Niemantsverdriet, F.H. Ribeiro, G.A. Somorjai, Catal. Rev. Sci. Eng. 39(1-2) (1997) 77.

5. L. Coulier, V.H.J. de Beer, J.A.R. van Veen, J.W. Niemantsverdriet, Top. Catal. 13 (2000) 99.

6. G. Kishan, L. Coulier, V.H.J. de Beer, J.A.R. van Veen, J.W. Niemantsverdriet, J. Catal. 196 (2000) 180.

7. L. Coulier, V.H.J. de Beer, J.A.R. van Veen, J.W. Niemantsverdriet, J. Catal. 197 (2001) 26.

8. G. Kishan, L. Coulier, V.H.J. de Beer, J.A.R. van Veen, J.W. Niemantsverdriet, J. Catal. 200 (2001) 194.

9. P.C. Thüne, C.P.J. Verhagen, M.J van den Boer, J.W. Niemantsverdriet, J. Phys. Chem. B 101 (1997) 8559.

10. P.C. Thüne, J.W. Niemantsverdriet, Isr. Chem. 38 (1998) 385.

11. E.W. Kuipers, C. Laszlo, W. Wieldraaijer, Catal. Lett. 17 (1993) 71.

12. E.W. Kuipers, C. Doornkamp, W. Wieldraaijer, R.E. van den Berg, Chem. Mat. 5 (1993) 1367.

13. M. van Hardeveld, P.L.J. Gunter, L.J. van IJzendoorn, W. Wieldraaijer, E.W. Kuipers, J.W. Niemantsverdriet, Appl. Surf. Sci. 84 (1995) 339.

14. A. Borgna, B.G. Anderson, A.M. Saib, H. Bluhm, M. Havecker, A. Knop-Gericke, A.E.T. Kuiper, Y. Tamminga, J.W. Niemantsverdriet, J. Phys. Chem. 108 (2004) 17905.

15. A.M. Saib, Towards a cobalt Fischer-Tropsch synthesis catalyst with enhanced stability: A combined approach, Ph.D. thesis, Eindhoven University of Technology 2006.

16. J.J. Thomson, Philos. Mag. 5:48 (1899) 547.

17. A. Einstein, Ann. Phys. (Leipzig) 17 (1905) 132.

18. J.W. Niemantsverdriet, Spectroscopy in Catalysis, Wiley-VCH, Weinheim, 2007.

19. D. Briggs, M.P. Seah, Practical Surface Analysis, John Wiley & Sons, Chichester, 1983, Ch. 3.

20. S. Hüfner, Photoelectron Spectroscopy – Principles and Applications, Springer: Berlin, 1996.

21. G. Binning, C.F. Quate, C. Gerber, Phys. Rev. Lett. 56 (1986) 930.

22. S.N. Magonov, M.-H. Whangbo, Surface Analysis with STM and AFM, Wiley-VCH, Weinheim, 2000.

23. S.N. Magonov, M.-H. Whangbo, Surface Analysis with STM and AFM, Wiley-VCH, Weinheim, 1996.

24. E. Kontturi, Surface Chemistry Of Cellulose from natural fibres to model surfaces, Ph.D. thesis, Eindhoven University of Technology 2005.

25. J.N. Israelachvili, Intermolecular and Surface Forces, Academic Press, San Diego 1992.

26. B.V. Derjaguin, V.M. Muller, Y.P. Toporov, J. Colloid Interface Sci. 53 (1975) 314.

27. M. Schenk, M. Füting, R. J. Reichelt, Appl. Phys. 84 (1998) 4880.

28. S.S. Sheiko, Adv. Polym. Sci. 151 (2000) 61.

29. Y. Martin, C.C. Williams, H.K. Wickramasinghe, J. Appl. Phys. 61 (1987) 4723.

30. Q. Zhong, D. Imniss, K. Kjoller, V.B. Elings, Surf. Sci. 290 (1993) L688.

31. T.R. Albrecht, P. Grütter, D. Horne, D. Rugar, J. Appl. Phys. 69 (1991) 668.

32. R. García, R. Pérez, Surf. Sci. Reports 47 (2002) 197.

33. G. de Silveira, P. Forsberg, T.E. Conners, Scanning Electron Microscopy: A Tool for the Analysis of Wood Pulp Fibres and Paper in Surface Analysis of Paper, T.E. Conners, S. Banerjee, Eds.; CRC Press: Boca Raton, New York, 1995, Ch. 2.

34. K. Wetzig, D. Schultze, In situ Scanning Electron Microscopy in Materials Research; Akademie Verlag: Berlin, 1995.

35. M.W. Urban, Attenuated Total Reflectance Spectroscopy of Polymers, American Chemical Society, Washington DC, 1996.

36. F.M. Mirabella, Internal Reflexion Spectroscopy, Dekker, New York, 1993.

# Chapter 3

## Ethylene polymerization over a planar Ziegler-Natta model catalyst

*An active model for a Ziegler Natta ethylene polymerization catalyst has been prepared by spin coating of a MgCl$_2$ solution in ethanol on a flat silicon (100) substrate covered by amorphous silica. The flat model approach facilitates the characterization of the catalyst using surface spectroscopy and microscopy techniques. This model catalyst features a Ti/Mg atomic ratio of 0.15 and a primary MgCl$_2$ crystal size of about 15 nm. The flat model is active for ethylene polymerization, producing smooth polymer films. Scanning electron microscopy of these films reveals pillary polymer growth, in the direction perpendicular to the flat support surface.*

## 3.1   Introduction

Ziegler-Natta catalytic systems are very widely used in industrial olefin polymerization processes. They consist of a $MgCl_2$ support, $TiCl_4$ and an internal electron donor and are used in combination with an aluminum alkyl cocatalyst $AlR_3$ [1]. Lewis bases (external electron donors) are added in polymerization to produce highly isotactic polypropylene. One of the functions of the internal electron donor, typically a monoester, diester or diether incorporated in the catalyst preparation, is to control the amount and distribution of $TiCl_4$ on the support surface. Giannini [2] has indicated (as noted in **chapter one**) that, on the lateral cleavage surfaces of the $MgCl_2$ crystallites making up the support, the magnesium atoms are coordinated with 4 or 5 chlorine atoms, as opposed to 6 chlorine atoms in the bulk of the crystal. These tetra- and pentacoordinate Mg atoms are present on the (110) and (100) lateral cuts of $MgCl_2$. In this thesis, however, we will denote the five-coordinate face as (104) rather than (100), following a re-evaluation of the crystal structure of $MgCl_2$ supports recently reported by Busico et al. [3]. Figure 3.1a represents a monolayer of a $MgCl_2$ crystal showing the most probable 104 and 110 cleavage cuts. Treatment with $TiCl_4$ will lead to adsorbed $TiCl_4$ species on one or both of the (104) and (110) cuts. Upon reaction with the cocatalyst $(AlR_3)$, $Ti^{4+}$ is reduced to $Ti^{3+}$ and a Ti-C bond is introduced that is necessary for the insertion of the monomer.

In spite of numerous efforts, questions regarding which of the $MgCl_2$ surface planes is the most preferred cut for $TiCl_4$ fixation, and the precise structure of the titanium active centers formed by treatment of the catalyst with the alkylaluminum cocatalyst, have still not yet found definitive answers. It has been suggested [4, 5] that dimeric species $(Ti_2Cl_8)$ epitactically coordinated to the (100) lateral cut; now indexed [3] as the (104) cut, could lead to the formation of stereospecific active sites. Possible modes of coordination of $TiCl_4$ on $MgCl_2$ are illustrated in Figure 3.1b [6].

Nevertheless, an investigation of the Raman spectra of the products of co-milling mixtures of $MgCl_2$ and $TiCl_4$ came to the conclusion, supported by *ab initio* calculations, that the adsorption of $TiCl_4$ gave a species with octahedrally coordinated titanium, on the (110) lateral cut of $MgCl_2$ [7, 8]. This stable complex was not removed by washing with solvent, whereas dimeric species $(Ti_2Cl_8)$ on the (104) cut were easily removed. The monomeric

species with octahedrally coordinated titanium was thus concluded to be the precursor for stereospecific active sites in MgCl$_2$-supported catalysts.
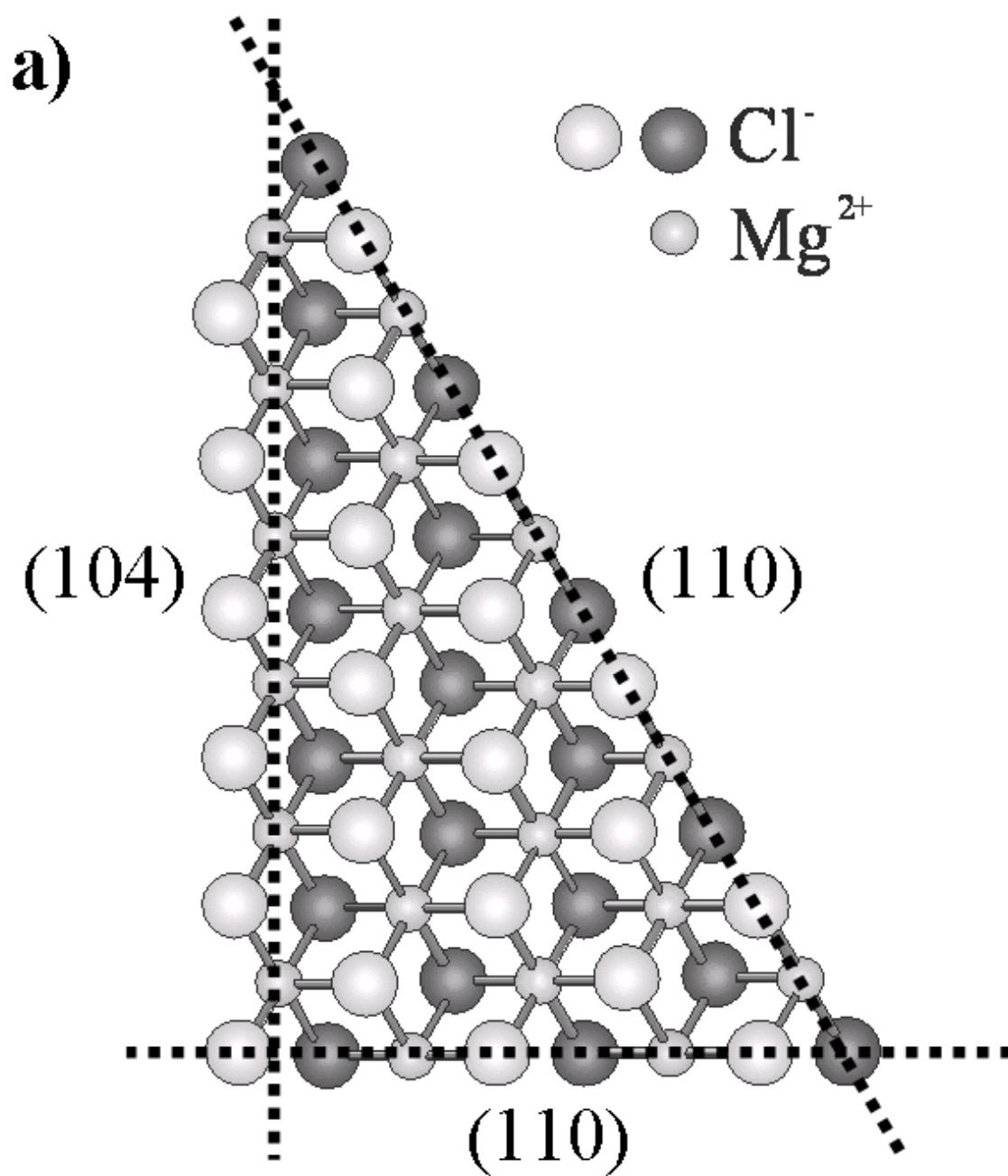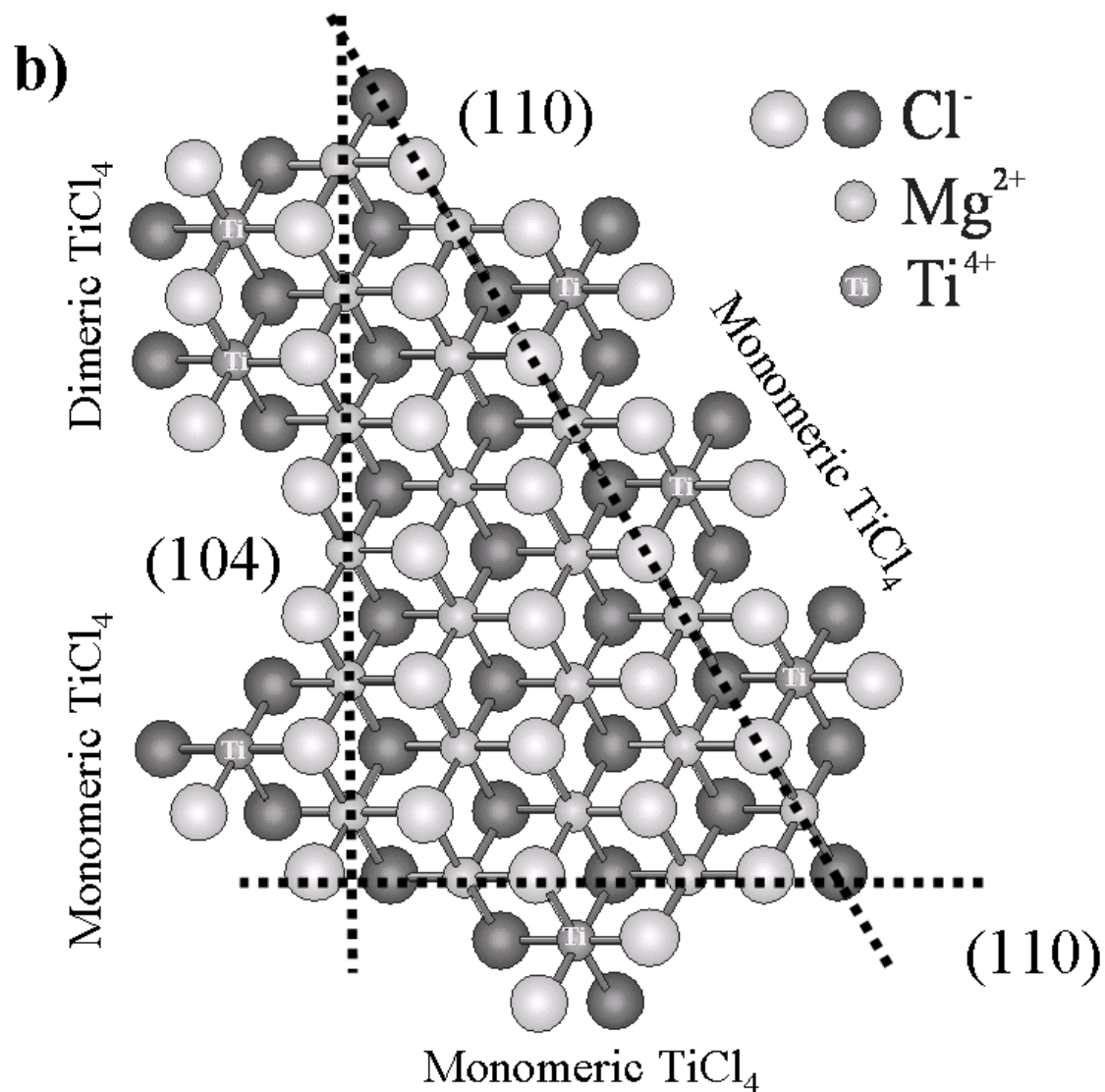
**Figure 3.1:** *a) Model for a monolayer of a MgCl$_2$ crystal showing the most probable (104) and (110) cleavage cuts. b) Proposed coordination modes of TiCl$_4$ species on MgCl$_2$ lateral cuts, showing dimeric and monomeric species on (104) cut and monomeric species on (110) cut [3, 6].*

Various attempts to characterize the active species in Ziegler-Natta catalysts have involved the use of advanced surface science techniques. Somorjai and coworkers have published a series of papers describing two synthetic routes to Ziegler-Natta model catalysts under UHV conditions. Ultra-thin films of MgCl$_2$ were prepared via sublimation onto a gold foil, followed by gas phase deposition of TiCl$_4$, whereas TiCl$_4$/TiCl$_2$ films were obtained by TiCl$_4$

and Mg codeposition on $MgCl_2$ and Au [9-14]. These systems were active for ethylene and propylene polymerization. X-ray photoelectron spectroscopy (XPS) analysis revealed the presence of $TiCl_2Et$ species on the catalyst surface after exposure to the cocatalyst, $AlEt_3$. Prolonged reaction with $AlEt_3$ produced further reduced species with possible stoichiometry $TiClEt_n$ (n=1 and/or 2). No evidence was found for $TiCl_3$ formation. It was suggested that $TiCl_4$ reduction and alkylation could not be separated under these experimental conditions [9-13].

The same group of authors reported the reduction of $MgCl_2$ by $AlEt_3$ in the presence of Au, forming Mg clusters or islands; a large fraction of the resulting support surface was capable of $TiCl_4$ chemisorption [15]. These systems were active for ethylene and propylene polymerization. The polymers produced were characterized by means of surface science techniques, atomic force microscopy and vibrational spectroscopies and it was shown that polypropylene films had a high degree of isotacticity [16–18]. By alternating the supply of propylene and ethylene monomers, alternating polypropylene and polyethylene films were produced on one model Ziegler–Natta catalyst [19]. By means of this approach, it was shown that the active sites were present at the interface of the catalyst and the growing polymer and polymerization at the active sites occurred by the diffusion of monomers through the growing polymer layer. In the same framework, using the above models, temperature-programmed desorption (TPD) was used with physisorbed mesitylene as nondestructive surface probe to distinguish the surface adsorption sites of model Ziegler–Natta polymerization catalysts [20–22]. Following the work of Somorjai, Pilling et al. [23] reported the use of reflection absorption infrared spectroscopy (RAIRS) and XPS for a study of the interaction of $TiCl_4$ with metallic Mg films grown on an Au surface.

Siokou and Ntais [24, 25] introduced a surface science model of Ti-based Ziegler-Natta catalysts supported on $SiO_2/Si(100)$ and prepared by spin coating THF solutions of $TiCl_4 \cdot (THF)_2$ and $MgCl_2/TiCl_4 \cdot (THF)_2$. The surface composition was characterized by XPS. Following the same approach, $TiCl_4 \cdot (THF)_2$ was impregnated by spin coating on a Si(100) wafer covered with a thin SiO$x$ layer and on a polycrystalline Au foil [26]. Atomic force microscopy (AFM) measurements revealed a homogeneous distribution of nanosized TiO$x$ clusters of semiellipsoid shape and increased contact area with the underlying silica.

Fregonese et al. [27] reported XPS studies of Ziegler–Natta catalysts prepared by exposure of $\delta$-MgCl$_2$ to TiCl$_4$ and cocatalyst (AlEt$_3$) under UHV conditions. Additionally, Freund et al. [28] and Risse et al. [29] introduced a model system of a Pd(111) substrate covered by a MgCl$_2$ film onto which TiCl$_4$ was anchored and applied electron spin resonance to study intermediately formed radicals in the Ziegler–Natta polymerization of ethylene. In more recent studies, Kaushik et al. [30] applied XPS to show that the productivity of a catalyst can be correlated to the dispersion of titanium atoms on the MgCl$_2$ support.

Following previous studies on surface science characterization of chromium species on flat Si wafers [31-33], we are now aiming to develop a realistic flat model system for Ziegler-Natta catalysts that allows a detailed study of the surface chemistry and morphology of the support, catalyst and polymer. Surface science and microscopy techniques such as XPS, Atomic Force Microscopy (AFM) and Scanning Electron Microscopy (SEM) are being utilized throughout this work. Application of a flat model makes these techniques suitable for characterization and visualization of both the catalyst and the polymer produced. Our approach involves spin coating of MgCl$_2$ from ethanol solution onto a silica/silicon wafer, followed by contact with TiCl$_4$ in toluene at room temperature. In this way we attempt to mimic an industrial catalyst preparation, in which supports formed by cooling emulsions of molten MgCl$_2 \cdot n$EtOH adducts in paraffin oil are reacted with TiCl$_4$ [1]. We circumvent, in this respect, catalyst preparation under the UHV conditions utilized previously by other groups, which is often far removed from the nature of real industrial catalysts [24, 27]. In this feasibility study, we demonstrate the construction of a realistic flat model of a Ziegler-Natta catalyst which is active for ethylene polymerization, demonstrating the viability of this approach for the preparation and characterization of realistic catalytic models.

## 3.2 Experimental

### 3.2.1 Materials

Anhydrous magnesium chloride (beads, 99.9 %), absolute ethanol (99.9 %), titanium tetrachloride (99.9 %) and triethylaluminium (25 wt. % in toluene) were purchased from Aldrich Chemicals and used as received. HPLC-grade toluene was taken from an argon-

flushed column packed with aluminium oxide and stored over 4 Å molecular sieves. Ethylene was supplied by Praxair (3.5).

## 3.2.2 Catalyst preparation and ethylene polymerization

The catalyst preparation is summarized in Figure 3.2. All manipulations of air or water sensitive compounds were carried out using standard Schlenk or glovebox techniques. The $SiO_2$/Si(100) wafer was prepared as described elsewhere (calcination at 750 $^0$C, followed by etching with $H_2O_2$/$NH_3$) [31] to obtain an amorphous silica layer (20 nm) on a silicon (100) wafer.

The wafer was partially dehydroxylated at 500 $^0$C in air for 16 hours. A small amount of surface hydroxyl groups was retained in order to facilitate a homogenous $MgCl_2$ film formation. Such a wafer was then spin coated with different concentrations of $MgCl_2$ in ethanol (2, 42 and 105 mmol/L). Upon spinning, most of the liquid is ejected from the flat silica surface, leaving behind a thin film of solution. The remaining solvent evaporates and the solute precipitates upon the support surface. The rotation speed applied was 2800 r.p.m.

The wafer was afterwards dried under nitrogen and was then used as such for XPS and/or AFM analysis. Grafting of $TiCl_4$ onto the $MgCl_2$ support was carried out by treatment with a 10 % v/v $TiCl_4$ solution in toluene at room temperature. After washing with toluene to remove the physisorbed $TiCl_4$, the model catalyst was dried under nitrogen. Thus the flat silica/silicon wafer containing the immobilized catalytic components can be used for either ethylene polymerization or XPS analysis. Both the $TiCl_4$ treatment and the washing step took 30 min. unless stated otherwise.

Ethylene polymerization was carried out at room temperature in a glass reactor equipped with a magnetic stirrer. The Si wafer after deposition of $MgCl_2$ and treatment with $TiCl_4$ was dipped into about 20 mL of a 1 mg/mL solution of the cocatalyst, $AlEt_3$, in toluene, inside the glass reactor. The reactor was pressurized with 2 bar of ethylene and the polymerization was allowed to run for the desired time. After the polymerization, the wafer was washed with toluene.
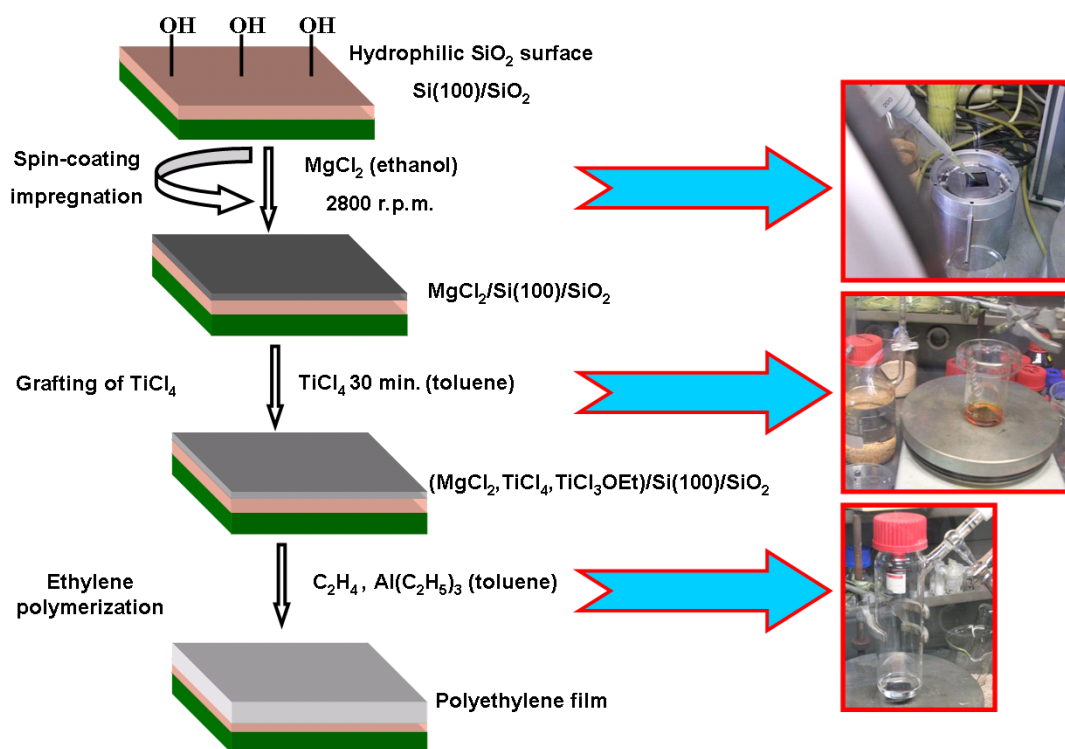
**Figure 3.2:** *Schematic representation of sample preparation for Ziegler-Natta catalyst on flat silica/silicon surface for ethylene polymerization along with pictures of operations steps carried out in the glove box.*

## 3.2.3 Analytical techniques

AFM measurements were performed inside a glove box with Solver P47 base with SMENA head. The cantilever of choice was a non-contact gold-coated NSG11 (long end), manufactured by Micromasch. A typical force of the tip was 5.5 N/m and a typical resonance frequency 164 kHz. The measurements were performed in non-contact mode. The thickness of the catalyst support, $MgCl_2$, was determined using the height difference between the Si-substrate and $MgCl_2$ surface after scratching the layer with a scalpel.

The amounts of Mg in solution and on Si wafer were determined by an inductively coupled plasma optical emission spectrometry (ICP-OES) technique using a Spectro Circos CCD spectrometer. All the solutions and the $MgCl_2$ of the spin coated wafers were dissolved in $HCl_{aq}$ (0.1 M).

X-ray photoelectron spectroscopy measurements were performed with a VG escalab 200 using a standard aluminum anode (Al-Kα 1486.3 ev) operation at 300 W. Spectra were recorded at normal emission background pressure 1 x $10^{-9}$ mbar. Binding energies were calibrated to C 1s peak at 285 eV.

SEM was performed using a Philips environmental scanning electron microscope XL-30 ESEM FEG (Philips, The Netherlands, now Fei Co.) in high-vacuum mode using a low accelerating voltage (low-voltage SEM, LVSEM) and a secondary (SE) detector.

Size exclusion chromatography (SEC) was used to determine the molecular weight of the polyethylene samples. The required sample amount (at least 1 mg) was obtained by removal of the polymer from the catalyst surface using a scalpel. Molecular weight and molecular weight distribution of the resulting polyethylenes were determined by high-temperature SEC in 1,2,4-trichlorobenzene at 140 $^0$C using a PL 220 instrument and a calibration with polystyrene standards.

A Q100 DSC (TA Instruments) was used to determine the melting points of the polyethylene samples. The required sample amount was in all cases at least 1 mg and was obtained by removal of the polymer from the catalyst surface using a scalpel. Scans were performed at a rate of 10 $^0$C/min from 0 to 160 $^0$C and again back to 0 $^0$C, after which the heating scan was repeated.

## 3.3  Results

### 3.3.1 Quantification of $MgCl_2/SiO_2/Si(100)$

The spin coating of magnesium chloride as a solution in ethanol resulted in the formation of adducts of type $MgCl_2 \cdot n$EtOH on the surface of the Si wafer. The residual ethanol content depends on the conditions under which the wafer is dried after spin coating, because $MgCl_2 \cdot n$EtOH adducts can be at least partially dealcoholated under relatively mild conditions [34]. The amounts of $MgCl_2$ on Si wafers were quantified with ICP. The amount of Mg on silica/silicon was almost linearly proportional to the concentration of the spin coating

solutions (Figure 3.3). Our standard catalyst used for ethylene polymerization was prepared from a 42 mmol/L solution, resulting in a Mg loading of 200 atoms/nm$^2$.
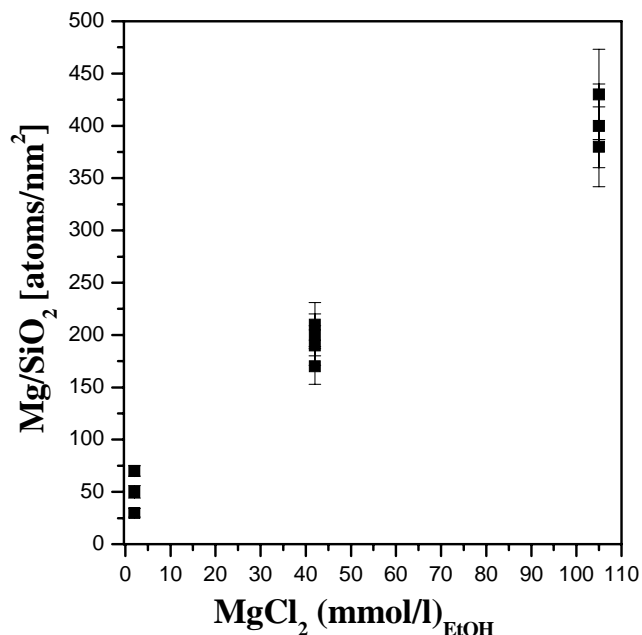


**Figure 3.3:** *Loading of Mg (atoms/nm$^2$) on silica/silicon wafers as determined with ICP versus concentration of spin coated MgCl$_2$ solutions.*

## 3.3.2 XPS analysis

The evolution of the MgCl$_2$ film on the flat Si support was followed with XPS. Upon increasing the MgCl$_2$ loading from 50 Mg atoms/nm$^2$ to 200 and 400 Mg atoms/nm$^2$, respectively, the corresponding signals Mg 2p, 2s and Cl 2p, 2s also increase in the overview spectra (Figure 3.4a). The silica contributions Si 2p, 2s (Figure 3.4a and 3.4b) diminish upon increasing the loading. As the Si peak becomes invisible, C 1s and O 1s remain significant in the spectra, likely due to the presence of residual ethanol in the spin coated adduct MgCl$_2 \cdot n$EtOH.

Unfortunately, however, the possible presence of adsorbed water and/or hydrocarbons (the latter present in the atmosphere of the glove box) prevented reliable quantification of the amount of residual ethanol (i.e., the value of *n* in MgCl$_2 \cdot n$EtOH). Angle resolved XPS indicated that carbon and oxygen are largely present on top of the actual MgCl$_2$ film. The Si 2s/Mg 2s ratio for our standard catalyst (200 Mg atoms/nm$^2$) was 0.17. This corresponds to a

film thickness of about 11±2 nm, assuming a flat homogeneous $MgCl_2$ film over a large area [35, 36]. The Mg/Cl ratio (1.00:1.96) closely resembles that of anhydrous $MgCl_2$, indicating that $MgCl_2$ has deposited without any significant hydrolysis.
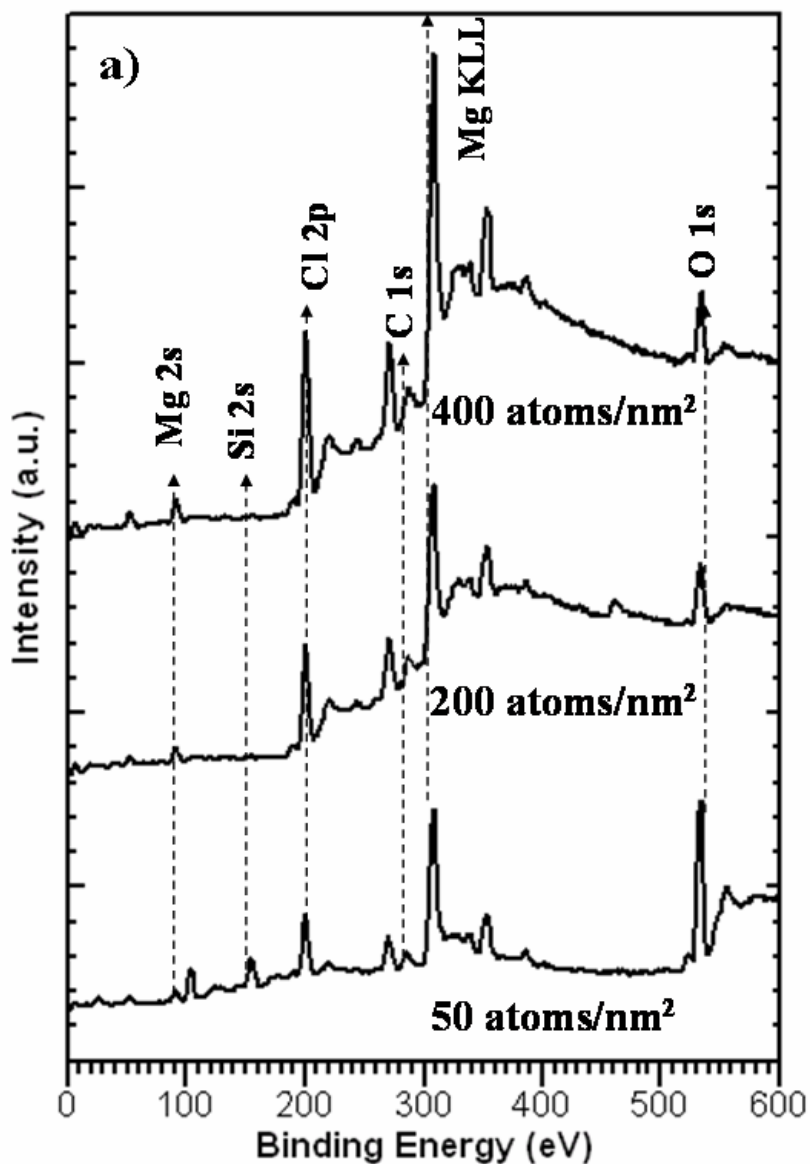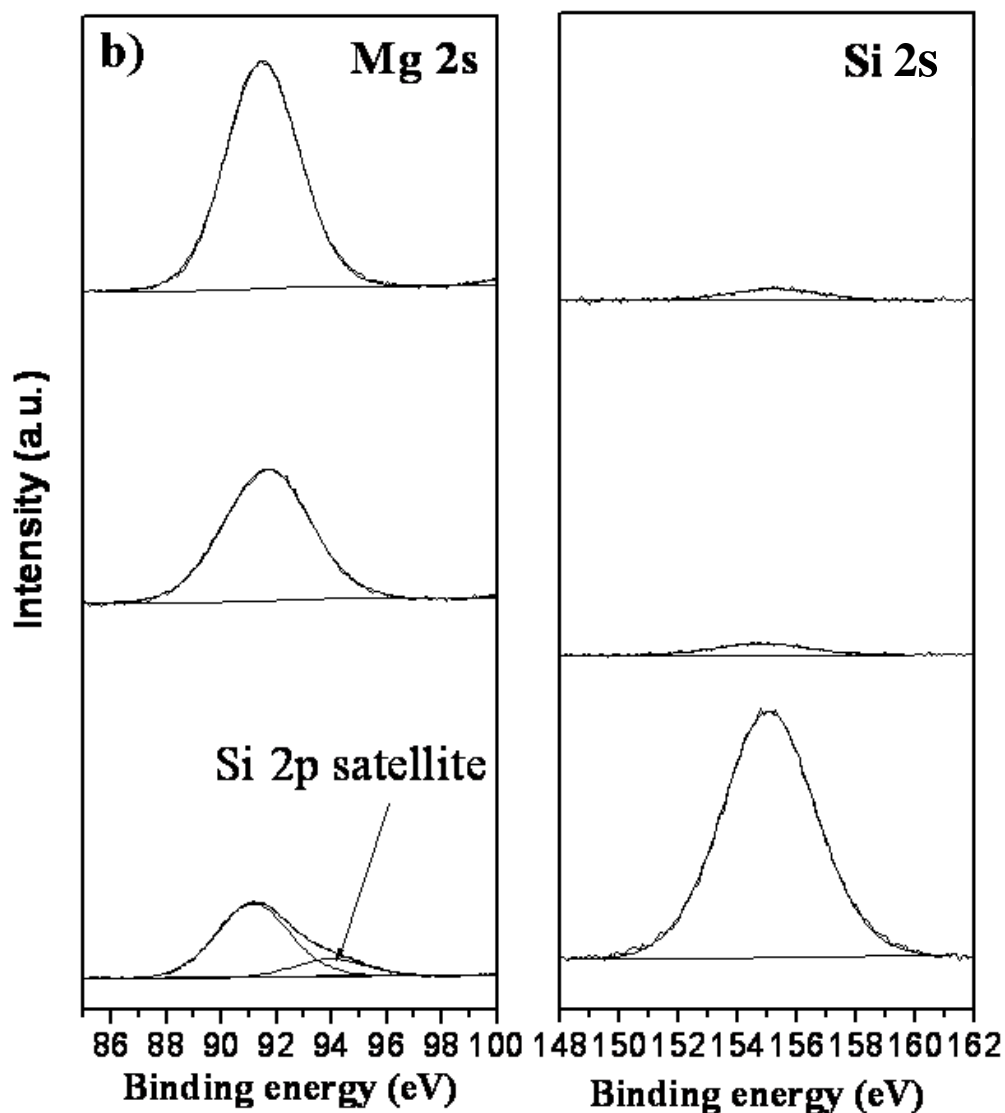
**Figure 3.4:** *a) Wide scan of XPS spectra upon increasing the loading of MgCl$_2$·nEtOH on Si (from bottom to top the loading increases successively i.e., 50, 200 and 400 atoms/nm$^2$) b) XPS spectra of the same system recorded in the regions of Mg 2s and Si 2s for the same loadings.*

The Ti 2p$_{3/2}$ peak appeared slightly broader after contacting with AlEt$_3$. The FWHM was 4.1 eV, compared to 3.0 eV before alkylation. The increase in width of the Ti 2p$_{3/2}$ peak after reaction with the cocatalyst indicates some reduction to oxidation states lower than (+4), although a well resolved peak for titanium atoms in lower oxidation state was not evident. Treatment with TiCl$_4$ was carried out on a Si wafer with a loading of 200 Mg atoms/nm$^2$. Such a wafer was contacted for 30 min. with a 10 % v/v TiCl$_4$ solution in toluene, followed

by a 30 min. extraction with toluene to remove weakly bound $TiCl_4$. Figure 3.5 displays overview spectra before and after contacting the support with $TiCl_4$. The inserted spectra show the Mg 2s and Si 2s peaks before and after the $TiCl_4$ treatment, together with the Ti 2p peak after the contact with $TiCl_4$.

The Si/Mg ratio does not change upon treating with $TiCl_4$. The Mg 2s and Mg 2p emissions showed maxima at BE 90.7 eV and 51.8 eV, whereas Cl $2p_{3/2}$ appeared at 199.5 eV. The maximum of the Ti $2p_{3/2}$ emission was at 459.3 eV. The Ti2p/Mg2s ratio of the $TiCl_4/MgCl_2/SiO_2/Si(100)$ system corresponds to a Ti/Mg atomic ratio of 0.15 [37]. This ratio remained constant when changing the take-off angle for the photoelectrons from $0^0$ to $60^0$ relative to the surface, indicating a homogeneous distribution of the Ti in the $MgCl_2$ film.
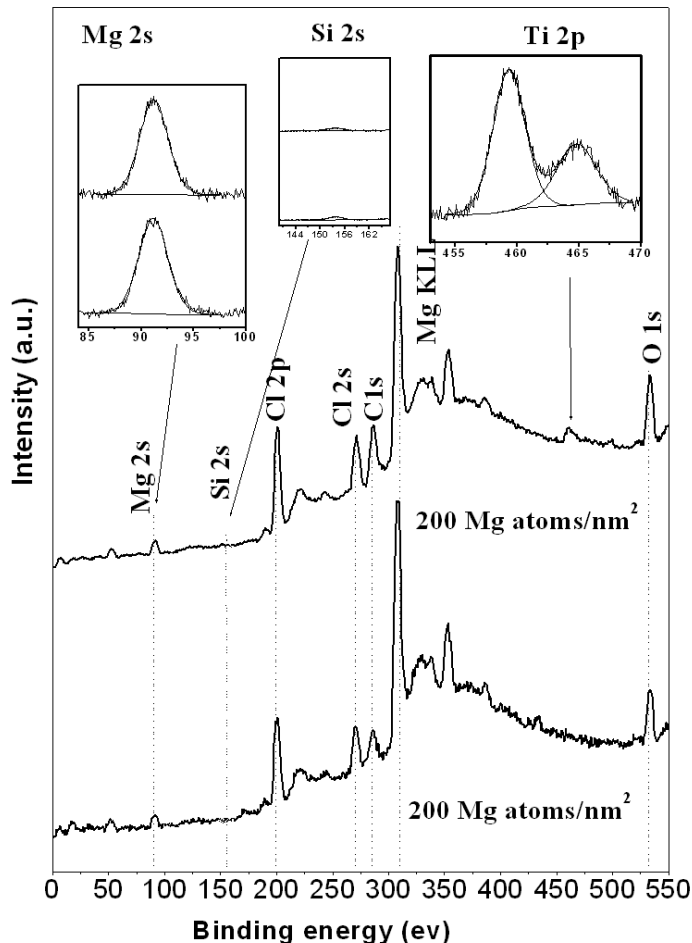


**Figure 3.5:** *Wide scan of XPS spectra before and after the $MgCl_2/SiO_2/Si(100)$ model support was treated with $TiCl_4$. The inserted spectra represent the Ti 2p peak after treatment with $TiCl_4$ and the Mg 2s and Si 2s peaks before and after treatment with $TiCl_4$.*

### 3.3.3 AFM analysis

The morphology of the $MgCl_2/SiO_2/Si(100)$ model catalyst with a $MgCl_2$ loading of 200 atoms/$nm^2$ was probed with AFM after impregnation of $MgCl_2$ and after treatment with $TiCl_4$. The spin coated $MgCl_2$ yielded a smooth film with a surface roughness of 1-3 nm (Figure 3.6). At high magnification the AFM image indicated a granular structure. The size of the grains varied from 10-40 nm.
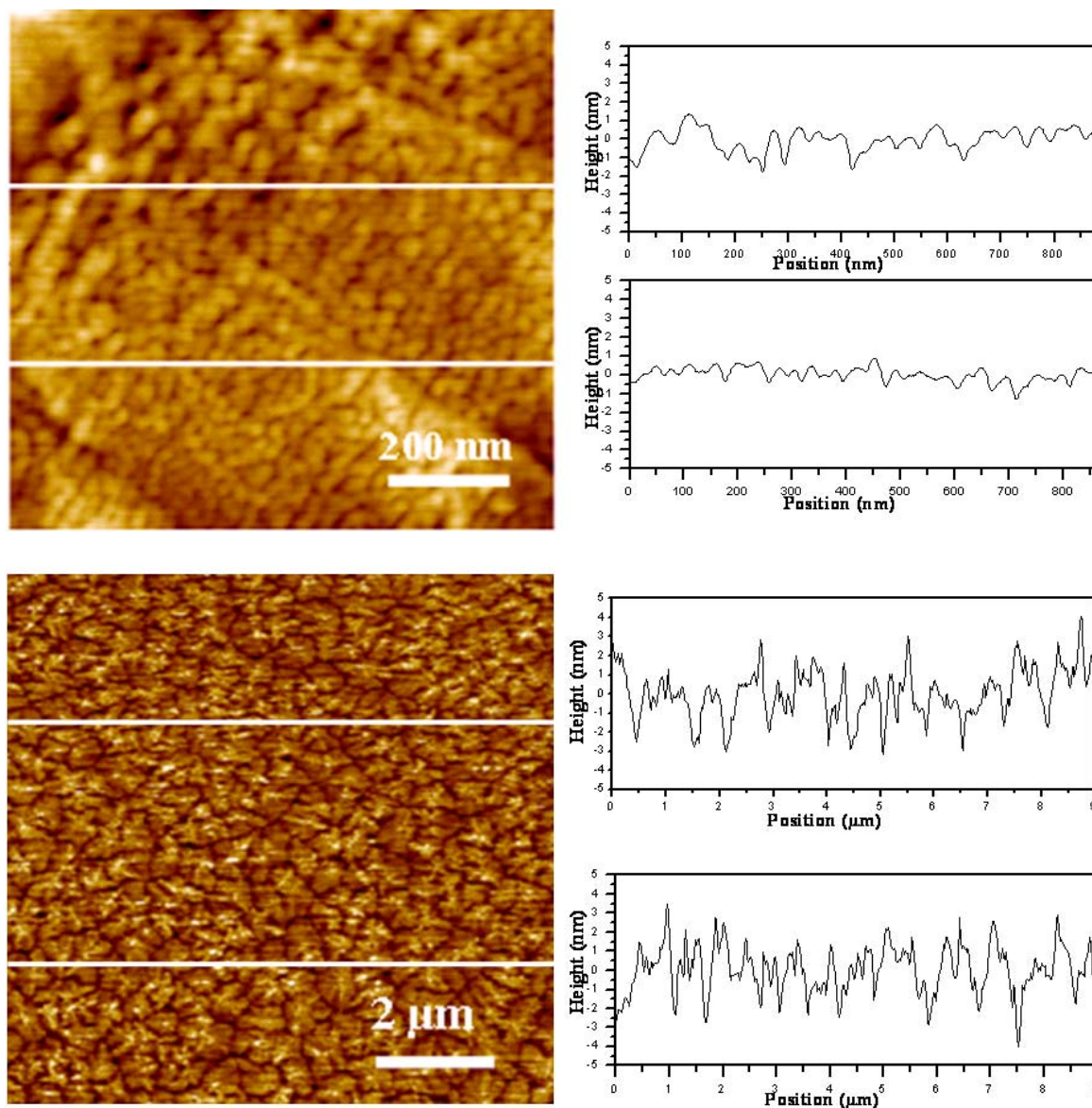


**Figure 3.6:** *(Left) AFM height images of $MgCl_2 \cdot nEtOH$ film for loading of 200 atoms/$nm^2$ on Si; (right) the corresponding cross-sectional height scans.*

Figure 3.7a represents the scratching of a typical $MgCl_2$ film (200 Mg atoms/$nm^2$), with the corresponding height profile. The film thickness was proportional to the loading of the Mg on silica (Figure 3.7 b). Our standard loading (200 atoms/$nm^2$) corresponds to a film thickness of $12\pm2$ nm, in excellent agreement with the XPS results.
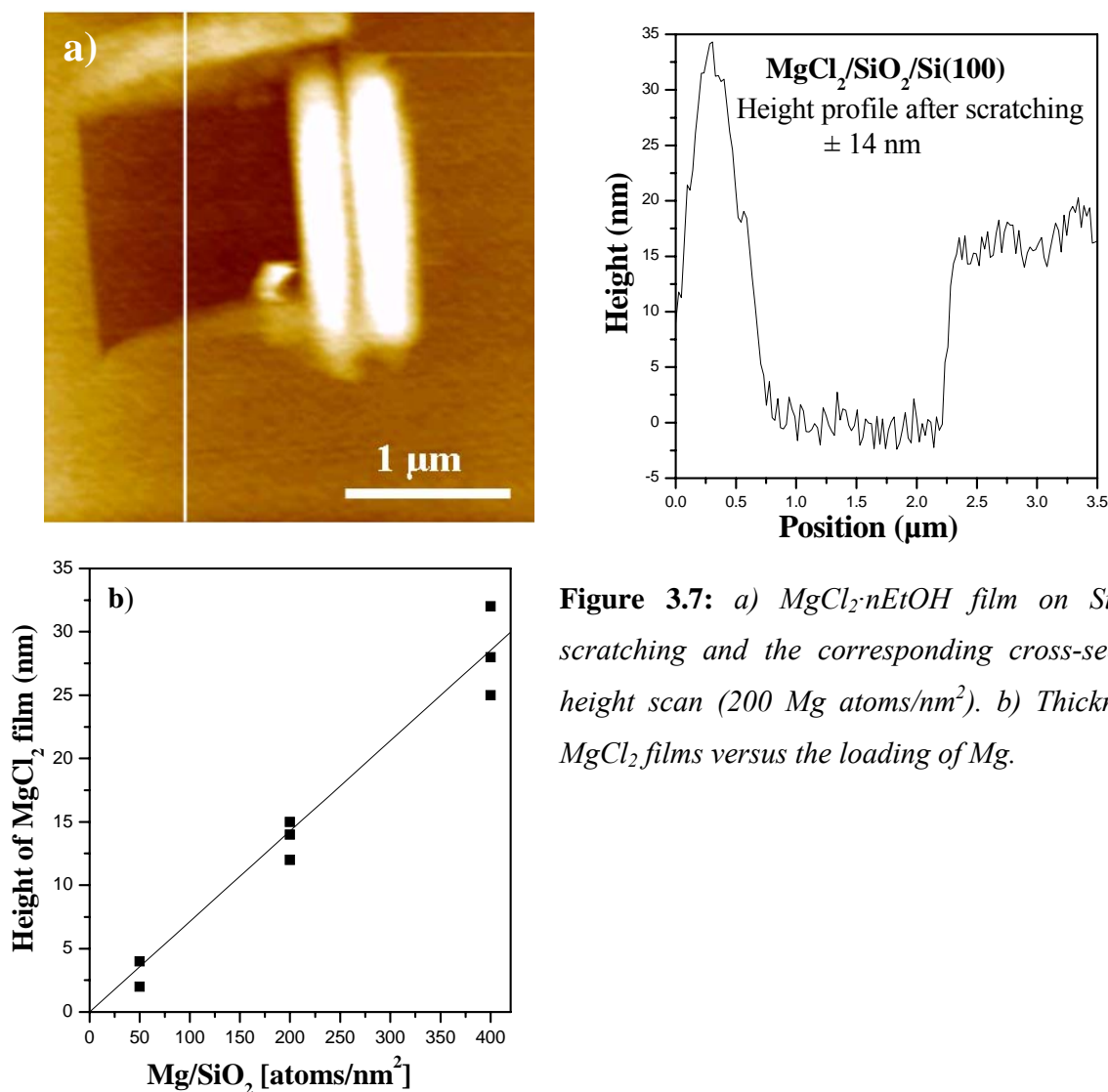


**Figure 3.7:** *a) MgCl₂·nEtOH film on Si after scratching and the corresponding cross-sectional height scan (200 Mg atoms/$nm^2$). b) Thickness of MgCl₂ films versus the loading of Mg.*

Treatment of the $MgCl_2$ film with $TiCl_4$ for 30 min. induced minor changes in morphology (Figure 3.8a). The thickness of the $MgCl_2$ film after the $TiCl_4$ treatment remained constant. AFM (Figure 3.8a) showed a homogeneous film with a small number of small holes having a penetration depth of several nm. These holes possibly could have resulted from detachment of small grains of magnesium chloride from the wafer surface, as shown in the higher resolution image in Figure 3.6. Another possible explanation of the holes formation is the shrinkage of the $MgCl_2$ film upon ethanol removal during the treatment with $TiCl_4$. This

effect is more pronounced at longer (e.g. 18 hours) treatments with $TiCl_4$. Figure 3.8b shows the formation of larger holes with a penetration depth up to ±12 nm.
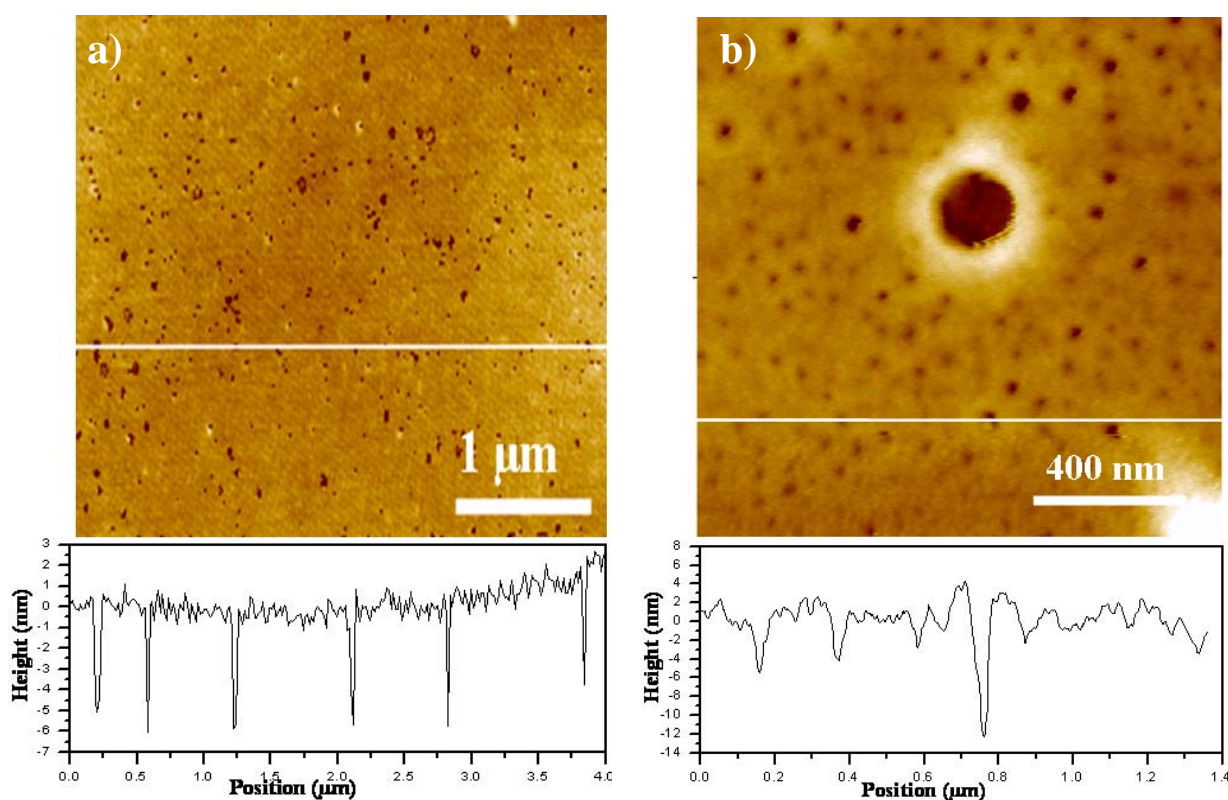


**Figure 3.8:** *a) AFM height image after treatment of $MgCl_2 \cdot nEtOH$ film (200 Mg atoms/nm$^2$) with $TiCl_4$ for 30 min. with the corresponding cross-sectional height scans. b) AFM images after treatment of a similar film with $TiCl_4$ for18 hours, with the corresponding cross-sectional height scans.*

## 3.3.4 Ethylene polymerization

The model catalyst prepared as described above proved to be active for ethylene polymerization at 2 bar ethylene pressure and room temperature. PE is formed, in milligram quantities, as a thin film on the Si surface (3x3 cm$^2$). No polymer formation was observed in the solution. Scanning electron microscopy (SEM) indicated a thickness of the polymer film of 4 μm after 30 min. (Figure 3.9b). In the SEM image (Figure 3.9a) the polymer film appears to be composed of a mass of somewhat small spherical particles when viewed from top.

After 16 hours polymerization 100 µm thick film was produced. This corresponds to a polymer yield of 3.5 kg PE/g MgCl$_2$ after 16 hours. In the SEM images (Figure 3.10a) the polymer film appears to consist of a mass of spherical particles when viewed from above. A lateral view, however, clearly reveals that the polymer films consist of closely packed pillars that are aligned perpendicular to the surface of the support, indicating a vertical growth of the polyethylene film (Figure 3.10b and 3.10c).
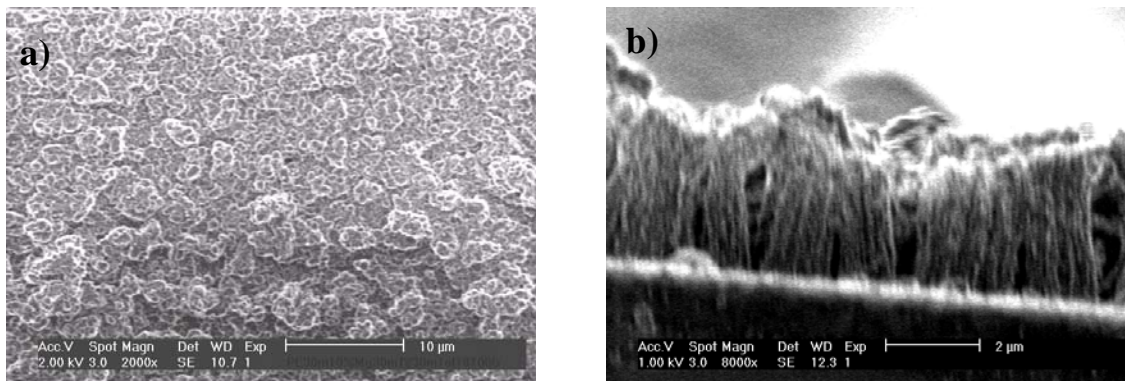


**Figure 3.9:** *SEM image of polyethylene obtained after 30 min. polymerization. a) Top view. b) Side view on Si wafer.*

The polymer obtained after 16 hours polymerization had an $M_w$ of 2.5 x 10$^6$ g·mol$^{-1}$, a molecular weight distribution ($M_w/M_n$) of 4.4 and m$_p$ of 137 $^0$C. Figure 3.10d displays a picture of a sample wafer before and after polymerization. The black wafer appears covered with a visible white layer of polymer which has been grown on top of it.
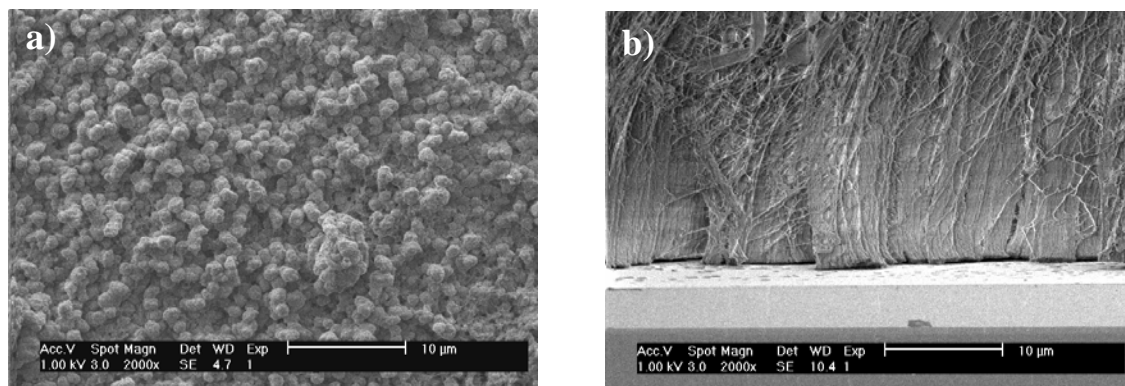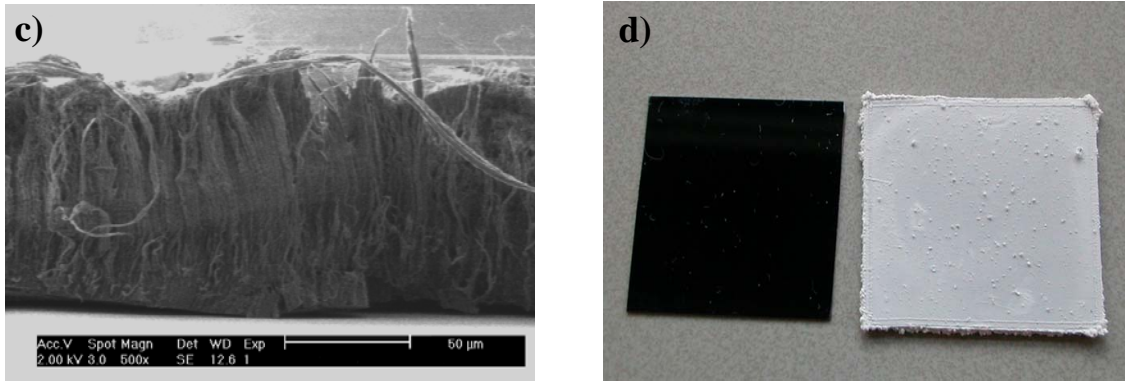
**Figure 3.10:** *SEM image of polyethylene obtained after 16 hours polymerization. a) Top view. b) and c) Side view on Si wafer. c) Picture of the wafer before and after ethylene polymerization.*

After 24 hours ethylene polymerization the polyethylene film thickness extended up to 200 µm (Figure 3.11). This suggests that the catalyst remains active after 24 hours polymerization. The lateral view of SEM images of polyethylene growth after 24 hours reveals that the polymer films consist of closely packed pillars that are aligned perpendicular to the surface of the planar wafer. This is indicative of a vertical growth of the polyethylene film consistent with the pillary morphology already observed after 16 hours ethylene polymerization. The top view, however, exhibits polymer particles which have further expanded.
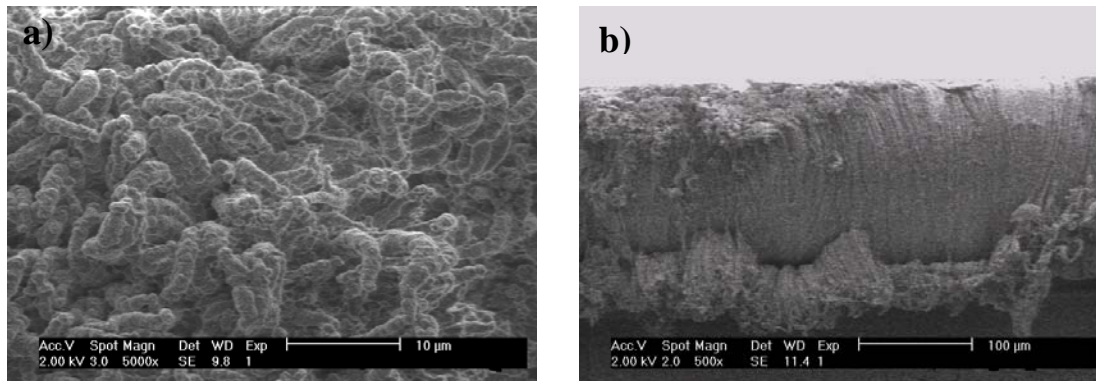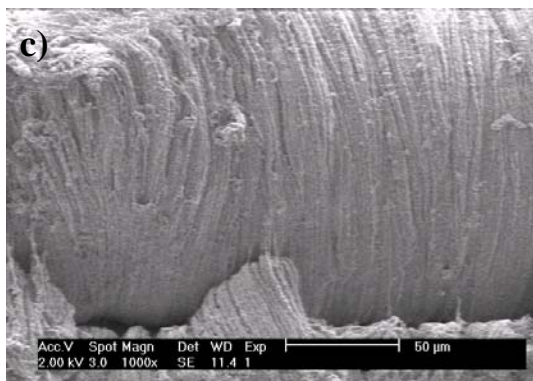
**Figure 3.11:** *SEM image of polyethylene obtained after 24 hours polymerization. a) Top view. b) Side view on Si wafer. c) Higher magnification of the lateral view.*

## 3.4   Discussion

A flat model catalyst, prepared by spin coating of $MgCl_2 \cdot n$EtOH from ethanol solution onto a flat silica/silicon wafer and subsequent treatment with $TiCl_4$, has been studied using XPS, AFM and SEM with the aim to characterize and visualize the Ziegler-Natta catalyst and also the polymer produced. Our model resembles industrial counterparts in several aspects.

AFM in combination with XPS showed that, by varying the loading of Mg on Si, the thickness of the $MgCl_2 \cdot n$EtOH film can be tuned. The spin coating of $MgCl_2 \cdot n$EtOH yielded smooth films which consisted of grains with a size ranging from 10-40 nm, not too different to the size of primary particles in industrial Ziegler-Natta catalysts [38-40]. The density of the $MgCl_2 \cdot n$EtOH film prepared at our standard loading was ~14 atoms/nm$^3$, which is close to the density of anhydrous $MgCl_2$ (~15 atoms/nm$^3$).

Upon treatment of the $MgCl_2 \cdot n$EtOH/$SiO_2$/Si(100) model support with $TiCl_4$, the spin coated film stays largely intact. AFM revealed only minor effects on morphology and no change in the layer thickness was observed. The Ti/Mg ratio was ~0.15 according to XPS analysis. Ti distributes homogeneously in the film. In previous work, Magni and Somorjai [9] reported a Ti/Mg ratio of ~0.2-0.8 upon increasing the exposure of their model $MgCl_2$ film to $TiCl_4$, whereas Kaushik et al. [30] reported a Ti/Mg ratio of ~0.12-0.29 for Ziegler-Natta catalysts. Ti/Mg ratios of around 0.04-0.15 are typical for Ziegler-Natta catalysts used for polypropylene [41]. The chemical state of the $TiCl_4$ in our model catalyst remains ambiguous. The binding energy of 459.3 eV is typical for Ti (+4) and is close to that of $TiO_2$. During the

reaction of the spin coated support precursor (MgCl$_2 \cdot n$EtOH) with TiCl$_4$, compounds of type TiCl$_{4-n}$(OEt)$_n$ are formed. Removal and replacement of such species by TiCl$_4$ is relatively difficult [40] and it is probable that they are present in this model system, despite the use of a large excess of TiCl$_4$ in the catalyst preparation.

The MgCl$_2 \cdot n$EtOH/SiO$_2$/Si(100) model catalyst after treatment with TiCl$_4$ polymerizes ethylene in the presence of AlEt$_3$. We were able to produce a polyethylene layer 10,000 times thicker than the spin coated support layer (100 µm thickness PE, as opposed to 12±2 nm thickness of support MgCl$_2$). SEM indicated the formation of a 4 µm layer of polyethylene after 30 min., the thickness having increased to 100 µm after 16 hours and to 200 µm after 24 hours. The final polyethylene yield after 16 hours was 3.5 kg/g MgCl$_2$. This was obtained under very mild conditions (room temperature, 2 bar ethylene pressure). Magni and Somorjai [11] and Koranyi et al. [13] reported that titanium chloride systems formed by both electron irradiation-induced and by metallic Mg-induced chemical vapor deposition on thin films of Au and MgCl$_2$ were active for ethylene polymerization under UHV conditions with a nominal monomer insertion rate of 1.3 C$_2$H$_4$ molecules/(Ti atom)·s at 760 Torr and 300-350 K. Our system has a nominal insertion rate of 1.4 C$_2$H$_4$ molecules/(Ti atom)·s at 2 bar and room temperature.

## 3.5   Conclusions

Model Ziegler-Natta catalysts, active in ethylene polymerization, can be prepared by the spin coating of MgCl$_2$ from ethanol solution onto a flat silica/silicon wafer, followed by contact with TiCl$_4$. The flat model approach is beneficial in many ways. It allows a surface chemistry and morphological study of the catalyst and nascent polymer at the nanometer scale, at each stage of the catalyst preparation and polymerization, employing electron and scanning probe microscopy as well as surface science techniques such as XPS.

The catalyst preparation method is relevant for industrial Ziegler-Natta catalysts and produces MgCl$_2$ grains which, according to AFM observations, have sizes ranging from 10 to a few tens of nm. Treatment of the MgCl$_2$ support with TiCl$_4$ results in a homogenous distribution of Ti and in Ti/Mg ratios similar to those in industrial catalysts. The

$TiCl_4/MgCl_2/SiO_2/Si(100)$ model system, together with $AlEt_3$ as cocatalyst, shows a reasonable activity in ethylene polymerization, polymer growth taking place perpendicular to the flat support surface.

## References

1.  E. Albizzati, G. Cecchin, J.C. Chadwick, G. Collina, U. Giannini, G. Morini, L. Noristi, Polypropylene Handbook, 2nd Edition, ed. N. Pasquini, Hanser, Munich 2005, Ch. 2.
2.  U. Giannini, Makromol. Chem. Suppl.  5 (1981) 216.
3.  V. Busico, M. Causà, R. Cipullo, R. Credendino, F. Cutillo, N. Friederichs, R. Lamanna, A. Segre, V. Van Axel Castelli, J. Phys. Chem. C  112 (2008) 1081.
4.  P. Corradini, V. Busico, G. Guerra, Transition Metals and Organometallics as Catalysts for Olefin Polymerization, W. Kaminsky, H. Sinn, Eds., Springer-Verlag, Berlin 1988, p. 337.
5.  V. Busico, P. Corradini, L. De Martino, A. Proto, V. Savino, E. Albizzati, Makromol. Chem. 186 (1985) 1279.
6.  J.C. Chadwick, T. Garoff, J.R. Severn, Tailor-Made Polymers via Immobilization of Alpha-Olefin Polymerization Catalysts, Eds. J.R. Severn, J.C. Chadwick, WILEY-VCH, Weinheim, 2008, Ch. 2.
7.  L. Brambilla, G. Zerbi, S. Nascetti, F. Piemontesi, G. Morini, Macromol. Symp. 213 (2004) 287.
8.  L. Brambilla, G. Zerbi, F. Piemontesi, S. Nascetti, G. Morini, J. Mol. Catal. A Chem. 263 (2007) 103.
9.  E. Magni, G.A. Somorjai, J. Phys. Chem. B 102 (1998) 8788.
10. E. Magni, G.A. Somorjai, Surf. Sci. 345 (1996) 1.
11. E. Magni, G.A. Somorjai, Surf. Sci. 377-379 (1997) 824.
12. E. Magni, G.A. Somorjai, Surf. Sci. 341 (1995) L1078.
13. T.I. Koranyi, E. Magni, G.A. Somorjai, Top. Catal. 7 (1999) 179.
14. S.H. Kim, G.A. Somorjai, J. Phys. Chem. B 104 (2000) 5519.
15. E. Magni, T.I. Koranyi, G.A. Somorjai, Langmuir 16 (2000) 8113.
16. S.H. Kim, G.A. Somorjai,  Surf. Interface Anal. 31 (2001) 701.
17. E. Magni, G.A. Somorjai, Catal. Lett. 35 (1995) 205.
18. S.H. Kim, G.A. Somorjai, J. Phys. Chem. B 106 (2002) 1386.

19. S.H. Kim, G.A. Somorjai, Catal. Lett. 68 (2000) 7.

20. S.H. Kim, C.R. Tewell, G.A. Somorjai, Langmuir 16 (2000) 9414.

21. S.H. Kim, G.A. Somorjai, Appl. Surf. Sci. 161 (2000) 333.

22. S.H. Kim, G.A. Somorjai, J. Phys. Chem. B 105 (2001) 3922.

23. M.J. Pilling, A.A. Fonseca, M.J. Cousins, K.C. Waugh, M. Surman, P. Gardner, Surf. Sci. 578 (2005) 78.

24. A. Siokou, S. Ntais, Surf. Sci. 540 (2003) 379.

25. A. Siokou, S. Ntais, Surf. Sci. 600 (2006) 4216.

26. S. Ntais, V. Dracopoulos, A. Siokou, J. Mol. Catal. A Chem. 220 (2004) 199.

27. D. Fregonese, A. Glisenti, S. Mortara, G.A. Rizzi, E. Tondello, S. Bresadola, J. Mol. Catal. A:Chem. 178 (2002) 115.

28. H.-J. Freund, M. Bäumer, J. Libuda, T. Risse, G. Rupprechter, S. Shaikhutdinov, J. Catal. 216 (2003) 223.

29. T. Risse, J. Schimidt, H. Hamann, H.-J. Freund, Angw. Chem. Int. Ed. 41 (2002) 1518.

30. V.K. Kaushik, V.K. Gupta, D.G. Naik, Appl. Surf. Sci. 253 (2006) 753.

31. P.C. Thüne, C.P.J. Verhagen, M.J.G. van den Boer, J.W. Niemantsverdriet, J. Phys. Chem. B 101 (1997) 8559.

32. P.C. Thüne, J. Loos, A.M. de Jong, P.J. Lemstra, J.W. Niemantsverdriet, Top. Catal. 13 (2000) 67.

33. E.M.E. van Kimmenade, A.E.T. Kuiper, Y. Tamminga, P.C. Thüne, J.W. Niemantsverdriet, J. Catal. 223 (2004) 134.

34. J.C.J. Bart, W. Roovers, J. Mater. Sci. 30 (1995) 2809.

35. J.H. Scofield, J. Electron. Spectrosc. Relat. Phenom. 8 (1976) 129.

36. P.J. Cumpson, M.P. Seah, Surf. Interface Anal. 25 (1997) 430.

37. J.F. Moulder, W.F. Stickle, P.E. Sobol, K.D. Bomben, J. Chastain (Ed.), Handbook of X-ray Photoelectron Spectroscopy and Physical Electronics, Perkin-Elmer Corporation Eden Prairie, MN, 1992.

38. J.C. Chadwick, Ziegler–Natta Catalysts, Encyclopedia of Polymer Science and Technology, vol. 6, 2003, p. 517.

39. H. Mori, M. Sawada, T. Higuchi, K. Hasebe, N. Otsuka, M. Terano, Macromol. Rapid Commun. 20 (1999) 245.

40. L.L. Böhm, Angew. Chem. Int. Ed. 42 (2003) 5010.

41. A.K. Yaluma, P.J.T. Tait, J.C. Chadwick, J. Polym. Sci: Part A: Polym. Chem. 44 (2006) 1635.

# Chapter 4

# Propylene polymerization over a planar Ziegler-Natta model catalyst

*An active model for a Ziegler Natta propylene polymerization catalyst has been prepared by spin coating of a MgCl$_2$/diether donor solution in ethanol on a flat silica/silicon substrate. The flat model approach allows the characterization of the catalyst using surface spectroscopy and microscopy techniques. This model catalyst features a Ti/Mg atomic ratio of 0.2. The planar model is active for propylene polymerization, producing polymer films up to 50 µm thick. Scanning electron microscopy of these films reveals polymer growth in the direction perpendicular to the flat support surface.*

## 4.1   Introduction

Donor-free MgCl$_2$-TiCl$_4$ catalysts are suitable for ethylene polymerization, as already noted in **chapters one** and **three**, but are not sufficiently isospecific to produce isotactic polypropylene. The major breakthrough was the discovery and development of the stereoregulating effect of electron donors [1], especially internal-external donor pairs for the production of highly isotactic polypropylene. For propylene polymerization, the incorporation of an internal donor is required in the catalyst preparation to control the amount and distribution of TiCl$_4$ on the support surface. External electron donors are included in the polymerization to produce highly isotactic polypropylene. Good performance in terms of stereospecificity can be reached only by preventing the displacement of the MgCl$_2$-coordinated internal donor by the cocatalyst AlR$_3$, a strong Lewis acid present in the polymerization reaction. Lewis bases (electron donors) also play an essential role in achieving high catalyst activity.

Research aimed at defining the most suitable combination of donors is still going on, but some general selection rules exist, mostly dictated by the nature of the internal donor. Especially, it should [2, 3]:

- be firmly bound to the MgCl$_2$ surface.
- be stable and not form complexes or by products with AlR$_3$ (as mentioned), TiCl$_4$, and Ti-C and Ti-H bonds of the polymerization centers.

In this respect, internal donors such as diethers and external donors such as dialkoxysilanes proved to be much more effective than the initial internal–external donor couple based on aromatic esters. In particular, dimethoxy silanes having bulky alkyl groups on the silicon atom, for example cyclohexyl or cyclopentyl, are the preferred external donors (Figure 4.1).
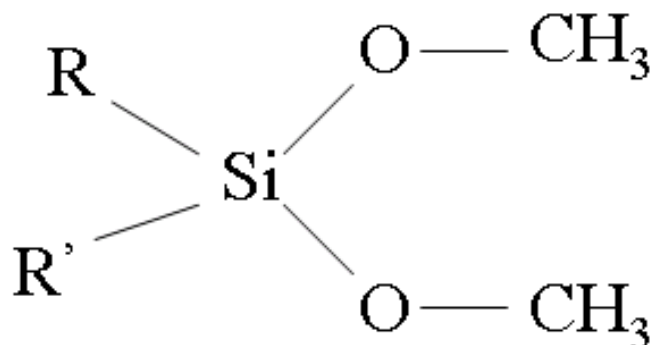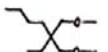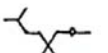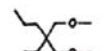
**Figure 4.1:** *General formula of dimethoxy silanes. R and R' represent the bulky alkyl groups.*

The first reason is that these donors are bidentate and thus tend to be more firmly bound to the $MgCl_2$ surface. The second is that they have the right oxygen–oxygen distance in their functional groups to form strong chelating complexes with the doubly unsaturated Mg atoms. On the other hand, phthalates have the tendency to react with the $AlR_3$ cocatalyst during polymerization due to the nucleophilic attack of the Al-C bond to the carbonyl group and hence they are easily displaced from the solid catalyst surface, where they are replaced by an alkoxysilane. The silanes cannot be used as internal donors due to reaction with the $TiCl_4$ present during catalyst preparation. In contrast, diethers having the general structure shown in Figure 4.2 can satisfy all the requirements for the ideal donor (4–14): chelating ability, suitable conformation to give a distance between the oxygen atoms in the range 2.5–3.3 Å, capability to coordinate to $MgCl_2$ also in the presence of $TiCl_4$ and $AlR_3$ and, finally, no side reaction with $TiCl_4$ during the catalyst synthesis and with Al-C, Ti-C, and Ti-H bonds during polymerization.
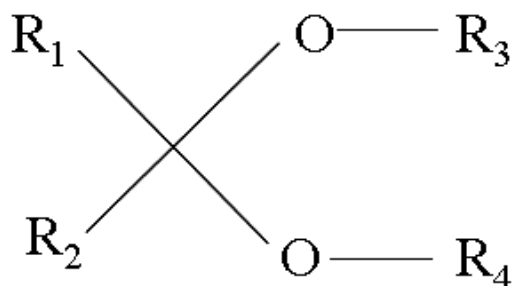


**Figure 4.2:** *General formula of 1,3-diether donors incorporated in the catalyst preparation.*

Table 4.1 illustrates the effect of the diether oxygen–oxygen distance on the isotactic index (I.I.) of polypropylene, based on experimental and theoretical data [2].

| | I.I. in % | O-O in Å | | I.I. in % | O-O in Å |
|---|---|---|---|---|---|
| | 64.9 | 2.9-4.7 | | 94.4 | 2.7-4.0 |
| | 74.9 | 3.9-7.2 | | 96.3 | 2.6-3.5 |
| | 89.8 | 2.7-4.8 | | 97.5 | 2.8 |
| | 92.5 | 2.6-4.0 | | 97.7 | 3.0 |
| | 93.6 | 2.8-4.1 | | 96.3 | 2.6-3.2 |
| | 93.6 | 3.1-4.5 | | 96.4 | 3.0 |

**Table 4.1.** *1,3-diether donors used as internal donors in MgCl$_2$ supported catalysts [2].*

The general trend is that when the O-O distance is near to 3 Å the catalyst performance in terms of isotacticity index (I.I.) is very good, whereas when the O-O can vary over a wide range the performance is poor. The O-O value also greatly affects polymer productivity [15].

An early mechanism to explain the stereoregulating effect of a Lewis base, proposed by Corradini et al. [16], was based on the competition of the Lewis base with TiCl$_4$ for selective coordination to unsaturated Mg atoms on the different lateral faces of MgCl$_2$. According to this model, dimeric stereospecific titanium species should be present on the (100) face, while the Lewis base should saturate the vacancies of tetracoordinated Mg atoms present on the (110) face, thus avoiding the formation on this plane of non-stereospecific sites. However, we will indicate the five-coordinate face as (104) rather than (100), following a re-evaluation of the crystal structure of MgCl$_2$ supports recently reported by Busico et al. [17] as noted in **chapter three**. Figure 4.3 indicates once more (already presented in **chapter three**) a model for a monolayer of a MgCl$_2$ crystal representing the most probable (104) and (110) cleavage surfaces and proposed coordination modes of TiCl$_4$ species on MgCl$_2$ lateral cuts, showing dimeric and monomeric species on a (104) cut and monomeric species on a (110) cut [19].
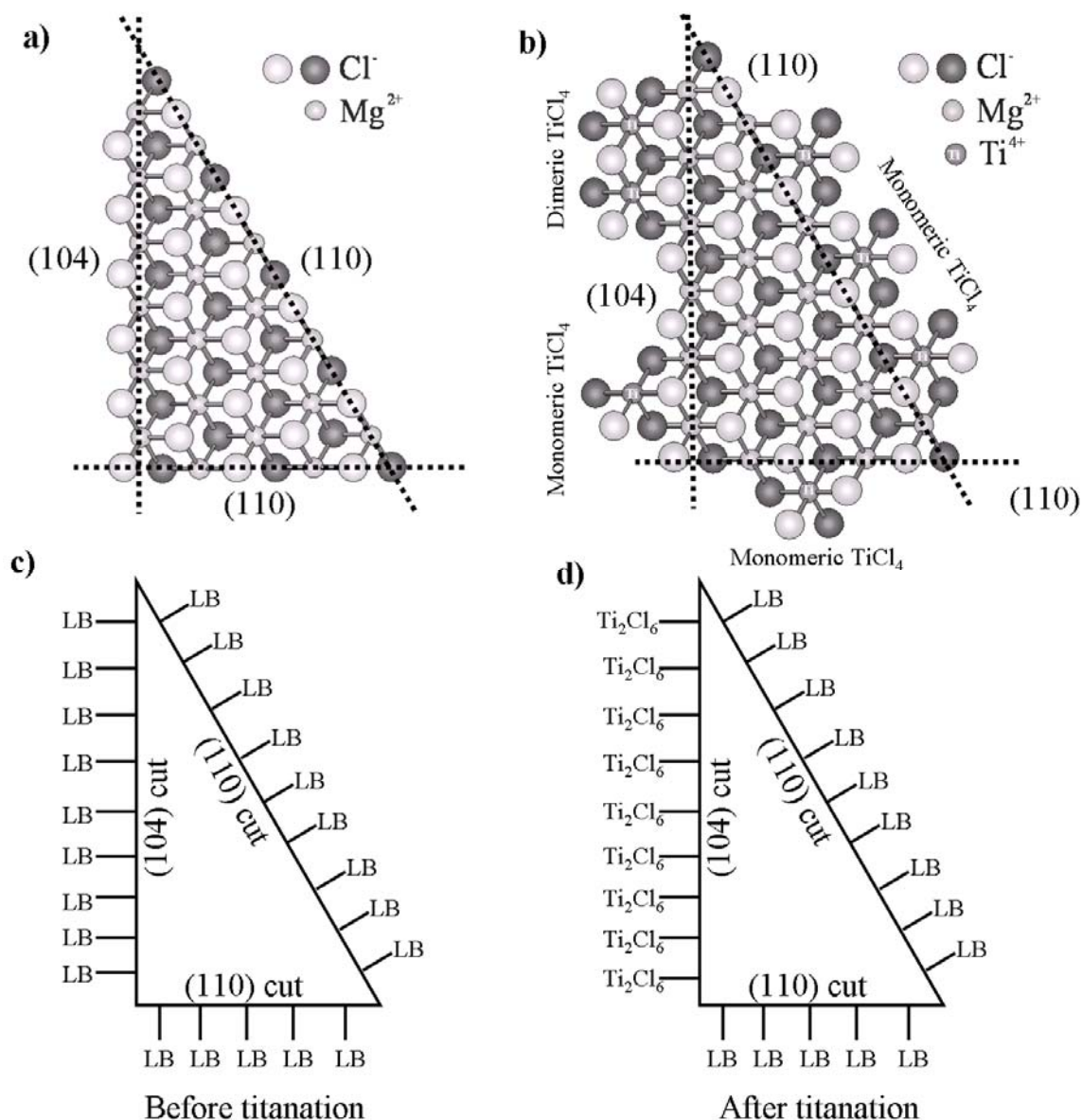
Schematic drawings of the hypothetical distribution of a Lewis Base (LB) on the (104) and (110) cuts before and after the reaction with $TiCl_4$ are also shown [18].

Nevertheless, a recent study of the Raman spectra of the products of co-milling mixtures of $MgCl_2$ and $TiCl_4$, supported by *ab initio* calculations, concluded that the adsorption of $TiCl_4$ gave a species with octahedrally coordinated titanium on the (110) lateral cut of $MgCl_2$ [20, 21]. This stable complex remained adsorbed upon washing with solvent, while dimeric species ($Ti_2Cl_8$) on the (100) cut, now indexed [17] as (104), were easily removed. The monomeric species with octahedrally coordinated titanium was as a consequence concluded to be the precursor for stereospecific active sites in $MgCl_2$-supported catalysts.

Yet again the utilization of advanced surface science techniques (as mentioned in **chapter three**) to characterize the active species in Ziegler-Natta catalysts has been introduced by Somorjai and coworkers, who have published a series of papers describing two synthetic routes to model Ziegler-Natta catalysts under UHV conditions. Ultra-thin films of $MgCl_2$ were prepared via sublimation onto a gold foil, followed by gas phase deposition of $TiCl_4$, whereas $TiCl_4/TiCl_2$ films were acquired by $TiCl_4$ and Mg codeposition on $MgCl_2$ and Au [22-27]. These systems were active for ethylene and propylene polymerization.

Furthermore, the same group of authors reported the reduction of $MgCl_2$ by $AlEt_3$ in the presence of Au, forming Mg clusters or islands; a large fraction of the resultant support surface was able to chemisorb $TiCl_4$ [28]. These systems were capable of producing polyethylene and polypropylene. The polymers obtained were characterized by means of surface science techniques, atomic force microscopy and vibrational spectroscopies and it was reported that polypropylene films having a high degree of isotacticity were obtained even when no donor was incorporated [29–31].

**Figure 4.3:** *a) Model for a monolayer of a MgCl$_2$ crystal showing the most probable (104) and (110) cleavage cuts. b) Proposed coordination modes of TiCl$_4$ species on MgCl$_2$ lateral cuts, showing dimeric and monomeric species on the (104) cut and monomeric species on the 110 cut [17, 19]. c) and d) Schematic drawings of hypothetical distribution of Lewis Base (LB) on the (104) and (110) cuts before and after reaction with TiCl$_4$ [17, 18].*

In the previous **chapter** (**chapter three**), we introduced the preparation and characterization of a model Ziegler-Natta catalyst, starting from the spin coating of a MgCl$_2$ solution in ethanol on a flat silica/silicon wafer. Subsequent contacts with TiCl$_4$ and AlEt$_3$ resulted in an

active catalyst for ethylene polymerization, allowing a study of the surface chemistry and morphology of the catalyst and polymer. We have now utilized the same model for propylene polymerization by firstly incorporating a diether donor in the spin coating of $MgCl_2$ from ethanol solution onto a Si wafer.

In this manner we endeavor to mimic yet again an industrial catalyst preparation, but now for propylene polymerization, taking into account the fact that catalysts produced by the reaction of $TiCl_4$ with $MgCl_2 \cdot n$EtOH adducts in the presence of a donor are widely used in polypropylene production [1]. We avoid, in this way, catalyst preparation under the UHV conditions developed previously by other groups, which is often far removed from the nature of real industrial catalysts [32, 33]. In this study, we disclose the construction of a realistic flat model of a Ziegler-Natta catalyst which is active for propylene polymerization, demonstrating the feasibility of this approach for the preparation and characterization of realistic catalytic models.

## 4.2   Experimental

### 4.2.1  Materials

Anhydrous magnesium chloride (beads, 99.9 %), absolute ethanol (99.9 %), titanium tetrachloride (99.9 %) and triethylaluminium (25 wt. % in toluene) were purchased from Aldrich Chemicals and used as received. HPLC-grade toluene was taken from an argon-flushed column packed with aluminium oxide and stored over 4 Å molecular sieves. Propylene was supplied by Linden (3.5).

### 4.2.2 Catalyst preparation and propylene polymerization

The catalyst preparation is summarized in Figure 4.4. All manipulations of air or water sensitive compounds were carried out using standard Schlenk or glovebox techniques. The $SiO_2/Si(100)$ wafer was prepared as described elsewhere (calcination at 750 $^0$C, followed by etching with $H_2O_2/NH_3$) [34] to obtain an amorphous silica layer (20 nm) on a silicon (100) wafer.
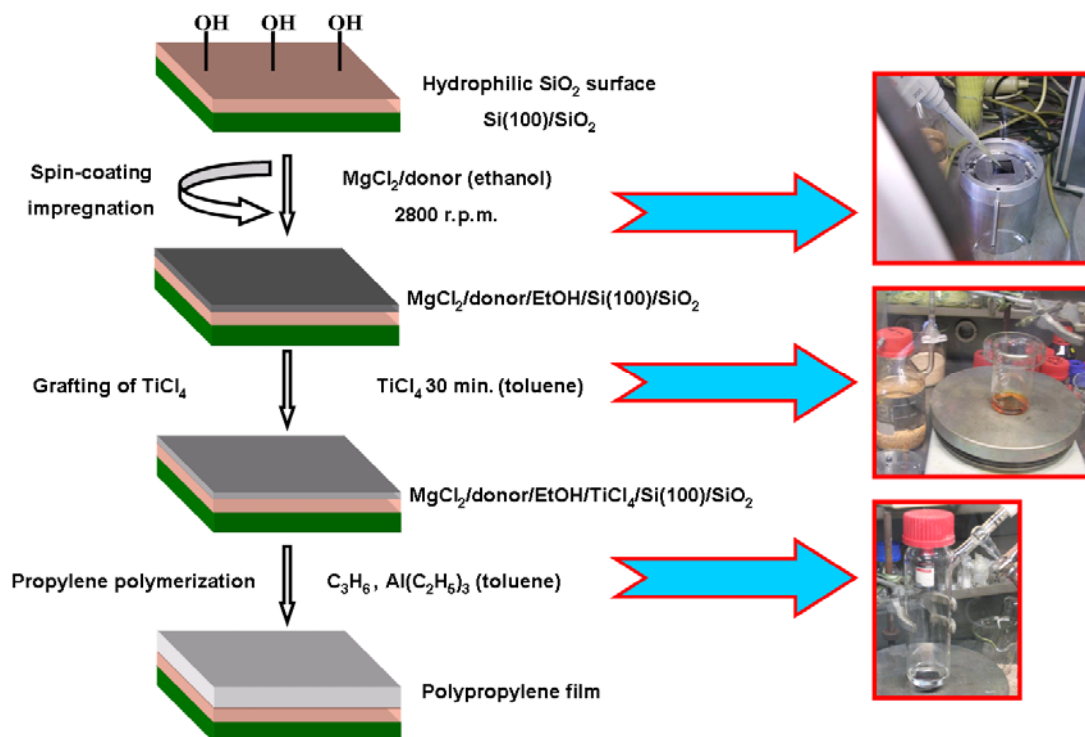
**Figure 4.4:** *Schematic representation of sample preparation for a Ziegler-Natta catalyst for propylene polymerization on a flat Si surface, along with images of steps carried out in the glove box.*

The wafer was partially dehydroxylated at 500 $^0$C in air for 16 hours. A small amount of surface hydroxyl groups was maintained with the intention to facilitate formation of a homogenous $MgCl_2$/diether film. Such a wafer was then spin coated with solutions of $MgCl_2$/diether in ethanol. Upon spinning, most of the liquid is ejected from the flat Si surface, leaving behind a thin film of solution. The remaining solvent evaporates and the solute precipitates upon the support surface. The rotation speed applied was 2800 r.p.m.

The diether donor used was 9,9–bis(methoxymethyl)fluorene [35] (Figure 4.5). The desired quantities of the diether were added to a solution of $MgCl_2$ in ethanol (42 mmol/L) and heated up to 60 °C until the solution became clear.

The wafer was afterwards dried under nitrogen and was then used as such for XPS and/or AFM analysis. Grafting of $TiCl_4$ onto the $MgCl_2$ support was carried out by treatment with a 10 % v/v $TiCl_4$ solution in toluene at room temperature. After washing with toluene to

remove the physisorbed $TiCl_4$, the model catalyst was dried under nitrogen. Thus the flat silica/silicon wafer containing the immobilized catalytic components can be used for either propylene polymerization or XPS analysis. Both the $TiCl_4$ treatment and the washing step took 30 min. unless otherwise stated.
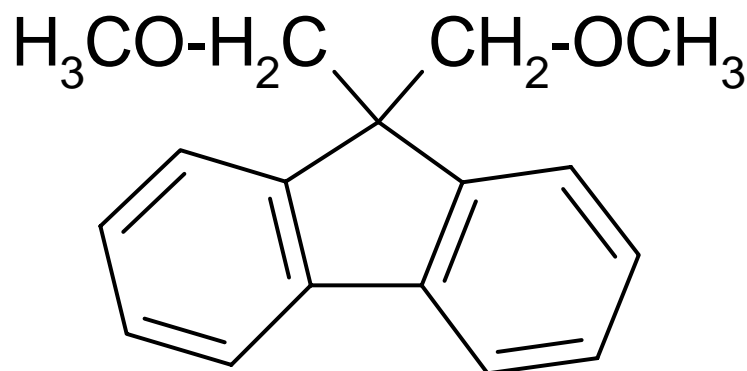


**Figure 4.5:** *Chemical structure of 9,9–bis(methoxymethyl)fluorene electron donor used in this work.*

Propylene polymerization was carried out at room temperature in a glass reactor equipped with a magnetic stirrer. The Si wafer after deposition of $MgCl_2$/diether donor and treatment with $TiCl_4$ was dipped into about 20 mL of a 1 mg/mL solution of the cocatalyst, $AlEt_3$, in toluene, inside the glass reactor. The reactor was pressurized with 3 bar of propylene and the polymerization was allowed to run for the desired time. After the polymerization, the wafer was washed with toluene.

## 4.2.3  Analytical techniques

AFM measurements were performed inside a glove box with Solver P47 base with SMENA head. The cantilever of choice was a non-contact gold-coated NSG11 (long end), manufactured by Micromasch. A typical force of the tip was 5.5 N/m and a typical resonance frequency 164 kHz. The measurements were performed in non-contact mode. The thickness of the catalyst support, $MgCl_2$, was determined using the height difference between the Si-substrate and $MgCl_2$ surface after scratching the layer with a scalpel.

The amount of Mg in solution and on the Si wafer was determined by an inductively coupled plasma optical emission spectrometry (ICP-OES) technique using a Spectro Circos CCD

spectrometer. All the solutions and the $MgCl_2$ of the spin coated wafers were dissolved in $HCl_{aq}$ (0.1 M).

X-ray photoelectron spectroscopy measurements were performed with a VG escalab 200 using a standard aluminum anode (Al-K$\alpha$ 1486.3 ev) operation at 300 W. Spectra were recorded at normal emission background pressure 1 x $10^{-9}$ mbar. Binding energies were calibrated to C 1s peak at 285 eV.

SEM was performed using a Philips environmental scanning electron microscope XL-30 ESEM FEG (Philips, The Netherlands, now Fei Co.) in high-vacuum mode using a low accelerating voltage (low-voltage SEM, LVSEM) and a secondary (SE) detector.

High-temperature size exclusion chromatography (SEC) was used to determine the molecular weight and molecular weight distribution of the polypropylene samples. The required sample amount (at least 1 mg) was obtained by removal of the polymer from the catalyst surface using a scalpel and the measurement was carried out in 1,2,4-trichlorobenzene at 140 ºC using a PL 220 instrument and a calibration with polystyrene standards.

A Q100 DSC (TA Instruments) was used to determine the melting points of the polypropylene samples. The required sample amount was in all cases at least 1 mg and was obtained by removal of the polymer from the catalyst surface using a scalpel. Scans were performed at a rate of 10 ºC/min from 0 to 160 ºC and again back to 0 ºC, after which the heating scan was repeated.

## 4.3  Results

### 4.3.1 Propylene polymerization over TiCl$_4$/MgCl$_2$/SiO$_2$/Si(100)

Propylene polymerization was initially tested with the spin coated layer of $MgCl_2 \cdot n$EtOH after treatment with $TiCl_4$. Polymerization was run for 24 hours at room temperature and at 3 bar pressure. Our standard catalyst used for propylene polymerization was prepared from a 42 mmol∕L solution, resulting in a Mg loading of 200 atoms∕$nm^2$ as noted in **chapter three** for ethylene polymerization. The Ti2p/Mg2s ratio of the $TiCl_4$/$MgCl_2$/$SiO_2$/Si(100) system

corresponded to a Ti/Mg atomic ratio of 0.15. Bearing in mind the morphology of MgCl$_2$·$n$EtOH film discussed in **chapter three**, the polymer obtained after propylene polymerization appeared a featureless film (Figure 4.6), which in the higher magnification of the SEM image appeared rather porous. The thickness of the polymer film was less than ~ 1 µm and the amount of polymer produced was less than 1 mg (on a wafer with a size of 3x3 cm$^2$). The isotacticity index (I.I.) of the polymer obtained was about 60 % and was determined by ATR-IR (attenuated total reflectance infrared). This will be discussed in detail in **chapter seven**.
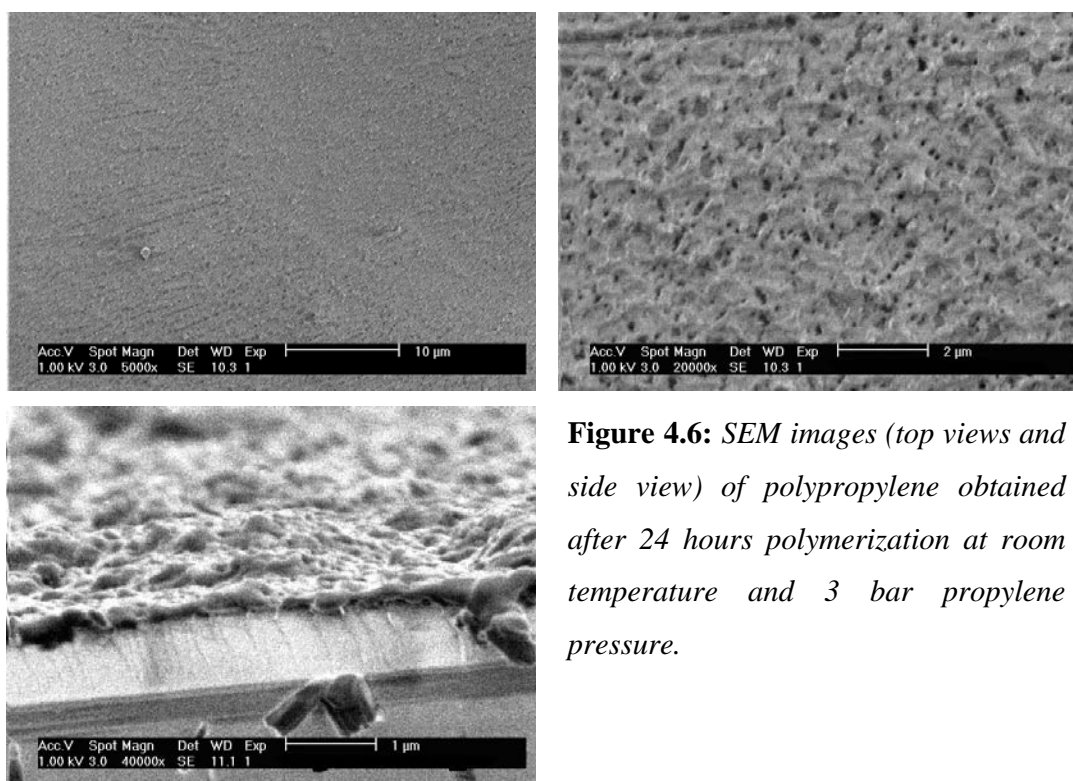


**Figure 4.6:** *SEM images (top views and side view) of polypropylene obtained after 24 hours polymerization at room temperature and 3 bar propylene pressure.*

## 4.3.2 XPS analysis of MgCl$_2$/diether·$n$EtOH/SiO$_2$/Si(100)

A planar model support, prepared by spin coating of MgCl$_2$/diether·$n$EtOH from ethanol solution onto a flat silica/silicon wafer, was studied using X-ray photoelectron spectroscopy (XPS). Figure 4.7 shows overview XPS spectra of spin coated MgCl$_2$·$n$EtOH films prepared with and without diether donor. In these experiments the diether/MgCl$_2$ molar ratio was 0.1, 0.4 and 2. It is apparent on comparing the bottom spectrum in Figure 4.7 with the successive spectra that, upon addition of the diether donor, the C 1s signals in the XPS spectra increase. The O 1s signal also increases upon addition of the diether donor. The Mg/Cl ratio in the spin

coated $MgCl_2 \cdot n$EtOH film prepared in the absence of donor was 1.00:1.96, indicating that the magnesium chloride had deposited without any significant hydrolysis as noted in the previous **chapter**. This ratio remained unchanged upon incorporation of the diether donor for all the loadings used.

The standard diether/$MgCl_2$ molar ratio of this work was 0.1, similar to that in typical Ziegler-Natta catalysts containing this donor [36]. Treatment with $TiCl_4$ was carried out on a Si wafer with a diether/$MgCl_2$ molar ratio of 0.1. Such a wafer was contacted for 30 min. with a 10 % v/v $TiCl_4$ solution in toluene, followed by a 30 min. extraction with toluene to remove weakly bound $TiCl_4$. Figure 4.8 shows the XPS spectrum after contacting the $MgCl_2 \cdot$diether$\cdot n$EtOH support with $TiCl_4$.

The inserted spectra show the Ti 2p peak after the contact with $TiCl_4$ and the Si 2s peaks before and after the treatment with $TiCl_4$. The Si/Mg ratio (0.10) [37] does not change upon treating with $TiCl_4$, indicating that the film stays intact. The Mg 2s and Mg 2p emissions showed maxima at binding energy 90.8 eV and 52.0 eV, whereas Cl $2p_{3/2}$ appeared at 199.5 eV. The maximum of the Ti $2p_{3/2}$ emission was at 459.5 eV, typical for Ti (+4). The Ti2p/Mg2s ratio corresponds to a Ti/Mg atomic ratio of 0.2 [37]. This ratio remained constant when changing the take-off angle for the photoelectrons from $0^0$ to $60^0$ relative to the surface, indicating a homogeneous distribution of the Ti in the spin coated film.
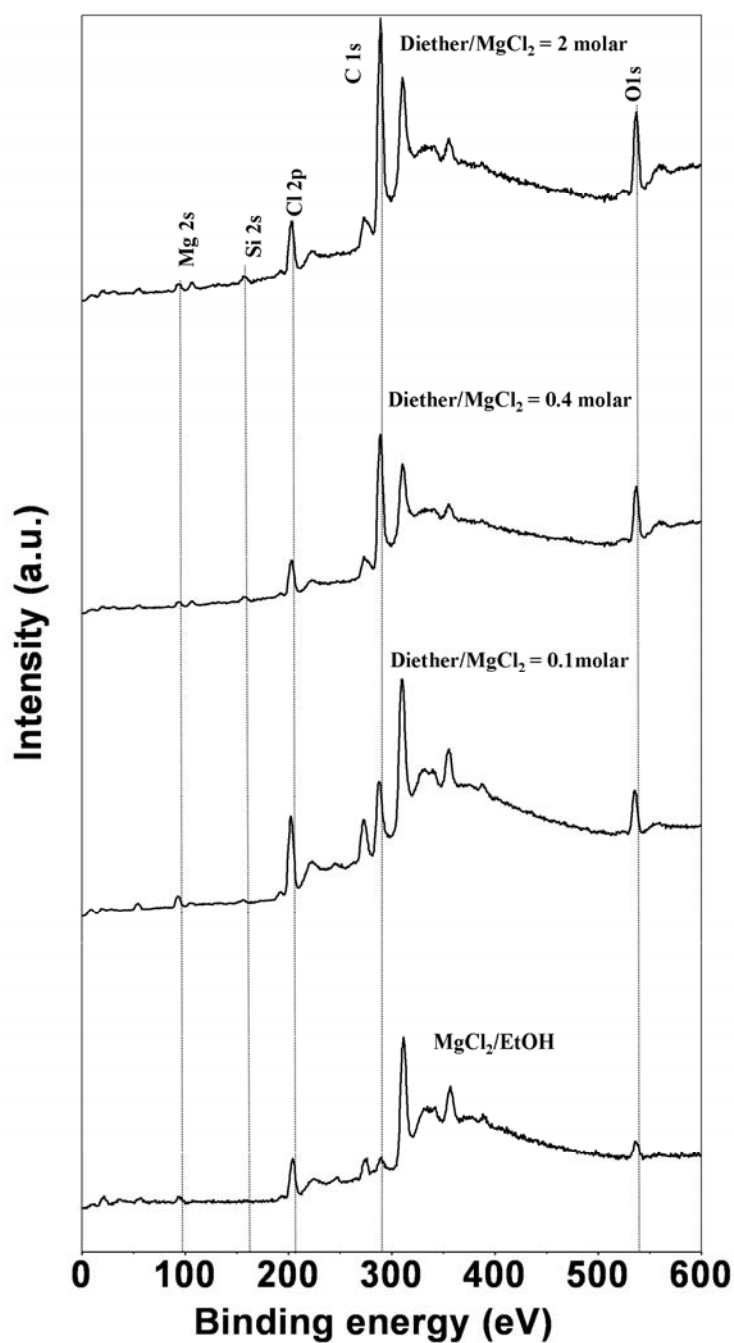
**Figure 4.7:** *XPS spectra of a spin coated layer of MgCl₂·nEtOH film (bottom) and successive MgCl₂/diether·nEtOH films. The loading of the diether donor has been successively increased from bottom to top diether/MgCl₂ = 0.1, 0.4 and 2 molar ratio.*
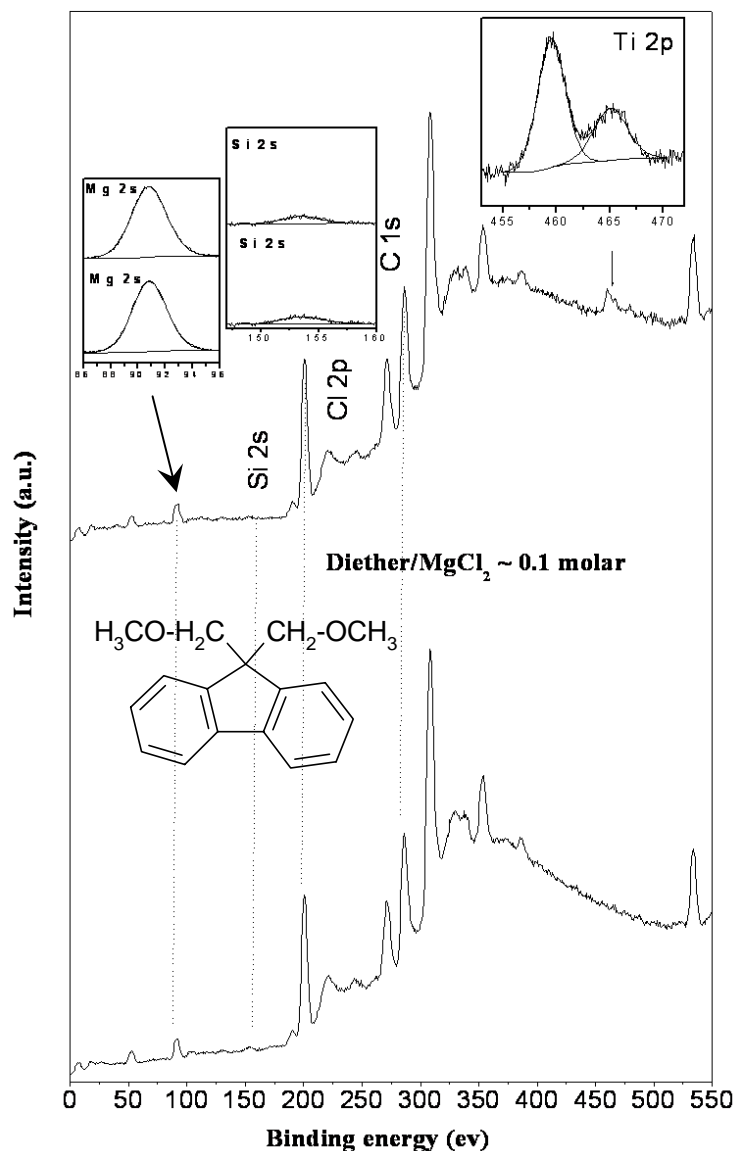
**Figure 4.8:** *Wide-scan XPS spectra of MgCl₂·diether·nEtOH film before and after treatment of with TiCl₄. The inserted spectra show the Ti 2p peak and the Si 2s peaks before and after treatment with TiCl₄.*

Additionally treatment with $TiCl_4$ of $MgCl_2$·diether·$n$EtOH film for the diether/$MgCl_2$ = 0.4 molar ratio gave a Ti/Mg atomic ratio of 0.2. This ratio remained invariable when changing the take-off angle for the photoelectrons from $0^0$ to $60^0$ relative to the surface, indicating a homogeneous distribution of the Ti in the spin coated film. However, treatment with $TiCl_4$ of $MgCl_2$·diether·$n$EtOH film for high loading i.e., diether/$MgCl_2$ = 2 molar ratio gave a Ti/Mg

atomic ratio of 1. This high ratio can be attributed to additional formation of a $TiCl_4$/diether complex.

### 4.3.3 AFM and SEM analysis of MgCl$_2$/diether·$n$EtOH/SiO$_2$/Si(100)

The morphology of the MgCl$_2$·diether·$n$EtOH model catalyst with a diether/MgCl$_2$ molar ratio of 0.1 (standard loading) was probed with AFM. The spin coated MgCl$_2$/diether from ethanol solution yielded a film with a surface roughness of 1-3 nm (Figure 4.9a). The thickness of diether-containing film was $25 \pm 5$ nm. Morphologies of the diether-containing films for the higher loadings (diether/MgCl$_2$ = 0.4 and 2) were also probed. Figure 4.9b is an AFM image (diether/MgCl$_2$ = 0.4) of a film which consists of moderately spherical particles.
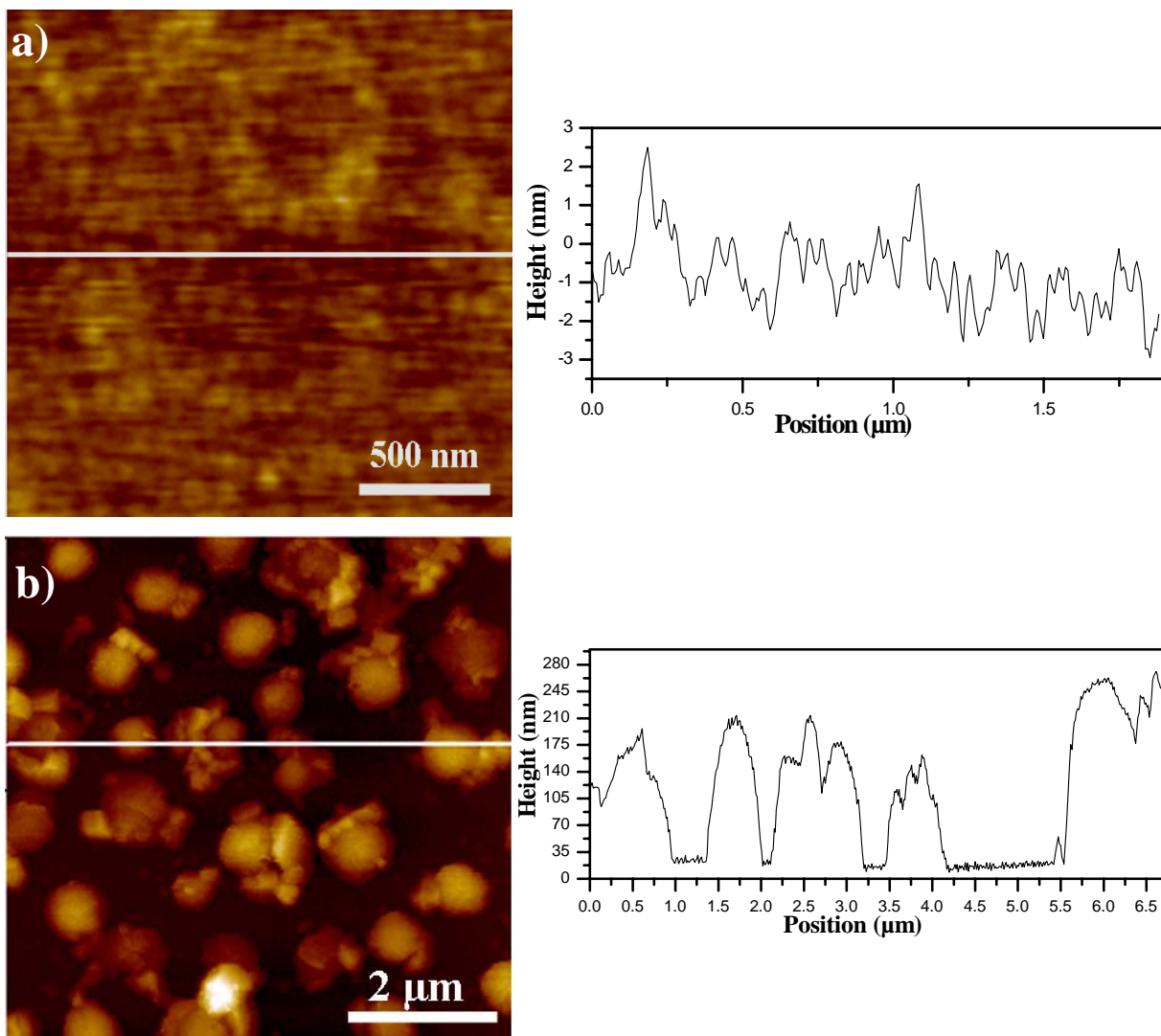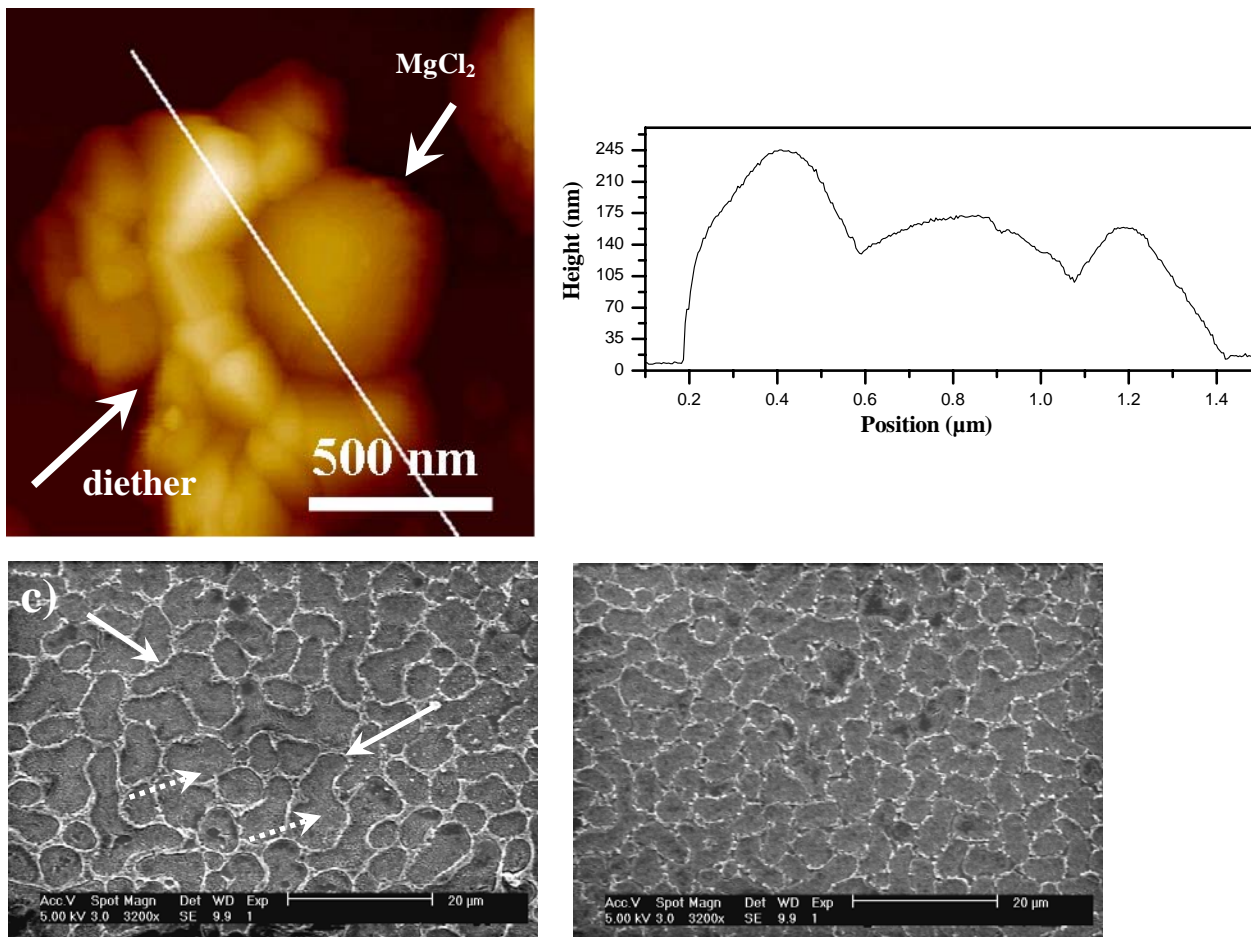
**Figure 4.9:** *a) and b) AFM images of diether/MgCl$_2$ spin coated layers from ethanol for 0.1 and 0.4 molar ratios, respectively. c) SEM images of diether/MgCl$_2$ spin coated layers from ethanol for 2 molar ratio. The solid arrows indicate the location of the donor, whereas the dashed arrows indicate the location of the MgCl$_2$.*

The diether donor appears to be allocated around the MgCl$_2$ particles. This is more evident in the higher resolution image. The height of the particles varies from 150 up to 250 nm. As the diether content increases further (diether/MgCl$_2$ = 2) the SEM images (AFM was impossible to be operated on such rough films) disclose more pronouncedly the effect of the diether donor, which seems to have fully coordinated around MgCl$_2$ particles. The location of the diether donor and MgCl$_2$ is indicated by the solid and the dashed arrows, respectively, in Figure 4.9c. The coordination of the diether donor around MgCl$_2$ particles will be more evident in **chapter seven**, in which the donor will be shown to be located at the edges and corners of MgCl$_2$ crystallites. It is essential to mention that the diether-containing films for

this high loading were transferred in sealed bottles. They were quickly opened under nitrogen flow before transfer to the SEM chamber and vacuumed afterwards before imaging.

The changes that the diether-containing films experience in terms of morphology are depicted in Figure 4.10. Let us assume that the film of the standard loading i.e., diether/MgCl$_2$ = 0.1, consists of small particles around which the diether donor coordinates, similar to the morphology of AFM images observed for diether/MgCl$_2$ = 0.4 (Figure 4.10a). As the content of the diether increases (diether/MgCl$_2$ = 0.4), the film is composed of rather spherical particles surrounded by the diether donor (Figure 4.10b). Lastly, at even higher loadings (diether/MgCl$_2$ = 2), the diether breaks the film of MgCl$_2$ creating random shapes of the latter, enclosing the edges of the MgCl$_2$ particles (Figure 4.10c).
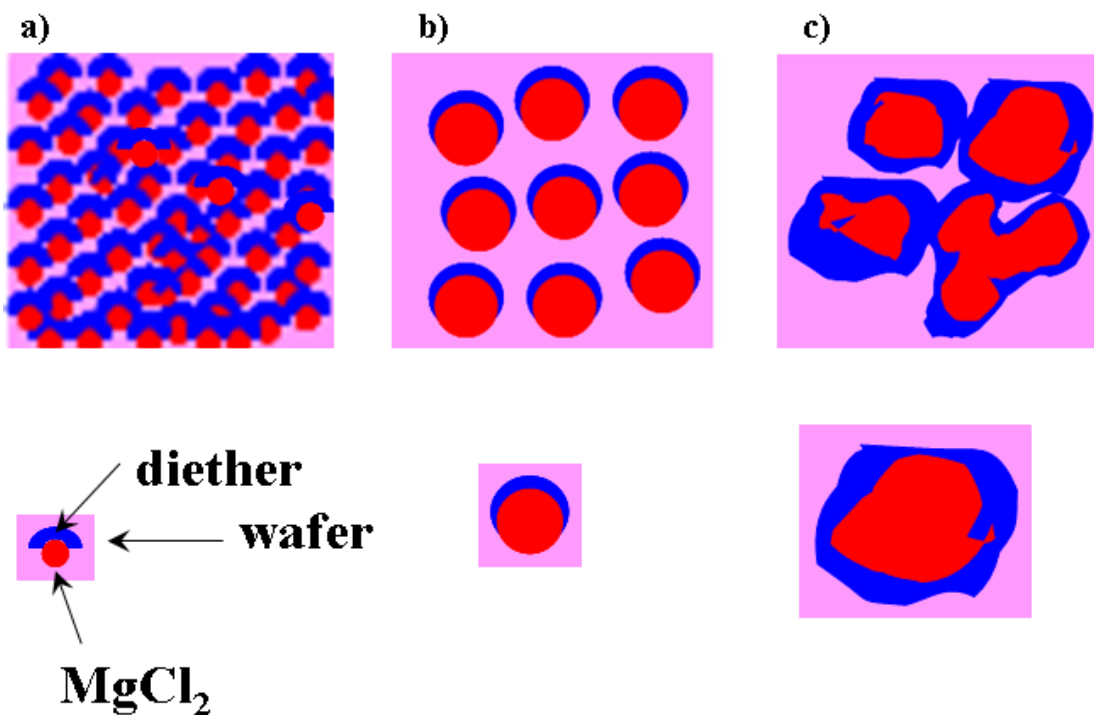


**Figure 4.10:** *Schematic representation of diether-containing films for the loadings a) Diether/MgCl$_2$ = 0.1, b) Diether/MgCl$_2$ = 0.4, c) Diether/MgCl$_2$ = 2.*

## 4.3.4 Propylene polymerization over TiCl$_4$/MgCl$_2$/diether·$n$EtOH /SiO$_2$/Si(100)

The model catalyst prepared as described above proved to be active for propylene polymerization at 3 bar propylene pressure and room temperature (for the standard loading). Polypropylene (PP) is formed, in milligram quantities, as a thin film on the silica/silicon surface (3x3 cm$^2$). No polymer formation was observed in the solution. SEM indicated a thickness of the polymer film of up to 50 μm after 24 hours polymerization when diether donor was incorporated into the system. This corresponds to a polymer yield of 1.0 kg PP/g MgCl$_2$ after 24 hours.

In the SEM images (Figure 4.11a) the polymer films appear to consist of a mass of elongated particles when viewed from the top. A lateral view, however, clearly reveals that the polymer films consist of a folded layer which is aligned perpendicular to the surface of the support, indicating a vertical growth of the polypropylene film. The polymer obtained after 24 hours polymerization had an $M_w$ of 404,300 g·mol$^{-1}$ and a molecular weight distribution ($M_w/M_n$) of 8.8. The polymer melting point, determined by DSC, was 153 °C. Figure 4.11a also shows a white film of polypropylene formed on the wafer, and a black wafer from which the polymer layer has been peeled off. The isotacticity index (I.I.) of the polymer obtained was about 80 % and was determined by ATR-IR (attenuated total reflectance infrared). We will come back to this in **chapter seven**.

The model catalysts prepared with the higher loadings of the diether donor also proved to be active for propylene polymerization, at 3 bar monomer pressure and room temperature. Polypropylene (PP) is again formed, in milligram quantities, as a thin film on the wafer surface (3x3 cm$^2$). No polymer was formed in the solution. SEM indicated a polymer film thickness of up to 50 μm after 24 hours polymerization when the diether/MgCl$_2$ molar ratio was 0.4. The top-views SEM images in Figure 4.11b for PP obtained at diether/MgCl$_2$ = 0.4 show a morphology analogous to that of the morphology of the film obtained at diether/MgCl$_2$ = 0.1. This implies that that the morphologies of the spin coated layers from ethanol solutions with diether/MgCl$_2$ molar ratios of 0.1 and 0.4 are also similar and justifies the assumption in the drawing in Figure 4.10a. The catalyst prepared with the highest diether loading (diether/MgCl$_2$ = 2) also produced polypropylene, but the thickness of the layer did

not exceed 10 μm (after 24 hours propylene polymerization at room temperature and 3 bar monomer pressure), according to the lateral views of the SEM images. Nevertheless, the top views of these polymers (SEM images in Figure 4.11c) indicate a morphology identical to that of the corresponding spin coated layers.
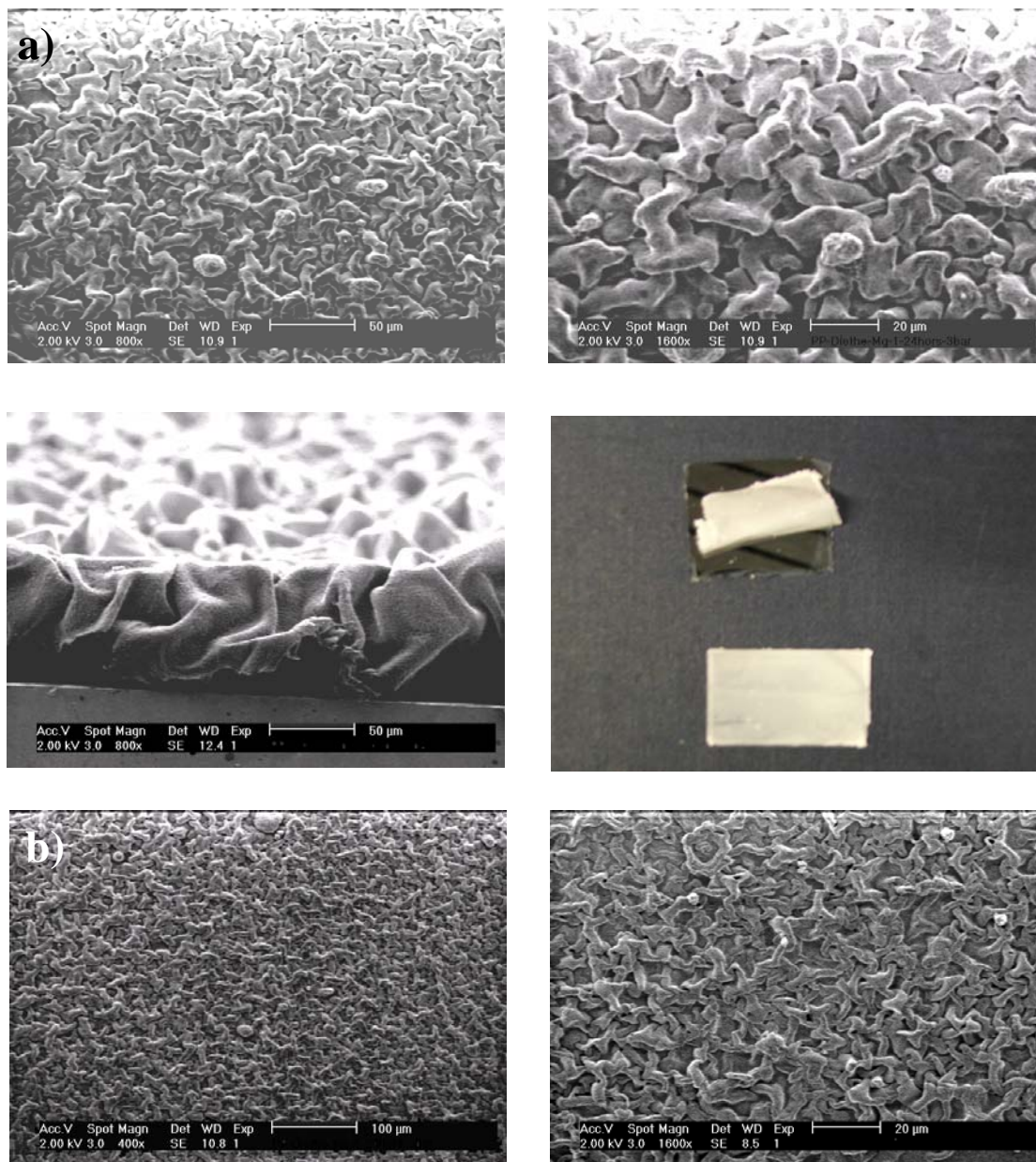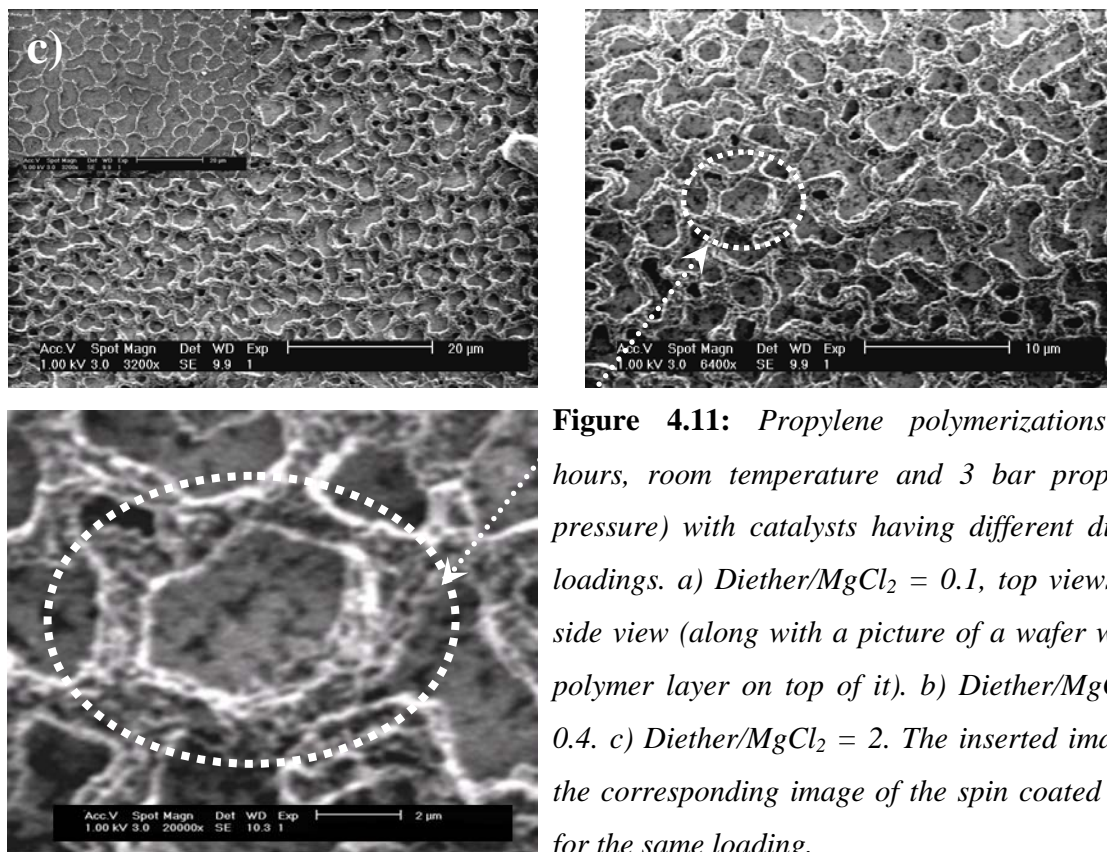
**Figure 4.11:** *Propylene polymerizations (24 hours, room temperature and 3 bar propylene pressure) with catalysts having different diether loadings. a) Diether/MgCl₂ = 0.1, top views and side view (along with a picture of a wafer with a polymer layer on top of it). b) Diether/MgCl₂ = 0.4. c) Diether/MgCl₂ = 2. The inserted image is the corresponding image of the spin coated layer for the same loading.*

This is apparent when comparing the SEM images of the polymer in the Figure 4.11c with the inserted image or with the SEM images of the spin coated layers in Figure 4.9c. Surprisingly, the SEM images in Figure 4.11c indicate the formation of an apparently hexagonal structure. This is more evident in the higher magnification SEM image of the polypropylene, indicated by a dashed circle. We will discuss this in more detail in **chapter six**.

The polymer yield obtained at diether/MgCl₂ = 0.4 was comparable to the yield of polymer for the standard loading (diether/MgCl₂ = 0.1). However, the polymer yield decreased when a diether/MgCl₂ molar ratio of 2 was used.

## 4.4  Discussion

A flat model catalyst, prepared by spin coating of MgCl$_2$/diether·$n$EtOH from ethanol solution onto a flat silica/silicon wafer followed by treatment with TiCl$_4$, has been studied by means of XPS, AFM and SEM with the purpose of characterizing and visualizing the Ziegler-Natta catalyst and also the polymer produced.

The polymer produced when no donor was incorporated appeared as a featureless film according to SEM observations; but major changes in the polymer morphology occurred when the diether donor was incorporated. Furthermore, this was associated with an increase in the yield and isotacticity index (I.I.) of the polymer produced.

XPS showed that, by varying the amount of the diether in MgCl$_2$/ethanol solutions the loading of the diether donor in the MgCl$_2$·$n$EtOH films can also be tuned. The spin coating of MgCl$_2$/diether·$n$EtOH yielded films which consisted of MgCl$_2$ particles bordered by diether donor. This was more pronounced for the higher diether loadings.

Upon treatment of the MgCl$_2$/diether·$n$EtOH/SiO$_2$/Si(100) model support with TiCl$_4$, the spin coated film stays intact according to XPS analysis for the standard diether loading. The Ti/Mg ratio was ~0.2 according to XPS. However, the film prepared at diether/MgCl$_2$ = 0.4 also had a Ti/Mg ratio of ~0.2 according to XPS. Ti distributes homogeneously in the film. Ti/Mg ratios of around 0.04-0.15 are typical for Ziegler-Natta catalysts used for polypropylene [36]. The chemical state of the TiCl$_4$ in our model catalyst remains ambiguous. The binding energy of 459.5 eV is typical for Ti (+4) and is close to that of TiO$_2$. However, Kaushik et al. reported a BE of 459.8 eV for the Ti 2p3/2 peak for a catalyst containing ethyl benzoate as internal donor [38].

The MgCl$_2$/diether·$n$EtOH/SiO$_2$/Si(100) model catalyst after treatment with TiCl$_4$ polymerizes propylene in the presence of AlEt$_3$. We were able to produce a polypropylene layer with a thickness of 50 μm after 24 hours. The final polypropylene yield after 24 hours was 1.0 kg/g MgCl$_2$. This was obtained under very mild conditions (room temperature, 3 bar propylene pressure). Magni and Somorjai [30] reported a turnover frequency of 0.2 molecules/(site·s) for propylene polymerization with a model Ziegler-Natta catalyst, prepared

by gas phase deposition of an ultra-thin TiCl$_4$/MgCl$_2$ film in UHV conditions, at 760 torr and 300 K. Our system has a nominal insertion rate of 0.14 C$_3$H$_6$/(Ti atom·s) at 3 bar pressure and room temperature.

We tentatively attribute the particular morphology of the polypropylene films (top views observed by SEM) to the morphology of the MgCl$_2$/diether films observed by AFM. Bearing in mind the schematic representation in Figure 4.10 and assuming that TiCl$_4$ is adsorbed in vicinity of the diether donor, the shape of the polymer particle will be dictated by the distribution/coordination and the amount of the donor around each MgCl$_2$ grain/particle. This was especially obvious when the diether donor amount was increased further to give a diether/MgCl$_2$ molar ratio of 2. A tentative schematic representation for the polymer morphology formation is depicted in Figure 4.12.
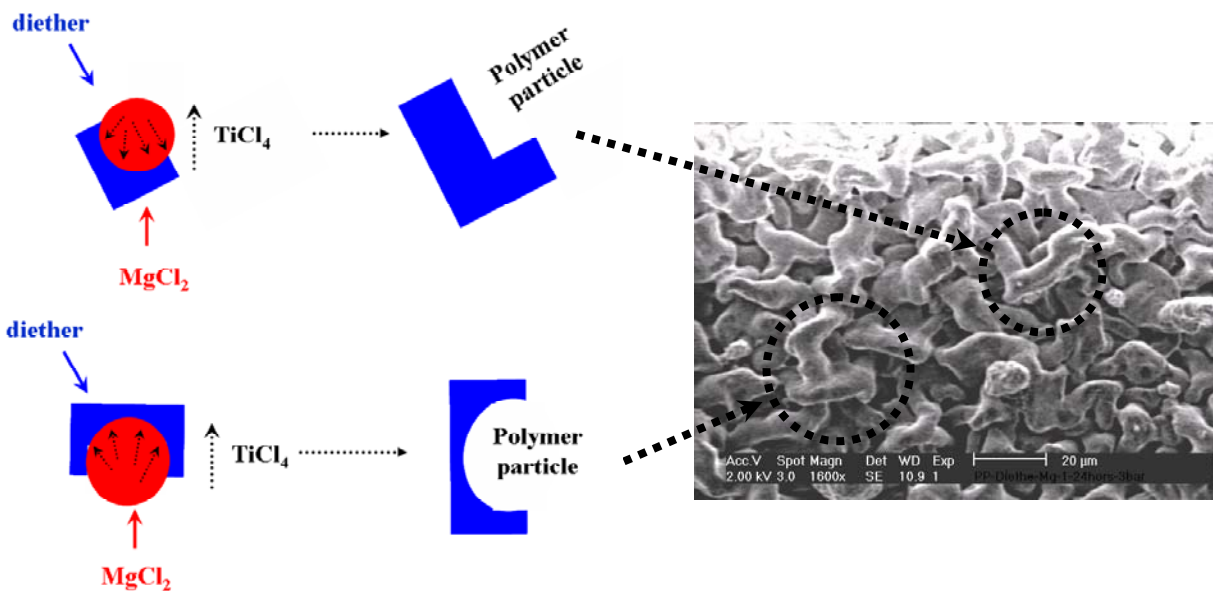


**Figure 4.12:** *A tentative schematic representation for the polypropylene morphology formation. The arrows indicate similarities between the drawn particles and those observed on the top view of the SEM image.*

## 4.5 Conclusions

Model Ziegler-Natta catalysts, active in propylene polymerization, can be prepared from supports obtained by the spin coating of $MgCl_2$/diether·$n$EtOH from ethanol solution onto a flat Si wafer. The flat model is valuable as it allows a surface chemistry and morphological study of the catalyst and nascent polymer, employing microscopy techniques (SEM) as well as surface science techniques such as XPS.

The catalyst preparation produces $MgCl_2$/diether films which, according to SEM observations, determine the morphology of the polypropylene obtained. Treatment of the $MgCl_2$/diether film (standard loading) with $TiCl_4$ results in a homogenous distribution of Ti and in Ti/Mg ratios close to those in industrial catalysts. The $TiCl_4$/$MgCl_2$/diether/$SiO_2$/Si(100) model system, together with $AlEt_3$ as cocatalyst, shows a reasonable activity in propylene polymerization, polymer growth taking place perpendicular to the flat support surface.

## References

1. U. Giannini, A. Cassata, P. Longi, R. Mazzocchi U.S. Pat. 4,336,360, June 22, 1982 (to Montedison).
2. L. Barino, R. Scordamaglia, Theory Simul. 7 (1998) 399.
3. L. Barino, R. Scordamaglia, Theory Simul. 7 (1998) 407.
4. G. Morini, E. Albizzati, G. Balbontin, G. Baruzzi, A. Cristofori, Eur. Pat. 728,769, Aug. 28, 1996 (to Montell North America Inc.).
5. G. Morini, E. Albizzati, G. Balbontin, G. Baruzzi, A. Cristofori, Eur. Pat. 728,770, Aug. 28, 1996 (to Montell North America Inc.).
6. G. Morini, A. Cristofori, Eur. Pat. 728,724, Aug. 28, 1996 (to Montell North America Inc.).
7. E. Albizzati, P.C. Barbe, L. Noristi, R. Scordamaglia, L. Barino, U. Giannini, G. Morini, Eur. Pat. 361,494, Apr. 4, 1990 (to Himont, Inc.).
8. P.C. Barbe, L. Noristi, R. Scordamaglia, L. Barino, E. Albizzati, U. Giannini, G. Morini Eur. Pat. 362,705, Nov. 11, 1990 (Himont, Inc.).
9. J.C. Chadwick, G. Morini, G. Balbontin, I. Camurati, J.J.R. Heere, I. Mingozzi, F. Testoni, Macromol. Chem. Phys. 202 (2001) 1995.

10. M. Toto, G. Morini, G. Guerra, P. Corradini, L. Cavallo, Macromolecules, 33 (2000) 1134.

11. J.C. Chadwick, G. Morini, G. Balbontin, I. Mingozzi, E. Albizzati, O. Sudmeijer, Macromol. Chem. Phys. 198 (1997) 1181.

12. G. Morini, E. Albizzati, G. Balbontin, I. Mingozzi, M.C. Sacchi, F. Forlini, I. Tritto, Macromolecules 29 (1996) 5770.

13. M.C. Sacchi, F. Forlini, I. Tritto, P. Locatelli, G. Morini, L. Noristi, E. Albizzati, Macromolecules 29 (1996) 3341.

14. M.C. Sacchi, F. Forlini, I. Tritto, P. Locatelli, G. Morini, G. Baruzzi, E. Albizzati, Macromol. Symp. 89 (1995) 91.

15. E. Albizzati, U. Giannini, G. Morini, M. Galimberti, L. Barino, R. Scordamaglia, Macromol. Symp. 89 (1995) 73.

16. P. Corradini, V. Barone, R. Fusco, G. Guerra, Gazz. Chim. Ital. 113 (1983) 601.

17. V. Busico, M. Causà, R. Cipullo, R. Credendino, F. Cutillo, N. Friederichs, R. Lamanna, A. Segre, V. Van Axel Castelli, J. Phys. Chem. C 112 (2008) 1081.

18. E. Albizzati, U. Giannini, G. Morini, C.A. Smith, R.C. Zeigler, in G. Fink, R. Mülhaupt, H.H. Brintzinger, eds., Ziegler Catalysts. Recent Scientific Innovations and Technological Improvements, Springer-Verlag, Berlin, 1995, p. 413.

19. J.C. Chadwick, T. Garoff, J.R. Severn, Tailor-Made Polymers via Immobilization of Alpha-Olefin Polymerization Catalysts, Eds. J.R. Severn, J.C. Chadwick, WILEY-VCH, Weinheim, 2008, Ch. 2.

20. L. Brambilla, G. Zerbi, S. Nascetti, F. Piemontesi, G. Morini, Macromol. Symp. 213 (2004) 287.

21. L. Brambilla, G. Zerbi, F. Piemontesi, S. Nascetti, G. Morini, J. Mol. Catal. A Chem. 263 (2007) 103.

22. E. Magni, G.A. Somorjai, J. Phys. Chem. B 102 (1998) 8788.

23. E. Magni, G.A. Somorjai, Surf. Sci. 345 (1996) 1.

24. E. Magni, G.A. Somorjai, Surf. Sci. 377-379 (1997) 824.

25. E. Magni, G.A. Somorjai, Surf. Sci. 341 (1995) L1078.

26. T.I. Koranyi, E. Magni, G.A. Somorjai, Top. Catal. 7 (1999) 179.

27. S.H. Kim, G.A. Somorjai, J. Phys. Chem. B 104 (2000) 5519.

28. E. Magni, T.I. Koranyi, G.A. Somorjai, Langmuir 16 (2000) 8113.

29. S.H. Kim, G.A. Somorjai, Surf. Interface Anal. 31 (2001) 701.

30. E. Magni, G.A. Somorjai, Catal. Lett. 35 (1995) 205.

31. S.H. Kim, G.A. Somorjai, J. Phys. Chem. B 106 (2002) 1386.

32. A. Siokou, S. Ntais, Surf. Sci. 540 (2003) 379.

33. D. Fregonese, A. Glisenti, S. Mortara, G.A. Rizzi, E. Tondello, S. Bresadola, J. Mol. Catal. A:Chem. 178 (2002) 115.

34. P.C. Thüne, C.P.J. Verhagen, M.J.G. van den Boer, J.W. Niemantsverdriet, J. Phys. Chem. B 101 (1997) 8559.

35. G. Morini, A. Cristofori, Eur. Pat. 728724, 1996, Montell, invs.

36. A.K. Yaluma, P.J.T. Tait, J.C. Chadwick, J. Polym. Sci: Part A: Polym. Chem. 44 (2006) 1635.

37. J.F. Moulder, W.F. Stickle, P.E. Sobol, K.D. Bomben, in: J. Chastain (Ed.), Handbook of X-ray Photoelectron Spectroscopy and Physical Electronics, Perkin-Elmer Corp., Eden Prairie, MN, 1992.

38. V.K. Kaushik, E.K. Gupta, H. Patil, D.G. Naik, Catal. Lett. 121(1-2) (2008) 58.

# Chapter 5

# A preparation method for well-defined crystallites of MgCl$_2$-supported Ziegler-Natta catalysts and their observation by AFM and SEM

*A method for the preparation of well-defined crystallites of MgCl$_2$-supported Ziegler-Natta catalysts on Si wafers has been developed. This has been achieved by the spin coating of a MgCl$_2$ solution onto a flat Si wafer, followed by controlled crystal growth to give well-defined MgCl$_2$·nEtOH crystallites. The growth of the crystallites on the flat Si facilitates their characterization using Electron and Scanning Probe Microscopy. The relative proportions of 120° and 90° edge angles indicate the preference for the formation of a particular crystallite face for the MgCl$_2$. Polyethylene has been identified to be formed on the lateral faces of the crystallite.*

## 5.1   Introduction

Ziegler-Natta catalysts occupy a dominant position in polyolefin production. To improve the understanding of state-of-the-art $MgCl_2$-supported catalysts, with respect to polymerization behaviour and the effect of catalyst type on polymer composition and properties, detailed insight into the nature of the active species is required. Ziegler-Natta catalysts for polypropylene typically comprise a $MgCl_2$ support, $TiCl_4$ and an internal electron donor, and are used in combination with an aluminium alkyl cocatalyst $AlR_3$ [1].

It is well known that the internal donor (a monoester, diester or diether) is added in the catalyst preparation to control the amount and distribution of $TiCl_4$ on the support surface. External electron donors (Lewis bases) are included in the polymerization to produce highly isotactic polypropylene. As noted in **chapters three** and **four** $MgCl_2$ crystallites consists of lateral cleavage surfaces where magnesium atoms are coordinated with 4 or 5 chlorine atoms, in place of 6 chlorine atoms in the bulk of the crystal [2]. These tetra- and pentacoordinate Mg atoms are present on the (110) and (100) lateral cleavage surfaces of $MgCl_2$. Nevertheless we have adopted the indexing of the five-coordinate face as (104) rather than (100), following a re-evaluation of the crystal structure of $MgCl_2$ supports recently reported by Busico et al. [3]. Due to the significance of this **chapter** we again show (already presented in **chapters three** and **four**) a schematic representation for a monolayer of a $MgCl_2$ crystal (Figure 5.1) showing the most probable (104) and (110) cleavage cuts. Treatment with $TiCl_4$ will give rise to adsorbed $TiCl_4$ species on one or both of the (104) and (110) cuts. Upon contact with the cocatalyst ($AlR_3$), $Ti^{4+}$ is reduced to $Ti^{3+}$ and a Ti-C bond is formed that is essential for the insertion of the monomer.

Various techniques are available for the characterization of the surface structure of heterogeneous catalysts. Techniques such as atomic force microscopy (AFM), scanning electron microscopy (SEM) and transmission electron microscopy (TEM) are capable of structure and morphology investigation and will prove very informative for our purpose.

Formerly, several groups have reported electron microscopic investigations of polyolefins made on Ziegler-Natta catalysts [5-15]. The earliest experiments were performed by Hargitay, Rodriguez and Miotta, who used optical microscopy to study the early stages of ethylene

polymerization [5]. Later on, several groups reported electron microscopic studies of propylene polymerization on single crystals of α-TiCl$_3$ [6-9]. They observed formation of hemispherical particles of polypropylene on hexagonal leaflets of TiCl$_3$. Murry et al. [10] studied TiCl$_3$-based catalysts by utilizing a simple milling method for the preparation of dispersed catalyst particles, enabling direct TEM observations. Kakugo et al. [11-13] studied morphological changes of TiCl$_3$-based catalysts during olefin polymerization by means of transmission electron microscopy (TEM). More recently, Mori et al. [15] investigated the surface atomic structure of MgCl$_2$ crystalline particles and MgCl$_2$-supported Ziegler catalysts by means of high resolution transmission electron microscopy (HRTEM).

A fundamental question in Ziegler-Natta catalysis is which crystallite face is most effective for coordination of the active site precursor, TiCl$_4$, and where the active species are located. In spite of numerous efforts, the exact nature of the various active species is still a subject of debate. For example, it has been suggested that dimeric species (Ti$_2$Cl$_8$) epitactically coordinated to the (100) lateral cut, now indexed [3] as the (104) cut, could lead to the formation of stereospecific active sites [16, 17]. However, recent spectroscopic studies using FT-Raman have provided evidence for strong adsorption of TiCl$_4$ on the (110) lateral cut of MgCl$_2$, giving a monomeric species with octahedrally coordinated titanium which can be the precursor for active and stereospecific sites [18, 19]. In this respect, probable modes of coordination of TiCl$_4$ on MgCl$_2$ are illustrated as a reminder to the reader (also mentioned in **chapters three** and **four**) in Figure 5.1b [3, 4].

In the previous chapters, we have described the preparation and characterization of a model Ziegler-Natta catalyst, starting from the spin coating of a MgCl$_2$ solution (with or without donor) in ethanol on a flat silica/silicon wafer. Subsequent contacts with TiCl$_4$ and AlEt$_3$ resulted in an active catalyst for ethylene and propylene polymerization, allowing a study of the surface chemistry and morphology of the catalyst and the nascent polymer. This preliminary study established the feasibility of the model Ziegler-Natta catalyst preparation, but did not result in well-defined crystallites of magnesium chloride. We have now identified a method by which the spin coated support precursor, MgCl$_2$·$n$EtOH, can be converted by controlled crystal growth to well-defined MgCl$_2$ crystallites large enough to facilitate

morphological characterization by AFM and SEM, and to identify polymer formation on the lateral faces of the crystallite.
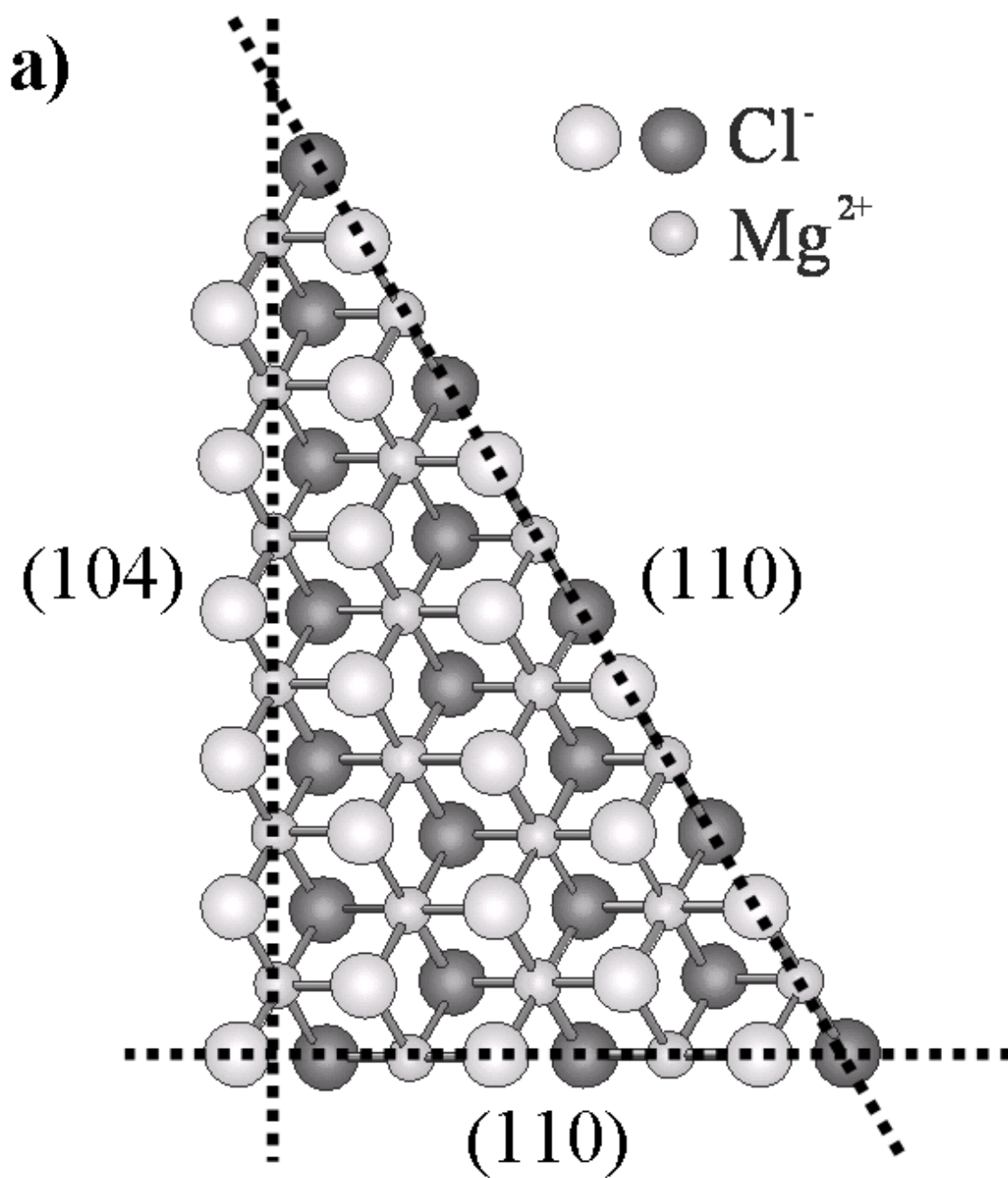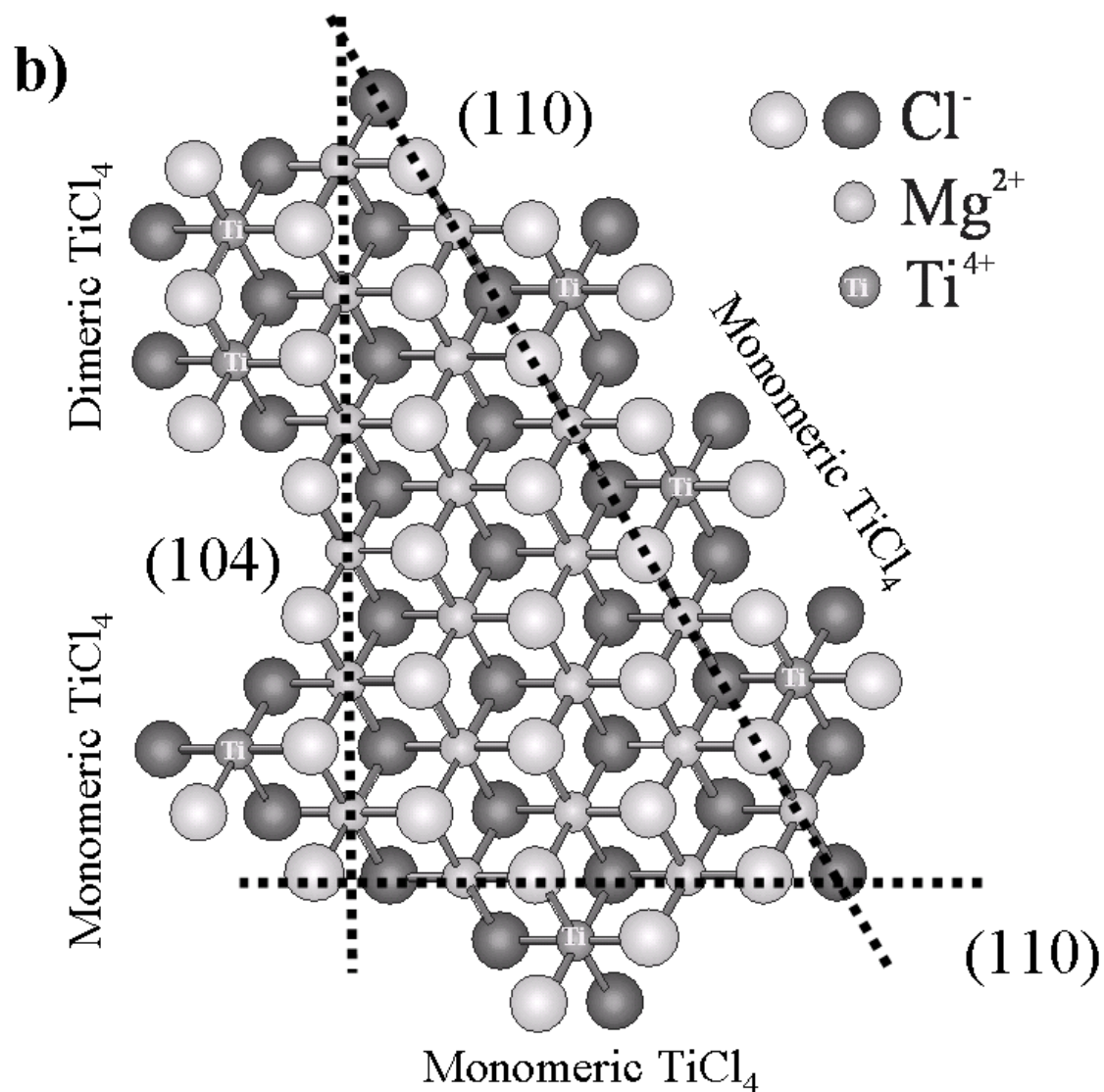
**Figure 5.1:** *a) Model for a monolayer of a MgCl$_2$ crystal showing the most probable (104) and (110) cleavage cuts. b) Proposed coordination modes of TiCl$_4$ species on MgCl$_2$ lateral cuts, showing dimeric and monomeric species on (104) cut and monomeric species on (110) cut [3, 4].*

## 5.2  Experimental

### 5.2.1  Materials

Anhydrous magnesium chloride (beads, 99.9 %), absolute ethanol (99.9 %), titanium tetrachloride (99.9 %) and triethylaluminium (25 wt. % in toluene) were purchased from Aldrich Chemicals and used as received. HPLC-grade toluene was taken from an argon-flushed column packed with alumina and stored over 4 Å molecular sieves. Ethylene was supplied by Praxair (3.5).

## 5.2.2 Catalyst preparation and ethylene polymerization

The catalyst preparation is summarized in Figure 5.2. All manipulations of air- or water-sensitive compounds were carried out using standard Schlenk or glovebox techniques. The $SiO_2/Si(100)$ wafer was prepared as described elsewhere (calcination at 750 $^0$C, followed by etching with $H_2O_2/NH_3$) [20] to obtain an amorphous silica layer (20 nm) on a silicon (100) wafer. The wafer was partially dehydroxylated at 500 $^0$C in air for 16 hours, where a small amount of surface hydroxyl groups was retained in order to facilitate a homogeneous $MgCl_2 \cdot n$EtOH film formation. Such a wafer was then spin coated with a solution of $MgCl_2$ in ethanol (42 mmol/L) resulting in a Mg loading of 200 atoms/nm$^2$. Upon spinning, most of the liquid is ejected from the flat Si surface, leaving behind a thin film of solution. The remaining solvent evaporates and the solute precipitates upon the support surface. The rotation speed applied was 2800 r.p.m.

The wafer was afterwards brought into contact with ethanol vapour, with the intention of converting a large number of small $MgCl_2 \cdot n$EtOH crystallites to a smaller number of larger crystallites, enabling the so-called Ostwald ripening process. Ostwald ripening or particle coarsening are terms for the stage of the separation of a second phase from a supersaturated solution. In other words, crystal growth by "Oswald ripening" occurs when smaller crystals, which have a larger total area than bigger crystals, dissolve in the liquid phase and then the material is transported through the continuous phase, to nucleation sites of the bigger crystals [21, 22]. Many small crystals that are formed initially slowly disappear, except for a few that grow larger, at the expense of the smaller crystals. The smaller crystals act as "nutrients" for the bigger crystals. As the larger crystals grow, the area around them is depleted of smaller crystals.
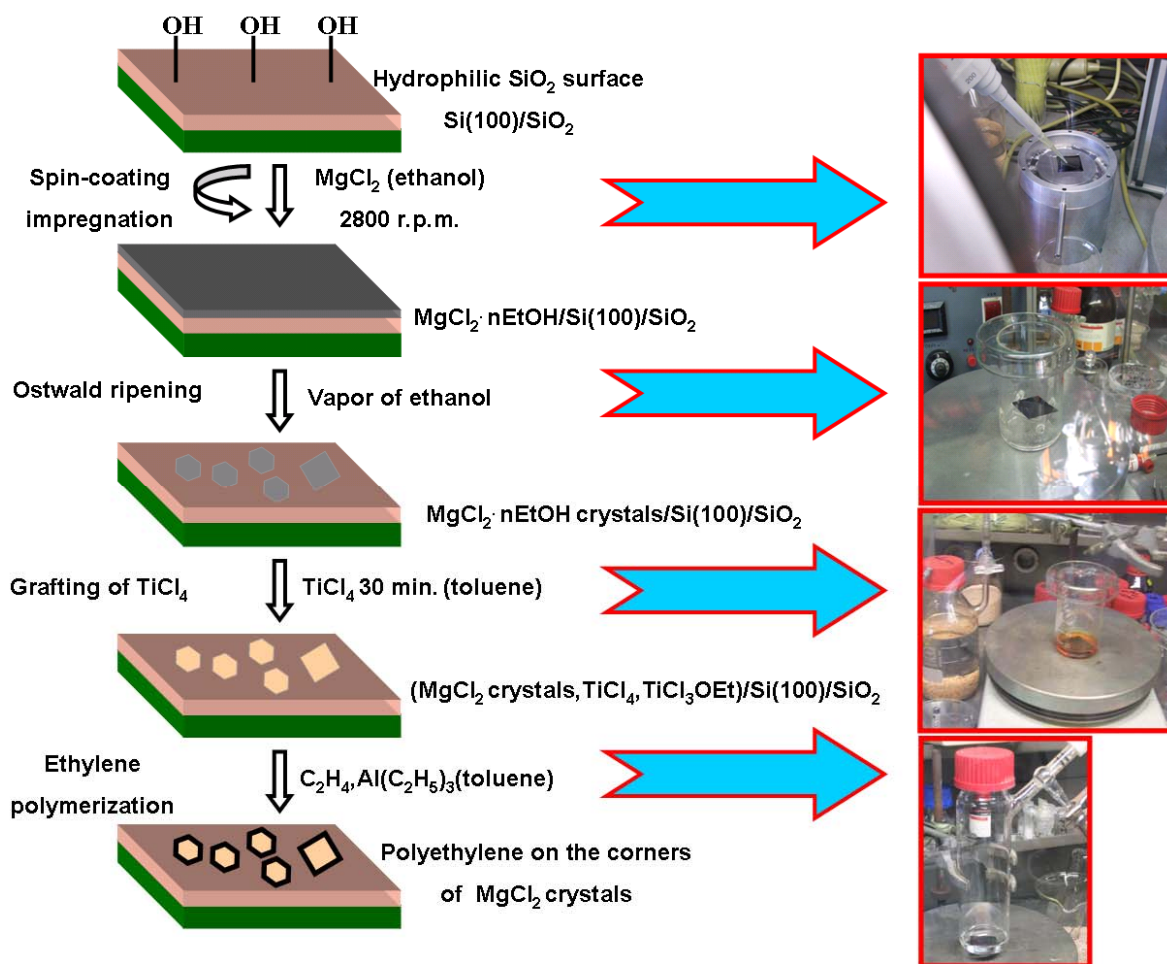
**Figure 5.2:** *Preparation scheme of MgCl₂·nEtOH crystallites for Ziegler-Natta catalyst on flat silica/silicon surface for ethylene polymerization along with pictures of operational steps carried out in the glove box.*

Ostwald ripening is a spontaneous process that occurs because larger crystals are more energetically favored than smaller crystals. While the formation of many small crystals is *kinetically* favored, (i.e., they nucleate more easily) large crystals are *thermodynamically* favored. Thus, from a standpoint of kinetics, it is easier to nucleate many small crystals. However, small crystals have a larger surface to volume ratio than large crystals. Atoms on the surface are energetically less stable than the ones already well ordered and packed in the interior. Large crystals, with their greater volume to surface area ratio, represent a lower energy state. Thus, many small crystals will attain a lower energy state if transformed into large crystals and this is what we observe in Ostwald ripening.

The sample treatment is illustrated in Figure 5.3. The spin coated wafer was placed inside a glass vessel, the bottom of which was filled with several mL of a saturated solution of $MgCl_2$ in ethanol. The closed system was heated for 30 min. at 60 $^0$C and subsequently at 50 $^0$C for 100 min. The use of the saturated solution slows down the evaporation of ethanol, so that the growth of the $MgCl_2$ crystallites will also occur slowly. Slow growth in general enhances the size and perfection of the crystals. After this procedure, the wafer was left overnight to dry under a flow of nitrogen and then treated with a 10 % v/v $TiCl_4$ solution in toluene at room temperature for 30 min. after which the wafer was washed with toluene to remove physisorbed $TiCl_4$ and dried under nitrogen.
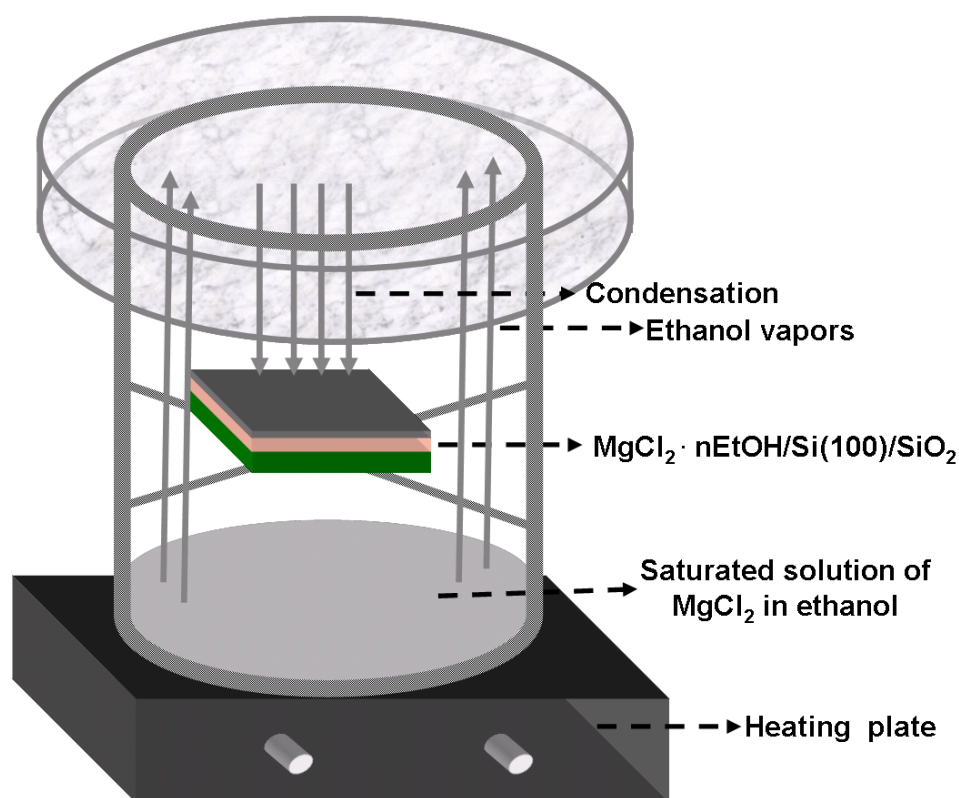


**Figure 5.3:** *Preparation process of MgCl$_2$·nEtOH film conversion into MgCl$_2$·nEtOH crystallites induced by ethanol vapors.*

Ethylene polymerization was carried out at room temperature in a glass reactor equipped with a magnetic stirrer. The Si wafer, with the model catalyst prepared as above, was dipped into about 20 mL of a 1 mg/mL solution of the cocatalyst, $AlEt_3$, in toluene, inside the glass reactor. The reactor was pressurized with 2 bar of ethylene and the polymerization was allowed to run shortly. After the polymerization, the wafer was washed with toluene.

### 5.2.3 Analytical techniques

Atomic force microscopy (AFM) measurements were performed inside a glove box with Solver P47 base with SMENA head. The cantilever of choice was a non-contact gold-coated NSG11 (long end), manufactured by Micromasch. A typical force of the tip was 5.5 N/m and a typical resonance frequency 164 kHz. The measurements were performed in non-contact mode. The thickness of the catalyst support was determined using the height difference between the Si-substrate and the $MgCl_2$ surface.

Scanning electron microscopy (SEM) was performed using a Philips environmental scanning electron microscope XL-30 ESEM FEG (Philips, The Netherlands, now Fei Co.) in high-vacuum mode using a low voltage (low-voltage SEM, LVSEM) and a secondary (SE) detector. High accelerating voltage was used for Energy Dispersive X-Ray (high-voltage SEM-EDX, HVSEM-EDX) and a secondary (SE) detector.

## 5.3 Results

Spin coating of a solution of magnesium chloride in ethanol onto a flat Si wafer results in a solid layer comprising small grains of $MgCl_2 \cdot n$EtOH. AFM images indicated a surface roughness of 1-3 nm with a grain size ranging from 10-40 nm (as indicated in **chapter three**). Aiming to convert this material to well-defined crystallites of magnesium chloride large enough to be characterized by both SEM and AFM, the spin coated layer was subjected to a process of Ostwald ripening. As described in the experimental section, this was carried out by exposing the film to ethanol vapour at 50-60 °C.

The growth of crystallites was initially carried out (tested) in a supersaturated solution of $MgCl_2$ in ethanol. Such a solution can be prepared by dissolving $MgCl_2$ in ethanol until a solution is formed above a layer of $MgCl_2$ (Figure 5.4). Several mL of this supersaturated solution are heated up to 50-60 °C in a Petri dish and in a closed system (applying in this way the Ostwald ripening process) to obtain large crystallites of $MgCl_2 \cdot 6$EtOH.
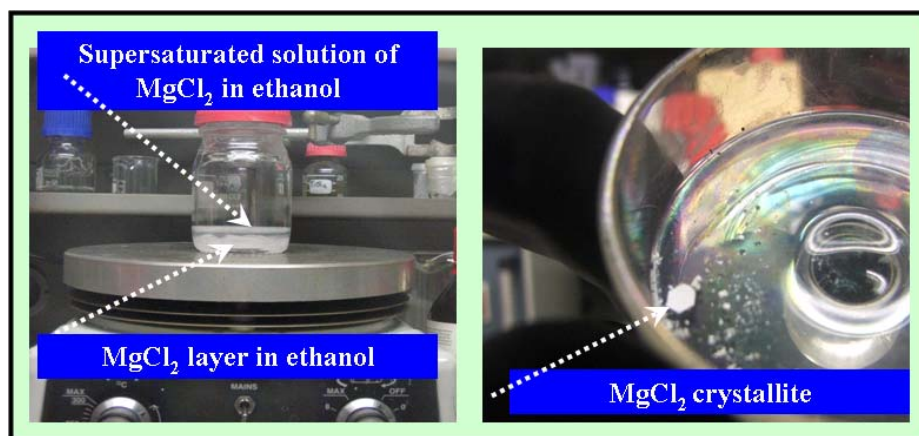
**Figure 5.4:** *Supersaturated solution of MgCl$_2$ in ethanol was heated up at 50 and 60 $^0$C to obtain crystallites of MgCl$_2$·6EtOH, as displayed in the adjacent picture.*

The crystals obtained were imaged by SEM as displayed in Figure 5.5, which reveals a hexagonal crystal structure with sharp edges. It is important to mention that the crystallites were transferred in sealed bottles. They were quickly opened under nitrogen flow before transfer to the SEM chamber and vacuumed afterwards before imaging.
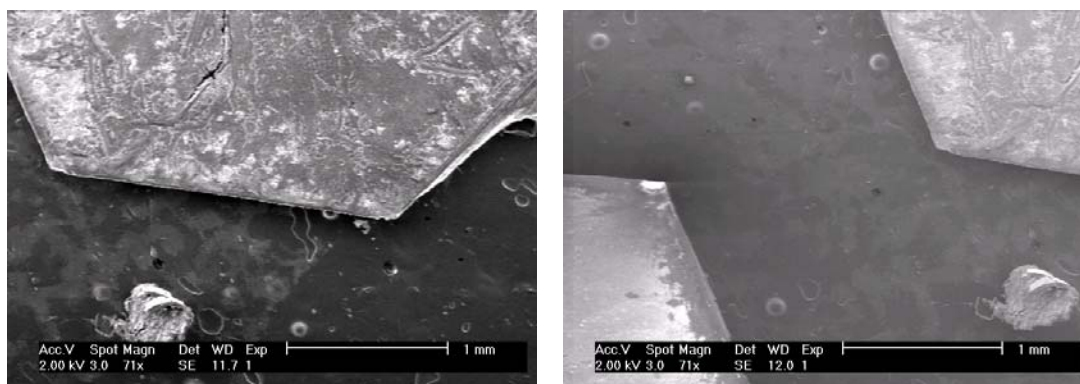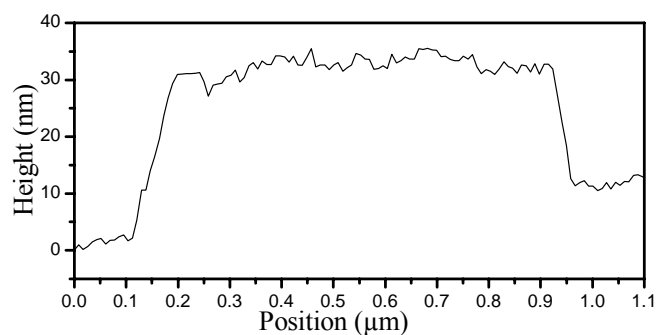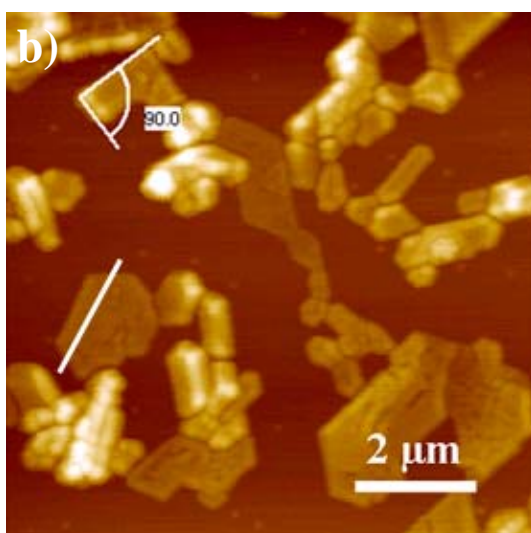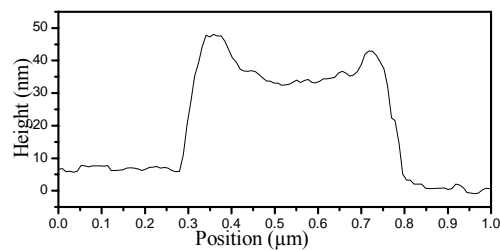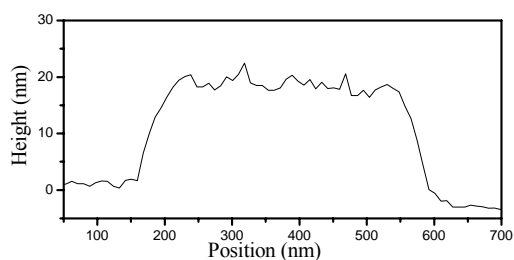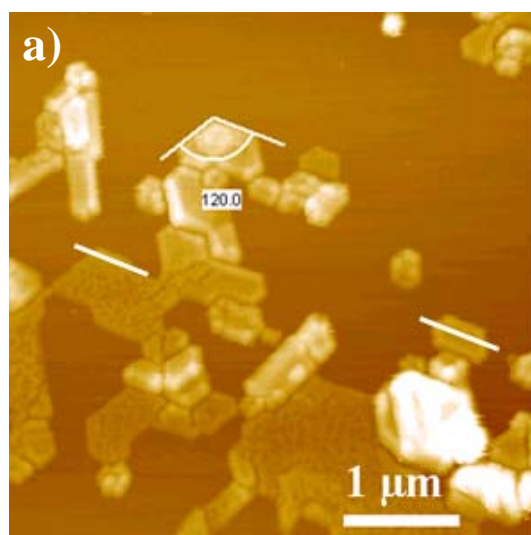


**Figure 5.5:** *SEM images of MgCl$_2$·6EtOH crystallites obtained after the Ostwald ripening process was applied onto a supersaturated solution of MgCl$_2$ in ethanol.*

Application of the Ostwald ripening process to spin coated MgCl$_2$ on a Si wafer resulted in large changes in crystallite size and morphology. AFM images of the crystallites obtained are shown in Figure 5.6, which reveals the presence of relatively large, micron-sized crystallites, with variations in both size and height. Well-defined crystal faces and angles are apparent in these AFM images. In Figure 5.6a, hexagonal structures and 120$^0$ angles are apparent, while

in Figure 5.6b, $90^0$ angles can also be seen. The corresponding cross-sectional height scans of the crystallites show flat surfaces with a roughness $\pm$ 5 nm. In some cases, higher edges compared to the basal plane are observed.

Treatment of the MgCl$_2$·$n$EtOH crystallites with TiCl$_4$ for 30 min. induced no changes in the structure (Figure 5.6c). The hexagonal structure and $120^0$ angle formation are still clearly evident from the AFM image. The height of the crystal reaches up to 400 nm, with a basal plane roughness of about 50 nm. The AFM image taken after treatment with TiCl$_4$, exhibiting well-defined crystallites with $120^0$ angles, suggests that the crystallites remain intact under this treatment.
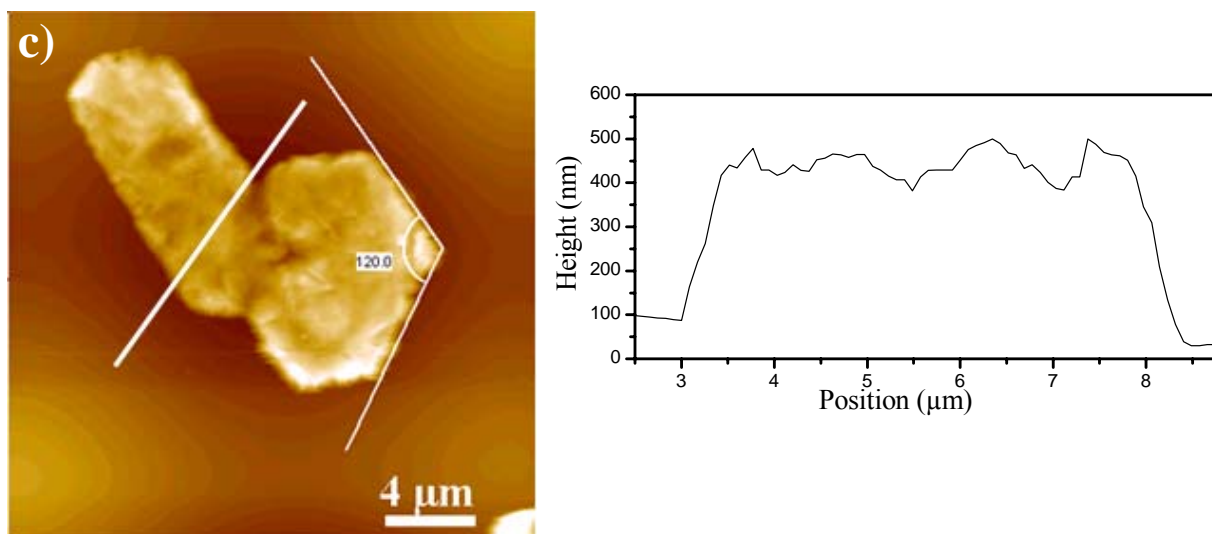
**Figure 5.6:** *a) and b) AFM height images of MgCl$_2$·nEtOH crystallites on silica/silicon for a loading of 200 atoms/nm$^2$, showing angle measurements (120$^0$ and 90$^0$) and cross-sectional height scans. c) AFM height image of MgCl$_2$·nEtOH crystallites after treatment with TiCl$_4$ and washing with toluene, along with the corresponding cross-sectional height scan.*

The model catalysts prepared as described above proved to be active for ethylene polymerization at 2 bar ethylene pressure and room temperature. After several minutes of polymerization, SEM images (Figures 5.7a and 5.7b) suggest polymer growth on the corners and edges of the hexagonal structure of the crystallites. Especially the SEM image in Figure 5.7a (left image) clearly indicates how Ostwald ripening occurs. As the small particles dissolve in ethanol on the Si wafer, the material moves to nucleation sites of the bigger particle (located in the centre), causing it to grow.

In addition to the hexagonal structure, it is noticeable that the crystallites shown in Figure 5.7a have grown in a particular stacking fashion. Figure 5.7b shows that, among the different crystallite shapes and angles, a rectangular structure can also be identified (indicated by the inserted arrow). Figure 5.7c shows a lateral view of polyethylene growth after 3 min. polymerization. The inserted arrows indicate a heightened polymer growth along the edges of MgCl$_2$ crystallites.
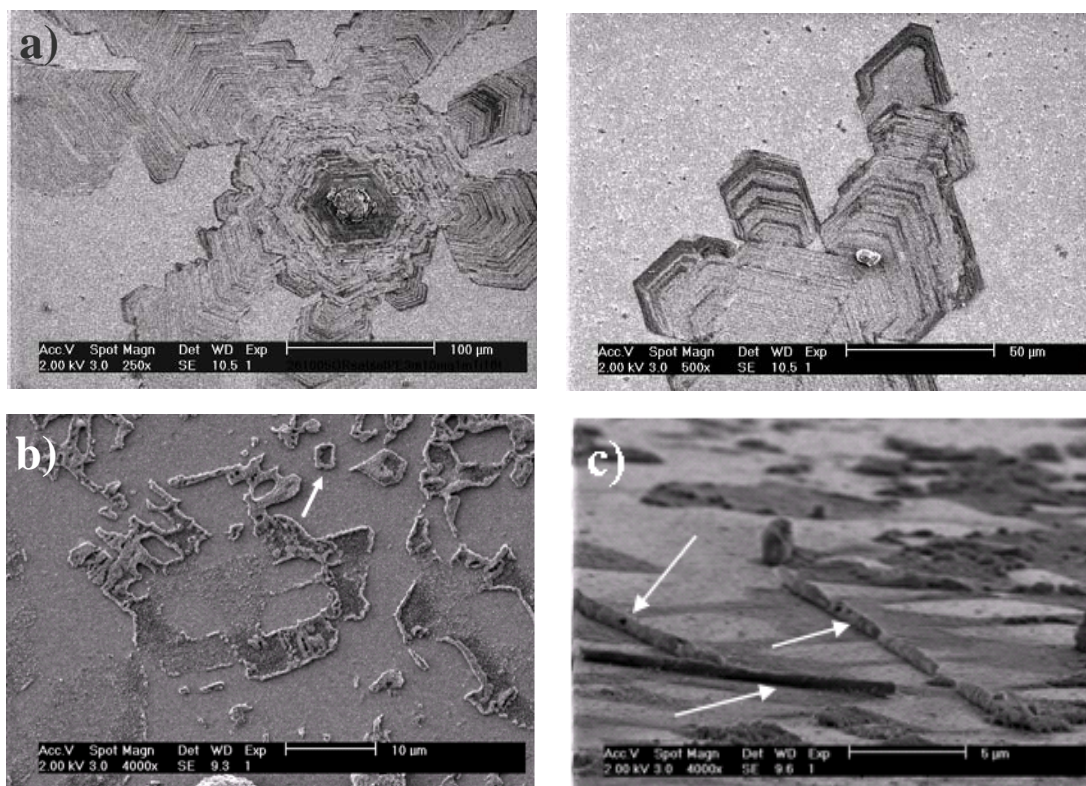
**Figure 5.7:** *SEM images of polyethylenes obtained after short (3-7 min.) polymerizations on Si wafers. The inserted arrow in b) indicates formation of a rectangular structure. The inserted arrows in c) indicate polymer growth along the edges of MgCl$_2$ crystallites.*

The observations from SEM images for the short ethylene polymerizations are supported by the energy dispersive X-ray (EDX) mapping of the C-K$_\alpha$ and Al-K$_\alpha$ distribution after 3 min. polymerization on the Si wafer as shown in Figure 5.8. Carbon is located predominantly on the corners and edges of the crystallites, although a small amount of polymer appears to have formed also on the basal plane of the crystallites. Additionally, Al-K$_\alpha$ mapping indicates that aluminium originating from the cocatalyst is located all over the Si wafer.
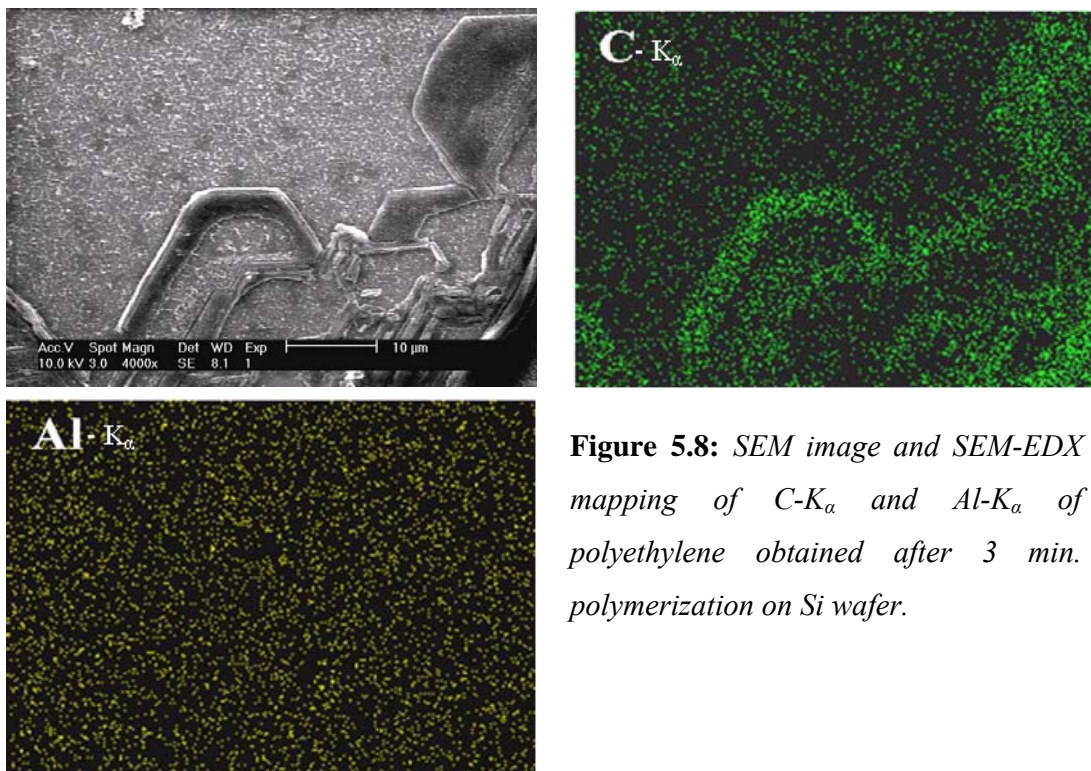
**Figure 5.8:** *SEM image and SEM-EDX mapping of C-K$_\alpha$ and Al-K$_\alpha$ of polyethylene obtained after 3 min. polymerization on Si wafer.*

The crystallites in Figure 5.7 and Figure 5.8 are much larger than those shown in Figure 5.6, facilitating their morphological characterization by SEM as opposed to AFM. These results indicate that the Ostwald ripening procedure used for crystal growth results in a very broad range of crystallite sizes, but Figures 5.7 and 5.8 show that the formation of hexagonal crystallites with $120^0$ angles, as well as some crystallites with $90^0$ angles, is independent of the crystallite size.

Overall, the height of the crystals varied from a few tens of nm up to hundreds of nm. Most of the crystallites appeared higher at the edges than on the basal plane. This could arise from a solvent effect during the Ostwald ripening process, resulting in transportation of material from the centre to the corners and edges of the crystallites. However, it is also possible that the apparent differences in crystal height are artefacts related to the scanning speed used in the AFM measurements.

Additionally, the crystals formed after Ostwald ripening process were heated up to 100 $^0$C, treated with $TiCl_4$ and used in polymerization shortly (1 min.) at 2 bar ethylene pressure and room temperature. The SEM images in Figure 5.9 indicate that the $MgCl_2$ crystallites have

preserved their structure after heating, as evidenced by the presence of $90^0$ and $120^0$ angles edge angles (the latter indicating a hexagonal structure).
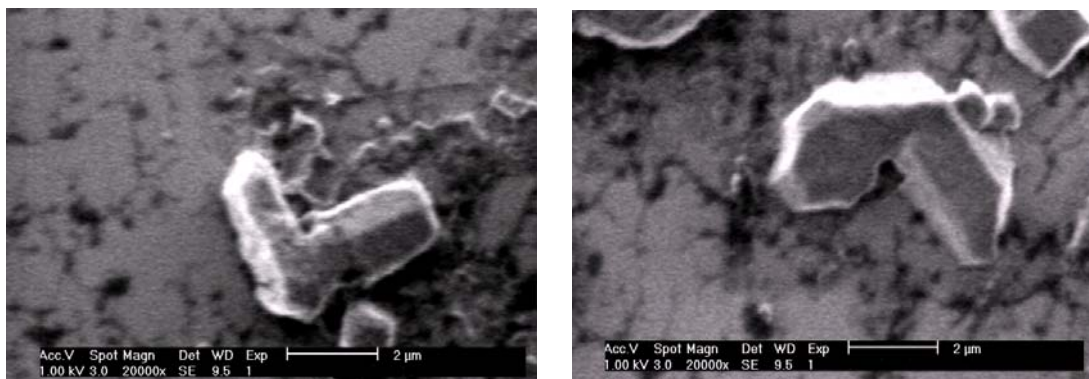


**Figure 5.9:** *SEM images of MgCl$_2$ crystallites heated up to 100 $^0$C and polymerized for 1 min. at 2 bar ethylene pressure and room temperature.*

## 5.4 Discussion

The crystallization of magnesium chloride from a solution in ethanol gives hexagonal single crystals of the adduct MgCl$_2$·6EtOH [23]. The melting point of the MgCl$_2$·6EtOH single crystals was reported to be 72 $^0$C. In the present work, the crystallites formed on silica/silicon wafers did not melt or decompose up to 100 $^0$C as observed by SEM images in Figure 5.9[*]. This implies that the Oswald ripening process applied to a MgCl$_2$·$n$EtOH film does not result in MgCl$_2$·6EtOH crystallites. In other words, the value of $n$ in the support obtained after Ostwald ripening is (significantly) less than 6. Supports used in the preparation of Ziegler-Natta catalysts typically contain between 1 and 3 mol EtOH per mol MgCl$_2$. The molecular structure of MgCl$_2$·$n$EtOH adducts is complex. Using solid-state $^{13}$C NMR, Sozzani et al. found that $n$ values of 1.5 and 2.8 represent defined and stable complexes [24]. MgCl$_2$-ethanol adducts with different EtOH/MgCl$_2$ molar ratios have also been studied by means of Raman spectroscopy by Tewell et al. [25].

The preparation method of converting a large number of small MgCl$_2$·$n$EtOH crystallites of nm size to a smaller number of larger crystallites of μm size, revealed valuable information regarding the structure of MgCl$_2$ and the initial stages of ethylene polymerization. Overall,

---

[*] The Si wafer was heated in a closed glassware on a heating plate and thus its surface will be subjected to a temperature slightly lower than 100 $^0$C.

SEM images disclosed the presence of moderately large, micron-sized crystallites, varying in both size and height. This indicates that Oswald ripening process is effective in obtaining crystallites with diversity in size and height. Another observation was that crystallites imaged with SEM were much larger than those imaged with AFM, enabling the morphological characterization by SEM rather than AFM. The formation of hexagonal crystallites with $120^0$ angles, in addition to some crystallites with $90^0$ angles, was found to be independent of the crystallite size.

Furthermore, the conversion of smaller crystallites into bigger ones facilitates the study and visualization of $MgCl_2$ face(s) and polymer growth on the corners and edges of the crystallites. The controlled crystal growth to give well-defined $MgCl_2$ crystallites with $120^0$ and $90^0$ edge angles, shown by AFM, indicates a preference for the formation of a particular crystallite face i.e., (110) versus (104) or vice versa. It may be speculated that the formation of hexagonal crystallites, with $120^0$ angles, indicates the formation of the (110) cut, taking into account the fact that strong adsorption of $TiCl_4$ on the (110) lateral cut of $MgCl_2$ has recently been noted using FT-Raman spectroscopy [18, 19]. Additionally, the polymer growth at the edges of the crystallites clearly indicates the presence of the active site precursor, $TiCl_4$ or $TiCl_n(OEt)_{4-n}$. On the other hand it has been demonstrated that, for neat $MgCl_2$ (i.e., in the absence of a donor), the (104) cut is more stable than (110) cut [3]. Therefore, the whole issue remains controversial.

## 5.5  Conclusions

A preparation method for well-defined crystallites of $MgCl_2$-supported Ziegler-Natta catalysts has been established, comprising first the spin coating of a $MgCl_2$ solution in ethanol on a Si wafer, followed by controlled crystal growth. Treatment of the resulting $MgCl_2 \cdot n$EtOH crystallites with $TiCl_4$, $AlEt_3$ and ethylene resulted in a system active in ethylene polymerization and each step of the preparation was easily characterized by Electron and Scanning Probe Microscopy.

Atomic Force Microscopy divulged important information regarding the structure of $MgCl_2$. The controlled crystal growth gives large, well-defined $MgCl_2$ crystallites in

which the relative proportions of $120^0$ and $90^0$ edge angles indicate the preference for the formation of a particular crystallite face. Short polymerizations clearly revealed polymer growth at the edges of the crystallites.

## References

1. E. Albizzati, G. Cecchin, J.C. Chadwick, G. Collina, U. Giannini, G. Morini, L. Noristi in Polypropylene Handbook, $2^{nd}$ Edition, ed. N. Pasquini, Hanser, Munich 2005, Ch. 2.
2. U. Giannini, Makromol. Chem. Suppl. 5 (1981) 216.
3. V. Busico, M. Causà, R. Cipullo, R. Credendino, F. Cutillo, N. Friederichs, R. Lamanna, A. Segre, V. Van Axel Castelli, J. Phys. Chem. C 112 (2008) 1081.
4. J.C. Chadwick, T. Garoff, J.R. Severn, Tailor-Made Polymers via Immobilization of Alpha-Olefin Polymerization Catalysts, Eds. J.R. Severn, J.C. Chadwick, WILEY-VCH, Weinheim, 2008, Ch. 2.
5. B. Hargitay, L.A.M. Rodriguez, M. Miotta, J. Polym. Sci. 35 (1959) 359.
6. L.A.M. Rodriguez, J.A. Gabant, J. Polym. Sci. Part C 4 (1963) 125
7. L.A.M. Rodriguez, H.M. van Looy, J. Polym. Sci. Part A-1 4 (1966) 1971.
8. J.Y. Guttman, J.E. Guillet, Macromolecules 1 (1968) 461.
9. J.Y. Guttman, J.E. Guillet, Macromolecules 3 (1970) 470.
10. R.T. Murry, R. Pearce, D. Platt, J. Polym. Sci., Polym. Lett. Ed. 16 (1978) 303.
11. M. Kakugo, H. Sadatoshi, J. Sakai, M. Yokoyama, Macromolecules 22 (1989)3172.
12. M. Kakugo, H. Sadatoshi, M. Yokoyama, K. Kojima, Macromolecules 22 (1989) 547.
13. M. Kakugo, H. Sadatoshi, J. Sakai, in Catalytic Olefin Polymerization, T. Keii, K. Soga, Eds., Kodansha-Elsevier, Tokyo 1990, p. 345.
14. T. Keii, in Kinetics of Ziegler-Natta Polymerization, Kodansha, Tokyo 1972, p. 235.
15. H. Mori, M. Sawada, T. Higuchi, K. Hasebe, N. Otsuka, M. Terano, Macromol. Rapid. Commun. 20 (1999) 245.
16. P. Corradini, V. Busico, G. Guerra, in Transition Metals and Organometallics as Catalysts for Olefin Polymerization, W. Kaminsky, H. Sinn, Eds., Springer-Verlag, Berlin 1988, p. 337.
17. V. Busico, P. Corradini, L. De Martino, A. Proto, V. Savino, E. Albizzati, Makromol. Chem. 186 (1985) 1279.

18. L. Brambilla, G. Zerbi, S. Nascetti, F. Piemontesi, G. Morini, Macromol. Symp. 213 (2004) 287.

19. L. Brambilla, G. Zerbi, F. Piemontesi, S. Nascetti, G. Morini, J. Mol. Catal. A: Chem. 263 (2007) 103.

20. P.C. Thüne, C.P.J. Verhagen, M.J.G. van den Boer, J.W. Niemantsverdriet, J. Phys. Chem. B  101 (1997) 8559.

21. M. Petersen, A. Zangwill, C. Ratsch, Surf. Sci. 536 (2003) 55.

22. R.N. Stevens, C.K.L. Davies, Scripta Materialia 46 (2002) 19.

23. (a) N.Ya. Turova, E.P. Turevskaya, A.V. Novoselova, Russ. J. Inorg. Chem. 12 (1967) 901; (b) G. Valle, G. Baruzzi, G. Paganetto, G. Depaoli, R. Zannetti, A. Marigo, Inorg. Chim. Acta. 156 (1989) 157.

24. P. Sozzani, S. Bracco, A. Comotti, R. Simonutti, I. Camurati, J. Am. Chem. Soc. 125 (2003) 12881.

25. C.R. Tewell, F. Malizia, J.W. Ager III, G.A. Somorjai, J. Phys. Chem. B 106 (2002) 2946.

# Chapter 6

# The Role of electron donors on lateral surfaces of MgCl$_2$-supported Ziegler-Natta catalysts; Observation by AFM and SEM

*An active model for a Ziegler-Natta propylene polymerization catalyst has been prepared by spin coating of a MgCl$_2$/diether donor solution in ethanol on a flat silica/silicon wafer, followed by crystal growth by Ostwald ripening to give well-defined MgCl$_2$·donor·nEtOH crystallites. The growth of the crystallites on the flat wafer indicates the formation of only 120° edge angles in the presence of the diether donor, suggesting the preference for the formation of one particular crystallite face for the MgCl$_2$. In contrast, the presence of diisobutyl phthalate or ethyl benzoate leads to the formation of both 120° and 90° edge angles, indicating the formation of more than one face for the MgCl$_2$. Subsequent treatment with TiCl$_4$ generates the catalyst and in propylene polymerization polymer forms on the lateral face of each crystallite. This work represents the first visualization of the effect of an internal donor in controlling the crystallite faces of magnesium chloride formed during a Ziegler-Natta catalyst preparation.*

## 6.1   Introduction

Highly active MgCl$_2$-supported catalysts, containing MgCl$_2$, TiCl$_4$, and an "internal" electron donor, play a significant role in polypropylene (PP) production. In combination with a trialkylaluminium cocatalyst and in most cases an "external" electron donor, they are highly active systems for the production of isotactic polypropylene. Successive "generations" of highly active MgCl$_2$-supported catalyst systems for PP are listed below [1].

| Catalyst | Cocatalyst | External donor |
|---|---|---|
| MgCl$_2$/TiCl$_4$/ethyl benzoate | AlR$_3$ | aromatic ester |
| MgCl$_2$/TiCl$_4$/dialkyl phthalate | AlR$_3$ | alkoxysilane |
| MgCl$_2$/TiCl$_4$/diether | AlR$_3$ | |

The internal donor plays an important role in controlling the amount and the distribution of TiCl$_4$ in the catalyst. Giannini [2] indicated, as noted already in the previous chapters, that on the lateral cleavage surfaces of MgCl$_2$, the magnesium atoms are coordinated with 4 or 5 chlorine atoms, as opposed to 6 chlorine atoms in the bulk of the crystal. These cleavage surfaces were assigned to the (110) and (100) faces of MgCl$_2$. It has been proposed that bridged Ti$_2$Cl$_8$ species can coordinate to the (100) face of the MgCl$_2$ and could lead to the formation of the chiral, isospecific active species [3, 4]. Preferential coordination of a donor on the more acidic (110) face of MgCl$_2$ would therefore lead to the (100) face being prevailingly occupied by Ti$_2$Cl$_8$ dimers.

However, recent mechanistic and modelling studies, in particular spectroscopic studies using FT-Raman [5, 6], have provided evidence for strong adsorption of TiCl$_4$ on the (110) lateral cut of MgCl$_2$, giving a monomeric species with octahedrally coordinated titanium which can be the precursor for active and stereospecific sites. Good performance in terms of stereospecificity can be reached only by preventing the displacement of the internal donor coordinated to MgCl$_2$. Internal donors such as ethyl benzoate and diisobutyl phthalate are, to a large extent, removed from the support by alkylation and complexation reactions with the AlR$_3$ cocatalyst, necessitating the use of an external donor in the polymerization [7]. In contrast, diethers such as 2,2-disubstituted-1,3-dimethoxypropanes remain strongly coordinated to the support when the catalyst is brought into contact with the cocatalyst, so

that high stereospecificity can be obtained even in the absence of an external donor [8]. Modelling studies carried out by Barino and Scordamaglia [9] have indicated that the 1,3-diethers giving the greatest stereoregulating effect are those which have the greatest preference for coordination on the (110) rather than the (100) face of $MgCl_2$.

Very recently, the crystal structure of $MgCl_2$ supports has been re-evaluated by Busico et al. who concluded that the surface with five-coordinate Mg cations should be indexed as (104) rather than (100) [10]. Periodic DFT calculations indicated that the (104) surface has relatively low energy and is the dominant lateral surface in well-formed large crystals, as well as in activated supports prepared by ball milling [10]. It was also shown that a monodentate alkoxysilane donor $RMe_2Si(OMe)$ was able to bind to both the (104) and the (110) edge surfaces, whereas a bidentate alkoxysilane, $RMeSi(OMe)_2$, was able to bind only on coordinatively unsaturated sites such as those on the (110) surface. In the present work we will adopt the indices (110) and (104), as advised by Busico and co-workers, for the four- and five-coordinate surfaces, respectively [10].

Additionally, it is worthwhile and relevant to the work of this **chapter**, to re-visit Figure 6.1 which represents a model for a monolayer of a $MgCl_2$ crystal showing the most probable (104) and (110) cleavage cuts and proposed coordination modes of $TiCl_4$ species on $MgCl_2$ lateral cuts, showing dimeric and monomeric species on the (104) cut and monomeric species on the (110) cut [10, 12] along with schematic drawings of hypothetical distribution of Lewis Base (LB) on the (104) and (110) cuts before and after reaction with $TiCl_4$ according to Giannini's model [10, 11].
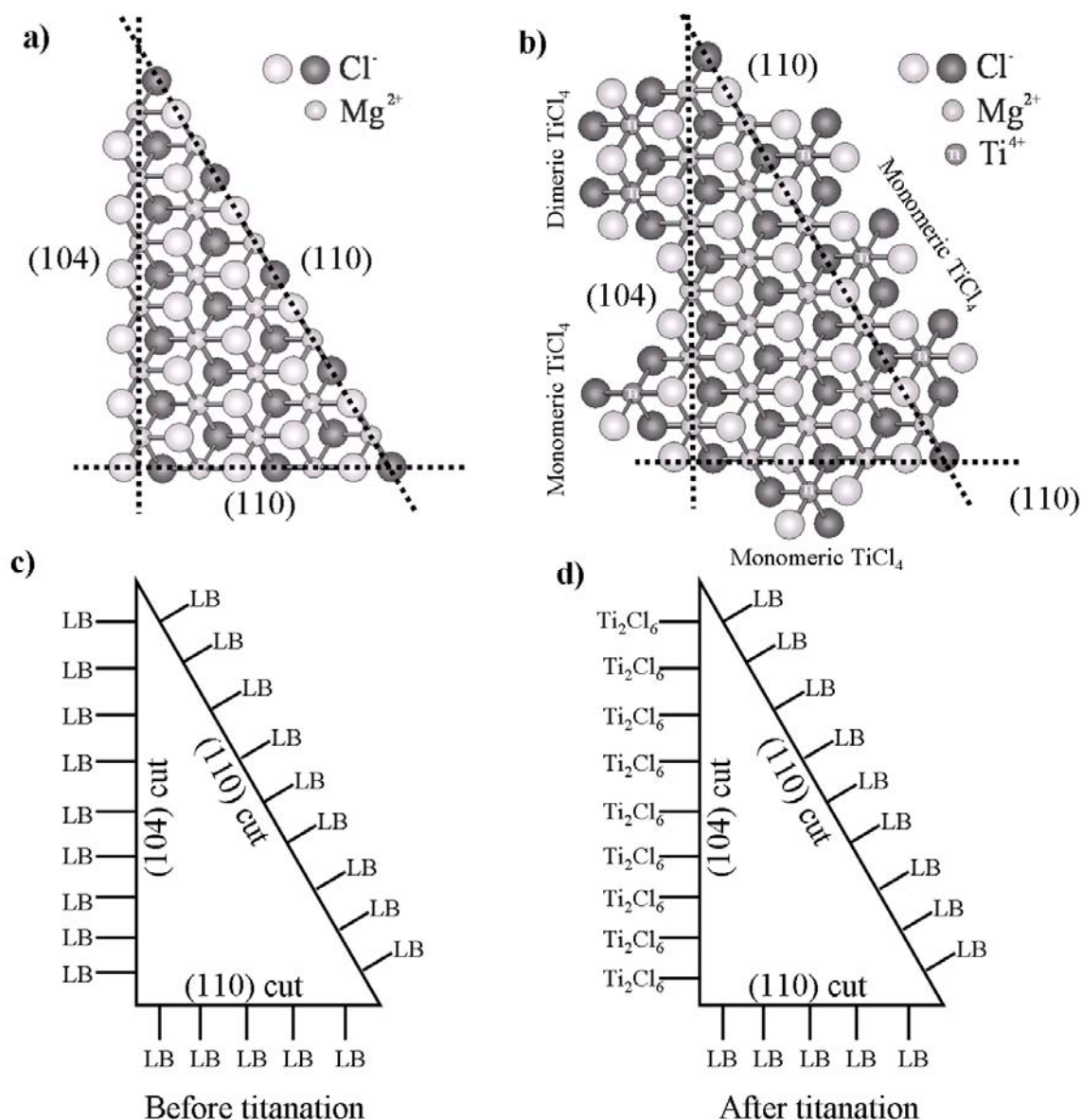
**Figure 6.1:** *a) Model for a monolayer of a MgCl₂ crystal showing the most probable (104) and (110) cleavage cuts. b) Proposed coordination modes of TiCl₄ species on MgCl₂ lateral cuts, showing dimeric and monomeric species on the (104) cut and monomeric species on the (110) cut [10, 12]. c) and d) Schematic drawings of hypothetical distribution of Lewis Base (LB) on the (104) and (110) cuts before and after reaction with TiCl₄ [10, 11].*

Our own research concerning fundamental aspects of olefin polymerization catalysis has been based on the synthesis and characterization of catalysts on flat Si wafers. Studies of Phillips catalysts for polyethylene involved atomic force microscopy (AFM) investigation of ethylene polymerization catalyzed by chromium species anchored on a silica/silicon wafer, identifying

polymer growth at a nm scale during the early stages of polymerization [13, 14]. In **chapters three** and **four** we introduced the preparation and characterization of a model Ziegler-Natta catalyst, starting from the spin coating of a $MgCl_2$ (incorporating a donor or not) solution in ethanol on a flat silica/silicon wafer. Subsequent contacts with $TiCl_4$ and $AlEt_3$ resulted in an active catalyst for ethylene/propylene polymerization, enabling a study of the surface chemistry and morphology of the catalyst and polymer. This first study established the viability of the model Ziegler-Natta catalyst preparation, but did not result in well-defined crystallites of magnesium chloride. Next, we developed a preparation method (**chapter five**) by which the spin coated support precursor, $MgCl_2 \cdot n$EtOH, could be converted by controlled crystal growth to well-defined $MgCl_2$ crystallites large enough to facilitate their morphological characterization by AFM and scanning electron microscopy (SEM), and to identify polymer formation on the lateral faces of the crystallite.

We have now utilized the same model for propylene polymerization by firstly incorporating a diether donor in the spin coating of $MgCl_2$ from ethanol solution onto a Si wafer. Next, crystal growth by Ostwald ripening was applied to generate large crystallites, allowing the effect of the diether to be investigated by morphological characterization of the crystallites by SEM and, after polymerization, by the identification of polymer growth on the lateral faces of the crystallites.

We have discovered that the type of internal donor present in the support and catalyst preparation has a profound effect on the formation of different crystallite faces of magnesium chloride. In the present work, we describe the different effects obtained with 9,9–bis(methoxymethyl)fluorene, diisobutyl phthalate and ethyl benzoate, and the implications of these results with respect to the location and nature of the active species present in Ziegler-Natta catalysts for polypropylene.

## 6.2   Experimental

### 6.2.1  Materials

Anhydrous magnesium chloride (beads, 99.9 %), absolute ethanol (99.9 %), titanium tetrachloride (99.9 %) and triethylaluminium (25 wt. % in toluene) were purchased from

Aldrich Chemicals and used as received. HPLC-grade toluene was taken from an argon-flushed column packed with alumina and stored over 4 Å molecular sieves. The diether donor used was 9,9–bis(methoxymethyl)fluorene [15]. Diisobutyl phthalate (≥98 %) and ethyl benzoate (≥99 %) were provided by Aldrich and used as received. Propylene was supplied by Linden (3.5).

## 6.2.2 Catalyst preparation and propylene polymerization

All manipulations of air- or water-sensitive compounds were carried out using standard Schlenk or glove box techniques. The $MgCl_2 \cdot n$EtOH support and $SiO_2$/Si(100) wafer used in this work were prepared as described in the former chapters. The donors used were 9,9–bis(methoxymethyl)fluorene, diisobutyl phthalate and ethyl benzoate. The donor was added to a solution of $MgCl_2$ in ethanol (42 mmol/L); in the case of the diether donor, the mixture was heated at 60 °C until the solution became clear. The donor/$MgCl_2$ molar ratio was 0.1 in the case of the diether donor, 0.1 in the case of the similarly bidentate donor DIBP and 0.2 for the monodentate donor EB. The resulting solutions were used to spin coat a Si wafer.

The spin coated $MgCl_2$/donor·$n$EtOH layer was contacted with ethanol vapour in a closed system for 30 min. at 60 °C and subsequently at 50 °C for 100 min. aiming to convert a large number of small $MgCl_2$/diether·$n$EtOH crystallites to a smaller number of larger crystallites via a process of Ostwald ripening. Details of this procedure have been reported in **chapter five**. The $MgCl_2$/donor·$n$EtOH crystals were treated with a 10 % v/v $TiCl_4$ solution in toluene at room temperature for 30 min. After washing with toluene to remove the physisorbed $TiCl_4$, the model catalyst was dried under nitrogen.

Propylene polymerization was carried out at room temperature in a glass reactor equipped with a magnetic stirrer. The wafer, with the model catalyst prepared as above, was dipped into about 20 mL of a 1 mg/mL solution of the cocatalyst, $AlEt_3$, in toluene, inside the glass reactor. The reactor was pressurized with 3 bar of propylene and polymerization was allowed to run for the desired time, after which the wafer was washed with toluene. Figure 6.2 gives a schematic representation of sample preparation for propylene polymerization (including Ostwald ripening process) accompanied with pictures of steps carried out in the glove box.
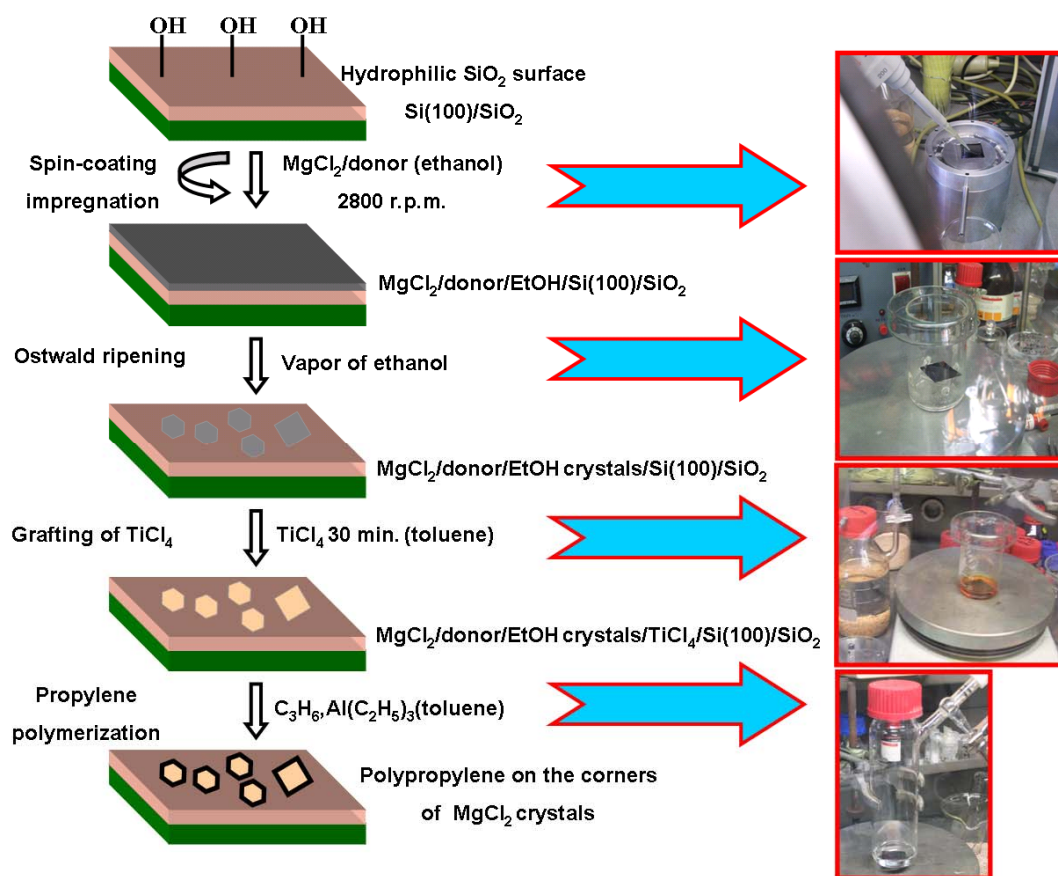
**Figure 6.2:** *Schematic representation of sample preparation for a Ziegler-Natta catalyst for propylene polymerization on a flat Si surface (including Ostwald ripening process), along with pictures of steps carried out in the glove box.*

## 6.2.3 Analytical techniques

AFM measurements were performed inside a glove box with a Solver P47 base with SMENA head. The cantilever of choice was a non-contact gold-coated NSG11 (long end), manufactured by Micromasch. A typical force of the tip was 5.5 N m$^{-1}$ and a typical resonance frequency was 164 kHz. The measurements were performed in non-contact mode. The thickness of the catalyst support was determined using the height difference between the Si-substrate and the MgCl$_2$ surface.

SEM was performed using a Philips environmental scanning electron microscope XL-30 ESEM FEG (Philips, The Netherlands, now Fei Co.) in high-vacuum mode using a low voltage (low-voltage SEM, LVSEM) and a secondary (SE) detector. High accelerating

voltage and a secondary (SE) detector was used for Energy Dispersive X-Ray (high-voltage SEM-EDX, HVSEM-EDX) analyses.

## 6.3 Results

As previously noted (**chapter three**), spin coating of a solution of magnesium chloride in ethanol onto a flat Si wafer results in a solid layer consisting of small grains of $MgCl_2 \cdot nEtOH$. AFM images indicated a surface roughness of 1-3 nm with a grain size ranging from 10-40 nm.

Spin coating was carried out under similar conditions in the present work, with the exception that a diether donor, 9,9-bis(methoxymethyl)fluorene, was incorporated into the magnesium chloride solution. A 0.1 molar ratio diether/$MgCl_2$ was applied, comparable to that present in a typical Ziegler-Natta catalyst [16]. Spin coating of a solution of magnesium chloride and a donor in ethanol onto a flat Si wafer produces a solid layer which may be expected to consist of small particles of $MgCl_2 \cdot donor \cdot nEtOH$. In order to convert this material to well-defined crystallites large enough to be characterized by AFM and SEM, the spin coated layer was subjected to a process of Ostwald ripening.

This process induced large changes in crystallite size and morphology. AFM images of the crystallites obtained are shown in Figure 6.3a and 6.3b, which reveals the formation of micron-sized crystallites. Well-defined crystal faces and angles are apparent in these AFM images. In Figure 6.3a, hexagonal structure is apparent. The corresponding cross-sectional height scan of the crystallite demonstrates a rather flat surface with a height profile of ± 225 nm and with a roughness of ± 25 nm. Figure 6.3b represents an AFM image recorded after the Ostwald-ripened support was treated with $TiCl_4$. A sharp 120° edge angle is noticeable, indicating that the crystallites preserve their structure during the catalyst preparation.

Figure 6.3c represents a SEM image and SEM-EDX mapping of carbon after propylene polymerization was carried out for 16 hours at ambient temperature. It is essential to mention that the SEM images presented in this work were taken after transport of the polymerized catalyst through air. While the original $MgCl_2$ crystal is destroyed, the polypropylene formed

remains intact, creating an image of the distribution of polymerization activity on the model catalyst. A well-defined hexagonal crystal structure and 120° edge angles are evident in this image, suggesting formation of only one crystallite face i.e., either the (110) or the (104) face.

In addition, the SEM-EDX mapping of the C-$K_\alpha$ distribution reveals polymer formation on the corners and edges of the hexagonal crystallite. In contrast to the carbon mapping, Al-$K_\alpha$ mapping (not shown) indicated that aluminium, originating from the cocatalyst, is located all over the Si wafer. The crystallite in Figure 6.3c is much larger than those shown in Figure 6.3a and 6.3b, enabling easy morphological characterization by SEM as opposed to AFM. These results indicate that the Ostwald ripening procedure used for crystal growth results in a broad range of crystallite sizes, but the formation of hexagonal crystallites with 120° angles is independent of the crystallite size; the hexagonal crystallite morphology exemplified in Figures 6.3 was consistently obtained in repeated experiments whenever the diether was present.
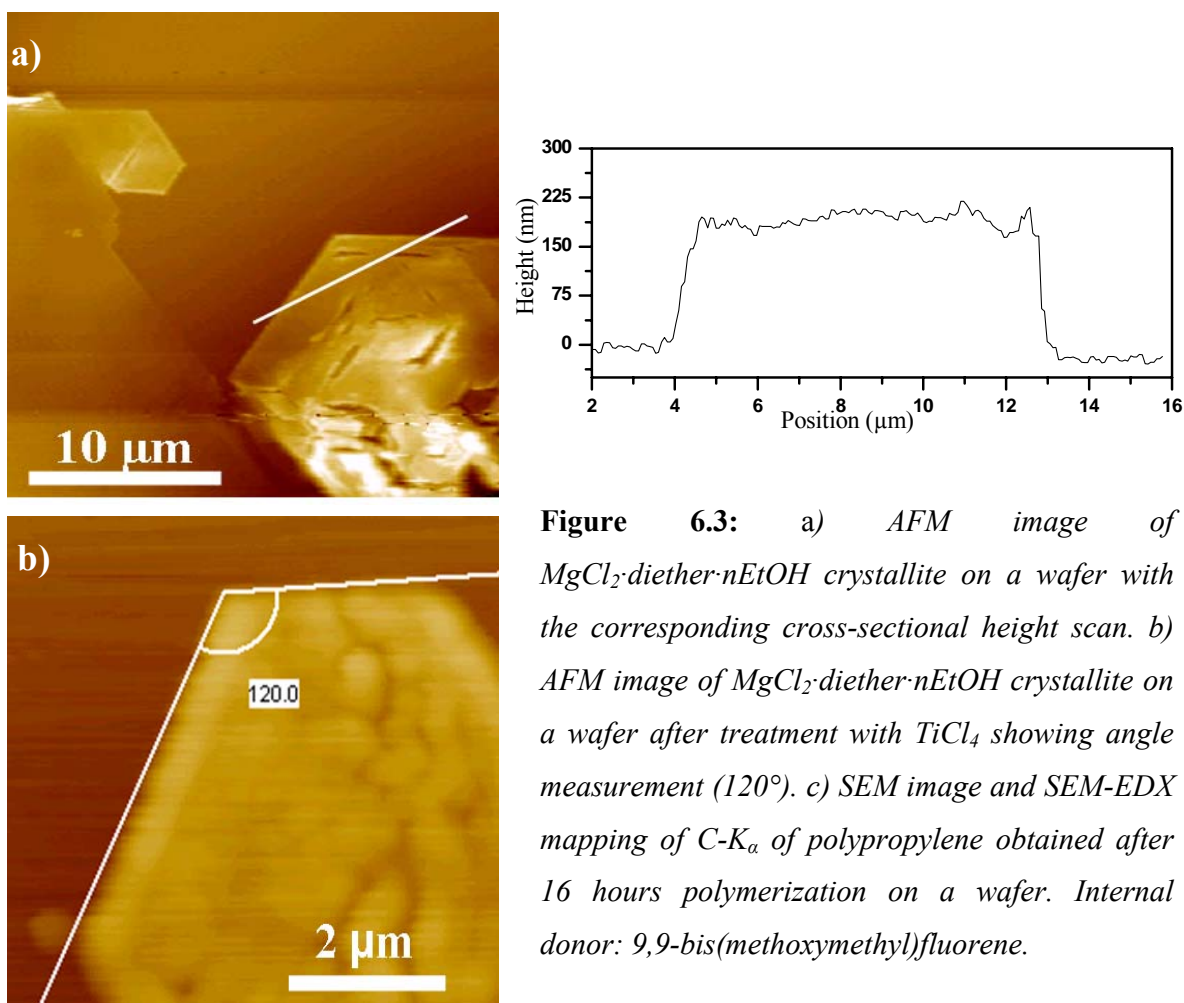


**Figure 6.3:** a*) AFM image of MgCl$_2$·diether·nEtOH crystallite on a wafer with the corresponding cross-sectional height scan. b) AFM image of MgCl$_2$·diether·nEtOH crystallite on a wafer after treatment with TiCl$_4$ showing angle measurement (120°). c) SEM image and SEM-EDX mapping of C-$K_\alpha$ of polypropylene obtained after 16 hours polymerization on a wafer. Internal donor: 9,9-bis(methoxymethyl)fluorene.*
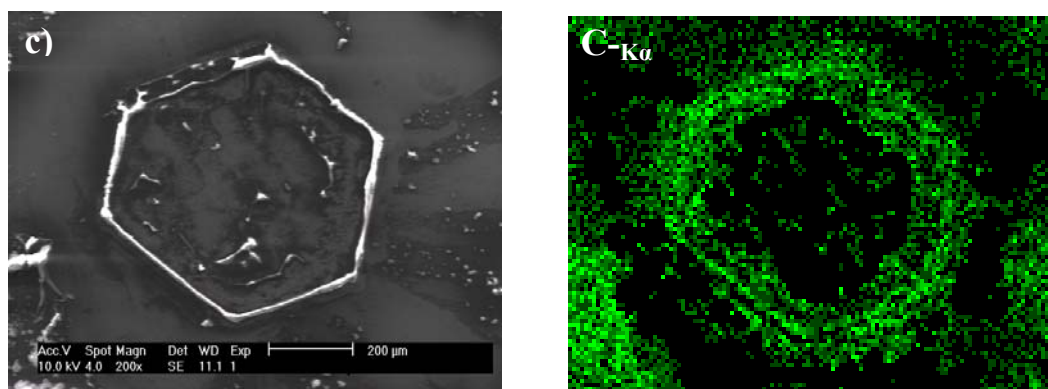
Crystal growth by Ostwald ripening was also applied to spin coated layers with higher diether donor loadings (diether/MgCl$_2$ molar ratios 2 and 0.4). Well-defined crystal faces and angles were apparent in the SEM images in Figure 6.4 (after 16 hours polymerization) and hexagonal structures and 120° edge angles were evident, irrespective of the amount of diether incorporated into the system.

Figure 6.5 shows SEM images taken after a spin coated layer (diether/MgCl$_2$ = 2) was subjected to Ostwald ripening. The carbon mapping clearly indicated that after the Oswald ripening the diether donor is exclusively located at the corners and edges of a hexagonal structure i.e., where a MgCl$_2$ crystallite has grown. The crystallite itself did not survive the transfer to SEM, but a hexagonal structure can nevertheless be identified from the magnesium mapping in Figure 6.5. In **chapter four** we observed that, at high diether loading (diether/MgCl$_2$ = 2), hexagonal structure could even be identified in the spin coated layer after propylene polymerization (Figure 4.11).
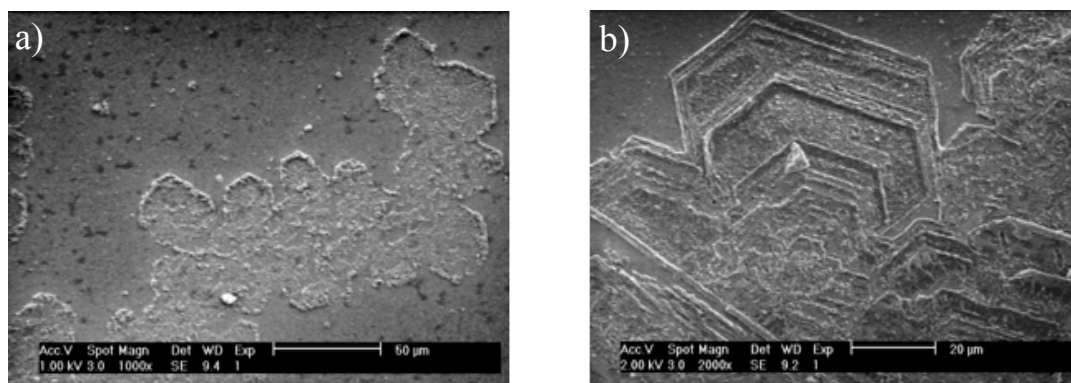


**Figure 6.4:** *SEM images of polypropylene obtained after 16 hours polymerization; mol ratio diether/MgCl$_2$: a) 2, b) 0.4.*
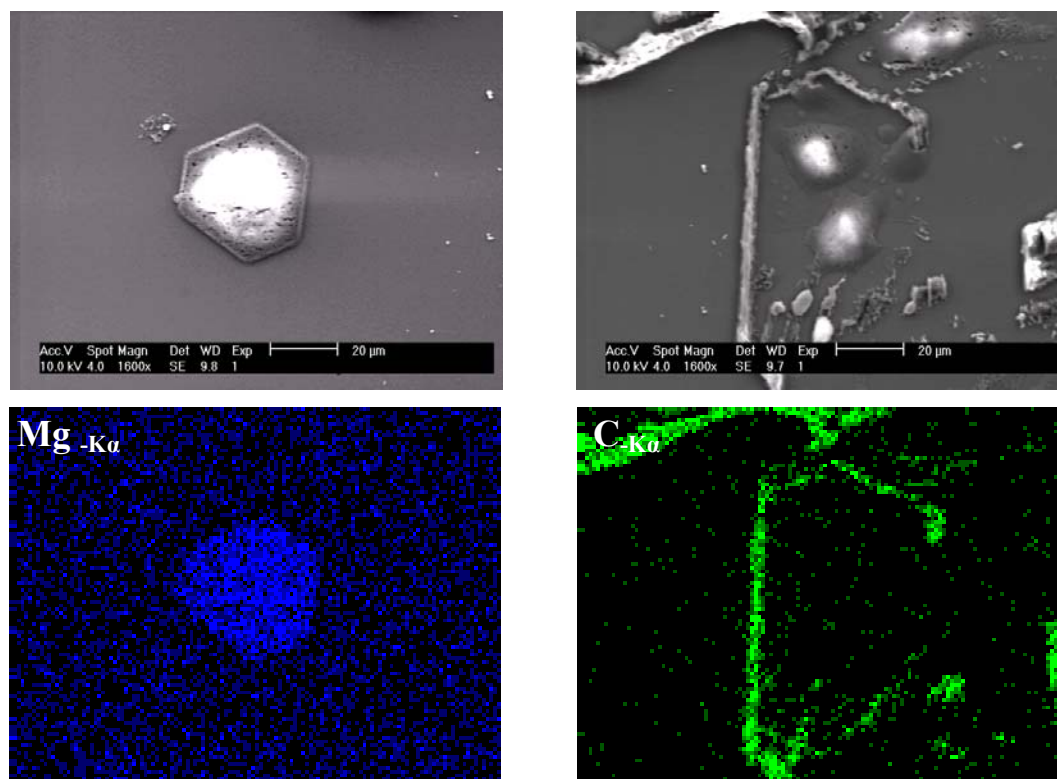
**Figure 6.5:** *SEM images of MgCl₂/diether after the Ostwald ripening was applied along with the Mg and C mapping for the loading diether/MgCl₂ = 2 mol ratio.*

Replacing the diether by diisobutyl phthalate (DIBP) or ethyl benzoate (EB) has a profound effect on the morphology of the magnesium chloride crystals. SEM images taken after 2 hours polymerization, with DIBP and ethyl benzoate as internal donor, reveal (Figure 6.6a and 6.7a) again well-defined structures, but now rectangular as well as hexagonal crystallites are apparent. The controlled crystal growth to give well-defined MgCl₂ crystallites with a mixture of 120° and 90° edge angles indicates that both the (110) and (104) crystallite faces of magnesium chloride have been generated in the presence of DIBP and EB.

Further investigation of this system also revealed the co-existence of 120° and 90° edge angles in a single crystallite, as shown in Figure 6.6b and 6.7b. The additional SEM-EDX images of carbon indicate polymer growth on the edges and corners of the crystallites, although it is not possible to determine the relative amounts of polymer formed on each crystallite face. Aluminium mapping (not shown) revealed that in both systems the cocatalyst was located all over the Si wafer. The presence of 90° and 120° edge angles crystallites

*Chapter 6*

exemplified in Figures 6.6 and 6.7 was consistently obtained in repeated experiments whenever the diester or monoester was present.
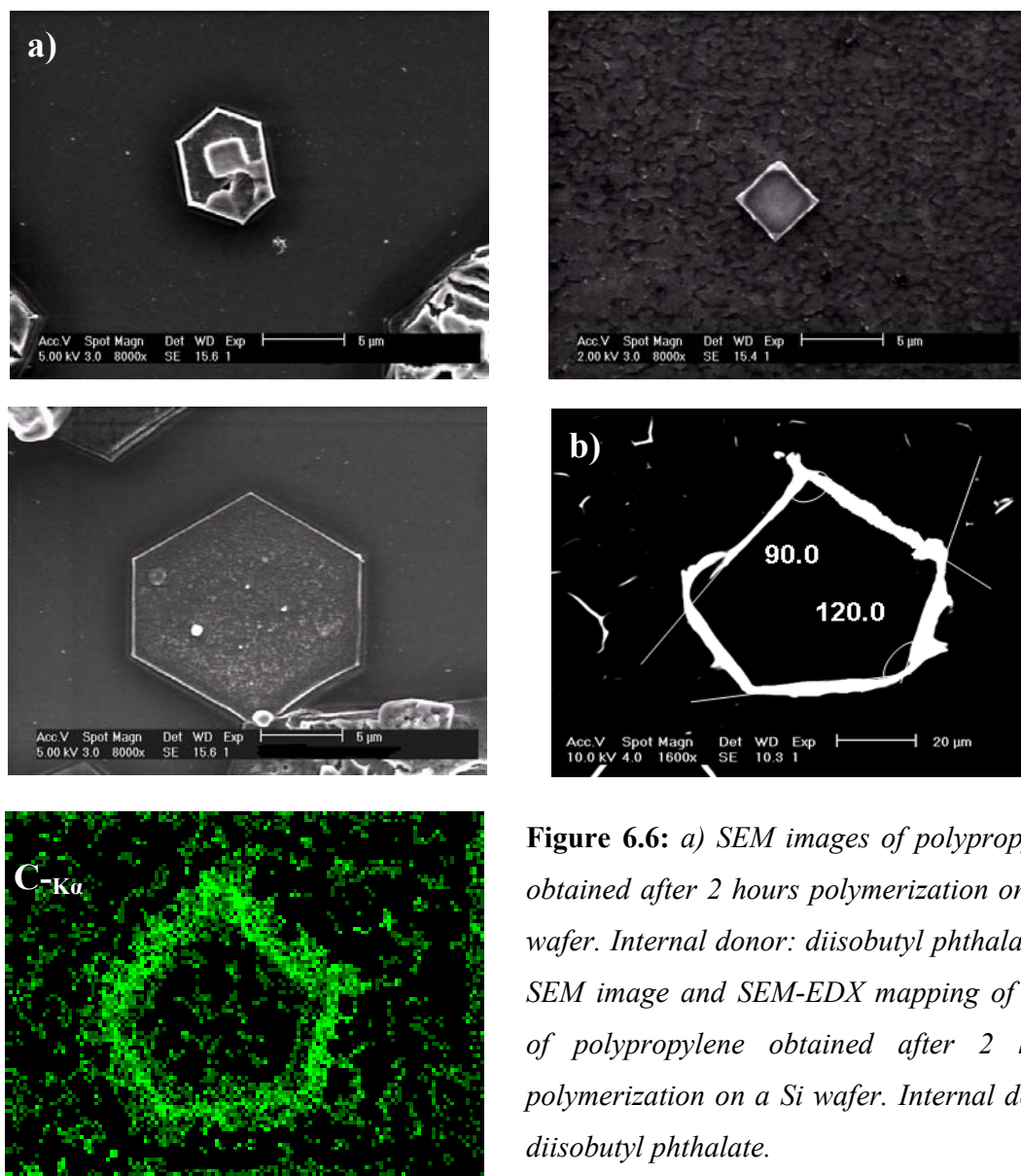


**Figure 6.6:** *a) SEM images of polypropylene obtained after 2 hours polymerization on a Si wafer. Internal donor: diisobutyl phthalate. b) SEM image and SEM-EDX mapping of C-K$_\alpha$ of polypropylene obtained after 2 hours polymerization on a Si wafer. Internal donor: diisobutyl phthalate.*
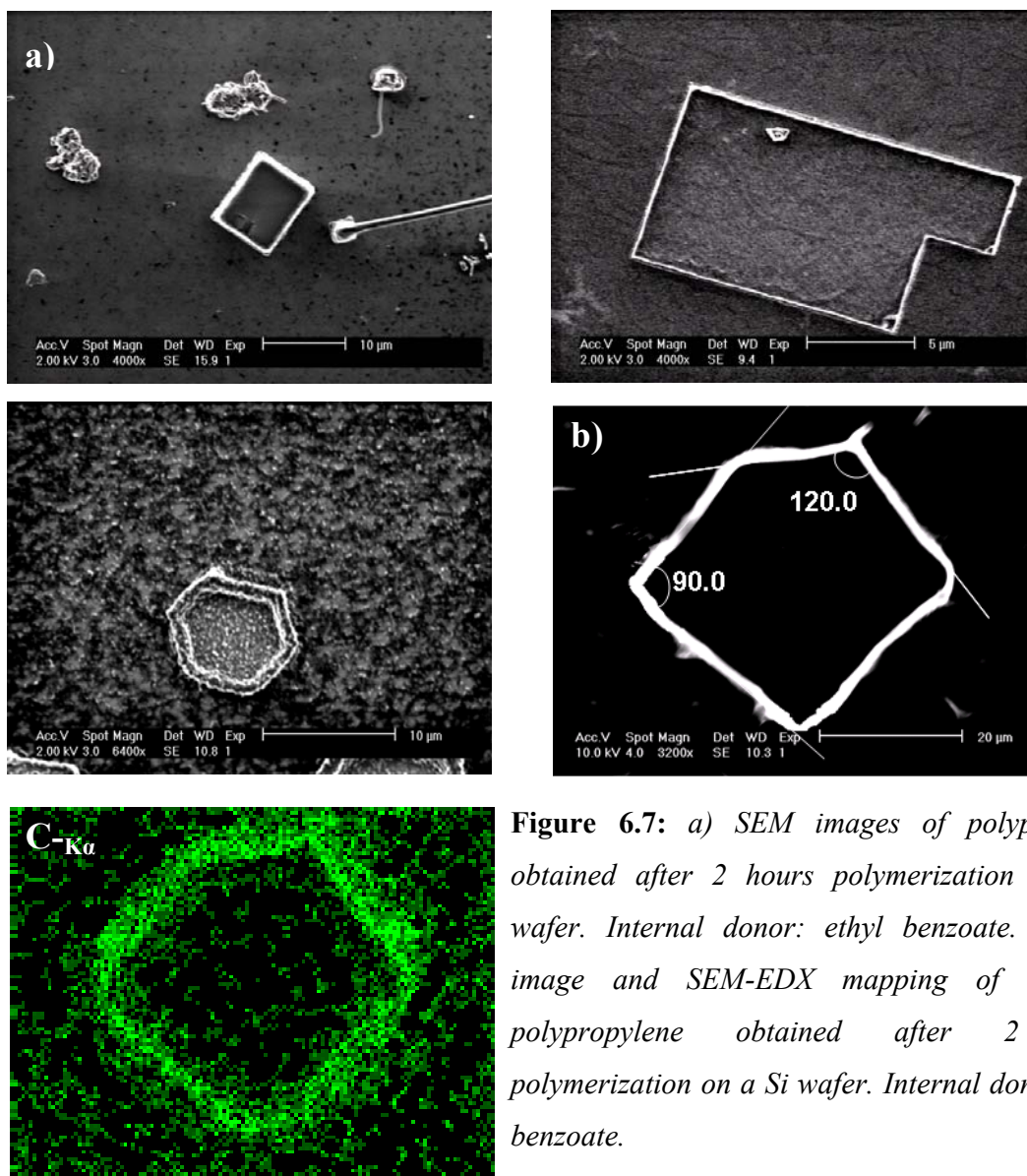
**Figure 6.7:** *a) SEM images of polypropylene obtained after 2 hours polymerization on a Si wafer. Internal donor: ethyl benzoate. b) SEM image and SEM-EDX mapping of C-K$_\alpha$ of polypropylene obtained after 2 hours polymerization on a Si wafer. Internal donor: ethyl benzoate.*

## 6.4 Discussion

The crystallization of magnesium chloride from a solution in ethanol gives hexagonal single crystals of the adduct $MgCl_2 \cdot 6EtOH$ [17]. In the present work, the formation of hexagonal crystallites with only 120° edge angles in the presence of the diether points to the exclusive formation of only one crystallite face i.e., either the (110) or the (104) face. The preferential formation of the (110) face is most probable, taking into account the strong indications from

modelling studies that the dominant coordination mode of diethers to $MgCl_2$ is via bidentate coordination on the (110) cut [18, 29].

It has indeed been suggested [20] that the incorporation of a bidentate internal donor such as a 1,3-diether may lead to the preferential formation of the (110) face of $MgCl_2$ and that active Ti species are present on the same face, on account of the strong evidence for close interaction between electron donors and isospecific active species on the support surface [21-23]. It is well known that the use of a diether as internal donor gives polymers with relatively narrow molecular weight distribution, indicating a more uniform distribution of active species than is present in catalysts containing an ester as internal donor [1, 20, 24, 25]. The present finding that $MgCl_2$ crystallites with exclusively 120° edge angles are formed in the presence of a diether indicates that the relatively uniform nature of the active species in this system may be due to the formation of a single crystallite face, most likely the (110) face [18, 19].

Another feature of polypropylene catalysts of type $MgCl_2/TiCl_4/$diether is their particularly high activity, which can be around twice that obtained with catalysts containing a diester as internal donor. Interestingly, when a diether is used as external donor with a catalyst of type $MgCl_2/TiCl_4/$DIBP, the active species are very similar to those formed when the diether is used as internal donor [8, 26, 27]. However, the catalyst activity is lower. A possible explanation for this would be that, in catalyst preparation using an ester as internal donor, $MgCl_2$ crystallites containing both the (110) and the (104) edge faces are formed but that active species having high activity and stereospecificity are formed only on the (110) face. Recent density functional calculations by Taniike and Terano have indicated that, with ethyl benzoate, interaction between the donor and the Ti species takes place selectively on the (110) surface of the $MgCl_2$ support [28].

Correa et al. have described possible active species on the (110) lateral cut of $MgCl_2$, taking into account the preferential coordination of a diether on this surface, in contrast to a variety of possible modes of coordination of phthalates and succinates on $MgCl_2$ support surfaces [29]. These authors indicated also that the broader polydispersity ($M_w/M_n$) observed with a phthalate or succinate internal donor than with the diether-containing catalysts can be

attributed to the variety of possible modes of coordination of esters on $MgCl_2$ support surfaces.

The present study provides strong evidence that the dependence of the distribution of active species in Ziegler-Natta catalysts for polypropylene on the nature of the internal donor is related to the ability of the donor to steer the formation of a particular $MgCl_2$ crystallite face during catalyst preparation. The results are as yet qualitative rather than quantitative, but indicate that a diether is effective in promoting the formation of the (110) surface, even though this surface has substantially higher energy than the (104) surface. It has been noted by Busico and co-workers that chemisorption of a donor on different surfaces may lower surface energies to different extents, thus changing their relative stabilities [10].

## 6.5 Conclusions

The characteristics of magnesium chloride supports generated in the synthesis of Ziegler-Natta catalysts are strongly dependent on the type of electron donor present in the support and catalyst. Comparison of the effects of diether and ester donors in the controlled growth of $MgCl_2$ crystallites, following spin coating of $MgCl_2 \cdot n$EtOH from ethanol solution onto a flat silica/silicon wafer, reveals that the presence of a diether leads to the formation of well-defined $MgCl_2$ crystallites in which the presence of only 120° edge angles indicates a strong preference for the formation of a particular crystallite face. In contrast, the use of a monoester or diester as internal donor generates crystallites with 120° and 90° edge angles, indicating the presence of both the (110) and the (104) edge surfaces of $MgCl_2$.

Polymer growth takes place at the edges of the crystallites. The high activity and relatively uniform nature of the active species in catalysts of type $MgCl_2/TiCl_4/$diether is likely to be due to preferential formation of the (110) face of $MgCl_2$ when using a diether as internal donor in catalyst preparation.

# References

1. E. Albizzati, G. Cecchin, J.C. Chadwick, G. Collina, U. Giannini, G. Morini, L. Noristi, in: Polypropylene Handbook, 2$^{nd}$ edition, N. Pasquini, Ed., Hanser Publishers, Munich, 2005, Ch. 2.

2. U. Giannini, Makromol. Chem. Suppl. 5 (1981) 216.

3. V. Busico, P. Corradini, L. De Martino, A. Proto, V. Savino, E. Albizzati, Makromol. Chem. 186 (1985) 1279.

4. P. Corradini, V. Busico, G. Guerra, in: W. Kaminsky, H. Sinn (Eds.), Transition Metals and Organometallics as Catalysts for Olefin Polymerization, Springer-Verlag, Berlin, 1988, p.337.

5. L. Brambilla, G. Zerbi, S. Nascetti, F. Piemontesi, G. Morini, Macromol. Symp. 213 (2004) 287.

6. L. Brambilla, G. Zerbi, F. Piemontesi, S. Nascetti, G. Morini, J. Mol. Catal. A: Chem. 263 (2007) 103.

7. M.C. Sacchi, I. Tritto, C. Shan, R. Mendichi, L. Noristi, Macromolecules 24 (1991) 6823.

8. E. Albizzati, U. Giannini, G. Morini, M. Galimberti, L. Barino, R. Scordamaglia, Macromol. Symp. 89 (1995) 73.

9. L. Barino, R. Scordamaglia, Macromol. Theory Simul. 7 (1998) 407.

10. V. Busico, M. Causà, R. Cipullo, R. Credendino, F. Cutillo, N. Friederichs, R. Lamanna, A. Segre, V. Van Axel Castelli, J. Phys. Chem. C 112 (2008) 1081.

11. E. Albizzati, U. Giannini, G. Morini, C.A. Smith, R.C. Zeigler, in G. Fink, R. Mülhaupt, H.H. Brintzinger, eds., Ziegler Catalysts. Recent Scientific Innovations and Technological Improvements, Springer-Verlag, Berlin, 1995, p. 413.

12. J.C. Chadwick, T. Garoff, J.R. Severn, Tailor-Made Polymers via Immobilization of Alpha-Olefin Polymerization Catalysts, Eds. J.R. Severn, J.C. Chadwick, WILEY-VCH, Weinheim, 2008, Ch. 2.

13. E.M.E. van Kimmenade, A.E.T. Kuiper, Y. Tamminga, P.C. Thüne, J.W. Niemantsverdriet, J. Catal. 223 (2004) 134.

14. P.C. Thüne, J. Loos, X. Chen, E.M.E. van Kimmenade, B. Kong, J.W. Niemantsverdriet, Top. Catal. 46 (2007) 239.

15. G. Morini, A. Cristofori, Eur. Pat. 728724, Montell, 1996.

16. A.K. Yaluma, P.J.T. Tait, J.C. Chadwick, J. Polym. Sci. Part A Polym. Chem. 44 (2006) 1635.

17. (a) N.Ya. Turova, E.P. Turevskaya, A.V. Novoselova, Russ. J. Inorg. Chem. 12 (1967) 901; (b) G. Valle, G. Baruzzi, G. Paganetto, G. Depaoli, R. Zannetti, A. Marigo, Inorg. Chim. Acta. 156 (1989) 157.

18. R. Scordamaglia, L. Barino, Macromol. Theory Simul. 7 (1998) 399.

19. M. Toto, G. Morini, G. Guerra, P. Corradini, L. Cavallo, Macromolecules 33 (2000) 1134.

20. J.C. Chadwick, Macromol. Symp. 173 (2001) 21.

21. M.C. Sacchi, F. Forlini, I. Tritto, R. Mendichi, G. Zannoni, L. Noristi, Macromolecules 25 (1992) 5914.

22. G. Morini, E. Albizzati, G. Balbontin, I. Mingozzi, M.C. Sacchi, F. Forlini, I. Tritto, Macromolecules 29 (1996) 5770.

23. V. Busico, R. Cipullo, G. Monaco, G. Talarico, M. Vacatello, J.C. Chadwick, A.L. Segre, O. Sudmeijer, Macromolecules 32 (1999) 4173.

24. J.C. Chadwick, G. Morini, G. Balbontin, I. Camurati, J.J.R. Heere, I. Mingozzi, F. Testoni, Macromol. Chem. Phys. 202 (2001) 1995.

25. J.C. Chadwick, F.P.T.J. van der Burgt, S. Rastogi, V. Busico, R. Cipullo, G. Talarico, J.J.R. Heere, Macromolecules 37 (2004) 9722.

26. M.C. Sacchi, F. Forlini, I. Tritto, P. Locatelli, G. Morini, L. Noristi, E. Albizzati, Macromolecules 29 (1996) 3341.

27. J.C. Chadwick, G. Morini, G. Balbontin, I. Mingozzi, E. Albizzati, Macromol. Chem. Phys. 198 (1997) 1181.

28. T. Taniike, M. Terano, Macromol. Rapid Commun. 28 (2007) 1918.

29. A. Correa, F. Piemontesi, G. Morini, L. Cavallo, Macromolecules 40 (2007) 9181.

# Chapter 7

## Attenuated total reflection infrared spectroscopy for studying planar Ziegler-Natta model catalysts

*A sensitive method is presented for investigating planar Ziegler-Natta model catalysts by attenuated total internal reflection Fourier transform infrared spectroscopy (ATR-FTIR). A solution of $MgCl_2$ in ethanol, optionally containing an internal donor, is spin coated directly onto a planar ZnSe ATR crystal. Ethylene and propylene polymerization has been monitored in situ and ex situ, respectively, and interactions of internal donors such as esters and a diether with $MgCl_2$ and $TiCl_4$ have been investigated. The isotacticity of the polypropylene produced in the presence and absence of donor has been estimated based on characteristic peaks in the infrared spectra.*

## 7.1    Introduction

The internal donor is an important component in supported Ziegler-Natta catalysts for propylene polymerization, as it is a major factor determining the stereospecificity of the catalyst [1-3]. Internal donors bind strongly to the $MgCl_2$ support [4-7]. It has been proposed that the internal donor blocks particular sites on the $MgCl_2$ surface which otherwise, upon coordination with $TiCl_4$, would generate precursors of non-stereospecific active sites [4, 8, 9]. On the other hand, as previously indicated in this thesis, there is strong evidence for the presence of a donor in the vicinity of isospecific active species.

Infrared (IR) spectroscopy is one of the most useful research tools for the study of surface species in solid catalysts. It can be applied to probe the state of carbonyl groups in ester internal donors, since the $\nu_{C=O}$ absorption band is very sensitive to coordination with a Lewis acid. IR spectroscopy has been extensively applied to Ziegler-Natta catalysts [10]. With regard to propylene polymerization catalysts, most of the work has focused on the spectral changes in the $\nu_{C=O}$ of the internal aromatic ester in various stages of catalyst preparation [10-23]. In the case of a diether internal donor, the spectral changes in the $\nu_{C-O}$ stretching frequency following coordination to $MgCl_2$ have been investigated [24].

In previous **chapters** of this thesis, we introduced a flat model approach utilizing a Si wafer as a planar carrier to investigate Ziegler-Natta catalytic systems. The deposition of $MgCl_2$ (with or without an internal donor) from ethanol solution onto the planar wafer was carried out by means of the spin coating technique. Next, treatment with $TiCl_4$ was carried out followed by ethylene or propylene polymerization under very mild conditions (room temperature and low monomer pressure) in the presence of a solution of the cocatalyst, $AlEt_3$. The $MgCl_2/TiCl_4$ and $MgCl_2/donor/TiCl_4$ catalysts (on Si wafer) were active towards ethylene and propylene polymerization, respectively. Each step of preparation was characterized employing XPS, AFM and SEM to study the surface chemistry and morphology of $MgCl_2 \cdot nEtOH/TiCl_4$ and $MgCl_2 \cdot donor \cdot nEtOH/TiCl_4$ catalysts, along with the polymer films obtained. These studies established the feasibility of a new model for Ziegler-Natta catalyst preparation and characterization. We further extended this work by developing a novel preparation method comprising the application of an Ostwald ripening process, aiming to convert the spin coated layer of $MgCl_2 \cdot nEtOH$ film, consisting of small

grains/particles at the nm scale, into large, well-defined crystallites. In this manner, we were able to facilitate the morphological characterization by AFM and SEM, and identify polymer formation on the lateral faces of the crystallite. Incorporation of different internal donors such as diether and esters into the solution of $MgCl_2$ in ethanol, followed by the spin coating onto the flat carrier and Ostwald ripening, generated large crystallites, allowing investigation of the effect that a certain donor has on the formation of different crystallite faces of magnesium chloride.

Analogous to this spin coating onto the planar carrier (wafer), we are now using a ZnSe crystal to deposit the $MgCl_2$ (with or without donor) from ethanol solution via spin coating, aiming to investigate the Ziegler-Natta catalysts by means of a new technique (for us): attenuated total reflectance (ATR) infrared spectroscopy. To this end, the wafer has now been replaced by an internal reflection element such as ZnSe, which allows application of ATR-FTIR spectroscopy.

The purpose of the present work is to explore the feasibility of applying ATR-FTIR to monitor ethylene polymerization in situ and, most importantly, to investigate the interactions of internal donors such as a mono- or diester and a diether with the $MgCl_2$ support and with $TiCl_4$. Additionally, an attempt is made to estimate the isotacticity index (I.I.) of polypropylene prepared in systems with and without donor.

## 7.2 ATR-FTIR of electron donors in solution

A series of ATR-FTIR experiments was carried out using different concentrations of donors in suitable solvents. The aim was merely to establish the detection level of the donors in solution, obtaining a series of calibration lines and, most importantly, identifying the most relevant/significant features (peaks) of pure donors and donors in solution. The latter is especially worthwhile when investigating interactions of the internal donors with $MgCl_2$ and $TiCl_4$.

### 7.2.1 Experimental

Experiments were carried out by flowing solutions of bis(methoxymethyl)fluorene [25] diether donor in toluene onto a ZnSe crystal contained in a closed cell within the ATR-FTIR set up. The spectra were measured in transmittance mode using ZnSe with toluene as background, masking in this manner toluene and allowing the visibility of only diether signals. In the case of the esters (mono- and diester), ethanol was the solvent of choice. The spectra were measured in transmittance mode using ZnSe with ethanol as background. In this way ethanol is masked and the characteristic bands of the esters can become evidently visible in the spectra. The neat donors were also measured in transmittance mode using ZnSe crystal as background. The data points of the collected spectra were the average of 4 scans at a spectral resolution of 4 cm$^{-1}$. Diisobutyl phthalate (≥98 %) and ethyl benzoate (≥99 %) were provided by Aldrich and used as received. Absolute ethanol (99.9 %) was purchased from Aldrich Chemicals and used as received. HPLC-grade toluene was taken from an argon-flushed column packed with aluminum oxide and stored over 4 Å molecular sieves.

## 7.2.2 Results

***Diether bis(methoxymethyl)fluorene donor in toluene***: Figure 7.1 represents an ATR-FTIR overview spectrum of the neat diether powder, whereas Figure 7.2 displays a series of ATR-FTIR spectra (in the region of interest) of the diether donor in toluene as the concentration of diether increases. An important feature in the ATR-FTIR spectrum of the neat diether donor (Figure 7.1) is the strong band of C-O stretching frequency at about 1090 cm$^{-1}$ [24]. The C-O stretch of an ether involves the C-O-C linkage and is more properly called a "C-O-C asymmetric stretch" [26]. Aromatic ring modes (signals) are observed in the region 1500-1400 cm$^{-1}$. The cluster of bands at about 1200 cm$^{-1}$ may be due to C-C stretching vibrations [26].
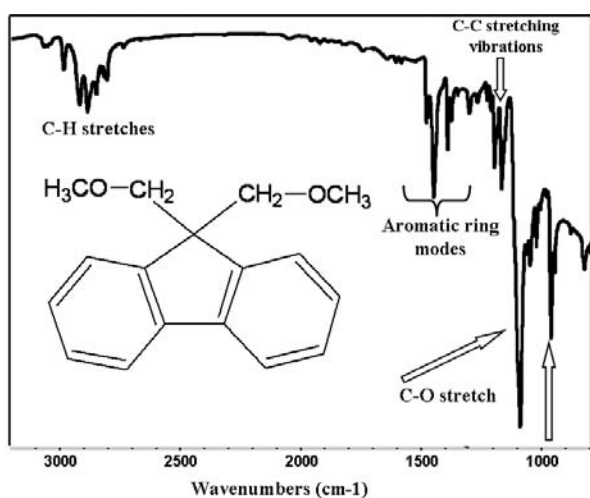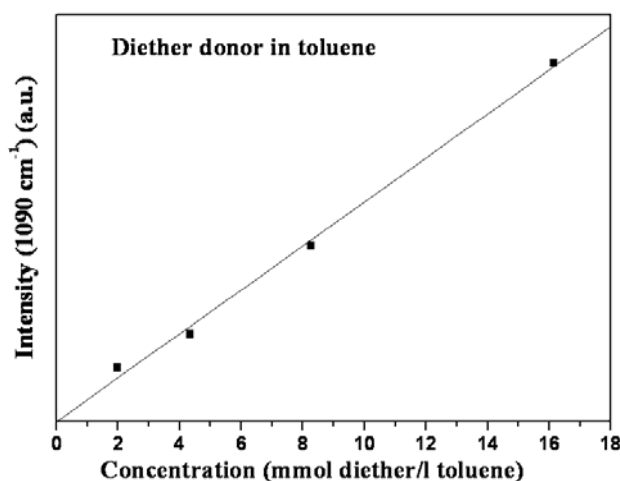


**Figure 7.1:** *Spectrum of diether bis(methoxymethyl)fluorene donor along with the inserted chemical structure.*

The series of spectra for the diether at different concentrations in toluene (Figure 7.2) also indicates the presence of a strong band at about 1090 cm$^{-1}$, which is more evident as the concentration of the diether increases in toluene. Aromatic ring modes signals are observed as well. The band at around 1200 cm$^{-1}$ (also present in the Figure 7.1) may arise from C-C stretching vibrations as noted [26]. Another feature in the spectrum of Figure 7.1 and spectra of Figure 7.2 is the peak at around 960 cm$^{-1}$ denoted by an arrow in both Figures. This vibration may arise from symmetric C-O-C stretching frequency, knowing that ethers give rise to symmetric C-O-C stretching frequency in the region 890-820 cm$^{-1}$ [26]. Additionally, Figure 7.3 shows a plot of the intensity of the C-O band versus the concentration of the diether in toluene. The intensity refers to the integrated area of the C-O band in absorbance unit in the ATR-FTIR spectra. The integrated area of the ATR-FTIR signals for the C-O bands is linearly proportional to the concentration of the diether in toluene. The lowest detectable concentration of the diether donor in toluene was about 2 mmol/L.
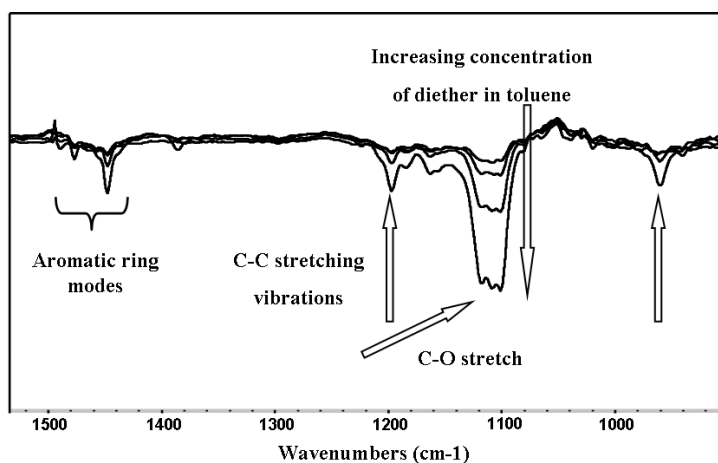


**Figure 7.2:** *Spectra of diether bis(methoxymethyl)fluorene donor in toluene as the concentration of the donor increases.*



**Figure 7.3:** *Plot of IR intensity (C-O band) versus diether bis(methoxymethyl)fluorene donor concentration in toluene.*

***Ethyl benzoate (EB) and diisobutyl phthalate (DIBP) donors in ethanol***: Similar series of solutions were prepared for EB and DIBP in ethanol. Figure 7.4 displays overview spectra of neat EB and DIBP. The spectra appear somewhat crowded, but the most important features are the three most intense bands at ~1720, 1280 and 1120-1110 cm$^{-1}$. The positions of these bands are attributed to the C=O, C-C-O and O-C-C stretch of an aromatic ester [26]. The aromatic ring modes are located at 1600 and 1580 cm$^{-1}$ (indicated with a dashed line ended at both sides with arrows in Figure 7.4). The peaks in the region 3000-2800 cm$^{-1}$ are attributed to C-H stretching, either methyl or aromatic [26].
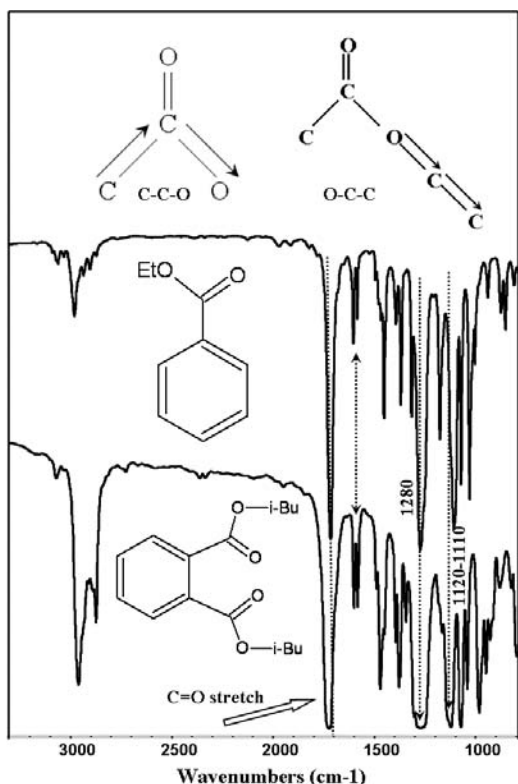


**Figure 7.4:** *Spectra of EB and DIBP along with the inserted chemical structure and schematic representations of C-C-O and O-C-C vibrations.*

The dissolution of EB in ethanol gave rise to a twin peak in the C=O region (Figure 7.5), most probably indicative of weak interaction between the proton originating from the ethanol (-OH) and the C=O functional group of the ester (hydrogen bonding). This is supported by the ATR-FTIR spectrum of EB in toluene (Figure 7.5, the inserted spectrum). The dissolution of EB in toluene gave rise to a peak at ~1720 cm$^{-1}$ (no splitting occurred). Overall the series of the spectra for EB in ethanol in Figure 7.5 clearly indicate that, upon increasing the concentration of the monoester in ethanol, the intensities of the C=O, C-C-O and O-C-C bands increase as well.
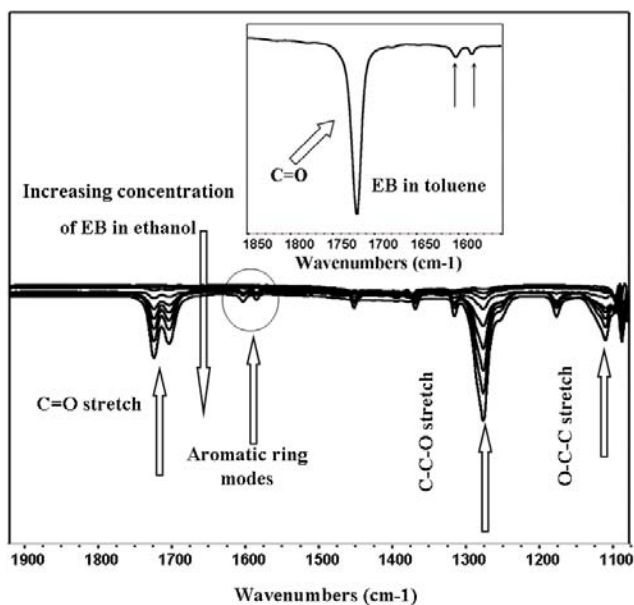
**Figure 7.5:** *Spectra of EB donor in ethanol as the concentration of the donor increases. The inserted spectrum shows EB in toluene indicating by arrows the C=O region and aromatic rings mode.*

Figure 7.6 shows a plot of the intensity of the C=O band versus the concentration of the EB in ethanol. The intensity refers to the integrated area of the C=O band in absorbance unit in the ATR-FTIR spectra (the peak split into two bands; both of them were integrated). The integrated area of the ATR-IR signals for the C=O bands is linearly proportional to the concentration of the EB in ethanol. The lowest detectable concentration of EB in ethanol was about 2 mmol/L.
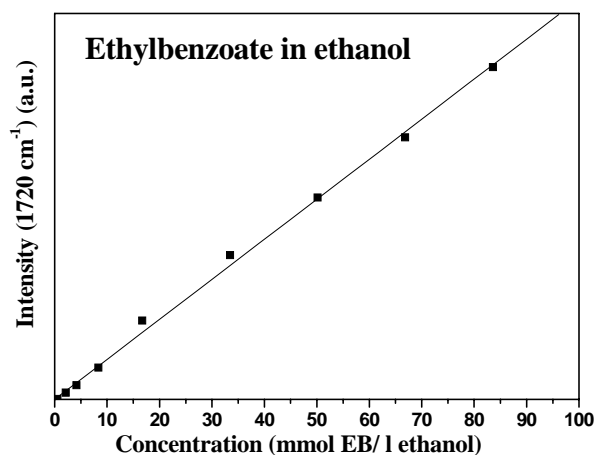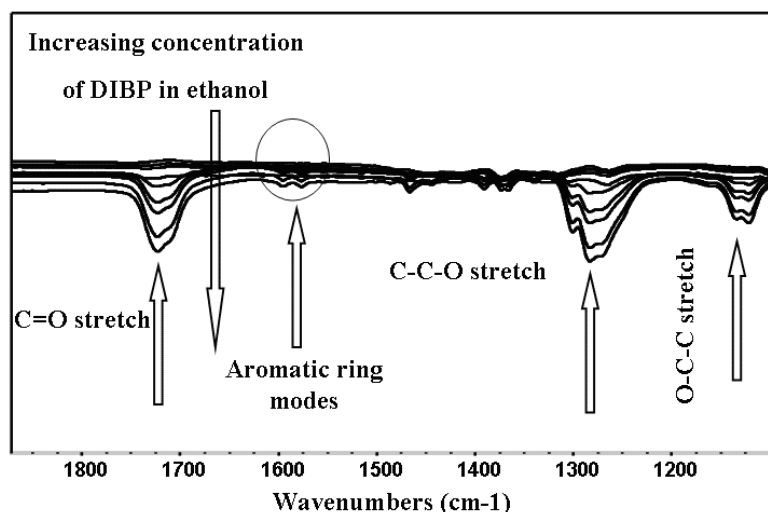


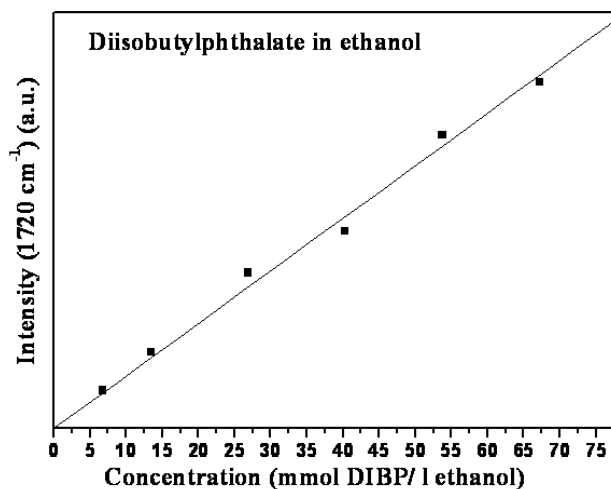**Figure 7.6:** *Plot of IR intensity (C=O band) versus EB donor concentration in ethanol.*

DIBP in ethanol also shows the presence of C=O, C-C-O and O-C-C bands, the intensities of which enhance as the concentration of the diester increases (Figure 7.7). The C=O band appears now as a singlet (no peak splitting occurred). Figure 7.8 shows a plot of the intensity of the C=O band versus the concentration of the DIBP in ethanol. The intensity refers to the

integrated area of the C=O band in absorbance unit in the ATR-FTIR spectra. The integrated area of the ATR-IR signals for the C=O bands is linearly proportional to the concentration of the DIBP. The lowest detectable DIBP concentration was about 7 mmol/L.



**Figure 7.7:** *Spectra of DIBP donor in ethanol as the concentration of the donor increases.*



**Figure 7.8:** *Plot of IR intensity (C=O band) versus DIBP donor concentration in ethanol.*

## 7.2.3 Discussion

Basic information regarding IR spectra of the donors was acquired using the abovementioned technique. Different solutions of donors were prepared and the most important features in the IR spectra were identified. The most intense band of the neat bis(methoxymethyl)fluorene diether donor was the C-O stretching vibration. This was supported by the ATR-FTIR spectra

of the diether donor dissolved in toluene. Upon increasing the concentration of the diether in toluene, the C-O band became more intense and the intensity scaled linearly with increasing concentration. The ATR-FTIR spectra of neat EB and neat DIBP indicated that the most intense bands were the C=O stretching frequency along with C-C-O and O-C-C vibrations. This was more evident in the series of infrared spectra for EB and DIBP in ethanol. These three brands became more intense upon increasing the content of EB and DIBP in ethanol. Yet again the infrared intensity scaled linearly with increasing concentration.

## 7.2.4 Conclusions

We conclude that the most important bands for the electron donors were readily identified by means of ATR-FTIR. C-O vibration was the most intense band in the case of the diether donor, whereas in the case of esters (mono- and diester) C=O, C-C-O and O-C-C vibrations were the most distinctive ones. Their intensities (C-O and C=O bands) linearly increased upon increasing the concentration of the donors in solution.

## 7.3 ATR-FTIR of the $MgCl_2 \cdot n$EtOH and EtOH

In the previous chapters we reported the deposition of $MgCl_2$ from ethanol solution with or without internal donor onto a silica/silicon wafer via a spin coating technique. The XPS results were ambiguous (**chapter three**) regarding whether the spin coated layer contained a minor amount of ethanol or not. In the current section the presence of ethanol in the film layer of $MgCl_2$ has been confirmed.
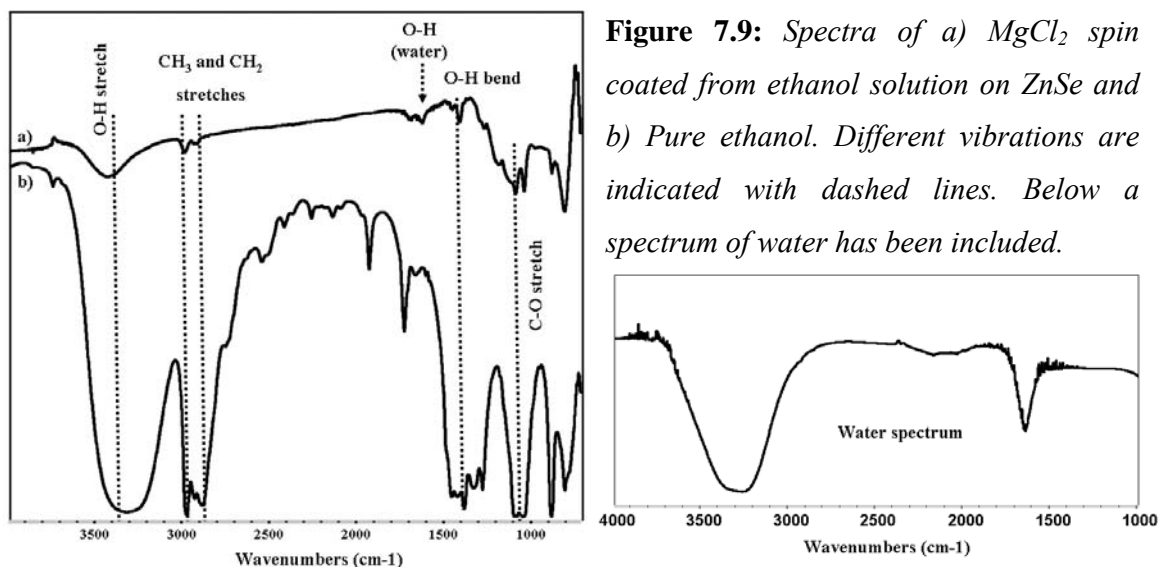
## 7.3.1 Experimental

A ZnSe ATR-IR crystal was spin coated with a solution of $MgCl_2$ in ethanol under glove box conditions (42 mmol/L). The spin coated film has a thickness (12±2 nm) as reported in **chapter three** (spin coating on Si wafer from a solution of $MgCl_2$ in ethanol (42 mmol/L)). The rotation speed applied was 2800 r.p.m. The ZnSe ATR-IR crystal was assembled into the flow cell then closed/sealed and transferred afterwards to the ATR-FTIR set up. The spectra were measured in transmittance mode using ZnSe as background. The data points of the collected spectra were the average of 4 scans at a spectral resolution of 4 cm$^{-1}$. Anhydrous

magnesium chloride (beads, 99.9 %) and absolute ethanol (99.9 %) were purchased from Aldrich Chemicals and used as received.

## 7.3.2 Results

In Figure 7.9, ATR-FTIR spectra of the spin coated layer of $MgCl_2$ from ethanol (spectrum a) and pure ethanol (spectrum b) are shown. Additionally an ATR-FTIR spectrum of water has been included as well. When comparing spectra a and b, it is noticeable that ethanol is present in the spin coated layer. However, we were not able to quantify the amount of ethanol. In spectrum a, the O-H stretch originating from ethanol is apparent, although it should be noted that water (traces of which can be present in the glove box or from leakage in the cell) also gives a broad, intense O-H stretch between 3500 and 3000 $cm^{-1}$ which is very similar in position and shape to the O-H stretch of an alcohol [26]. Auspiciously, other sections of the spectrum show differences. Water gives rise to a band at 1630 $cm^{-1}$, due to the scissoring of the two O-H bonds. This vibration is unique to water. The presence of this band along with an O-H stretch is very strong evidence for the presence of liquid water in a sample [26].



**Figure 7.9:** *Spectra of a) MgCl₂ spin coated from ethanol solution on ZnSe and b) Pure ethanol. Different vibrations are indicated with dashed lines. Below a spectrum of water has been included.*

In spectrum a, the O-H vibration (at around 1630 $cm^{-1}$) indicated by a dashed arrow is possibly due to the minor amount of water present in the spin coated layer of $MgCl_2$/ethanol. Another diagnostic peak which distinguishes an alcohol from water is the C-O stretch in the region 1075-1000 $cm^{-1}$ [26] also indicated in Figure 7.9 by a dashed line. Additionally,

alcohols give rise to signals in the regions $1350\pm50$ cm$^{-1}$ (also present in the abovementioned spectra) and $650\pm50$ cm$^{-1}$ due to O-H bending.

## 7.3.3 Concluding remarks

The ATR-FTIR spectrum of the spin coated $MgCl_2$ layer from ethanol solution revealed the presence of the latter. Although a minor amount of water was present in the film, the spin coated layer $MgCl_2$/EtOH after treatment with $TiCl_4$ was active towards ethylene polymerization (in presence of the cocatalyst and monomer) as will be shown in the upcoming sections. Determination of the amount of ethanol in the spin coated layer of the $MgCl_2$ support was not possible via ATR-FTIR, although IR studies of $MgCl_2$/ethanol adducts have been reported by Di Noto et al. [27] and Tewell et al. [28]. Accurate quantification of ethanol in the $MgCl_2$ film requires not only the characteristic peaks of ethanol but also those originating from $MgCl_2$ as internal standard (50-500 cm$^{-1}$) [29, 30].

## 7.4 ATR-FTIR of $MgCl_2$/donor·$n$EtOH, $MgCl_2$/donor·$n$EtOH /TiCl$_4$ and TiCl$_4$/donor

In this section coordination of the diether and ester(s) donors onto the $MgCl_2$ surface and subsequent treatment with $TiCl_4$ will be investigated (ex situ studies). Interactions of $TiCl_4$ with donors in the absence of $MgCl_2$ support will be reported in addition to possibilities for in situ studies of donor coordination onto the surface of $MgCl_2$.

## 7.4.1 Experimental

The donors used for the study of interactions with the $MgCl_2$/ethanol support were 9,9–bis(methoxymethyl)fluorene, diisobutyl phthalate and ethyl benzoate (as already mentioned in the preceding section 7.2). The donor was added to a solution of $MgCl_2$ in ethanol (42 mmol/L); in the case of the diether donor, the mixture was heated at 60 °C until the solution became clear. The donor/$MgCl_2$ molar ratio was 0.1 in the case of the diether donor, 0.1 in the case of the similarly bidentate donor DIBP and 0.2 for the monodentate donor EB. The resulting solutions were used to spin coat the ZnSe crystal. The spin coated $MgCl_2$/donor·$n$EtOH layers were treated with a 10 % v/v $TiCl_4$ solution in toluene at room

temperature for 30 min. After washing with toluene to remove the physisorbed TiCl$_4$, the model catalyst was dried under nitrogen. Figure 7.10 shows yet again as a reminder to the reader the chemical structures of the donors used in this work. The spectra were measured in transmittance mode using ZnSe as background. FTIR spectra of donors in solutions have been incorporated as well for comparison purposes. They were measured in transmittance mode using as background ZnSe with toluene for the diether and ZnSe with ethanol for the esters. The data points of the collected spectra were the average of 4 scans at a spectral resolution of 4 cm$^{-1}$.
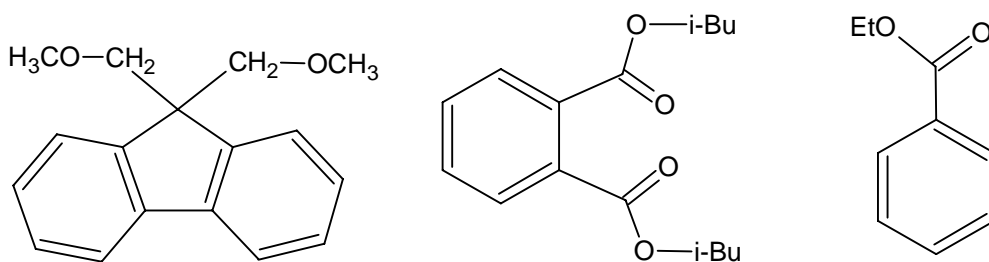


**Figure 7.10:** *Chemical structures of the internal donors used in this study. From left to right bis(methoxymethyl)fluorene, diisobutyl phthalate and ethyl benzoate.*

## 7.4.2 Results

It is well established by now that the coordination of donors such as diether and esters onto the MgCl$_2$ support occurs via the functional group i.e., C-O (in the case of a diether) [24] and C=O (in the case of an ester) [10-13, 16, 18, 20-23]. Figure 7.11 represents a series of ATR-FTIR spectra of the neat diether donor (spectrum a), diether donor in toluene (spectrum b) and spectra of MgCl$_2$/diether deposited on ZnSe crystal via spin coating from ethanol (spectrum c and d). A 0.1 molar ratio diether/MgCl$_2$ was applied, comparable to that present in a typical Ziegler-Natta catalyst [31].

The content of diether is increased from a diether/MgCl$_2$ molar ratio of 0.1 (spectrum c) up to 0.4 (spectrum d). The diether donor shows a strong band of C-O stretching frequency at about 1090 cm$^{-1}$ as noted. Upon coordination onto MgCl$_2$, the C-O band has shifted to lower frequency at 1060 cm$^{-1}$ and 1039 cm$^{-1}$ (spectrum c). These bands manifest the presence of MgCl$_2$/diether complexes. In Figure 7.9 we observed that the spin coated layer of MgCl$_2$/ethanol gives rise to C-O stretch (originating from ethanol) in the region 1075-1000

cm$^{-1}$ (close to the range of the C-O bands of the diether upon complexation with MgCl$_2$). Nevertheless, as the loading of the diether increases (spectrum d in Figure 7.11), the bands originating from the aromatic ring modes at about 1500-1400 cm$^{-1}$ become more intense and the band at about 1200 cm$^{-1}$ becomes more evident. This suggests that that the bands at 1060 cm$^{-1}$ and 1039 cm$^{-1}$ originate in fact from the diether and not ethanol. These bands have experienced an enhancement in the intensity upon increasing the loading of the diether from 0.1 to 0.4 molar ratio, which supports the abovementioned suggestion.
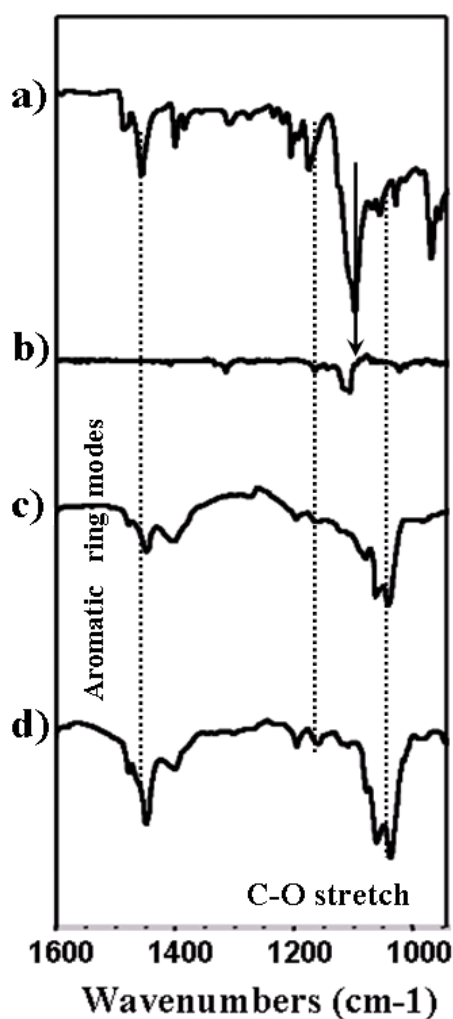


**Figure 7.11:** *Spectra of: a) Neat diether bis(methoxymethyl)fluorene donor. b) Diether donor in toluene (~4 mmol/L). c) Spin coated layer of diether/MgCl$_2$ from ethanol (diether/MgCl$_2$ = 0.1). d) Spin coated layer of diether/MgCl$_2$ from ethanol (diether/MgCl$_2$ = 0.4).*
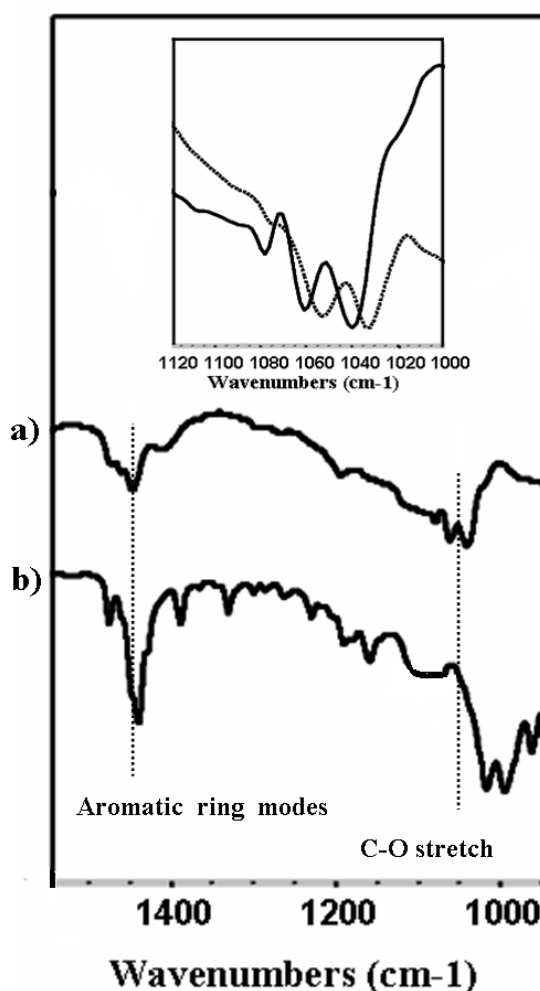
**Figure 7.12:** *Spectra of: a) Spin coated layer of diether/MgCl$_2$ from ethanol (diether/MgCl$_2$ = 0.1). b) TiCl$_4$/diether bis(methoxymethyl)fluorene complex (1:1). The inserted spectra represent diether/MgCl$_2$ (0.1) before (solid line) and after treatment with TiCl$_4$ (dashed line).*

Figure 7.12 shows the ATR-FTIR spectrum of the diether donor coordinated onto $MgCl_2$ (diether/$MgCl_2$ = 0.1) (spectrum a), together with a spectrum of $TiCl_4$/diether donor complex (spectrum b). The inserted spectra in Figure 7.12 represent the C-O region of the 0.1 diether/$MgCl_2$ complex before (solid line) and after (dashed line) treatment with $TiCl_4$. It is apparent from spectrum b in Figure 7.12 that there is a strong interaction between the diether donor and $TiCl_4$ (pure). The C-O band of the $TiCl_4$/diether complex is shifted to lower frequencies at 1016 $cm^{-1}$ and 994 $cm^{-1}$. The treatment of the diether/$MgCl_2$ film with $TiCl_4$ (solution in toluene) on the other hand, gave rise to a minor downshift of the C-O band as shown in the inserted spectra in Figure 7.12.

Coordination of the esters (monoester and diester) onto $MgCl_2$ showed similar features in the ATR-FTIR spectra. Figure 7.13 displays the spectrum of neat EB and EB in ethanol (spectrum a and b) and upon coordination to $MgCl_2$ (spectrum c and d). Upon coordination to $MgCl_2$, the C=O band of EB has shifted to lower stretching frequency. The C=O band of uncoordinated EB has a stretching frequency at ~1720 $cm^{-1}$. Upon complex formation with $MgCl_2$, the C=O band shifts down to 1687 $cm^{-1}$. This is apparent in spectrum c (EB/$MgCl_2$ = 0.2 molar ratio). Spectrum d, however, evidently demonstrates that, upon increasing the content of EB in the solution of $MgCl_2$ in ethanol (EB/$MgCl_2$ = 1), the C=O band becomes more intense and aromatic ring modes become visible as well.

This is more noticeable in Figure 7.14, where only the section of the C=O band and aromatic ring modes is shown. These modes (aromatic rings) remain unperturbed upon coordination to $MgCl_2$. Traces of water are present in the spectra at around 1630 $cm^{-1}$. A strong band appears at around 1400 $cm^{-1}$ in spectrum c (Figure 7.13). We attribute it to ethanol, since alcohols give rise to signals in the regions 1350±50 $cm^{-1}$. Nevertheless, this band diminishes in spectrum d due to the high content of EB in the $MgCl_2$/ethanol film.

The spectrum of neat EB is composed of other bands as well, such as C-C-O and O-C-C stretching frequencies positioned at about 1280 $cm^{-1}$ and 1110 $cm^{-1}$, respectively. As the monoester (EB) coordinates to $MgCl_2$, two new peaks appear (spectrum c and d) in the vicinity of the C-C-O band. As the latter (C-C-O band) strongly attenuates in spectrum c and becomes almost invisible in spectrum d, the new bands indicated by arrows in Figure 7.13

(spectrum c and d) position themselves at 1327 cm$^{-1}$ and 1305 cm$^{-1}$. Additionally, we will not discuss the O-C-C band (~1110 cm$^{-1}$ in the neat ester) after complexation (MgCl$_2$/EB) due to the fact that the spin coated layer of MgCl$_2$/ethanol generates a stretching frequency (C-O, originating from ethanol) in the region 1075-1000 cm$^{-1}$.

Treatment of EB/MgCl$_2$/EtOH with TiCl$_4$ gave rise to only a minor downshift (a few wavenumbers) of the C=O band as indicated in the inserted ATR-FTIR spectra (C=O region) in Figure 7.15. However, the ATR-FTIR spectrum of TiCl$_4$ (pure)/EB complex gave rise to a large downshift at 1591 cm$^{-1}$ and 1563 cm$^{-1}$ (spectrum  b and inserted spectrum in Figure 7.15). The TiCl$_4$/EB complex formation resulted in a yellowish solid product.
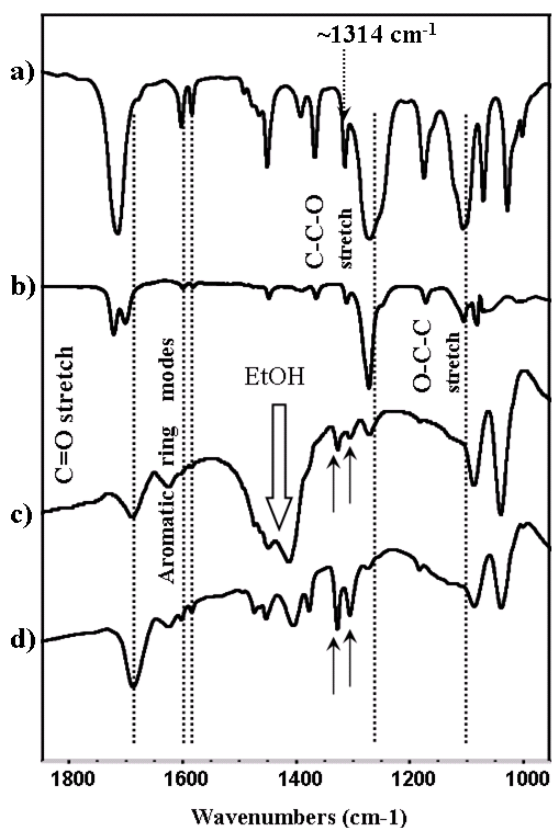


**Figure 7.13:** *Spectra of: a) Neat EB donor. b) EB in ethanol (10 mmol/L). c) Spin coated layer of EB/MgCl$_2$ from ethanol (EB/MgCl$_2$ = 0.2 molar ratio). d) Spin coated layer of EB/MgCl$_2$ from ethanol (EB/MgCl$_2$ = 1 molar ratio).*
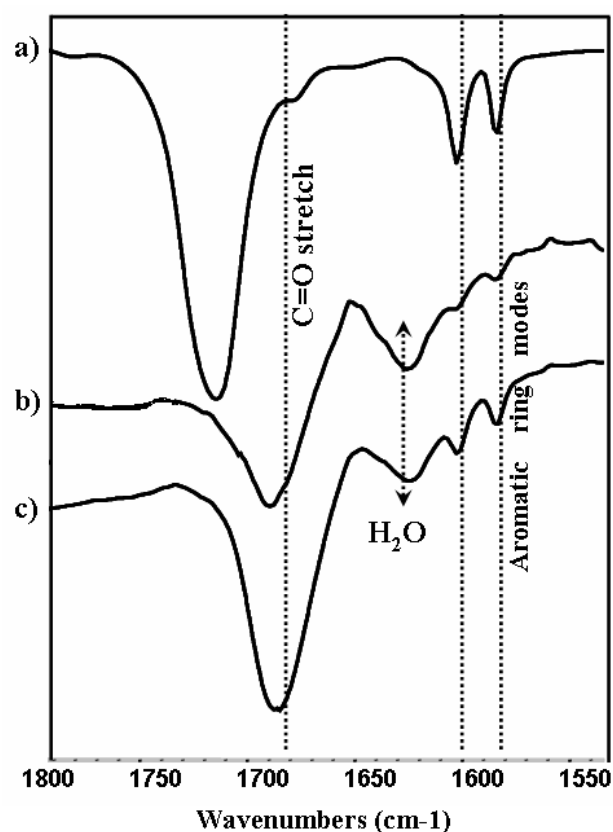
**Figure 7.14:** *Spectra of: a) Neat EB donor. b) Spin coated layer of EB/MgCl$_2$ from ethanol (EB/MgCl$_2$ = 0.2). c) Spin coated layer of EB/MgCl$_2$ from ethanol (EB/MgCl$_2$ = 1) in the C=O and aromatic ring modes region.*

157
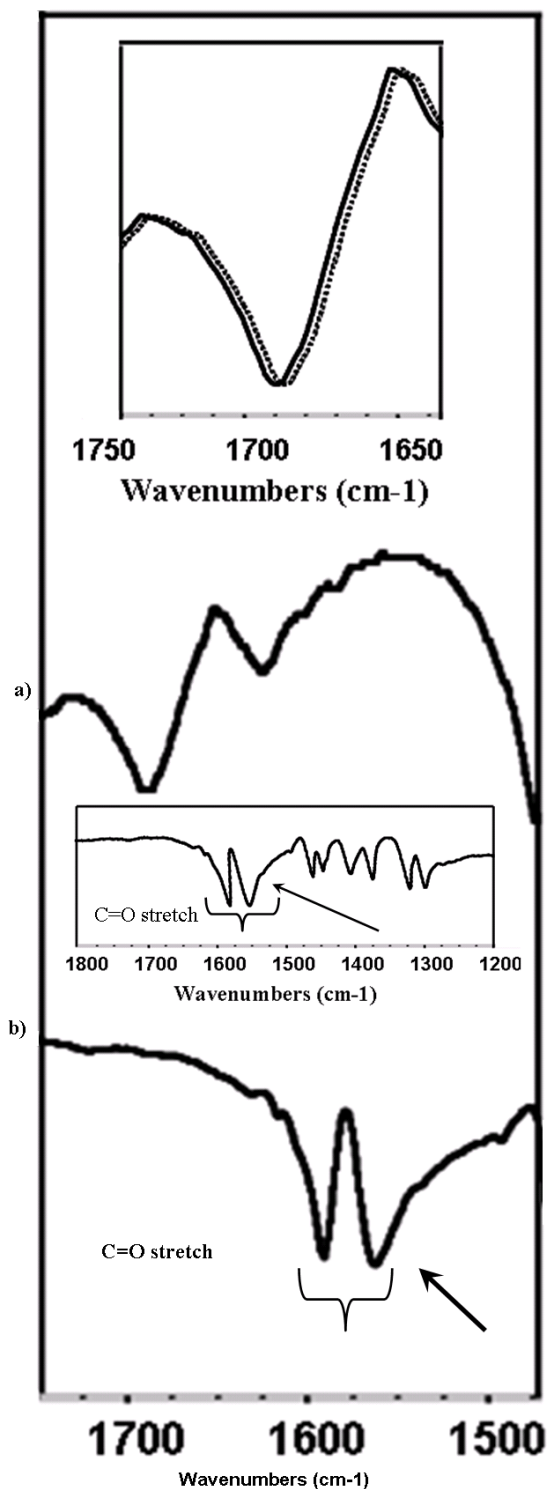
**Figure 7.15:** *Spectra of: a) EB donor upon coordination onto MgCl₂ in the C=O region (EB/MgCl₂ = 0.2). b) TiCl₄/EB complex in the C=O region (1:1). The inserted spectra represent spin coated EB/MgCl₂ (0.2 molar ratio) before (solid line) and after treatment with TiCl₄ (dashed line) along with the overview spectrum of TiCl₄/EB complex.*

Lastly, coordination of the diester onto MgCl₂ along with the treatment with TiCl₄ was studied. Similar to EB, the C=O band of DIBP upon complexation with MgCl₂ undergoes a shift to lower wavenumbers i.e., 1695 cm⁻¹ (Figure 7.16 spectrum c and d). The aromatic ring modes maintain their position upon coordination to MgCl₂ (Figure 7.16 spectrum a, b, c and

d). Upon increasing the concentration of DIBP in the MgCl$_2$/ethanol solution, the DIBP signals become stronger as observed in spectrum d of Figure 7.16. Another observation in Figure 7.16 is the shift to higher wavenumbers i.e., ~1320 cm$^{-1}$ of the C-C-O band (spectrum c and d) upon complex formation with MgCl$_2$. Like in the case of EB, we will not comment on the O-C-C band upon complexation (DIBP/MgCl$_2$). The spin coated layer of MgCl$_2$/ethanol, as noted, generates the C-O stretching frequency (originating from ethanol) in the region 1075-1000 cm$^{-1}$ which is close to the O-C-C vibration. The inserted spectra in Figure 7.16 illustrate the downshift of the C=O band upon coordination to the support (dashed lines), while the aromatic ring modes remain unperturbed (solid and dashed lines in the inserted spectra).

The next step involved treatment with TiCl$_4$. Figure 7.17 shows the spectra of DIBP/MgCl$_2$ and TiCl$_4$/DIBP complexes (spectra a and b, respectively). The C=O band of the TiCl$_4$/DIBP complex has shifted further downward, generating a peak splitting in the region 1640-1581 cm$^{-1}$. The TiCl$_4$/DIBP complex formation resulted in a yellowish solid product. Lastly, as in the cases of the diether/MgCl$_2$ and EB/MgCl$_2$ complexes, treatment of DIBP/MgCl$_2$ film with TiCl$_4$ induced a minor downshift in the vibrational frequency of the functional group i.e., C=O band. The inserted spectra in Figure 7.17 show the C=O bands of a DIBP/MgCl$_2$ complex, along with aromatic ring modes, before (solid line) and after (dashed line) treatment with TiCl$_4$. The spectrum after treatment with TiCl$_4$ indicates yet again that only a minor shift to lower wavenumbers of the C=O band has occurred.
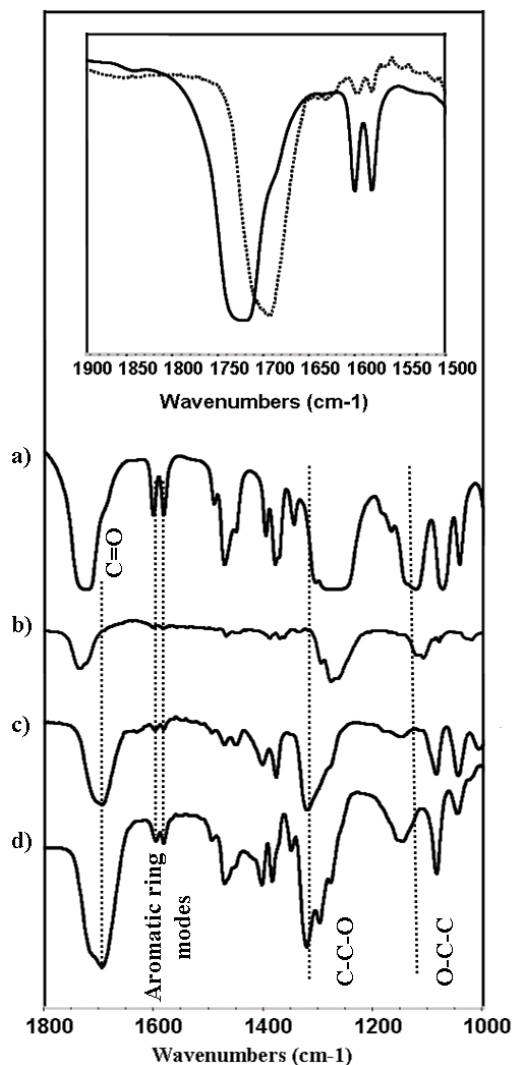
**Figure 7.16:** *Spectra of: a) Neat DIBP donor. b) DIBP in ethanol (15 mmol/L). c) Spin coated layer of DIBP/MgCl₂ from ethanol (DIBP/MgCl₂ = 0.1). d) Spin coated layer of DIBP/MgCl₂ from ethanol (DIBP/MgCl₂ = 0.4 molar ratio). The inserted spectra represent C=O band and aromatic ring modes of DIBP before complexation with MgCl₂ (solid line) and after complexation with MgCl₂ (dashed line).*
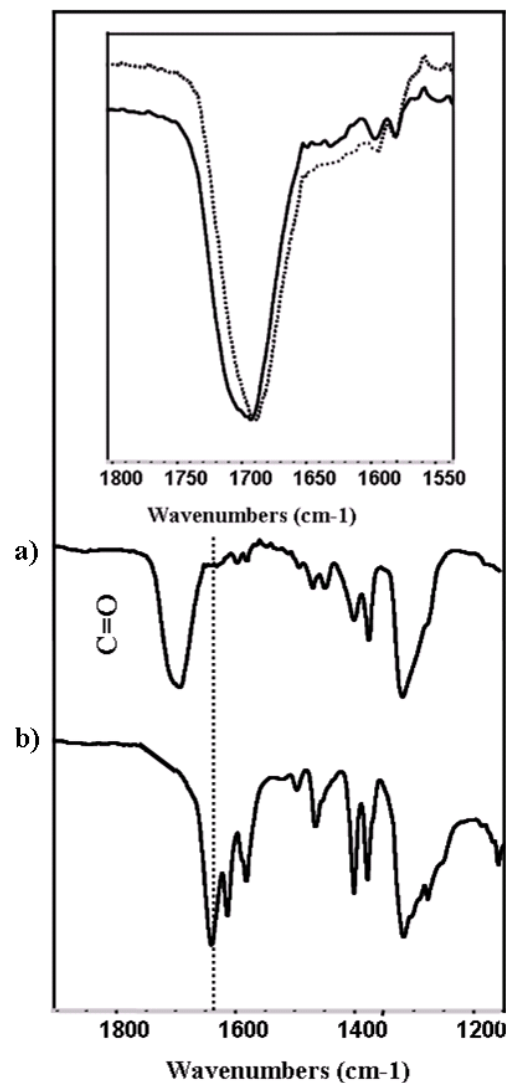


**Figure 7.17:** *Spectra of: a) DIBP donor upon coordination onto MgCl₂ (DIBP/MgCl₂ = 0.1). b) TiCl₄/DIBP complex (1:1). The inserted spectra represent spin coated DIBP/MgCl₂ (0.1 molar ratio) before (solid line) and after treatment with TiCl₄ (dashed line) in the C=O and aromatic ring modes region.*
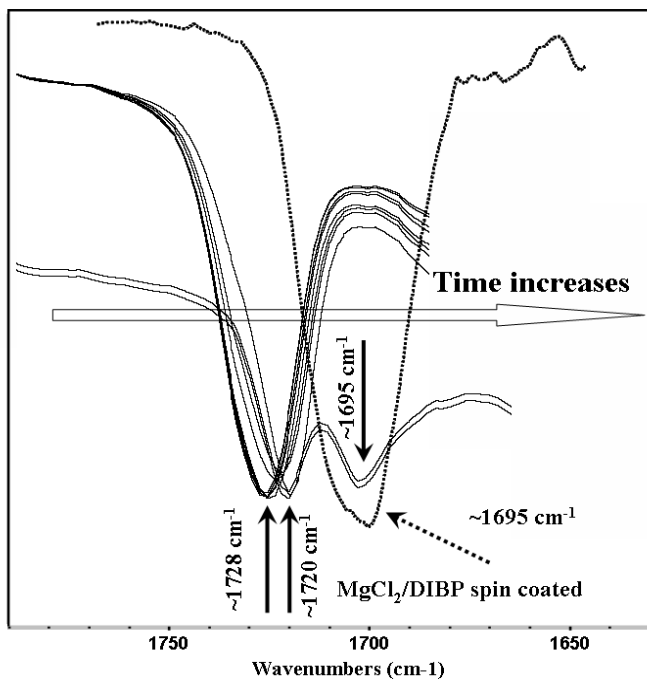
## 7.4.2.1 In situ coordination of DIBP onto MgCl₂/ethanol film

In the preceding sections of the current **chapter** the donors were spin coated onto the ZnSe crystal from a solution of $MgCl_2$ in ethanol. The ZnSe crystal was assembled into the cell, sealed and transferred to the ATR-FTIR set up, allowing the ex situ measurement of the donor coordination onto the $MgCl_2$ support. In this section we have attempted to prove that investigation of in situ coordination of the donors is also achievable. In other words, instead of dissolving the donor in the solution of $MgCl_2$ in ethanol followed by spin coating and subsequently measurement with ATR-FTIR, the spin coated layer of $MgCl_2$/EtOH is brought in contact with a solution of donor in toluene.

The deposition of $MgCl_2$ onto a Si crystal (cut-off 1500 $cm^{-1}$) was yet again carried out via spin coating. Meanwhile a solution of DIBP donor in toluene was prepared (20 μL DIBP/mL toluene) under glove box conditions, poured into a bottle, sealed and transferred to the new modified ATR-FTIR set up as shown in Figure 7.18 (bottom panel). Initially a transmittance ATR-FTIR spectrum of the background was measured (Si crystal located in cell was filled with toluene and measured afterwards). The in situ measurement was carried out in a timeframe of 20 min. As the DIBP in toluene flows into the cell, a band at ca. 1728 $cm^{-1}$ appears in the ATR-FTIR spectrum. This band corresponds to the C=O stretching frequency of uncoordinated DIBP.

In a meantime, a new band becomes visible at ca. 1720 $cm^{-1}$. The band at 1720 $cm^{-1}$ is close to the carbonyl stretching vibrations in neat ester and can be attributed to carbonyl groups in loosely coordinated DIBP. The striking observation in the ATR-FTIR spectra of Figure 7.18 is that with time (while the solution of the donor flows in the cell) the band at ca. 1720 $cm^{-1}$ appears as a twin peak with stretching frequencies at about 1720 $cm^{-1}$ and 1695 $cm^{-1}$. This value corresponds to the C=O band of the coordinated donor. The position of the peak/component at 1695 $cm^{-1}$ completely overlies the position of the C=O band originated from the spin coated DIBP/$MgCl_2$ layer (ex situ coordination) indicated by a dashed line spectrum in Figure 7.18. The splitting of the C=O band into two peaks suggests/implies the co-existence of loosely coordinated (1720 $cm^{-1}$) and coordinated (1695 $cm^{-1}$) species of DIBP on the surface of the $MgCl_2$ support. Therefore with time, as the solution of the donor slowly flows in the cell, one would expect disappearance of the twin peak and appearance of a single

peak at ca. 1695 cm$^{-1}$. Unfortunately, contamination of water in the system/set up hampered the complete coordination of DIBP onto the MgCl$_2$ support. Nonetheless, the present experiment shows the possibility to investigate in situ coordination of electron donors onto the surface of the MgCl$_2$ support (provided that the system is water-free).



**Figure 7.18:** *Top panel represents spectra (solid lines) of the in situ coordination of DIBP (from toluene solution) on to MgCl$_2$/EtOH film in the C=O region. The measurements were carried out using Si with toluene as a background. The dashed line spectrum represents coordination of DIBP onto MgCl$_2$/ethanol ex situ (spin coating of a solution which contains MgCl$_2$ and DIBP in ethanol). The bottom panel represents a picture of the set up enabling in situ coordination of the donor onto MgCl$_2$/ethanol film. The solution of the donor in toluene (or other solvents) flows from the bottle into the cell with a definite speed which is controlled via the flow meter as indicated in the picture. In this particular experiment the flow speed was maintained at 0.5 ml donor solution/min.*
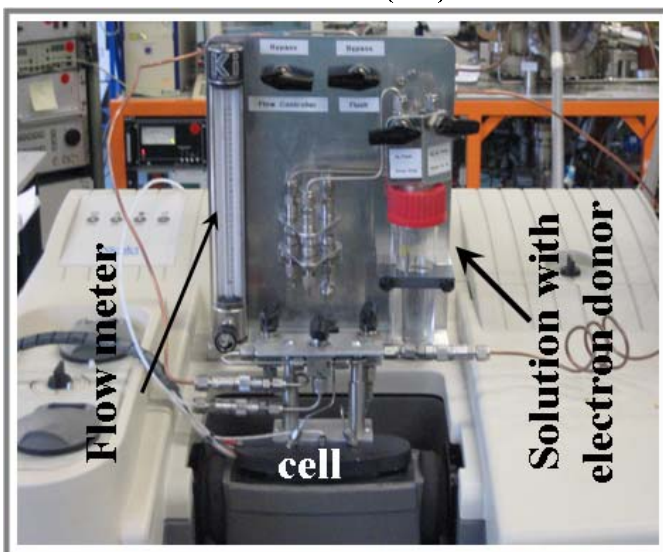
## 7.4.3 Discussion

Interactions of donors with MgCl$_2$ and TiCl$_4$ were studied by means of a new ATR-FTIR technique to obtain basic information about Ziegler-Natta catalysts. The most intense band of

the neat bis(methoxymethyl)fluorene diether donor was the C-O stretching vibration. While the C-O band maintained its position in solution in comparison to neat diether, upon complexation with $MgCl_2$ a downshift to lower wavenumbers was observed. The neat diether exhibits a C-O stretching frequency at about 1090 cm$^{-1}$, whereas upon coordination to $MgCl_2$ support, the C-O band appeared as a twin peak positioned at 1060 cm$^{-1}$ and 1039 cm$^{-1}$ manifesting the presence of $MgCl_2$/diether complex. Cui et al. [24] reported by means of IR spectroscopy that upon coordination of the bis(methoxymethyl)fluorene diether donor to a $MgCl_2$·2.5EtOH adduct, the C-O band downshifted from 1096 cm$^{-1}$ (free donor) to 1058 cm$^{-1}$ and 1035 cm$^{-1}$, which is in good agreement with our findings.

Upon treatment of the $MgCl_2$/diether complex with $TiCl_4$, the C-O bands underwent a minor downshift, whereas neat $TiCl_4$ strongly interacted with the diether donor, giving rise to C-O bands at 1016 cm$^{-1}$ and 994 cm$^{-1}$, also in good agreement with the results reported by Cui et al. [24]. The C-O bands of the 1:1 complex were reported to be 1020 cm$^{-1}$ and 997 cm$^{-1}$. The fact that the C-O band of the $MgCl_2$/diether complex experiences a minor downshift upon treatment with $TiCl_4$ indicates that the diether remains strongly coordinated to $MgCl_2$. Additionally, IR C-O stretching frequencies for $MgCl_2$/diether complexes at higher diether loadings (diether/$MgCl_2$ = 0.4) were coincident with the frequencies for the $MgCl_2$/diether complex at the standard loading (diether/$MgCl_2$ = 0.1) and completely different from those of diether/$TiCl_4$ complex, again indicating that the diether is coordinated to Mg in the Z-N catalyst and not to Ti species.

The ATR-FTIR spectra of neat EB and neat DIBP indicated that the most intense bands were the C=O stretching frequency along with C-C-O and O-C-C vibrations (often referred as to α-C-O). Upon coordination to $MgCl_2$ support, the C=O band of EB downshifted from ~1720 cm$^{-1}$ (neat EB) to 1686 cm$^{-1}$ indicating complex formation. This result is similar to the reported values in literature [11, 13, 15-18, 21-23]. The other observation in ATR-FTIR spectra of EB/$MgCl_2$ complexes (at standard and high content of EB i.e., EB/$MgCl_2$ = 0.2 and 1) was the appearance of the two new bands at 1327 cm$^{-1}$ and 1305 cm$^{-1}$ along with a strong attenuation of the C-C-O band (α-C-O) for the standard loading (EB/$MgCl_2$ = 0.2) and disappearance of the same band for the higher EB loading (EB/$MgCl_2$ = 1). These two bands have been observed for EB/$MgCl_2$ complexes by Chien et al. [15], Vizzini et al. [32] by means of IR and NMR spectroscopy, respectively, and by Bache et al. [16, 21] by means of

IR spectroscopy. Chien et al. [15] and Vizzini et al. [32] attributed the bands at 1327 cm$^{-1}$ and 1305 cm$^{-1}$ to α-C-O bands (C-C-O and O-C-C vibrations) which upon coordination to a MgCl$_2$ support have increased frequency. Their general observation was that the C=O stretching vibration in EB/MgCl$_2$ decreases in frequency, whereas the α-C-O bands increase in frequency upon complexation with MgCl$_2$. These authors asserted that EB coordinates to MgCl$_2$ through both oxygens. Ferreira and Damiani [12] also observed the same characteristic doublet and their interpretation was similar to this.

However, Bache et al. [16, 21] reported that all experiments involving EB complexation showed the same type of spectra. All spectra were characterized first and foremost by a negative shift of the C=O stretching frequency and a strong doublet at ca 1330/1305 cm$^{-1}$ (1327 cm$^{-1}$ and 1305 cm$^{-1}$ in this work), regardless of whether they were of well-defined stoichiometric complexes, or of ester-deficient catalyst supports.

These authors explained this observation by the scheme in Figure 7.19 [16]. The scheme shows the resonance hybridization for neat EB and for carbonyl and ether oxygen complexed to a Mg$^{2+}$-ion. The contributions from the right hand hybrids give rise in general to a strengthening of the α-C-O bond (C-C-O), a more nucleophilic character of the carbonyl oxygen and a more electrophilic character of the ether oxygen. Complexation of a metal ion on the carbonyl oxygen will increase the contribution from the right hand hybrid, hence increasing the double bond character of α-C-O (C-C-O), giving rise to the observed increase of the stretching frequency.
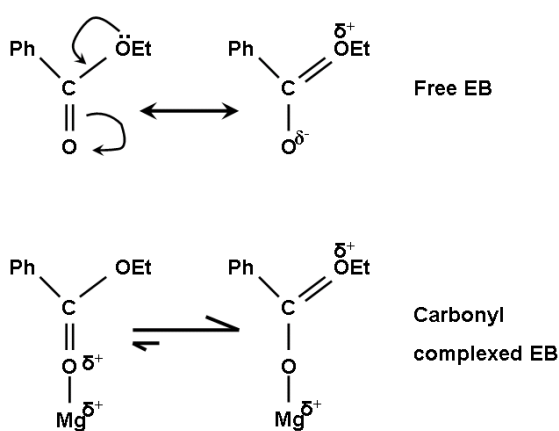


**Figure 7.19:** *Resonance stabilization of free EB and in probable complexes. The net effect of carbonyl complexation will be a weakening of the C=O bond and a strengthening of the to α-C-O bond (C-C-O) compared to the free ester giving rise to a negative and positive shifts for the frequency of the former and the latter band, correspondingly as observed in EB complexes [16].*

In other words, the scheme in Figure 7.19 explains the upshift of C-C-O vibration from ~1270 cm$^{-1}$ in neat EB to 1327 cm$^{-1}$ upon complexation with MgCl$_2$.

The upshift of the O-C-C band from 1110 cm$^{-1}$ in neat EB to 1305 cm$^{-1}$ upon complexation with MgCl$_2$ was explained by Bache et al. [16, 21] in a completely different way. In free EB the C-C-O skeletal mode couples mostly with the skeletal mode O-C-C at 1110 cm$^{-1}$. In the complex the C-C-O skeletal mode couples with the phenyl stretch at about 1314 cm$^{-1}$ (also present in the spectra in Figure 7.13) and some higher lying modes. Therefore, in neat EB the skeletal stretch O-C-C at 1110 cm$^{-1}$ is strong and the 1314 cm$^{-1}$ phenyl mode is rather weak, while in the complex the intensities are opposite. It is essential to note that the aforementioned doublet is a characteristic feature of all EB complexes i.e., TiCl$_4$/EB [20, 21] and Al(C$_2$H$_5$)$_3$/EB [19] and does not indicate two complexes. The authors based their conclusion on experiments carried out with deuteration of the phenyl ring [16, 21]. In this case the phenyl band is removed and only one strong band was found in the region 1300-1350 cm$^{-1}$.

It is reported in recent publications by Potapov et al. [22, 23] that IR spectra of carbonyl groups (C=O in EB and phthalates) of internal donors adsorbed on MgCl$_2$ could be best described as a superposition of several overlapping vibration bands from a variety of surface complexes.

Reaction of neat TiCl$_4$ with EB gave rise to a downshift of the C=O band at 1563 cm$^{-1}$ and 1591 cm$^{-1}$. Similar results were reported by Terano and Kataoka [11] for the same complex. However, after treatment of a EB/MgCl$_2$ complex with TiCl$_4$, the C=O band experienced only a minor downshift of the stretching frequency, implying that EB remains strongly coordinated to MgCl$_2$.

Another important observation from the FTIR spectra of the EB/MgCl$_2$ complexes was that ratios of 0.2 and 1 give similar shifts of the C=O band to lower stretching frequency. A donor/MgCl$_2$ ratio as high as 1:1 is not compatible with a support structure comprising, for example, hexagonal crystallites of MgCl$_2$ with coordination of the donor on surface sites, as such sites represent only a small fraction of the total Mg present. It is more likely that, at high donor/MgCl$_2$ ratios, the product has a chain-type structure, taking into account the fact that

2:1 adducts of (monodentate) Lewis bases and $MgCl_2$ comprise $MgCl_2$ chains with two molecules of Lewis base (LB) coordinated to each magnesium atom, as illustrated below [33].
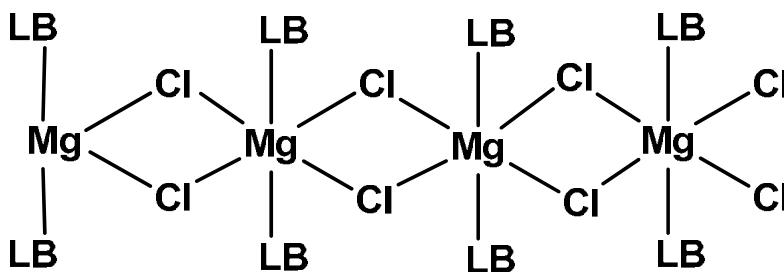


**Figure 7.20:** *Structure of adducts of composition MgCl₂·2LB (LB-Lewis base).*

The C=O band of DIBP upon complexation also shifted to lower stretching frequency from ~1720 $cm^{-1}$ (neat DIBP) to ~1695 $cm^{-1}$. Comparable values have been reported by Potapov et al. [23]. The shift to higher wavenumbers i.e., ~1320 $cm^{-1}$ of the C-C-O band upon complex formation with $MgCl_2$ can be explained with resonance structures similar to the $EB/MgCl_2$ complex in Figure 7.19. The $TiCl_4$(neat)/DIBP complex formation generated a downshift for the C=O band in the region 1640-1581 $cm^{-1}$. Comparable results have been reported in previous work [14]. Finally, in resemblance to diether/$MgCl_2$ and $EB/MgCl_2$ complexes, treatment of a DIBP/$MgCl_2$ film with $TiCl_4$ gave rise to a minor negative shift of the C=O band, indicating once more that DIBP stays coordinated to the $MgCl_2$ support. Furthermore, we demonstrated that in situ monitoring of DIBP coordination to a $MgCl_2$ support is also feasible. Here, we detected the co-existence of loosely coordinated DIBP species at ~1720 $cm^{-1}$ and strongly coordinated DIBP species at ~1695 $cm^{-1}$. Potapov et al. [22] reported for the $MgCl_2$/EB complexes the co-existence of 1649, 1675, 1697 and 1724 $cm^{-1}$ species in the C=O region.

## 7.4.4 Conclusions

The above ATR-FTIR results prove that diether and ester donors strongly coordinate to the $MgCl_2$ support, as observed by the downshift of the stretching frequencies for their functional groups upon complexation. The neat donors strongly interact with $TiCl_4$. However, after complexation of the donor with $MgCl_2$, subsequent treatment with $TiCl_4$ gave only minor

downshifts of the C=O and C-O bands, indicating that the donors remain strongly coordinated to the surface of $MgCl_2$.

# 7.5 ATR-FTIR of ethylene and propylene polymerizations

In this section, in situ experiments have been carried out to monitor ethylene polymerization and ex situ experiments have been performed to investigate propylene polymerization. An estimation of the isotacticity for the polypropylene produced with and without donor will be shown.

## 7.5.1 Experimental

### 7.5.1.1 Catalyst preparation and ATR-FTIR set up

The catalyst preparation is summarized in Figure 7.21. All manipulations of air- or water-sensitive compounds were carried out using standard Schlenk or glovebox techniques. A ZnSe ATR-IR crystal was spin coated with a solution of $MgCl_2$ in ethanol (42 mmol/L). Upon spinning, most of the liquid is ejected from the ZnSe surface, leaving behind a thin film of solution. The remaining solvent evaporates and the solute precipitates upon the ZnSe surface. The rotation speed applied was 2800 r.p.m.
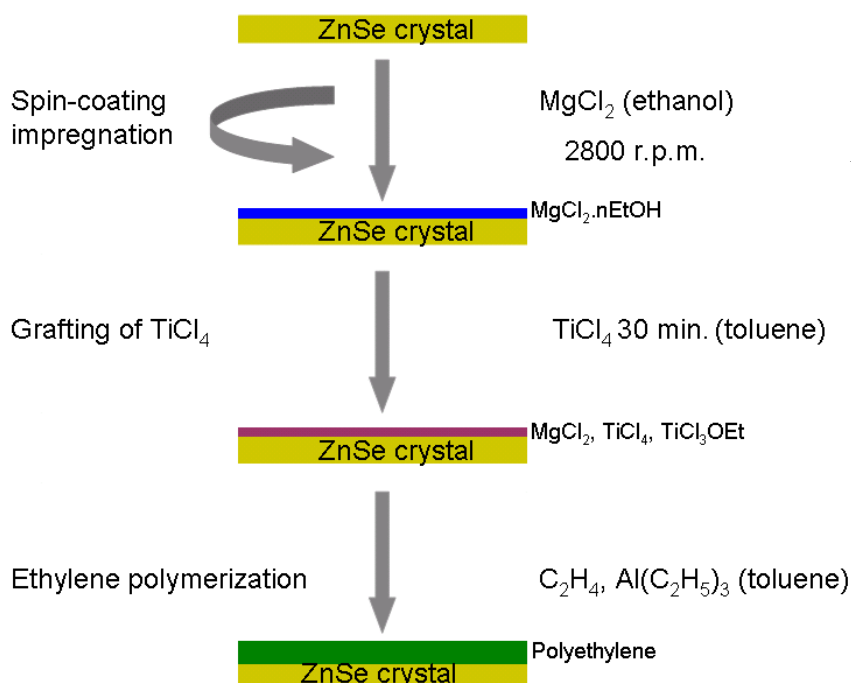


**Figure 7.21**: *Schematic representation of sample preparation for a Ziegler-Natta catalyst on a planar ZnSe surface for ethylene polymerization.*

The ZnSe crystal was afterwards dried under nitrogen and treated with $TiCl_4$. This treatment was carried out with a solution of 10 % v/v $TiCl_4$ solution in toluene at room temperature. After washing with toluene to remove the physisorbed $TiCl_4$, the model catalyst was dried under nitrogen. Thus the planar ZnSe crystal containing the immobilized catalytic components can be used for ethylene polymerization. Both the $TiCl_4$ treatment and the washing step took 30 min. unless stated otherwise. The cut-off of the ZnSe crystal is at 700 $cm^{-1}$.

The ZnSe ATR-IR crystal was assembled into the flow cell then closed/sealed and transferred afterwards to the ATR-FTIR set up. The time-resolved ATR-FTIR polymerization experiment at room temperature was performed as follows. Anhydrous benzene was introduced into the flow cell and a FTIR spectrum was collected for reference. In the meantime, a $Al(C_2H_5)_3$ solution in benzene (1 mg/mL) had been saturated with ethylene under a 2 bar pressure in a pre-reactor. After that, the $Al(C_2H_5)_3$ solution with ethylene was allowed to flow to the ATR flow cell at a speed of 20 g/h [34], which was the starting point of the reaction and collection of FTIR spectra. The data points of the collected spectra were the average of 4 scans at a spectral resolution of 4 $cm^{-1}$ and the spectra were automatically collected every 1 min. The ATR-FTIR flow cell set up has been described in **chapter two**. The FTIR spectra were collected using a Nicolet Protege 460 Fourier transform infrared spectrometer equipped with a heated HATR flow cell for Spectra-Tech ARK with a ZnSe $45^0$ crystal. Figure 7.22 displays a picture of the ZnSe crystal mounted on the spin coater along with a picture of the cell during ethylene polymerization.
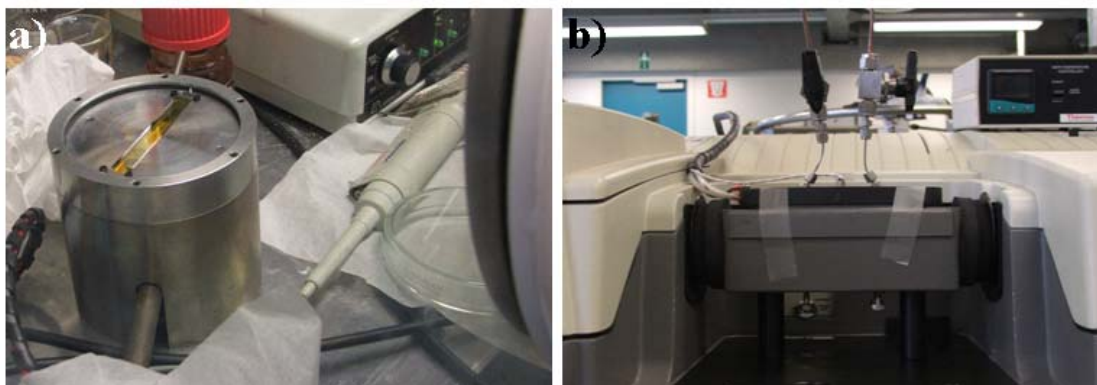


**Figure 7.22:** *a) ZnSe crystal mounted on the holder of the spin coater where spin coating can be applied. b) ZnSe crystal placed in the cell (closed/sealed in the glove box) during polymerization.*

In the case of the polypropylene, the polymerizations in this work were carried out in the glove box similar to those on a Si wafer. The ZnSe crystal was spin coated with a solution of $MgCl_2$ in ethanol, treated with $TiCl_4$ and polymerized in a Schlenk reactor in a solution of the cocatalyst at room temperature and 3 bar pressure. After polymerizations the ZnSe crystal was assembled into the flow cell then closed/sealed and transferred afterwards to the ATR-FTIR set up for measurements. The measurements were carried out using ZnSe as background.

## 7.5.2 Results

## 7.5.2.1 In situ ATR-FTIR of ethylene polymerization

Kinetic investigations of ethylene polymerization using supported catalysts are usually carried out using an indirect method by measuring the consumption of the ethylene gas [35, 36]. It is of interest to quantitatively monitor in real time the formation of the polyethylene inside the reactor. To this end, the ZnSe crystal, after deposition of $MgCl_2$ was treated with $TiCl_4$ and then polymerizations were allowed to run in the ATR-FTIR flow cell. Application of ATR-FTIR to monitor the vibrational bands of the PE offers the possibility to study the catalyst performance in its working state and acquire in situ information on the reaction kinetics.

ATR-FTIR results of a polymerization experiment using the Ziegler-Natta catalyst are shown in Figure 7.23. The polymerization was carried out in benzene, which has a clear window in the region 2800 to 2980 $cm^{-1}$. The model catalyst was initially treated with the solution of cocatalyst in benzene (carried out in situ in the cell) to remove ethanol/water present in the system, before starting the polymerization by introducing a cocatalyst solution saturated with ethylene (2 bar). Spectra collected during polymerization in this wavenumber region show the $CH_2$ asymmetric stretching band at 2917 $cm^{-1}$ and the symmetric stretching band at 2849 $cm^{-1}$ of polyethylene (Figure 7.23). These spectra have been measured every 1 min. The intensity of the band of 2917 $cm^{-1}$ is plotted versus polymerization time in Figure 7.24, where the intensity refers to the integrated area of the $CH_2$ stretching band in absorbance unit in the ATR-FTIR spectrum. The intensity of the $CH_2$ stretching band (2917 $cm^{-1}$) of polyethylene clearly increases with polymerization time. However, we cannot correlate the intensity of the ATR spectra directly with the polymerization rate. Since the evanescent ATR wave decays

with distance from the crystal surface (as described in **chapter two**), the intensity does not depend linearly on the thickness of the polymer layer.

In other words, the decay of the evanescent wave leads to saturated band intensity for thick polymer films. Therefore, to obtain kinetic information, a calibration curve of the dependence of the ATR-FTIR band intensity on the amount of the PE formed is needed. The amount of the PE formed on the crystal surface may be obtained by weight measurement or thickness determination. Our preliminary result of ATR-FTIR analysis during real-time polymerization demonstrates the future potential of the method to determine polymerization kinetics.
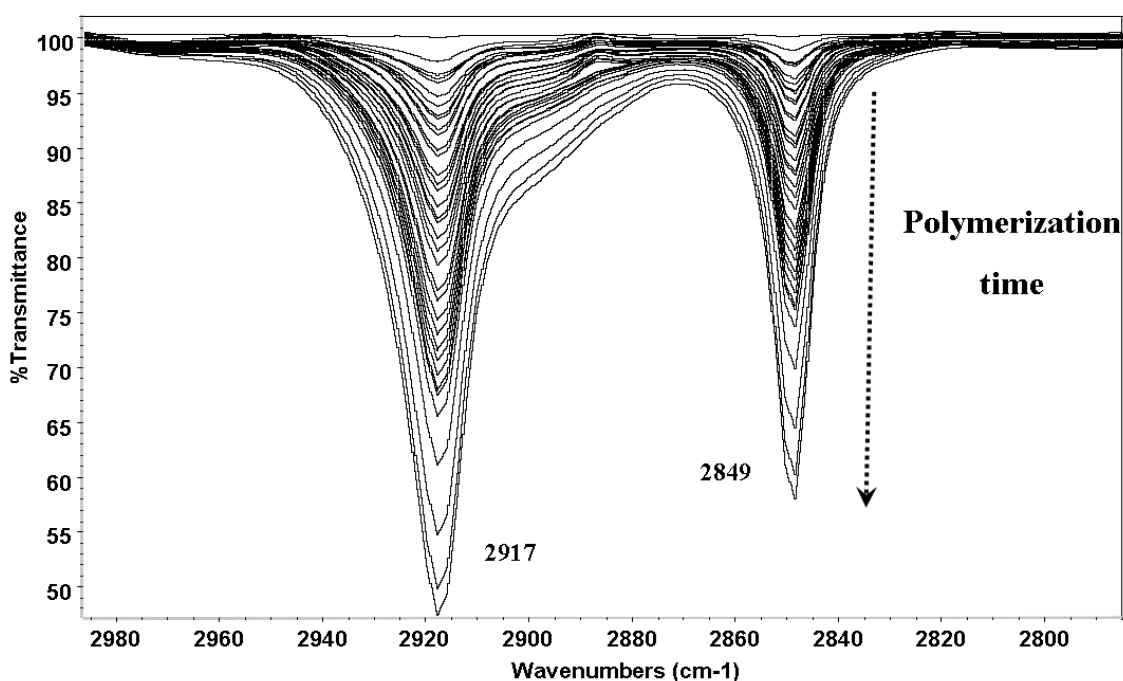


**Figure 7.23:** *Series of spectra of polyethylene growing on a flat ZnSe surface. Spectra are shown in the region of interest (asymmetric and symmetric band of CH₂).*
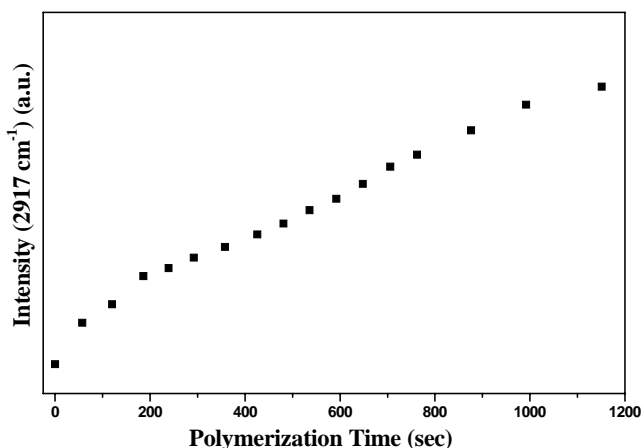


**Figure 7.24:** *Plot of the intensity of the band at 2917 cm⁻¹ versus polymerization time showing the increase in the intensity of CH₂ stretching bands of PE during polymerization.*

Additionally, polyethylene gives rise to a distinct doublet at 1473 cm$^{-1}$ and 1463 cm$^{-1}$ of the CH$_2$ bending region corresponding to the crystalline PE. In a former work of our group [34] the crystallinity of polyethylene grown from a supported iron catalyst has been investigated using ATR-FTIR. There, the polyethylene grown in situ on ZnSe was heated from room temperature to 145 $^0$C and then cooled back to room temperature at a rate of 1 $^0$C per min. In this way IR studies on pristine nascent polyethylene were reported for the first time.

## 7.5.2.2 Ex situ ATR-FTIR of propylene polymerization

ATR-FTIR spectroscopy offers the possibility of evaluating the isotacticity index (I.I.) of polypropylene. Figure 7.25 shows infrared spectra of 100 % isotactic polypropylene and 100 % atactic polypropylene. The absorption band at 995 cm$^{-1}$ is due to isotactic helices [37]. The band at 974 cm$^{-1}$ is independent of isotacticity [37].
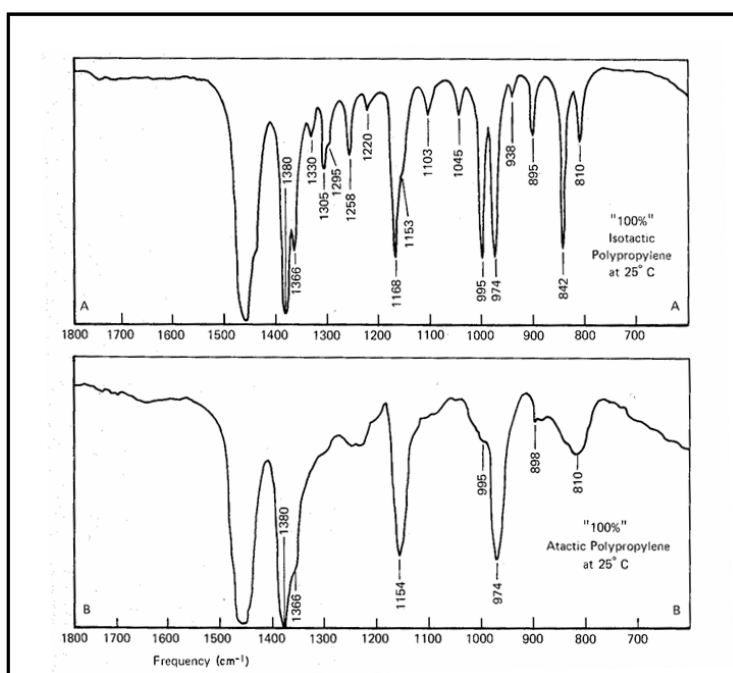


**Figure 7.25:** *Infrared spectra of 100 % isotactic (A) and 100 % atactic (B) polypropylene, both at 25 $^0$C [37].*

The propylene polymerizations in this work were carried out in the glove box similar to those on a silica/silicon wafer as noted in the experimental section. Polymerization was carried out in a Schlenk reactor in a solution of the cocatalyst for 24 hours at room temperature and 3 bar pressure. The thickness of the PP layer is less than 1 μm (**chapter four**).

When the diether donor was incorporated (diether/MgCl$_2$ = 0.1), propylene polymerization was run under the same conditions but for only 2 hours. The thickness of the PP layer is about 2-3 μm. Figure 7.26 shows spectra of polypropylene obtained with no internal donor incorporated (top spectrum) and polypropylene obtained when diether donor is incorporated (bottom spectrum). Both spectra reveal features similar to those of an IR spectrum of isotactic polypropylene (Figure 7.25, spectrum a). The band located at 997 cm$^{-1}$ (in our spectra), originating from isotactic helices of polypropylene (this band is due to the hybridized vibration of the methyl and methylene groups [38]), is present in both spectra. It is reported [39], that the volume fraction of long isotactic sequences is reflected in the intensity of this band. The intensity of this band is sensitive not only to the helical configuration but also to the long-range lateral packing.

The bands of solid isotactic polypropylene at 974 and 1167 cm$^{-1}$ [38] have been found to be due to the $\nu_a$ and $\nu_b$ vibrations which are schematically shown in Figure 7.27. These are the hybridized vibrations of the methyl rocking mode (asymmetric with respect to the H-C-methyl plane) and the asymmetric stretching mode of the main chain CH-CH$_2$ bonds (axial and equatorial) [38].

In the $\nu_a$ vibration (symmetric with respect to the screw axis) of isotactic polypropylene, these modes are excited in phase throughout the molecular chain as shown in Figure 7.27 (bottom). Then the vibrational modes of adjacent groups will tend to displace the common CH$_2$ groups in nearly the same direction, without bringing about strong coupling among CH(CH$_3$) groups in the chain [38]. The bands at 1458-1376 cm$^{-1}$ may arise from CH$_2$ scissoring [40]. The bands in the region 2949-2838 cm$^{-1}$ are attributed to asymmetric and symmetric CH$_2$ stretch.

The ratio of A$_{997}$/A$_{974}$ has been used as a measure of the tacticity [37-39, 41, 42]. Figure 7.28 again shows infrared spectra of polypropylene obtained without (spectrum a) and with a diether donor present during polymerization (spectrum b), showing the absorption band at 997 cm$^{-1}$ due to isotactic helices and absorption band at 974 cm$^{-1}$, along with the fitted curves (the inserted spectra) and a picture of the ZnSe crystal after propylene polymerization. Although not visually apparent from the Figure 7.28, our estimation in percentage (I.I. =

A$_{997}$/A$_{974}$ x 100) indicated around 60 % isotacticity for the polymer prepared in the absence of donor and around 80 % isotacticity for the polymer prepared in the presence of the diether.
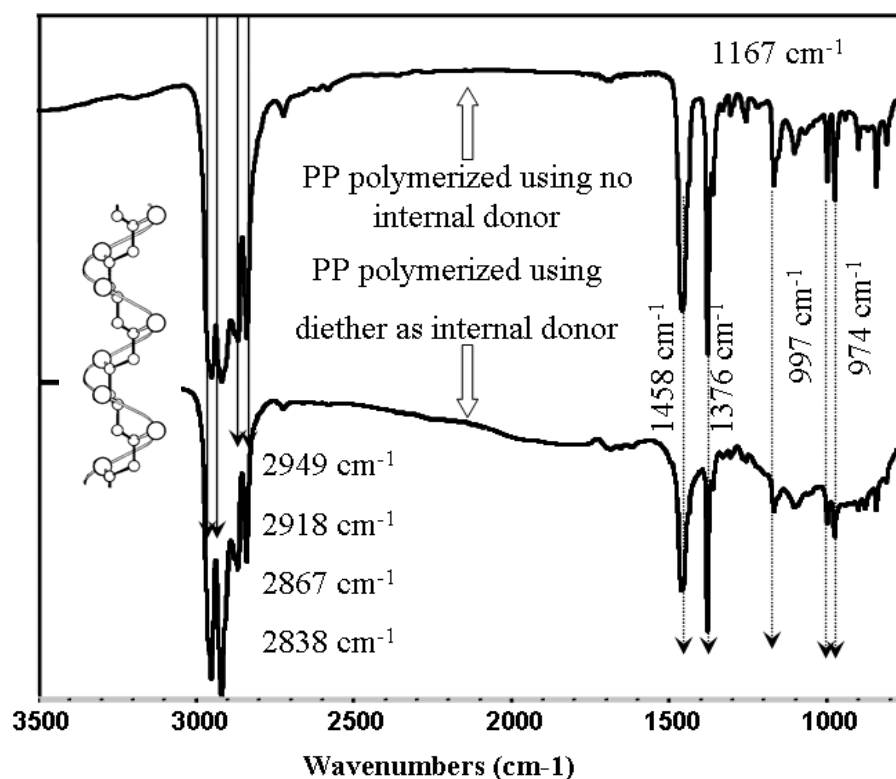


**Figure 7.26:** *Spectra of polypropylene obtained from a spin coated layer of MgCl$_2$/ethanol on ZnSe crystal (top spectrum, 24 hours polymerization) and polypropylene obtained from a spin coated layer of MgCl$_2$/diether/ethanol (diether/MgCl$_2$ = 0.1) on ZnSe crystal (bottom spectrum, 2 hours polymerization). The inserted structure represents chain model of isotactic PP showing the helix structure.*
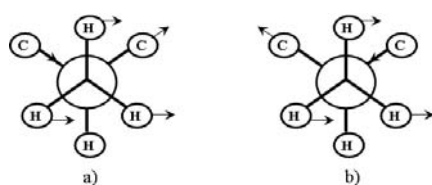


The atomic displacements of the v$_a$ and v$_b$ modes
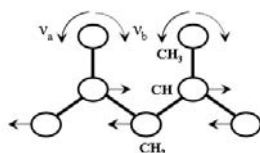
In-phase vibrations of the v$_a$ and v$_b$ modes of
-CH$_2$-CH(CH$_3$)-CH$_2$-CH(CH$_3$)-

**Figure 7.27**: *Schematic representation of v$_a$ and v$_b$ vibrations attributed to the bands at 974 and 1167 cm$^{-1}$ respectively [38].*

173

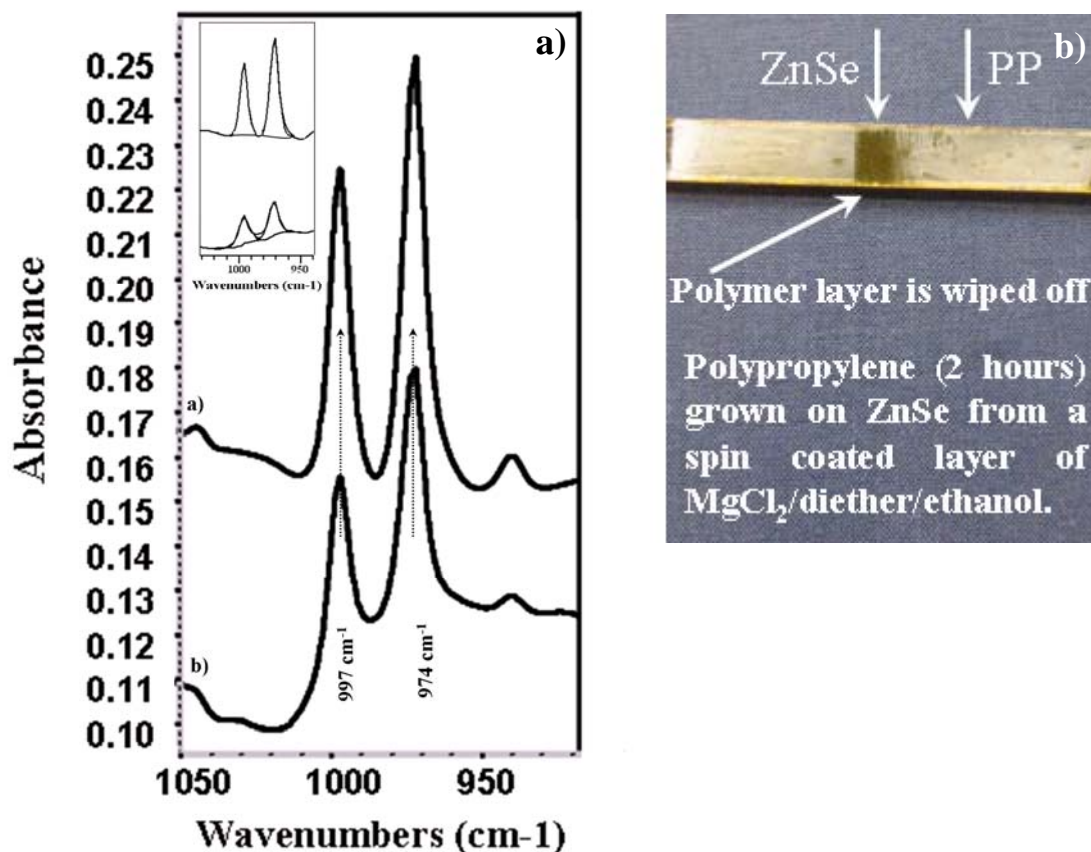**Figure 7.28:** *a) Infrared spectra of polypropylene including no donor during polymerization (spectrum a) and including a diether donor during polymerization (spectrum b) showing the absorption band at 997 cm⁻¹ due to isotactic helices and absorption band at 974 cm⁻¹. The inserted spectra show the fitted curves. b) Picture of ZnSe crystal after propylene polymerization (in the glove box).*

## 7.5.3 Discussion

Treatment of the spin coated MgCl$_2$ layer (on ZnSe crystal) from ethanol solution with TiCl$_4$ and subsequent contact with the cocatalyst resulted active for ethylene polymerization. In this manner a proof of principle was demonstrated regarding this new technique for the investigation of Z-N catalytic systems. Furthermore, this preliminary result of ATR-FTIR analysis during real-time polymerization demonstrated the future prospective of the current method to determine polymerization kinetics.

The attempt to estimate I.I. of the PP by means of ATR-FTIR with and without donor resulted in ~60 % isotacticity for polypropylene produced with no donor and ~80 % isotacticity when the donor of choice was diether. This results agree surprisingly well with the experimental reported values for PP produced with $MgCl_2/TiCl_4/AlR_3$ (I.I. = 40-60 %) and with $MgCl_2/TiCl_4/diether/AlR_3$ (fifth generation catalyst, I.I. = 95-98 %) [43]. It is essential to mention that the I.I. = 95-98 % of the PP for the fifth generation catalyst is obtained in propylene polymerization at around 70 °C and in the presence of hydrogen, factors which are known to increase the isotacticity [44]. Our polymerization was run at only ambient temperature without $H_2$.

## 7.5.4 Conclusion

We conclude that in situ ethylene polymerization and subsequently study by ATR-FTIR is also feasible for Ziegler-Natta catalytic systems. Furthermore the PP produced on ZnSe crystal (ex situ) could be easily analyzed by ATR-FTIR and an estimation of the isotacticity for the polypropylenes films obtained was possible.

## 7.6   General conclusions

Attenuated total reflection Fourier transform infrared spectroscopy (ATR-FTIR) can be applied to the detection of carbonyl and ether groups of electron donors in their free states and upon complexation with a $MgCl_2$ support for Ziegler-Natta catalysts. ATR-FTIR offers in this manner the application of a new method for in situ/ex situ experiments. It is established that coordination of the diether bis(methoxymethyl)fluorene and mono- and diester donors on $MgCl_2$ occurs via the functional groups C-O (ether) and C=O (esters). $TiCl_4$ and electron donors strongly interact with each other, but in the presence of $MgCl_2$ the donors strongly coordinate to the $MgCl_2$ support and remain relatively unperturbed by the presence of $TiCl_4$. ATR-FTIR can also be used to validate/estimate the isotacticity of polypropylene produced in a model catalytic system.

# References

1. E. Albizzati, U. Giannini, G. Collina, L. Noristi, L. Resconi, in: E.P. Moore Jr. (Ed.), Polypropylene Handbook. Polymerization, Characterization, Properties, Applications, Hanser Publishers, Munich-Vienna-New York, 1996, Ch. 2.

2. J.C. Chadwick, Macromol. Symp. 173 (2001) 21.

3. G. Cecchin, G. Morini, A. Pelliconi, Macromol. Symp. 173 (2001) 195.

4. S.A. Sergeev, G.D. Bukatov, V.A. Zakharov, E.M. Moroz, Makromol. Chem. 184 (1983) 2421.

5. M. Terano, T. Kataoka, T. Keii, in: T. Keii, K. Soga (Eds.), Catalytic Polymerization of Olefins, Kodansha-Elsevier, Amsterdam, 1986, p. 407.

6. P. Sormunen, T. Hjertberg, E. Iiskola, Makromol. Chem. 191 (1990) 2663.

7. M. Terano, M. Saito, T. Kataoka, Makromol. Chem. Rapid Commun. 13 (1992) 103.

8. V. Busico, P. Corradini, L. De Martino, A. Proto, V. Savino, E. Albizzati, Makromol. Chem. 186 (1985) 1279.

9. M.C. Sacchi, I. Tritto, C. Shan, R. Mendichi, L. Noristi, Macromolecules 24 (1990) 6823.

10. G.G. Arzoumanidis, N.M. Karayannis, Appl. Catal. 76 (1991) 221.

11. M. Terano, T. Kataoka, Macromol. Chem. 188 (1987) 1477.

12. M.L. Ferreira, D.E. Damiani, J. Polym. Sci. Part A: Polym. Chem. 32 (1994) 1137.

13. M. Terano, T. Kataoka, Macromol. Chem. Rapid Commun. 7 (1986) 725.

14. a) Y.-T. Jeong, D.-H. Lee, Macromol. Chem. 191 (1990) 1487. b) M. Terano, T. Kataoka, M. Hosaka, T. Keii, in: Transition Metals and Organometallics as Catalsyts for Olefin Polymerization, edited by W. Kaminsky and H. Sinn, Springer-Verlag, Berlin 1988, p. 56.

15. J.C.W. Chien, L.C. Dickinson, J.C. Vizzini, J. Polym. Sci. Part A: Polym. Chem. 28 (1990) 2321.

16. Ø. Bache, The Chemistry of $MgCl_2$-supported Ziegler-natta catalsyst studied by In situ Infrared spectroscopy, Ph.D. thesis, Institutt for uorganisk kjemi Norges Tekniske i Trondheim, Norway, 1994.

17. J.C.W. Chien, J.-C. Wu, C.-I. Kuo, J. Polym. Sci.: Polym. Chem. Ed. 21 (1983) 725.

18. M. Terano, T. Kataoka, J. Polym. Sci. Part A: Polym. Chem. 28 (1990) 2035.

19. R. Spitz, J.-L. Lacombe, M. Primet, J. Polym. Sci.: Polym. Chem. Ed. 22 (1984) 2611.

20. E. Rytter, Ø. Nirisen, M. Ystenes, H.A. Øye, Mikrochim. Acta. II (1988) 85.

21. Ø. Bache, M. Ystenes, Appl. Spec. 48 (1994) 985.

22. A.G. Potapov, G.D. Bukatov, V.A. Zakharov, J. Mol. Catal. A: Chem. 246 (2006) 248.

23. A.G. Potapov, G.D. Bukatov, V.A. Zakharov, Kinet. Catal. 48 (2007) 403.

24. N. Cui, Y. Ke, H. Li, Z. Zhang, C. Guo, Z. Lv, Y. Hu, J. Appl. Polym. Sci. 99 (2006) 1399.

25. G. Morini, A. Cristofori, Eur. Pat. 728724, Montell, invs.: 1996.

26. Infrared Spectral Interpretation: A Systematic Approach, B. Smith, CRC Press LLC, London, 1999.

27. V. Di Noto, R. Zannetti, M. Viviani, C. Marega, A. Marigo, S. Bresadola, Makromol. Chem. 193 (1992) 1653.

28. C.R. Tewell, F. Malizia, J.W. Ager III, G.A. Somorjai, J. Phys. Chem. B 106 (2002) 2946.

29. L. Brambilla, G. Zerbi, S. Nascetti, F. Piemontesi, G. Morini, Macromol. Symp. 213 (2004) 287.

30. L. Brambilla, G. Zerbi, F. Piemontesi, S. Nascetti, G. Morini, J. Mol. Catal. A Chem. 263 (2007) 103.

31. A.K. Yaluma, P.J.T. Tait, J.C. Chadwick, J. Polym. Sci. Part A Polym. Chem. 44 (2006) 1635.

32. J.C. Vizzini, J.-F. Shi, J.C.W. Chien, J. Appl. Polym. Sci. 48 (1993) 2173.

33. V. Di Noto, A. Marigo, M. Viviani, C. Marega, S. Bresadola, R. Zannetti, Makromol. Chem. 193 (1992) 123.

34. W. Han, Supported Homogenous Catalysts on Flat Model Surfaces for Ethylene Polymerization, Ph.D. thesis, Eindhoven University of Technology 2007.

35. F.A.R. Kaul, G.T. Puchta, H. Schneider, F. Bielert, D. Mihalios, W.A. Herrmann, Organometallics 21 (2002) 74.

36. N.V. Semikolenova, V.A. Zakharov, E.P. Talsi, D.E. Babushkin, A.P. Sobolev, L.G. Echevskaya, M.M. Khysniyarov, J. Mol. Catal. A: Chem. 182 (2002) 283.

37. J. Boor, Jr. Ziegler-Natta Catalysts and Polymerizations, Academic Press, New York, 1979, Ch. 3.

38. T. Miyazawa, Polym. Lett. 2 (1964) 847.

39. J.L. Koenig, A. Van Roggen, J. Appl. Polym. Sci. 9 (1965) 359.

40. D. Fregonese, A. Glisenti, S. Mortara, G.A. Rizzi, E. Tondello, S. Bresadola, G.A. Rizzi, E. Tondello, S. Bresadola, J. Mol. Catal. A: Chem. 178 (2002) 115.

41. D.R. Burfield, P.S.T. Loi, J. Appl. Polym. Sci. 36 (1988) 279.

42. T.I. Koranyi, E. Magni, G.A. Somorjai, Top. Catal. 7 (1999) 179.

43. G. Cecchin, G. Morini, F. Piemontesi, Kirk-Othmer Encyclopedia of Chemical Technology, vol. 26, 2001, p. 502.

44. J.C. Chadwick, G. Morini, G. Balbontin, O. Sudmeijer, Macromol. Chem. Phys. 199 (1998) 1873.

# Chapter 8

## Conclusions and outlook

## 8.1 Concluding remarks

Throughout this thesis we developed a realistic and active model for a Ziegler-Natta catalytic system that allows detailed study by XPS and ATR-IR (surface chemistry) and by AFM and SEM (catalyst and polymer morphology). The preparation of a Ziegler-Natta model catalyst on a flat Si wafer involved the spin coating of $MgCl_2$ from ethanol solution in an attempt to mimic an industrial catalyst preparation, in addition to allowing its characterization by the abovementioned techniques. The model catalyst was utilized to gain fundamental understanding, in particular with regard to the role of the donor molecules that are used to control the stereoselectivity of the catalyst in propylene polymerization.

The flat model was extensively tested for ethylene polymerization (**chapter three**). In this feasibility study, the construction of a realistic flat model of a Ziegler-Natta catalyst was demonstrated followed by basic characterization. The support and catalyst were visualized by utilizing AFM and found that the preparation via spin coating of $MgCl_2$ from ethanol solution generates grains/particles in the range 20-40 nm, close to the size of the primary particles of the support in an industrial catalyst. Elemental analysis obtained by XPS indicated loadings of Ti on the $MgCl_2$ support close to those of the industrial counterparts. Thick films of polyethylene, which grew perpendicular to the flat Si surface, were visualized by electron microscopy (SEM). Realistic polymerization activities were achieved.

The above model proved to be active also for propylene polymerization (**chapter four**). Polypropylene films were produced when no donor was incorporated, although in low yields. Incorporation of a diether donor in the $MgCl_2$/EtOH layer, however, greatly increased the yield of polypropylene, providing realistic activities under very mild conditions.

These studies established the feasibility of the model Ziegler-Natta catalyst preparation, but did not result in well-defined crystallites of magnesium chloride, necessary for the investigation of the crystal structure of the support in the absence and presence of electron

donors. It was therefore necessary to identify a method by which the spin coated support precursor, $MgCl_2 \cdot nEtOH$, could be converted by controlled crystal growth to well-defined $MgCl_2$ crystallites large enough to facilitate morphological characterization by AFM and SEM, and subsequently to identify polymer formation on the lateral faces of the crystallite (**chapter five**). Application of Ostwald ripening to the spin coated support precursor in the absence of the donor gave rise to the formation of well-defined and large crystallites. The growth of the crystallites in the presence of ethanol vapors (Ostwald ripening) clearly indicated the abundant formation of $120^0$ edge angles and the occasional appearance of $90^0$ edge angles, according to AFM imaging. This result evidently indicated the preference for the formation of a particular crystallite face. The polymer grew preferentially on the edges of the crystallites according to SEM imaging and proved the presence of the active site precursor, $TiCl_4$ or $TiCl_n(OEt)_{4-n}$.

The incorporation of internal donors such as 9,9–bis(methoxymethyl)fluorene, diisobutyl phthalate and ethyl benzoate in the formation of magnesium chloride crystallites greatly affected the geometry of the catalyst support (**chapter six**). Formation of exclusively $120^0$ edge angles in the presence of the diether donor, as observed by AFM and SEM, suggested a preference for the formation of one particular crystallite face for the $MgCl_2$. In contrast, the presence of diisobutyl phthalate or ethyl benzoate promoted the formation of both $120^0$ and $90^0$ edge angles, indicative of the formation of more than one face for the $MgCl_2$. The effect of the diether in promoting the formation of, most probably, the (110) face of $MgCl_2$ provided an explanation for the high activity and relatively uniform nature of the active species in Ziegler-Natta catalysts of type $MgCl_2/TiCl_4$/diether. In contrast to polyethylene, polypropylene formed exclusively on the crystal edges of the crystallite.

Unfortunately, no direct assignment of surface edges was possible for $MgCl_2$/EtOH and $MgCl_2$/donor/EtOH crystallites by means of TEM/electron diffraction (as it will be explained below). These results were as yet qualitative rather than quantitative. However, they provided strong evidence that the dependence of the distribution of active species in Ziegler-Natta catalysts for polypropylene on the nature of the internal donor is related to the ability of the donor to steer the formation of a particular $MgCl_2$ crystallite face during catalyst preparation.

Attenuated total reflection Fourier transform infrared spectroscopy (ATR-FTIR) proved, as a new technique in this field, to be a valuable tool in studying the chemistry of Ziegler-Natta catalysts (**chapter seven**). It was established that the coordination of the diether bis(methoxymethyl)fluorene and mono- and diester donors on $MgCl_2$ takes place via the functional groups C-O (ether) and C=O (esters). $TiCl_4$ and electron donors strongly interacted with each other, but in the presence of $MgCl_2$ the donors strongly coordinate to the $MgCl_2$ support and remain relatively unperturbed by the presence of $TiCl_4$. Estimation of the isotacticity of polypropylene produced on the planar model catalytic system was achievable.

## 8.2    Future perspectives

The final target of this project was to identify crystallographic indexes of the lateral terminations of $MgCl_2$, in addition to sufficient confirmation of their existence. While the latter was successfully verified, the former was not achieved. However, we successfully developed a variation of the planar model system which is suitable for Transmission Electron Microscopy (TEM) studies. Indeed, construction of a special TEM grid has enabled TEM analysis on flat silica/silicon wafers. The silica TEM substrate is composed of a silica window suspended in a silicon framework [1]. The silica window permits the transmission of the electron beam. In other words TEM grids not only facilitate imaging on a flat model catalyst but they can serve as a catalytic support as well.

Unfortunately all efforts to indentify the crystallographic orientation of the active surfaces by employing TEM were as yet unsuccessful, probably due to the remaining ethanol, which rendered the crystallites unstable under the intense beam. Figure 8.1 (left panel) gives a schematic representation of the TEM grid along with a picture of the TEM substrate. Figure 8.1a shows a TEM image of the grid containing $MgCl_2$ crystallites, along with a crystallite edge of $MgCl_2$ obtained by the Ostwald ripening process. In the adjacent AFM images (Figure 8.1b) we have attempted to visualize $MgCl_2$ crystallites obtained by mimicking the Bridgman-Stockbarger technique, which is also a method of growing single crystals [2]. The method involves heating crystalline material in a container above its melting point and slowly cooling it from one end where a seed crystal is located.
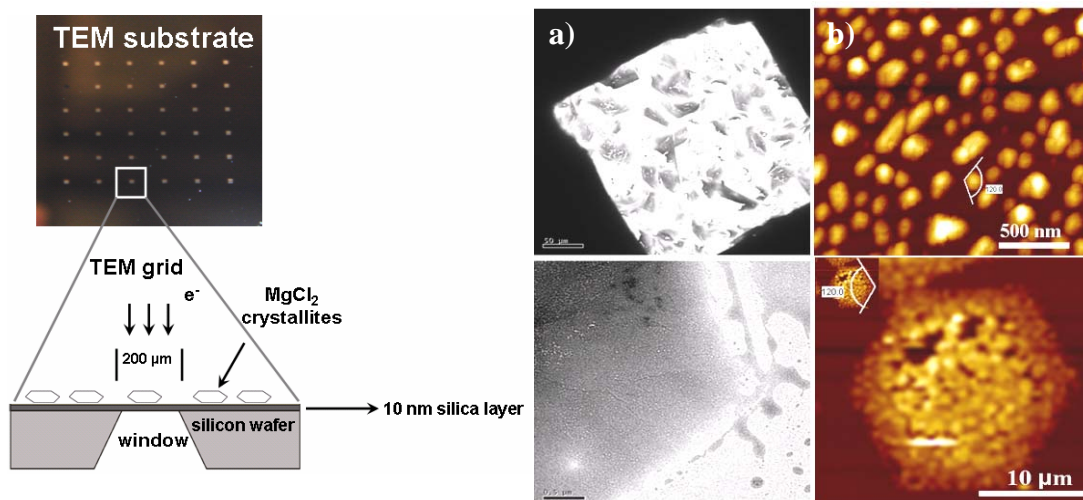
**Figure 8.1**: *Schematic representation of TEM grid along with TEM images of MgCl₂ crystallites obtained by Ostwald ripening process and AFM images of MgCl₂ crystallites obtained by mimicking the Bridgman-Stockbarger technique along with angle measurements.*

The small crystallites in Figure 8.1b (top image) were obtained by heating a 12 nm spin coated layer of $MgCl_2$/ethanol to high temperature (770 $^0$C), followed by cooling slowly to room temperature. The bottom image, on the other hand, represents a large crystallite of $MgCl_2$ obtained by heating, to a similarly high temperature, droplets of supersaturated $MgCl_2$ in ethanol, followed by slow cooling.

This method leads to crystallites which are probably free of ethanol and therefore easy to analyze by TEM. Although the "true" structure of the small crystallites (visualized by AFM) can be identified by TEM, the large hexagonal crystallite formed by heating to high temperature droplets of supersaturated $MgCl_2$ in ethanol clearly suffered from the presence of excess ethanol. The latter induces the formation of a porous structure (basal plane), which arises upon evaporation of the ethanol at elevated temperature. However, the formation of hexagonal structure evidently proves that the Bridgman-Stockbarger technique can be a promising method to prepare well-defined $MgCl_2$ crystallites. Instead of heating/melting a spin coated layer of $MgCl_2$/EtOH, an excellent substrate can also be a fine powder of neat $MgCl_2$ (ground or milled) on a planar Si surface or TEM grid. In this case well-defined crystallites of $MgCl_2$ free of ethanol can be prepared, allowing investigation/identification of the crystallographic orientation of the active surfaces. TEM studies have been carried out by

Mori et al. [3]. These authors prepared MgCl$_2$-supported Ziegler-Natta catalysts by grinding neat MgCl$_2$ with TiCl$_4$.

As a final thought, throughout this thesis the uses and possibilities offered by the planar model for the investigation of Ziegler-Natta catalysts have been shown. The most important achievement of this work was the identification of a novel method to convert small grains/particles of MgCl$_2$/EtOH into large and well-defined crystallites, which allowed morphological characterization by scanning electron and microscopy techniques, and subsequently easy identification of polymer formation on the lateral faces of the crystallites. Obviously, further studies are needed to achieve the final target (i.e., identification of the crystallographic indexes of the active surfaces) but we believe that this work offers new opportunities which hold great potential for further and complete characterization of MgCl$_2$-supported Ziegler-Natta catalysts.

## References

1.  F. Enquist, A. Spetz, Thin Solid Film, 145(1) (1986) 99.
2.  http://en.wikipedia.org/wiki/Bridgeman_technique.
3.  H. Mori, M. Sawada, T. Higuchi, K. Hasebe, N. Otsuka, M. Terano, Macromol. Rapid Commun. 20 (1999) 245.

# Summary

Throughout the evolution of Ziegler-Natta olefin polymerization catalysts, considerable efforts have been made to characterize the surface chemistry, structural and morphological aspects of the $MgCl_2$ support/catalyst which are known to greatly affect the performance and catalyst activity. The theme of this thesis was to develop an active and realistic model for a $MgCl_2$-supported Ziegler-Natta polymerization catalyst. This model offers unique possibilities for characterization of the surface chemistry and morphology of both support and catalyst by surface science and microscopic techniques.

In this thesis an active model was described for a $MgCl_2$-supported Ziegler-Natta polymerization catalyst, prepared by spin coating of a $MgCl_2$ solution in ethanol on a flat silica/silicon surface and subsequent treatment with $TiCl_4$. The support and catalyst were visualized employing surface microscopic techniques under inert conditions. The chemistry involved in this approach resembled that involved in industrial catalyst synthesis. The results showed that a supported Ziegler-Natta catalyst on the flat silica/silicon surface can serve as an excellent model for the real catalyst system and allows fundamental insight into the surface chemistry and morphological aspects of both the catalyst and the nascent polymer (**chapters three** and **four**).

Further a method was described for the preparation of well-defined crystallites of $MgCl_2$-supported Ziegler-Natta catalysts on Si wafers aiming to investigate the surface structure of the support material. This was achieved by the spin coating of a $MgCl_2$ solution onto a flat Si wafer, followed by controlled crystal growth to give well-defined $MgCl_2 \cdot n$EtOH crystallites. This work was a successful attempt to visualize the crystallite face(s) of $MgCl_2$ on a flat surface and to identify polyethylene formation preferably on the lateral faces of these crystallites (**chapter five**).

The same model was utilized for a Ziegler-Natta propylene polymerization catalyst which was prepared by spin coating of a $MgCl_2$/donor solution in ethanol on a flat silica/silicon wafer, followed by crystal growth by Ostwald ripening to give well-defined $MgCl_2 \cdot$donor$\cdot n$EtOH crystallites. The aim was to investigate to what extent the formation of a particular crystallite face of $MgCl_2$ is dependent on the type of internal donor present during

the formation of the support. Significant differences between diether and ester donors were found. The presence of a diether generated exclusively hexagonal crystallites with $120^0$ edge angles, whereas the use of ethyl benzoate or diisobutyl phthalate lead to the formation of crystallites with $120^0$ and $90^0$ edge angles. The results provided strong evidence that the use of a diether, as opposed to an ester, in Ziegler-Natta catalyst preparation promotes the selective formation of most probably the (110) face of $MgCl_2$. There is increasing evidence that the most active and stereospecific species are also formed on this crystallographic face, and we believe that the present results provide an explanation for the different activities and characteristics of $MgCl_2/TiCl_4$/diether and $MgCl_2/TiCl_4$/ester catalysts for polypropylene. In propylene polymerization, polymer formed exclusively on the lateral faces of $MgCl_2$ crystallites formed in the presence of the various donors (**chapter six**).

Finally, ATR-FTIR was utilized as new technique for the characterization of Ziegler-Natta catalytic systems. It was showed that coordination of the internal donors onto $MgCl_2$ supports occurs via their functional groups and proved that in situ investigations of donor coordination and olefin polymerization on model $MgCl_2$ supports and catalysts is possible (**chapter seven**).

# Samenvatting

Gedurende de evolutie van Ziegler-Natta katalysatoren voor olefinepolymerisatie zijn vele pogingen gedaan om inzicht te verkrijgen in de karakteristieke eigenschappen van $MgCl_2$ dragers die het gedrag van de katalysator, en vooral de katalysatoractiviteit, beïnvloeden. Het is bekend dat zowel het oppervlak als de morfologie van de drager een grote invloed kan hebben. Het doel van het onderzoek beschreven in dit proefschrift was het ontwikkelen van een actief en realistisch model voor een $MgCl_2$-gedragen Ziegler-Natta polymerisatiekatalysator. Dit model biedt unieke mogelijkheden voor karakterisering van het oppervlak en de morfologie van zowel de drager als de katalysator, door middel van spectroscopische en microscopische technieken.

In dit proefschrift is een actief model voor een $MgCl_2$-gedragen Ziegler-Natta katalysator beschreven. De katalysator is bereid door middel van spin coating van een oplossing van $MgCl_2$ in ethanol op een vlak silica/silicium oppervlak, gevolgd door behandeling met $TiCl_4$. De drager en katalysator oppervlaktes zijn bestudeerd met behulp van microscopische technieken onder inerte condities. De betreffende chemie in deze benadering is nauw verwant aan die van een industrieel gesynthetiseerde katalysator. De resultaten laten zien dat een Ziegler-Natta katalysator, gedragen op een vlak silica/silicium oppervlak, als een uitstekend model voor het echte katalysatorsysteem kan fungeren. Daardoor kon fundamenteel inzicht in de oppervlaktechemie en morfologische aspecten van zowel de katalysator als de vorming van polymeer worden verkregen (**hoofdstukken drie** en **vier**).

Verder is een methode voor de bereiding van goed gedefinieerde kristallieten van $MgCl_2$-gedragen Ziegler-Natta katalysatoren op plak Si ontwikkeld, om bestudering van de oppervlaktestructuur van het dragermateriaal mogelijk te maken. Dit werd bereikt door een oplossing van $MgCl_2$ te spin coaten op een vlakke Si wafel, gevolgd door gecontroleerde kristalgroei tot goed gedefinieerde $MgCl_2 \cdot n$EtOH kristallieten. Dit werk was een succesvolle poging om de kristalvlakken van $MgCl_2$ op een egaal oppervlak te visualiseren en om de vorming van polyethyleen te identificeren, vooral op de laterale vlakken van deze kristallieten (**hoofdstuk vijf**).

Hetzelfde model is gebruikt voor een Ziegler-Natta katalysator voor propeenpolymerisatie, gesynthetiseerd door een oplossing van $MgCl_2$ te spin coaten op een vlakke silica/silicium schijf, gevolgd door kristalgroei door middel van "Ostwald ripening" om goed gedefinieerde $MgCl_2 \cdot donor \cdot n$EtOH kristallieten te verkrijgen. Het doel van dit werk was om na te gaan in hoeverre de vorming van een bepaald kristallijn vlak van $MgCl_2$ afhankelijk is van het type interne donor die aanwezig is tijdens de vorming van de drager. Significante verschillen tussen diether and ester donoren zijn gevonden. De aanwezigheid van een diether leidt tot de exclusieve vorming van hexagonale kristallieten met hoeken van $120^0$, terwijl het gebruik van ethylbenzoaat of diisobutylftalaat leidt tot de vorming van kristallieten met zowel $120^0$ als $90^0$ hoeken. Op basis van deze resultaten lijkt het waarschijnlijk dat in de bereiding van een Ziegler-Natta katalysator het gebruik van een diether, in tegenstelling tot een ester, bevordelijk is voor de selectieve vorming van (waarschijnlijk) het (110) vlak van $MgCl_2$. Er zijn steeds meer aanwijzingen dat de meest actieve en stereospecifieke centra ook op dit vlak worden gevormd, waarbij wij geloven dat de huidige resultaten de verschillende activitieten en karakteristieke eigenschappen van $MgCl_2/TiCl_4/$diether en $MgCl_2/TiCl_4/$ester katalysatoren voor polypropeen kunnen verklaren. In propeenpolymerisatie werd polymeer alleen op de laterale vlakken van de $MgCl_2$ kristallieten gevormd in de aanwezigheid van de verschillende donoren (**hoofdstuk zes**).

Tenslotte werd ATR-FTIR gebruikt als nieuwe techniek voor de karakterisering van Ziegler-Natta katalysatorsystemen. Wij hebben laten zien dat coördinatie van interne donoren op een $MgCl_2$ drager plaats vindt via hun functionele groepen en dat in situ onderzoek van donorcoördinatie en olefinepolymerisatie op model $MgCl_2$ dragers en katalysatoren mogelijk is (**hoofdstuk zeven**).

# Përmbledhje

Gjatë zhvillimit të katalizatorit Ziegler-Natta për polimerizimin e etenit dhe propilenit janë bërë përpjekje të shumta për të karakterizuar kiminë e sipërfaqes, strukturën dhe morfologjinë e mbartësit të katalizatorit $MgCl_2$. Këta të fundit janë edhe faktorët kryesorë, të cilët influencojnë në mënyrë të fuqishme aktivitetin dhe efektivitetin e katalizatorit. Qellimi i kësaj teze ishte zhvillimi i një modeli aktiv dhe real për $MgCl_2$ si mbartës të katalizatorit Ziegler-Natta. Ky model krijon një mundësi unike per karakterizimin e kimisë së sipërfaqes dhe morfologjisë së $MgCl_2$ nëpërmjet teknikave të shkencës së sipërfaqes dhe atyre të mikroskopëve elektronikë.

Në këtë tezë, përshkrohet një model aktiv për $MgCl_2$-mbartës të katalizatorit Ziegler-Natta për polimerizimin duke përdorur teknikën e "rrotullo-veshjes" (spin coating). Për këtë u përdor një solucion i $MgCl_2$ në etanol, i cili u depozitua mbi një sipërfaqe të sheshtë të siliciumit ose silicium dioksidit, ndjekur nga trajtimi me $TiCl_4$. Imazhet e mbartësit ($MgCl_2$) dhe katalizatorit ($MgCl_2/TiCl_4$) u morën duke përdorur teknikat e mikroskopëve elektronikë të sipërfaqes në kushte inerte. Kimia e përdorur në këtë model është shumë e ngjashme me sintezën e katalizatorëve që përdoret në industri. Rezultatet treguan që depozitimi i mbartësit $MgCl_2$ mbi siliciumin e sheshtë shërben si një model i shkëlqyer për sistemet reale katalitike, si dhe lejon një studim të thellë të kimisë së sipërfaqes dhe aspekteve morfologjike të katalizatorit dhe polimerit (**kapitujt tre** dhe **katër**).

Më tutje në këtë tezë është përshkruar një metodë për përgatitjen e kristaleve të mbartësit ($MgCl_2$) me formë të definuar mbi silicium, duke synuar në këtë mënyrë studimin e strukturës së materialit mbartës. Kjo gjë u arrit duke përdorur në fillim teknikën e "rrotullo-veshjes", e ndjekur nga metoda e rritjes së kristaleve në mënyrë të kontrolluar. Ky kërkim shkencor ishte një përpjekje e suksesshme për vizualizimin e faqeve kristalore të $MgCl_2$ mbi një sipërfaqe të sheshtë, si dhe për identifikimin/formimin e polietilenit në mënyrë të definuar në faqet anësore të kristaleve (**kapitulli i pestë**).

Në këtë tezë u përdor i njëjti model për polimerizimin e propilenit nëpërmjet katalizatorit Ziegler-Natta si edhe e njëjta teknikë ("rrotullo-veshjes") për depozitimin e $MgCl_2$/elektron-dhënës. Për këtë u aplikua i njëjti solucion (në etanol) mbi siliciumin planar, pasuar nga

proçesi i rritjes së kristaleve (proçesi Ostwald) për të formuar kristale të definuara të MgCl$_2$·elektron-dhënës·$n$EtOH. Qëllimi ishte të studiohej roli që luajnë elektron-dhënësit (dieter dhe esterëve) në formimin e faqeve kristalore të MgCl$_2$. Ndryshime të mëdha u vunë re mes dieterit dhe esterëve. Ndërsa prezenca e dieterit çoi në formimin e kristaleve hegzagonalë me kënde 120$^0$, prezenca e esterëve (EB dhe DIBP) çoi në formimin e këndeve 120$^0$ dhe 90$^0$. Këto rezultate treguan qartë që përdorimi i dieterit, në dallim nga esteri, nxit formimin në mënyrë selektive të faqes më të mundshme (110) të MgCl$_2$. Rezultatet eksperimentale treguan se speciet më aktive dhe më stereospecifike janë formuar në këtë faqe kristalografike. Kjo është edhe arsyeja që rezultatet e kësaj teze japin një shpjegim për karakteristikat dhe aktivitetet e ndryshme të MgCl$_2$/TiCl$_4$/dieter dhe MgCl$_2$/TiCl$_4$/ester katalizatorë për prodhimin e polipropilenit. Gjatë polimerizimit të propilenit, polipropileni u formua në mënyrë ekskluzive në faqet anësore të MgCl$_2$, të cilat u gjeneruan në prezencën e elektron-dhënësve (**kapitulli i gjashtë**).

Së fundi, ATR-FTIR (Attenuated Total Reflectance-Furier Transformim Infrared) u përdor si teknikë e re për karakterizimin e sistemeve katalitike Ziegler-Natta. Me këtë tezë u tregua, që elektron-dhënësit kordinohen tek MgCl$_2$ nëpërmjet grupit funksional C=O (esters) dhe C-O (dieter), dhe se eksperimentet *in situ* janë të mundura për elektron-dhënësit dhe polimerizimin e etenit dhe propilenit me modelin MgCl$_2$ mbartës dhe katalizator (**kapitulli i shtatë**).

# Acknowledgments

I would like to express my profound gratitude to John (my second co-promoter) for being my optimal guide throughout this PhD. John, your contribution was indispensable! I would also like to express my appreciation to my supervisor Hans and first co-promoter Peter whose constant support and insights have guided me in my scientific pursuits.

I am indebted to the Dutch Polymer Institute (DPI) for its financial support (project #387). In particular, I would like to express my gratitude to Prof. Vincenzo Busico for his support, encouragement and scientific input throughout this PhD. Vincenzo, grazie di cuore. I am grateful to Dr. Jan Stamhuis (Programme Area Coordinator Polyolefins) for his willingness to financially support the invited front cover on Macromolecular Rapid Communication. I additionally thank all the industrial contact people related to my project. The DPI meetings in Schiphol definitely contributed to the success of this project.

I am grateful to Prof. Rutger van Santen for his support in my admission as the first Albanian student in this university. I thank Dr. Tonek Jansen for his guidance during the time I worked with the Theoretical Chemistry group. I am grateful to Dr. Jan Coumans for his guidance throughout my master's program.

Dr. Sasha Alexeev and Dr. Denis Ovchinnikov are greatly acknowledged for their help with the AFM measurements. I am thankful to: Adelheid Elemans-Mehring for her assistance with the ICP measurements, Dr. Joachim Loos for performing the TEM measurements, Dr. Marc van Maris for the SEM instructions.

I thank the members of the Theoretical Chemistry group for their help and support throughout my first and difficult year in the Netherlands in 2001. I would like to express my appreciation to Xavier R. for his willingness to help whenever needed. I wish you and Angelique all the best. I thank Chrétien, Bouke, Cristina and Joost for all the enjoyable coffee breaks and conversations during my graduation project and PhD time. Aan Mabel en Jos, hartelijk bedankt voor alles. Mabel, as always I will keep smiling! Joyce, hartelijk dank ook aan jou. Ik wens jou en Rob het allerbeste toe.

Many thanks to all the members of our Surface Science group past and present. STW 3.59 was my early location. And I remember it like this: Davy always calm and having everything under control (veel succes met alles); Han Wei very active, so much like a Kung Fu fighter; Eero the philosopher, trying to figure out the mystery of life; Emiel kind and helpful; Abdool cheerful (while Armando was in search for him) and CP (Vinod) very calm; Ben Nieuwenhuys always present in our group meetings; Sander drinking coffee and preparing himself for the long and

demanding EELS measurements. Sander, EELS was hard werken maar ik heb ervan genoten. Ik heb veel van je geleerd. Jouw toegewijde hulp is zeer gewaardeerd. Bedankt voor alles.

Then I moved to a new location, STW 3.49. While Sander started his job at Shell, Freek took over his desk and Emiel began to write his thesis. Freek en Emiel, ik heb een leuke en gezellige tijd met jullie gehad. Onze vrolijke gesprekken waren altijd ontspannen. Ik zal de aanstekelijke lach niet vergeten. Dankzij jullie werd mijn Nederlands verbeterd. Hartelijk bedankt voor alles. Freek, jij was het langst mijn kamergenoot. Gedurende de afgelopen vier jaar was je zeer behulpzaam. Bedankt daarvoor en wees altijd energiek. Ik wens je veel succes met het afronden van jouw project en promotie. I thank Noor for her lively presence in our room. Noor, I wish with all my heart that all your dreams and wishes come true. Verder wil ik ook Maarten bedanken, die altijd bij ons langs kwam. Maarten, ik zal je altijd als een harde werker herinneren. Aardig en vriendelijk. Ik wens je ook veel succes met je promotie. Verder wens ik Gilbère veel succes met het promotieonderzoek. Bedankt voor de verse koffie (samen met Freek) die iedere ochtend klaarstond.

I would like especially to thank the sub-group of the model catalysts (flat model approach). Emiel and Han Wei, your help when I started is greatly appreciated. You made everything easier. I will certainly remember the great time in Italy (Napoli and Roma). Han Wei, you were indeed an excellent guide. Svetlana, bedankt ook aan jou. Ik wens je veel succes met het afronden van jouw project en promotie.

Then Denzil and Prabashini joined the group. Guys, your friendship is invaluable to me. Thank you for everything. I really hope that in the near future I will be able to come and pay you a visit in South Africa. Prabs, I hope I will be around for your defence (much success with finalizing the thesis). Special thanks go to Neelesh and Dilip for the pleasant dinners and conversations. They will be remembered and cherished. Guys, I wish you both all the best.

Further I thank Ashriti and Gregory for their hospitality. I enjoyed the dinner at your place, surrounded by the lively presence of little Suhina. Good luck with finalizing the thesis.

I kindly thank Vijay for always taking time to answer all my work related questions. I certainly enjoyed the very tasty Indian food your wife prepared for us (the Moodleys and I). I wish you and your family all the best. Lianne, Ik wens je veel succes in de toekomst. I wish Akhtar much success with the completion of his PhD.

Verder wil ik Merijn bedanken, mijn eerste en enige student. Merijn, bedankt voor je bijdrage. Ik wens je veel succes met je promotie.

# List of publications

**Chapter three:**

**Adelaida Andoni**, John C. Chadwick, Stefania Milani, Hans (J.W.) Niemantsverdriet, Peter C. Thüne, *Introducing a new surface science model for Ziegler–Natta catalysts: Preparation, basic characterization and testing*, Journal of Catalysis, 247 (2007) 129-136.

**Chapter four:**

**Adelaida Andoni**, John C. Chadwick, Hans (J.W.) Niemantsverdriet, Peter C. Thüne, *A Flat Model Approach to Ziegler-Natta Catalysts for Propylene Polymerization and a Preparation Method of Well-defined Crystallites of $MgCl_2$-supported Catalysts*, Macromolecular Symposia, 260 (2007) 140-146. (**Award at the 5$^{th}$ international workshop on heterogeneous Ziegler-Natta catalysts for best poster, Ishikawa, Japan, March 2007**).

**Chapter five:**

**Adelaida Andoni**, John C. Chadwick, Hans (J.W.) Niemantsverdriet, Peter C. Thüne, *A Preparation Method for Well-Defined Crystallites of $MgCl_2$-Supported Ziegler-Natta Catalysts and their Observation by AFM and SEM*, Macromolecular Rapid Communications, 28 (2007) 1466-1471. (**Invited cover for Issue No. 14, sponsored by Dutch Polymer Institute**).

**Chapter six:**

**Adelaida Andoni**, John C. Chadwick, Hans (J.W.) Niemantsverdriet, Peter C. Thüne, *The role of electron donors on lateral surfaces of $MgCl_2$-supported Ziegler–Natta catalysts: Observation by AFM and SEM*, Journal of Catalysis, 257 (2008) 81-86. (**Featured in Chemical and Engineering News, 30 June 2008, Volume 86, Number 26, p12**).
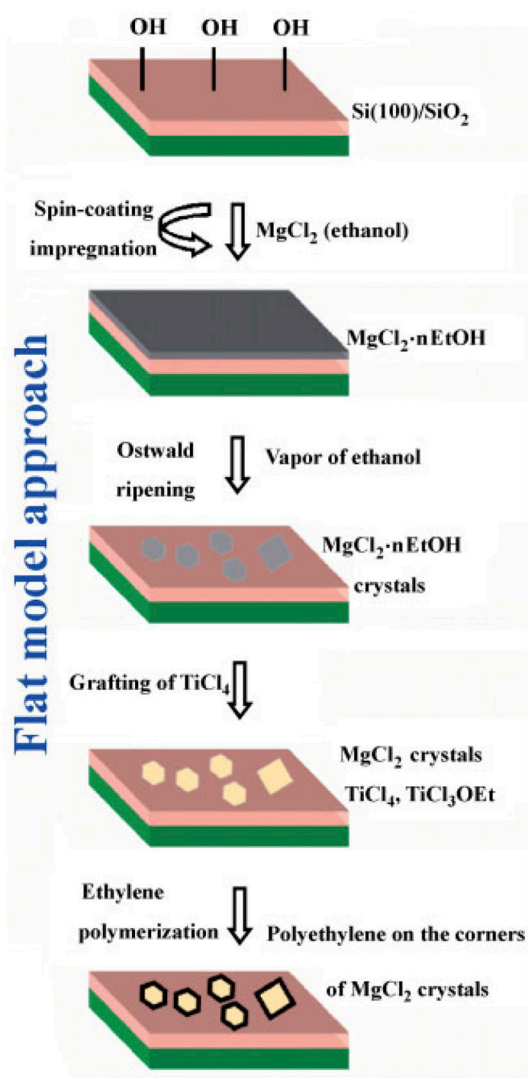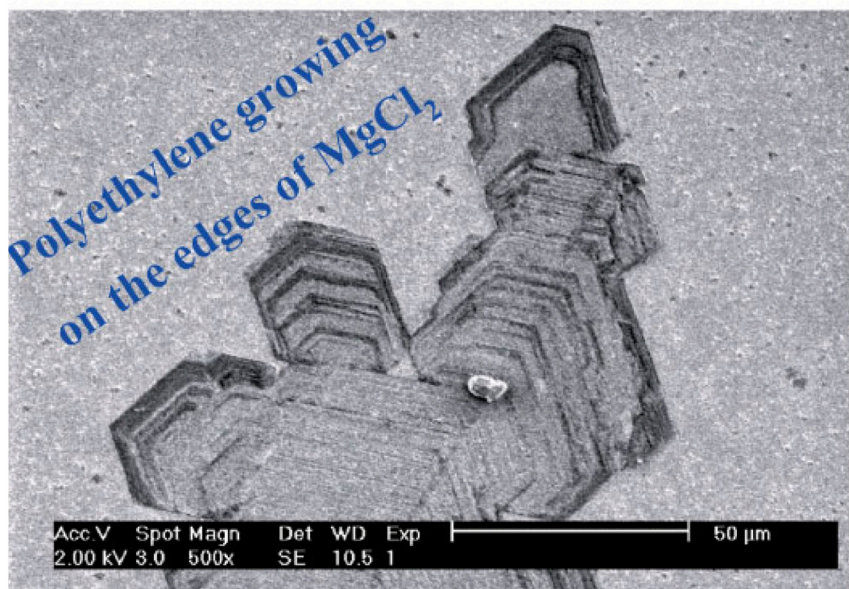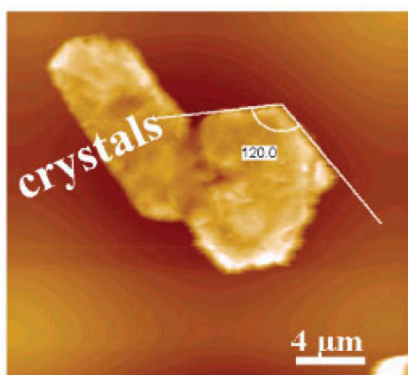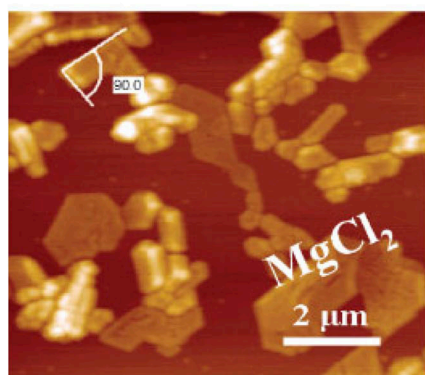
**Chapter seven:**

**Adelaida Andoni**, John C. Chadwick, Merijn E. Donders, Hans (J.W.) Niemantsverdriet, Peter C. Thüne, *Attenuated total reflection infrared spectroscopy for studying planar Ziegler-Natta model catalysts*, in preparation.

# Macromolecular
# Rapid
# Communications



MgCl₂

crystals

2 µm

4 µm

Polyethylene growing
on the edges of MgCl₂

Acc.V  Spot Magn   Det  WD  Exp
2.00 kV 3.0  500x   SE  10.5  1                          50 µm

**Flat model approach**

OH    OH    OH

Si(100)/SiO₂

Spin-coating
impregnation          MgCl₂ (ethanol)

MgCl₂·nEtOH

Ostwald
ripening          Vapor of ethanol

MgCl₂·nEtOH
crystals

Grafting of TiCl₄

MgCl₂ crystals
TiCl₄, TiCl₃OEt

Ethylene
polymerization          Polyethylene on the corners
of MgCl₂ crystals

# 14/2007

# Curriculum vitae

Adelaida Andoni was born in Fier, Albania on January 19, 1974. After she finished High School in 1993 in Fier/Albania she started her studies in 1994 at the University of Tirana/Albania, Faculty of Natural Sciences, Branch of General Chemistry, where she graduated in 1999.

In the period July 2001- July 2002 she worked as a researcher at the Department of Chemical Engineering and Chemistry (group of Theoretical Chemistry) at Eindhoven University of Technology. In December 2002 she joined the master's program in the same department, graduating in the Surface Science group, under the supervision of Prof. Dr. Hans Niemantsverdriet. The topic of the graduation project was "Spectroscopic investigation of CO and NO on Rh(100)".

During this time she worked as a researcher at Spinoza Institute at the Department of Chemical Engineering and Chemistry (group of Macro-Organic Chemistry). The topic of the research was "Synthesis of 2-oxo crown ethers to make well-defined hydrophilic polymers".

In January 2005 she completed her master's study and in February 2005, she commenced her PhD studies in the group of Prof. Dr. Hans Niemantsverdriet. Her research here involved Ziegler-Natta catalysis for olefin polymerization and the most important results of that work are described in this thesis.